

Alma Mater Studiorum - Università di Bologna

FACOLTÀ DI SCIENZE MATEMATICHE FISICHE E NATURALI

Dottorato di Ricerca in Astronomia

Ciclo XXIII

**Accretion Disk Winds in
Active Galactic Nuclei:
an X-ray View**

di

Margherita Giustini

Coordinatore:

Chiar.mo Prof.
Lauro Moscardini

Relatore:

Chiar.mo Prof.
Giorgio G. C. Palumbo

Co-Relatore:

Dr. Massimo Cappi

Co-Relatore:

Dr. Cristian Vignali

Settore Scientifico Disciplinare: Area 02 - Scienze Fisiche

FIS 05 - Astronomia e Astrofisica

Esame Finale 2011

This Ph.D. Thesis has been carried out
at the INAF–IASF Bologna as part
of the institute’s research activities

a Max,

a Cris,

a Giorgio G. C.

Contents

Abstract	1
1 Introduction	5
2 A brief review of accretion disk winds in AGN	9
2.1 Observational properties of UV outflowing absorbers	11
2.2 Observational properties of X-ray outflowing absorbers	16
2.3 Theoretical models for AGN accretion disk winds	20
2.4 X-ray observations of AGN accretion disk winds at the end of 2007	24
3 The Large SDSS/2XMM BAL QSO Sample	27
3.1 The Sample	28
3.2 Observations and data reduction	30
3.3 X-ray spectral Analysis	32
3.4 X-ray hardness ratio analysis	33
3.5 Optical/X-ray photometry	34
3.6 Results	35
3.7 Discussion	37
3.8 Conclusions	45
3.9 Tables and Spectra	46
4 Archival study of BAL, mini-BAL, and NAL PG QSOs	57
4.1 The Sample	58
4.2 Data reduction	60
4.3 X-ray spectral analysis	62
4.4 Results and Conclusions	69

4.5	Tables and Spectra	71
5	The new observational campaign on the mini-BAL QSO PG 1126-041	79
5.1	The source	79
5.2	Observations and data reduction	81
5.3	X-ray timing analysis	81
5.4	X-ray spectral analysis: the average spectra	83
5.5	X-ray time resolved spectral analysis	95
5.6	Optical/X-ray photometry	96
5.7	Discussion	99
5.8	Conclusions	104
6	Serendipitous studies	113
6.1	X-ray observations of high-velocity NAL QSOs	113
6.2	The X-ray BALs of APM 08279+5255	115
7	Theoretical considerations	117
8	Summary of observational results and Conclusions	127
	Appendices	133
A	Publications	133
B	List of acronyms	135
	List of Figures	137
	List of Tables	148
	References	149

Abstract

This Thesis focuses on the X-ray study of the inner regions of Active Galactic Nuclei, in particular on the formation of high velocity winds by the accretion disk itself. Constraining AGN winds physical parameters such as e.g. the outflow velocity, density, ionization state, geometry, and duty cycle, is of paramount importance both for understanding the physics of the accretion/ejection flow onto supermassive black holes, and for quantifying the amount of feedback between the SMBH and its environment across the cosmic time, once and for all. The sources selected for the present study are BAL, mini-BAL, and NAL QSOs, known to host high-velocity winds associated to the AGN nuclear regions. Altogether, these kind of QSO are estimated to be at least 50% of the whole population.

Observationally, a three-fold strategy has been adopted:

- substantial samples of distant $z \sim 2$ sources have been analyzed through spectral, photometric, and statistical techniques, to gain insights into their mean properties as a population;
- a moderately sized sample of $z \sim 0.5$ bright sources has been studied through detailed X-ray spectral analysis, to give a first flavor of the general spectral properties of these sources, also from a temporally resolved point of view;
- the best nearby $z \sim 0.1$ candidate has been thoroughly studied using the most sophisticated spectral analysis techniques applied to a large dataset with a high S/N ratio, to understand the details of the physics of its accretion/ejection flow.

There are three main channels through which this Thesis has been developed:

Archival Studies : the XMM-Newton public archival data has been extensively used to analyze both a large sample of distant BAL QSOs, and several individual bright sources, either BAL, mini-BAL, or NAL QSOs.

New Observational Campaign : I proposed and was awarded with new X-ray pointings of the mini-BAL QSOs PG 1126-041 and PG 1351+640 during the XMM-Newton AO-7 and AO-8. These produced the biggest X-ray observational campaign ever made on a mini-BAL QSO (PG 1126-041), including the longest exposure so far. Thanks to the exceptional dataset, a wealth of informations have been obtained on both the intrinsic continuum and on the complex reprocessing media that happen to be in the inner regions of this AGN. Furthermore, the temporally resolved X-ray spectral analysis field has been finally opened for mini-BAL QSOs.

Theoretical Studies : some issues about the connection between theories and observations of AGN accretion disk winds have been investigated, through theoretical arguments and synthetic absorption line profiles studies.

The Thesis outline is the following:

Chapter 1: the scientific case is introduced.

Chapter 2: accretion disk winds in AGN are reviewed from both an observational and a theoretical point of view.

Chapter 3: the X-ray/UV properties of a $\langle z \rangle \sim 2$ BAL QSOs sample, drawn from the cross-correlation of the SDSS and 2XMM catalogs, are presented.

Chapter 4: the X-ray spectral properties of a $\langle z \rangle \sim 0.5$ sample of BAL, mini-BAL, and NAL QSOs drawn from the PG catalog and observed by XMM-Newton are illustrated with the aid of both time averaged and time resolved X-ray spectral analysis.

Chapter 5: the new XMM-Newton observational campaign on the mini-BAL QSO PG 1126-041 is presented.

Chapter 6: collaborations to the X-ray study of the first NAL QSOs sample, and to the extensive monitoring of the X-ray BALs of APM 08279+5255, are described.

Chapter 7: the connection between theories and observations of AGN accretion disk winds is briefly introduced with the aid of simple absorption line case studies.

Chapter 8: results are summarized and discussed.

The publications related to this Thesis and a list of acronyms used throughout the text are included in the Appendices.

Chapter 1

Introduction

Active Galactic Nuclei (AGN) have been the subject of major astrophysical studies since their discovery, more than half a century ago (Seyfert 1943; Schmidt 1963). Nonetheless, our comprehension of the phenomenon is still far from being complete. Nowadays, AGN studies are of major interest both for the comprehension of the black hole accretion physics, and for understanding the evolution of the Cosmic structures at large.

AGN are the most luminous persistent sources of electromagnetic radiation of the Universe, with a spectral energy distribution (SED) spanning the whole electromagnetic spectrum (Elvis et al. 1994). The big bolometric luminosity of AGN, ($L_{acc} \sim 10^{10-15} L_{\odot}$), that usually outshines the stellar contribution of the host galaxy, is due to accretion onto supermassive black holes (SMBH, $M_{BH} = 10^6-10^9 M_{\odot}$, Rees 1984),

$$L_{acc} = \eta \dot{M} c^2$$

where η is the accretion efficiency, \dot{M} is the mass accretion rate, and c is the speed of light. Their most prominent observational signatures are an excess of emission in the optical/ultraviolet band (the big blue bump, Malkan & Sargent 1982), and a strong and highly variable non-thermal X-ray emission (Elvis et al. 1978; Mushotzky et al. 1993). The UV continuum emission is most probably due to the thermal emission of an optically thick, geometrically thin accretion disk (Shakura & Sunyaev 1973). The disk surrounds the supermassive black hole harbored in the center of the AGN host galaxy, spanning regions from a few up to several thousands of gravitational radii ($r_g \equiv GM_{BH}/c^2$), i.e. from the innermost stable circular orbit around the SMBH up to the disk self-fragmentation radius (e.g., Pringle 1981). The origin of the X-ray continuum emission is less clearly understood and is thought to be the result of the comptonization of accretion disk UV seed photons

into a “cloud” of very hot electrons, the so-called X-ray corona (Haardt & Maraschi 1991; Haardt et al. 1994). What is clear from both variability and microlensing studies is that the X-ray emission region is much smaller than the UV one and spans only a few up to tens of gravitational radii (e.g., Morgan et al. 2008; Chartas et al. 2009b; Dai et al. 2010). X-ray and UV observations are thus directly probing the sub-parsec scale regions of AGN, with X-rays being particularly privileged tracers of the very inner regions of the AGN accretion flow, where also general relativistic effects related to the SMBH spin can be investigated (e.g., Fabian et al. 2000a). The UV and X-ray continuum photons are then reprocessed (absorbed, re-emitted, scattered, reflected) in the interaction with the gas hosted in the inner regions of AGN, so that we almost never observe the primary bare continuum emission of these objects. Conversely, observing the reprocessing features in the UV and X-ray bands can put strong constraints on the geometry, the physical characteristics, and the dynamics of the AGN accretion flow.

Despite the small SMBH dynamical sphere of influence on the host galaxy, there is a strong small/large scale connection in AGN (Kormendy & Richstone 1995). This small/large scale connection has been observationally evident since decades, watching at the radio maps of about 10% of the AGN population, the radio loud (RL) ones, that show powerful jets originating close to the SMBH, and ending up in radio lobes extending, in the most spectacular cases, up to Mpc from the AGN host galaxy (e.g. 3C236, Willis et al. 1974). But in this sense the revolution happened at the crossway between the XX and the XXI century, and interested the whole AGN population, including the much more numerous radio quiet (RQ) one: the suggestion of a relation between the evolution of the SMBH and that of the host galactic spheroid, through some sort of self-regulation mechanism, or *feedback* (Silk & Rees 1998). The observational recognition of the presence of a SMBH at the center of virtually *every* galaxy (Magorrian et al. 1998), including our own (Ghez et al. 1998), coupled with the discovery of a tight correlation between the central M_{BH} and the host galaxy bulge stellar velocity dispersion σ_* (Ferrarese & Merritt 2000; Gebhardt et al. 2000), implied that (a) every galaxy underwent a phase of AGN while building up its central SMBH, and (b) the evolution of the galaxies and of the SMBH must be closely related. As a result, we nowadays usually talk about the “coevolution” of the central SMBH and the host galaxy (see e.g. the 2009 Proceedings of the IAU Symposium N.267). The recognition of this “coevolution” in turn started the search for the physical feedback

mechanism between the SMBH and its environments, and this has been the subject of tens of studies in the last decade.

During the AGN phase, two principal feedback mechanisms can affect the SMBH surrounding environment: radiation pressure and mechanical energy injection. The radiation emitted during the AGN activity can provide significant Compton heating capable of quenching both the cooling flow (Ciotti & Ostriker 2001) and the star formation (Sazonov et al. 2005) in galactic spheroids; however, also mechanical feedback must be invoked to match the observed $M_{\text{BH}} - \sigma_*$ relation (Ciotti et al. 2009). In RL AGN, a supply of mechanical feedback is of course provided by the impact of the radio jets and bubbles on the surrounding gas. The jet mechanical heating of the intergalactic medium helps quenching the star formation in the most massive spheroids and thus matching the Λ CDM model expectations with the observed bright end of the galaxy luminosity function (Croton et al. 2006). Radio jets are also responsible for inflating hot bubbles in the intracluster medium, thus quenching the cooling flow at the center of rich clusters of galaxies (Fabian et al. 2000b, 2006; Sanders et al. 2009), and for heating the intracluster and intragroup medium reproducing the observed $L_x - T$ relation in poor clusters and groups of galaxies (Lapi et al. 2005). Globally, the fraction of AGN involved in these phenomena is low, and the highly collimated nature of the jet disfavors an efficient deposition of energy over large solid angles. It is argued that the mechanical feedback due to radio jets is important only in low-accreting ($L/L_{\text{Edd}} < 0.01$) AGN (e.g., Ciotti et al. 2009), and it is not the dominant feedback mechanism from a Cosmological point of view.

Another way of providing mechanical feedback is through (radiatively) dark, massive, wide-angle *AGN winds/outflows*, that are naturally expected in highly accreting systems and during the merging phase of the AGN evolution (e.g., King & Pounds 2003; Proga & Kallman 2004; Hopkins et al. 2006). *This kind of feedback* is the most promising in explaining the observed $M_{\text{BH}} - \sigma_*$ relation (Di Matteo et al. 2005), the galaxy downsizing (Scannapieco et al. 2005), the metal enrichment of the IGM and the formation of dust at high redshift (Elvis et al. 2002), and the evolution of the Cosmic structures as a whole (Scannapieco & Oh 2004), thus reconciling several Cosmological Λ CDM model predictions with the experimental observations (see e.g. Elvis 2006). Outflows from AGN are actually observed as blueshifted absorption features imprinted in their UV and X-ray continua, associated to intrinsic nuclear winds. Once corrected for selection effects, intrinsic UV

absorption lines blueshifted by 10^{3-5} km s⁻¹ are present in about 50% of AGN (Crenshaw et al. 2003; Ganguly & Brotherton 2008; Allen et al. 2011). The X-ray warm absorbers and ultra fast outflows (UFOs, Tombesi et al. 2010a) are observed in about 50% and 40% of the local/bright AGN population, respectively (Reynolds 1997; Piconcelli et al. 2005; McKernan et al. 2007; Tombesi et al. 2010a). The range in ionization state of the outflowing gas is very large, from Mg II in LoBAL QSOs to Fe XXVI in X-ray UFOs. What is the physical link between the UV and X-ray outflowing absorbers, and what is the dynamical behavior of the wind, is far from being understood. Understanding the physical mechanism responsible for launching and accelerating AGN winds means unveiling the link between the accretion and ejection processes in AGN and their evolution, and quantifying the kinetic energy injection associated to AGN winds means quantifying their impact on the surrounding environment and so their role into the co-evolution of the cosmic structures.

This thesis focuses on the X-ray observational study of the most promising physical mechanism able to link the small and the large scale phenomena in AGN, to shed light on the physics of the accretion/ejection around SMBH, and to help quantifying the actual impact of AGN outflows on the surrounding environment: accretion disk winds. A brief review of observational and theoretical properties of accretion disk winds in AGN is presented in Chapter 2.

Chapter 2

A brief review of accretion disk winds in AGN

The vast majority of both theoretical and observational works about AGN outflows concerns the first class of objects discovered to host strong nuclear outflows: Broad Absorption Line Quasars¹ (BAL QSOs, e.g. Turnshek et al. 1980; Weymann et al. 1991). These are 10-15% of optically selected QSOs that show broad (FWHM $\gtrsim 2000 \text{ km s}^{-1}$) UV absorption lines due to resonant transitions of ionized metals such as Mg II, Al III, Si IV, C IV, N V, O VI, strongly blueshifted with respect to the systemic redshift of the source. This indicates outward motions along the line of sight with typical velocities of several 10^3 km s^{-1} , and extending up to $\sim 60\,000 \text{ km s}^{-1}$ (e.g. Q1414+087, Foltz et al. 1983). Other intrinsic blueshifted absorbers, narrower than the UV BALs, but involving the same ionic transitions and the same outflow velocity range, are often observed in the UV band of AGN. Depending on the width of the absorption troughs, quasars hosting such features are classified as mini-Broad Absorption Line Quasars (mini-BAL QSOs, $500 \text{ km s}^{-1} < \text{FWHM} < 2000 \text{ km s}^{-1}$), and Narrow Absorption Line Quasars (NAL QSOs, $\text{FWHM} < 500 \text{ km s}^{-1}$; Ganguly et al. 2001; Hamann & Sabra 2004). NAL and mini-BAL QSOs are much less studied than the BAL QSO population, and only in the last years systematic studies have been started. From top to bottom, the left column of Fig. 2.1 shows an example of BAL, mini-BAL, and NAL spectral profile.

In the X-ray band, absorption due to ionized species such as N VI-VII, O VII-VIII, Mg XI-XII, Al XII-XIII, Si XIII-XVI, as well as L-shell transitions of Fe XVII-XXIV, is observed to be blueshifted by a few $10^{2-3} \text{ km s}^{-1}$ in $\sim 50\%$ of type 1 AGN (the “warm

¹In this Thesis I will use the terms AGN, Quasar, QSO, as synonyms, unless otherwise stated.

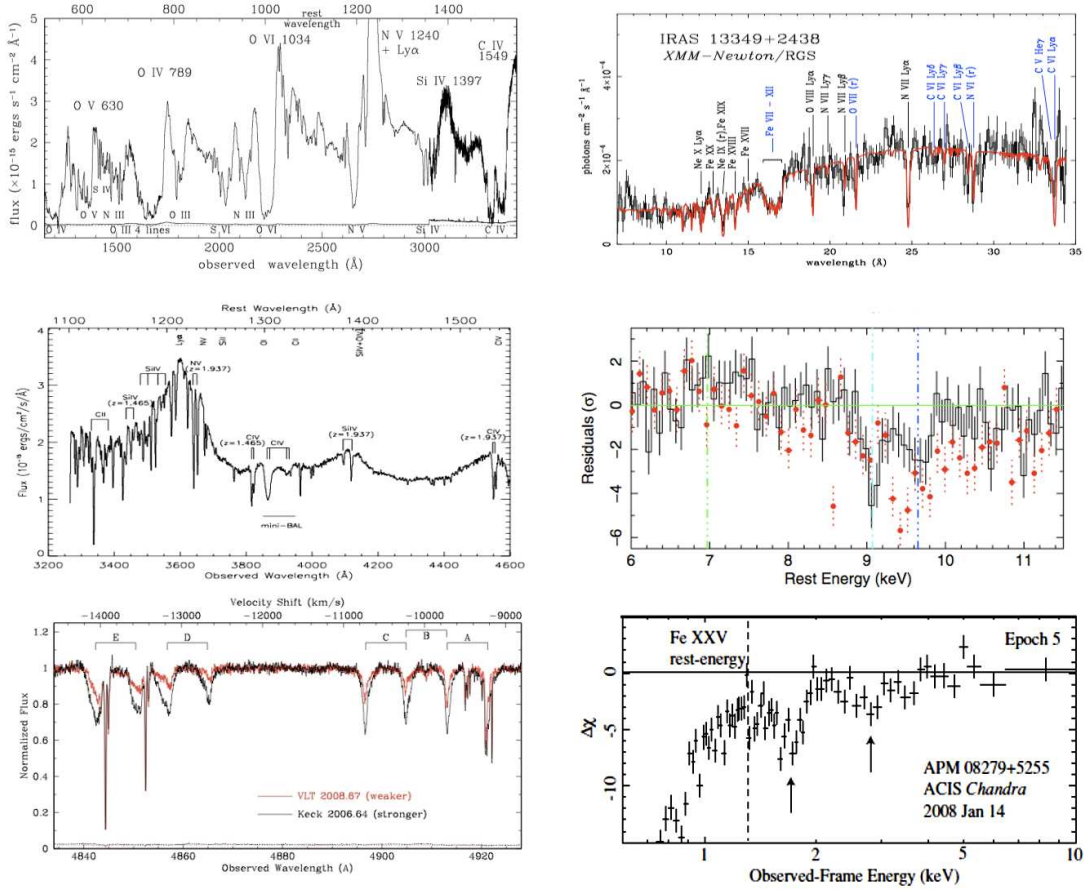


Figure 2.1. Top left panel: STIS spectrum of the BAL QSO PG 0946+301, from Arav et al. (2001). Middle left panel: Lick spectrum of the mini-BAL QSO PG 0935+417, from Rodríguez Hidalgo et al. (2011). Bottom left panel: VLT (red) and Keck (black) spectra of the NAL QSO J2123-0050, from Hamann et al. (2011). Top right panel: *XMM-Newton* RGS spectrum of IRAS 13349+2438, showing the X-ray warm absorber, from Sako et al. (2001). Middle right panel: Suzaku XIS spectrum of PDS 456, showing a X-ray UFO in the iron K band, from Reeves et al. (2009). Bottom right panel: X-ray BALs detected by *Chandra* ACIS in APM 08279+5255, from Chartas et al. (2009c) To appreciate the different width of the absorption features, notice the different wavelength/energy scale in the different panels.

absorber”, e.g. Reynolds 1997; Piconcelli et al. 2005; McKernan et al. 2007). Moreover, in the last years, thanks to the high collecting area of X-ray satellites such as *XMM-Newton*, *Chandra*, and *Suzaku*, blueshifted absorption lines due to highly ionized gas (i.e. Fe XXV, Fe XXVI) outflowing at much higher velocity ($v_{out} \sim 0.05-0.2c$) have been observed in a number of AGN, at both low and high redshift (see e.g. Pounds et al. 2003; Reeves et al. 2003; Dadina et al. 2005; Risaliti et al. 2005; Markowitz et al. 2006; Cappi 2006; Braitto

et al. 2007; Miniutti et al. 2007; Cappi et al. 2009; Ponti et al. 2009; Reeves et al. 2009; Tombesi et al. 2010a,b, and references therein). X-ray BALs in He-like iron, blueshifted up to $v_{out} \sim 0.7c$, have been observed in gravitationally lensed BAL and mini-BAL QSOs (Chartas et al. 2002, 2003, 2009c). The right column of Fig. 2.1 shows examples of recent observations of X-ray warm absorbers, UFOs, and BALs, from top to bottom.

In the following, I will review the main properties of the UV and X-ray outflowing absorbers from both observational and theoretical point of view. Observational evidences for the UV and the X-ray outflowing absorbers are presented in Section 2.1 and Section 2.2, respectively. Theoretical scenarios for the launch and the acceleration of accretion disk winds in AGN are reviewed in Section 2.3. State of the art X-ray observations of UV absorbed QSOs at the end of 2007 are presented in Section 2.4.

2.1 Observational properties of UV outflowing absorbers

BAL QSOs have been known since the late 60s (PHL 5200, Lynds 1967), but the first attempts to study them in a broad astrophysical context started at the beginning of the 80s (Weymann et al. 1981), and the first systematic study appeared only at the beginning of the 90s (Weymann et al. 1991). The first studies of BAL QSOs have been of course performed on optical spectra; the observation of the typical BAL transitions (e.g., C IV $\lambda 1549\text{\AA}$) from optical ground telescopes is possible only for sources with a cosmological redshift $z \gtrsim 1.5$. Coupled with the low occurrence of BALs among the optically selected QSO population (around 10-15%, Weymann et al. 1991; Hewett & Foltz 2003), this made these BAL studies very challenging and rare. Indeed, only about twenty BAL QSOs were known at the beginning of the 80s, and all of them at $z > 1.6$. Only after the launch of the *IUE* satellite in 1978 it became possible to discover BAL features in lower redshift QSOs and to start studying in detail the UV absorption properties of well known samples as the Palomar bright quasar survey (PG QSOs, Schmidt & Green 1983). The number of known low redshift BAL QSOs further increased after the launch of the *HST* (1990) and *FUSE* (1999) satellites, however also nowadays it still remains very low if compared with the number of known BAL QSOs at higher redshift, because of the predominance of large optical QSO surveys performed from ground. The Weymann et al. (1991) sample comprised about 30 BAL QSOs homogeneously selected from the LBQS, all of them at around $z \sim 2$. This study allowed to assess the great similarity of the UV emission lines

properties of BAL and non-BAL QSOs. Peculiar optical properties of BAL QSOs were instead discovered to be the strong Fe II and the weak [O III] emission (Weymann et al. 1991; Boroson & Meyers 1992), and the high degree of polarization (Moore & Stockman 1984), with respect to non-BAL QSOs. Furthermore, the greater amount of polarization in the absorption troughs than in the emission lines suggests a strong contribution by scattered emission with respect to direct emission, and the increase in polarization toward shorter wavelengths suggests dust to be a possible source of continuum scattering (Schmidt & Hines 1999; Ogle et al. 1999). As for the radio properties, for years BAL QSOs and radio loudness have thought to be mutually exclusive phenomena (e.g., Stocke et al. 1992). The first Radio Loud BAL QSO was discovered by Becker et al. (1997); since then, thanks to deeper and deeper radio surveys, the number of RL BAL QSOs has substantially increased. Today, the biggest BAL QSO samples are drawn from the largest optical survey ever made, the Sloan Digital Sky Survey (SDSS, York et al. 2000). Started around 2000, the SDSS now provides catalogs of several thousands of optically selected BAL QSOs (Reichard et al. 2003b; Trump et al. 2006; Gibson et al. 2009).

BAL QSOs are divided in three main classes of increasing rarity. High ionization BAL QSOs (HiBALs) show blueshifted, deep absorption troughs corresponding to resonant transitions of highly ionized elements (e.g., C IV, N V, Si IV, O VI) and are usually classified by means of their C IV $\lambda 1549$ BAL profile. Low ionization BAL QSOs (LoBALs, Weymann et al. 1991; Voit et al. 1993) show, in addition to the high ionization ones, absorption troughs due to less ionized elements (e.g., Mg II, Al II, Al III) and are generally identified as BALs by the Mg II $\lambda 2798$ line profile. While HiBALs are found in ~ 10 - 15% of optically selected QSOs, LoBALs are more unusual and comprise about 1% of optically selected QSOs. Even rarer are the so-called FeLoBALs (Hazard et al. 1987), that in addition to the above mentioned transitions, show broad absorption troughs in lowly ionized iron (e.g., Fe II, Fe III) and are found in about 0.1% of optically selected QSOs. The different spectral appearance of these BAL subclasses can be seen in Fig. 2.2 in comparison with the mean SDSS QSO spectrum. I stress here that FeLoBALs are a subsample of LoBALs, that in turn are a subsample of HiBALs, meaning that high ionization state transitions are always present in the spectrum of every BAL QSO. Given the wavelengths of the transitions used to identify BAL QSOs, in order to observe HiBALs and LoBALs from ground telescopes one must select sources at high redshift. As an

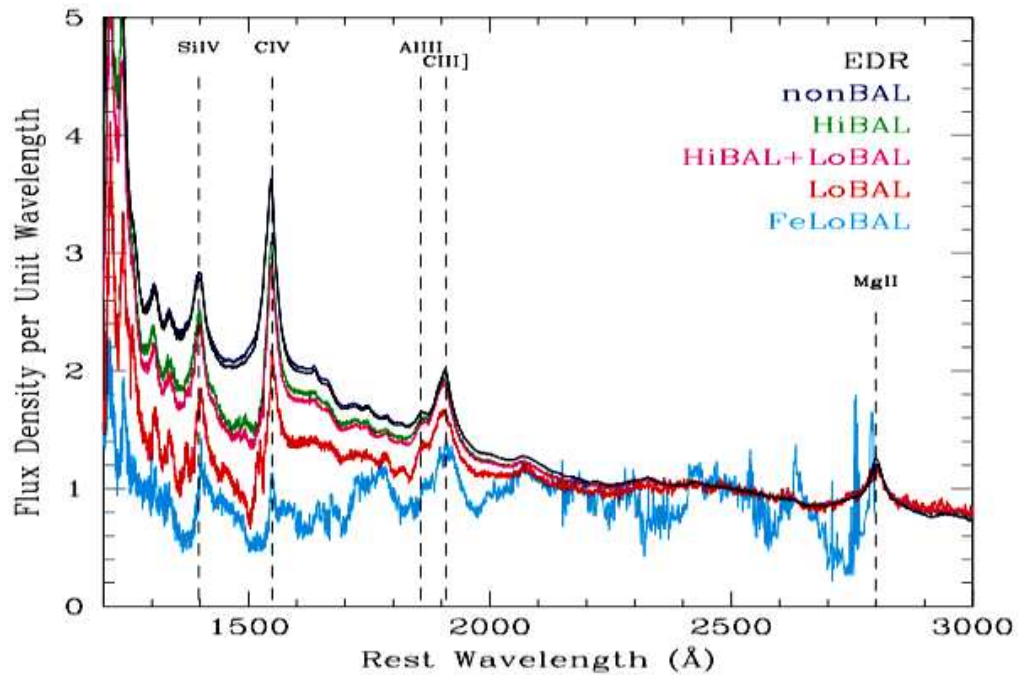


Figure 2.2. Composite SDSS spectra of different BAL subclasses, compared with the mean QSO (in black), taken from Reichard et al. (2003a).

example, the SDSS, covering the 3800-9200 Å window in the earth rest-frame, allows to search for HiBALs at $1.7 < z < 4.4$, for LoBALs at $0.5 < z < 2.2$.

Historically, two opposite interpretations have been given for the small observed fraction of optically selected BAL QSOs. The observed fraction could correspond either to the covering fraction of a wind present in all AGN and visible only for certain lines of sight (Junkkarinen 1983; Turnshek 1984), or to the intrinsic fraction of QSOs hosting totally covering massive nuclear winds, so tracing an evolutionary phase of the AGN activity lasting $\sim 10 - 15\%$ of their lives (Surdej & Hutsemekers 1987). The great similarities between the optical/UV emission line and continuum properties of BAL and non-BAL QSOs support the first scenario (e.g., Weymann et al. 1991; Reichard et al. 2003a). In the latter scenario, the large amount of gas and dust surrounding the central source should lead to enhanced far-infrared and submillimeter emission in BAL QSOs with respect to non-BAL QSOs. Recent studies found no (Willott et al. 2003) or little (Priddey et al. 2007) differences among the two populations; however, deeper observations of larger samples are needed to assess a firm conclusion. A support to the latter scenario came instead from radio observations of BAL QSOs, that showed both a variety of spectral indices

(indicating different inclination angles with respect to the line of sight, e.g. Becker et al. 2000), and/or that the host is a compact and young radio source for several BAL QSOs (e.g., Liu et al. 2008; Montenegro-Montes et al. 2009, and references therein). Despite the geometrical and the evolutionary scenarios are usually considered as mutually exclusive, we will see that the truth could be in the middle, as often, and as already been suggested by Morris (1988). To come to this conclusion however, a few decades of studies and new observations of always greater quality have been needed.

Thanks to the high data quality of modern surveys such as the SDSS, 2MASS, FIRST, and others, some statistically significant differences have been found in the properties of the different subclasses of BAL QSOs. For example, SDSS studies on the optical spectra showed how the amount of reddening dramatically increases from non-BAL, to HiBAL, to LoBAL, to FeLoBAL QSOs (e.g., Reichard et al. 2003a, see Fig. 2.2). Also the observed frequency of BAL QSO is strongly dependent on both the subclass, and wavelength used for the selection. Krolik & Voit (1998) suggested for a bias against optical detection of BAL QSOs, in that the intrinsic fraction could be much larger. Already Becker et al. (1997) and Becker et al. (2000), based on their small RL BAL QSO samples, argued that the radio selection yields a fraction of BAL QSOs much larger (by about a factor of two) than the optical selection, and that it is especially efficient in selecting the optically elusive LoBAL and FeLoBAL QSOs subpopulations. These early results were confirmed with much bigger samples by Shankar et al. (2008), that not only found a double fraction of radio-selected than optically-selected BAL QSOs, but also a significant anti-correlation between the BAL QSO fraction and the intrinsic radio power. A fraction of BAL QSOs double than optical was also found among IR-selected QSOs, (Dai et al. 2008). The especially distinct IR properties of LoBAL and FeLoBAL QSOs (such as hosting more dust than HiBAL QSOs, Sprayberry & Foltz 1992) paved the way to the suggestion of their actual representation of an evolutionary phase of the AGN life (e.g., Voit et al. 1993). Canalizo & Stockton (2001) found a high percentage of disturbed morphologies in LoBALs host galaxies, indicating a possible connection with the merger process. In their combined FIRST/2MASS sample of red QSOs, Urrutia et al. (2009) found again a very high ($\sim 37\%$) fraction of BAL QSOs, with a predominance (with respect to optically selected samples) of LoBAL QSOs; extraordinary IR properties pointing to a transitional phase of the AGN life were lately argued also for FeLoBAL QSOs (Farrah et al. 2007). It must be stressed

that the number statistics for LoBALs, and especially FeLoBALs studies, is really low. Furthermore, in their analysis of the SED characteristics of 38 BAL QSOs, Gallagher et al. (2007) found no significant differences in any band (including the IR) between BAL and non-BAL QSOs. Altogether, these observational evidences are suggesting again a scenario more complicated than the pure geometrical or the pure evolutionary one.

BAL QSOs are historically identified by means of their Balnicity Index (BI, Weymann et al. 1991), that is a C IV equivalent width measure modified in order to exclude, from low-resolution UV spectra, intervening absorbers and narrow intrinsic absorption lines. Specifically, BI is computed considering any absorption trough spanning $\geq 2000 \text{ km s}^{-1}$ in width, absorbing at least 10% of the local continuum, and blueshifted by $\geq 3000 \text{ km s}^{-1}$ with respect to the corresponding emission lines. While this widely used criterion assures that all QSOs with $\text{BI} > 0 \text{ km s}^{-1}$ are really BAL QSOs, it may exclude intrinsic absorption troughs if starting very near the emission lines and/or high velocity, but somewhat narrow ones, as mini-BALs and NALs. For these reasons, a less restrictive criterion to identify BAL QSOs has been introduced in the last years, the Absorption Index (AI, Hall et al. 2002). This index is computed in the same way as BI, but relaxing the 3000 km s^{-1} blueshift criterion and considering all absorption troughs with a blueshift $> 0 \text{ km s}^{-1}$ with respect to the corresponding emission lines, and with a width of at least 1000 km s^{-1} . The AI includes most of the mini-BALs, but excludes all the NAL QSOs from the census. It was demonstrated by Knigge et al. (2008) that while the use of BI excludes some BAL QSOs, the inattentive use of AI leads to an overestimate of the true fraction of BAL QSOs. For “true” BAL QSOs the AI is found to have values $\gtrsim 1000 \text{ km s}^{-1}$, independently from BI values. BAL QSO fraction estimates made using the whole range of AI are more or less double with respect to fraction estimates made using the more conservative BI, independently of the wavelength used for the selection (e.g., Trump et al. 2006; Dai et al. 2008; Shankar et al. 2008). The “non-true” BAL QSO family includes both mini-BALs, NALs, and non intrinsic, intervening absorption systems. While mini-BAL features are broad enough to be easily identified and ascribed to be intrinsic to the host QSO, and are usually considered as a low-velocity manifestation of the BAL phenomenon, determining the intrinsic nature of NAL features is much more difficult, and the association of some of them to powerful outflows intrinsic to the host AGN has only recently been recognized. As first pointed out by Barlow et al. (1997) and reviewed by Narayanan et al.

(2004), there are a few observational tests that can definitely discriminate between narrow absorption line systems intrinsic and extrinsic (i.e. intervening, physically unrelated) to the QSO: notably, time variability of the absorption line profiles, and partial coverage of the intrinsic continuum. Both methods require high S/N, high resolution optical/UV spectroscopy. The first intrinsic NAL system has been discovered by Hamann et al. (1995) by means of time variability studies of the absorption troughs profiles. Subsequently, a few other intrinsic NALs have been recognized (e.g., Hamann et al. 1997a,c,b; Barlow & Sargent 1997; Misawa et al. 2003; Ganguly et al. 2003; Wise et al. 2004; Misawa et al. 2005), but the census of NAL QSOs grew slowly, with about two dozens of intrinsic NAL systems known in 2005. Ganguly et al. (1999) and Ganguly et al. (2001) first discussed the origin of the gas responsible for the UV NALs in the context of accretion disk winds, suggesting a location at higher latitudes than the gas responsible for the UV BALs, and thus a purely geometrical cause for the appearance of narrow or broad absorption lines (Fig. 2.3, top panel). Also Elvis (2000) proposed a phenomenological, geometry-dependent scenario for explaining the observational characteristics of type 1 QSOs invoking the presence of an accretion disk wind. In this scenario, the gas responsible for the UV NALs is at low latitudes above the disk, in the inner flow that rises almost perpendicular before bending and becoming conical, and is thus predicted to reveal large obscuration when observed in X-rays (Fig. 2.3, bottom panel). The first sizeable sample of NAL QSOs has been presented by Misawa et al. (2007a), that also estimated the intrinsic fraction of NAL QSO to be around 50%.

A review of the nature of NAL, mini-BAL, and BAL QSOs can be found in Hamann & Sabra (2004).

2.2 Observational properties of X-ray outflowing absorbers

The first detection of ionized X-ray absorption in AGN is dated back at the beginning of the 80s (the warm absorber in MR2251-178, Halpern 1984), at the times of the *Einstein* satellite. Subsequent observations of AGN performed with satellites such as *Exosat*, *Ginga*, and *ROSAT* were able to confirm the presence of warm absorption (e.g. due to O VII/O VIII K shell transitions) in the X-ray spectra of several nearby AGN (e.g., Yaqoob et al. 1989; Nandra et al. 1990, 1993; Turner et al. 1993). However, only after the launch of the *ASCA* (1990) and *BeppoSax* (1996) satellites it was possible to resolve the O VII/O VIII

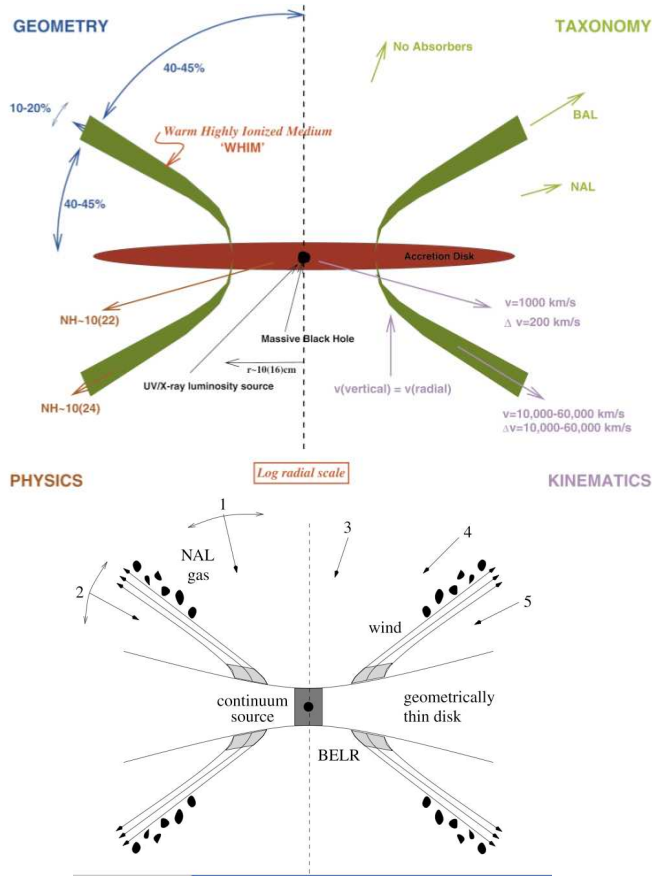


Figure 2.3. Two phenomenological scenarios for accretion disk winds. Top panel: Figure 1 from Elvis (2000). Bottom panel: Figure 13 from Ganguly et al. (2001).

absorption edges, and thus roughly measure the ionization state and the column density of the absorbing gas, and to perform such studies on large samples of nearby AGN. These studies revealed the presence of warm absorption by a gas with $\log \xi \sim 0 - 2 \text{ erg cm s}^{-1}$ and $\log N_H \sim 20 - 22 \text{ cm}^{-2}$ in $\sim 50\%$ of such AGN (e.g., Reynolds 1997; George et al. 1998). The great step forward in warm absorbers studies happened after the launch of the *Chandra* and *XMM-Newton* satellites, in 1999. The presence on board of high-resolution grating spectrometers allowed the detection of *blueshifted* narrow absorption lines in the soft X-ray band of several nearby AGN (e.g., Kaastra et al. 2000; Kaspi et al. 2000; Collinge et al. 2001; Sako et al. 2001; Kaspi et al. 2002). The first systematic high-resolution study of X-ray warm absorption in nearby, bright, type 1 AGN was performed by McKernan et al. (2007). These authors found warm absorption to be present in more than a half of their sample; the ionization state, the column density, and the velocity

shift of this gas was found to span a large range of values ($\log \xi \sim 0 - 4 \text{ erg cm s}^{-1}$, $\log N_H \sim 20 - 23 \text{ cm}^{-2}$, $\log v_{out} \sim 1 - 3 \text{ km s}^{-1}$), and usually multiple kinematic and ionization state components were required to reproduce the data. On the other hand, it is still not possible to perform grating observations on distant (e.g. QSOs) sources; anyway, the high collecting area of *Chandra* and especially of *XMM-Newton* allowed to detect through CCD-quality spectroscopy the presence of absorption edges due to highly ionized oxygen (i.e., the warm absorber) also in $\sim 50\%$ of the QSOs belonging to the PG Catalog (Piconcelli et al. 2005). It became evident that outflowing warm absorbers are a fundamental ingredient to understand the AGN structure.

Another spectacular breakthrough provided by *Chandra*, *XMM-Newton*, and *Suzaku* (launched in 2005), was the detection of extremely highly ionized ($\log \xi \gtrsim 3 - 4 \text{ erg cm s}^{-1}$) spectral absorption lines in the iron K band of a number of AGN (see e.g. Pounds et al. 2003; Reeves et al. 2003; Dadina et al. 2005; Risaliti et al. 2005; Markowitz et al. 2006; Cappi 2006; Miniutti et al. 2007; Ponti et al. 2009; Tombesi et al. 2010b, and references therein). The observed blueshift of such features implied outflow velocities of the order of $\sim 0.1c$ or more, and up to $\sim 0.3c$. The implied column densities and mass outflow rates associated to these outflows are very high, $\log N_H \sim 23 - 24 \text{ cm}^{-2}$, $\dot{M}_{out} \sim \dot{M}_{acc}$, suggesting an important contribution to the energetic of the AGN/host galaxy system. The veracity of such features has been questioned by McKernan et al. (2004) as possibly due to the contamination by hot gas in the vicinity of our galaxy (see panel a of Fig. 2.4): the lack of spatial correspondence between the position on the sky of the AGN with such detected features and of the hot diffuse emission of our galaxy as detected by *ROSAT* established that this was not the case (see panel b of Fig. 2.4, Cappi et al. 2008). The intrinsic nature of such absorption features is also supported by the strong temporal variability observed, often over very short time scales (e.g., Braitto et al. 2007; Cappi et al. 2009). Also the statistical significance of such features has been debated on the basis of the so-called “publication bias” (panel c of Fig. 2.4, Vaughan & Uttley 2008); the thorough statistical analysis of a large homogeneous sample of AGN performed by Tombesi et al. (2010a) solved also this issue, definitely assessing the veracity of highly ionized, high velocity outflows in AGN (panel d of Fig. 2.4). Tombesi et al. (2010a) also determined the frequency of such winds, called ultra-fast outflows (UFOs), to be $\sim 40\%$ in their sample of local, bright AGN.

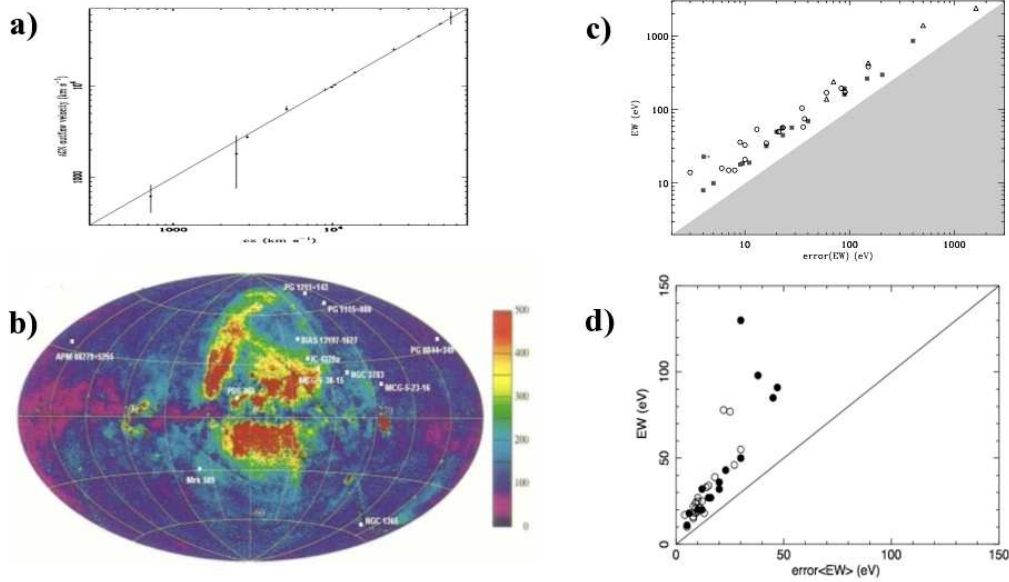


Figure 2.4. The veracity of X-ray UFOs has been lately confirmed. Panel a): measured outflow velocity versus cosmological recession velocity for a sample of high-velocity X-ray outflows, from McKernan et al. (2004). Panel b): location in the sky of the AGN with high-velocity X-ray outflows detected, taken from Cappi (2006), superimposed on the *ROSAT* 0.75 keV map taken from Snowden et al. (1997) where the color scale is in 10^{-6} ct s $^{-1}$ arcmin $^{-2}$. Panel c): equivalent width and its associate error for the absorption lines associated to high-velocity X-ray outflows taken from Vaughan & Uttley (2008), plotted in logarithmic scale. Panel d): equivalent width and its associate error for the absorption lines associated to high-velocity X-ray outflows taken from Tombesi et al. (2010a), plotted in linear scale.

Finally, spectacular broad absorption features in the iron K band have been observed in a number of high redshift, gravitationally lensed BAL and mini-BAL QSOs (APM 08279+5255 and PG 1115+080, Chartas et al. 2002, 2003). The observed blueshift of such X-ray BALs imply line of sight velocities up to $0.7c$ (Chartas et al. 2009c); they are found to be extremely variable in both velocity and equivalent width. X-ray BALs are briefly introduced in Section 2.4; the latest scientific developments are instead described in Chapter 6.

What is the physical link between the UV and X-ray outflowing absorbers, and what is the dynamical behavior of the wind, is far from being understood. There is a one-to-one correspondence between the presence of low-velocity ($v_{out} \sim 100 - 1000$ km s $^{-1}$) UV NALs and the X-ray warm absorbers in nearby AGN (Crenshaw et al. 1999). As for the other observed spectral features (high-velocity UV NALs, mini-BALs, BALs, X-ray UFOs,

X-ray BALs), there is no clear connection between them. For example, X-ray UFOs are observed in both BAL (e.g. PG 1126-041, Chapter 5 of this Thesis) and non-BAL QSOs (e.g. PG 1211+143, Pounds et al. 2003), while X-ray BALs have only been observed in BAL QSOs (Chartas et al. 2002, 2003). Furthermore, the presence of UV NALs, mini-BALs, and BALs, is not mutually exclusive: some AGN display all the three of them; in some others an evolution from mini-BAL to BAL, or viceversa, has been observed. A comprehensive review on the UV and X-ray observations of AGN outflows (prior to the discovery of X-ray UFOs and BALs) can be found in Crenshaw et al. (2003).

2.3 Theoretical models for AGN accretion disk winds

I will consider here the efficient accretion mode for AGN, in the form of a geometrically thin, optically thick accretion disk as first depicted by Shakura & Sunyaev (1973) and reviewed by Pringle (1981). For any detail, I refer to Frank et al. (2002). The luminosity emitted by accretion onto SMBH can be expressed as

$$L_{acc} = \eta \dot{M}_{acc} c^2 \quad \text{erg s}^{-1} \sim 5.7 \left(\frac{\eta}{0.1} \right) \left(\frac{\dot{M}_{acc}}{1M_{\odot}\text{yr}^{-1}} \right) \times 10^{45} \quad \text{erg s}^{-1}$$

where η is the accretion efficiency, $\eta \sim 0.06$ for non rotating (i.e. Schwarzschild-like) SMBH, $\eta \sim 0.4$ for maximally rotating (i.e. Kerr-like) SMBH, \dot{M}_{acc} is the mass accretion rate, and c is the speed of light. A useful quantity to compare the accretion luminosity of AGN with is the Eddington luminosity, that is, the maximum possible accretion luminosity due to a spherically symmetric distribution of fully ionized, pure hydrogen gas, where the radiation pressure due to accretion and the gravitational pull due to the SMBH are balanced:

$$L_{Edd} = \frac{4\pi G M_{BH} m_p c}{\sigma_T} \quad \text{erg s}^{-1} \sim 1.3 \left(\frac{M_{BH}}{10^8 M_{\odot}} \right) \times 10^{46} \quad \text{erg s}^{-1}$$

where G is the gravitational constant, M_{BH} is the SMBH mass, m_p is the proton mass, and σ_T is the Thomson cross section. The Eddington ratio is defined as $\lambda \equiv L_{acc}/L_{Edd}$. For “highly accreting AGN” one can assume in a conservative way $\lambda > 0.01$. The SMBH mass, M_{BH} , sets a normalization factor not only for the accretion rate, but also for the distance, with the gravitational radius

$$r_g = GM_{BH}/c^2 \quad \text{cm} \sim 1.5 \left(\frac{M_{BH}}{10^8 M_{\odot}} \right) \times 10^{13} \quad \text{cm}$$

from which, a “normalized” time scale follows, the light crossing time $t_L = r_g/c \sim 500(M_{BH}/10^8 M_\odot)$ s.

There are three main mechanisms that can launch a wind from the surface (the atmosphere) of the accretion disk: thermal, radiation, and magnetic pressure. In either case, a wind will be launched only if the pressure can overcome the SMBH gravity pull; as a rule of thumb, the closer to the SMBH is the launching point, the higher is the wind terminal velocity. The AGN radiation field, and especially X-rays, can heat up the disk atmosphere through Compton heating, and the resulting thermal pressure can be effective in launching a wind if the thermal velocity exceeds the local escape velocity. In AGN, thermal driving can account for winds launched at large radii (\sim pc scales), where the escape velocity is small. Such winds will have maximum terminal velocities of the order of a few 1000 km s^{-1} , and they have demonstrated to be successful in reproducing the observed characteristics of the X-ray warm absorber and the low-velocity UV NALs (e.g., Balsara & Krolik 1993; Krolik & Kriss 1995, 2001; Chelouche & Netzer 2005). In order to explain the other, high velocity outflowing UV and X-ray absorbers, either radiation or magnetic pressure launching and driving must be invoked.

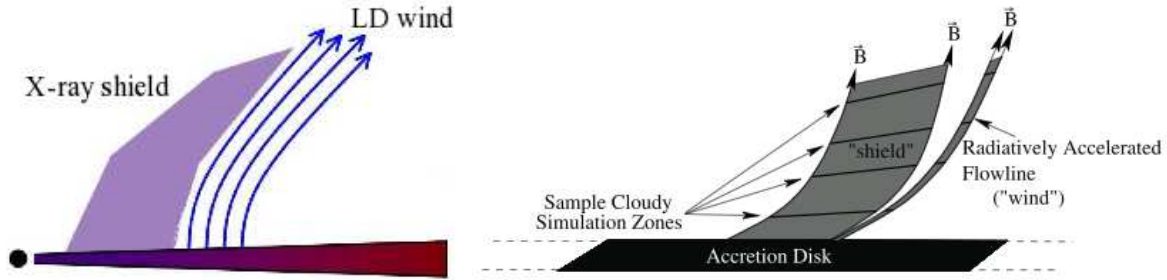


Figure 2.5. Sketches of two possible geometries for accretion disk winds. Left panel: the UV line-driven wind of Murray et al. (1995), as readapted by Gallagher & Everett (2007); right panel: the magnetically driven wind of Everett (2005).

The great amount of electromagnetic radiation is one of the most distinctive signatures of AGN. The momentum associated to L_{acc} accelerates the gas, with both continuum and spectral line driving. By definition, when $L_{acc} > L_{Edd}$ the continuum radiation pressure overcomes gravity, the accretion stops, and an episodic wind is expected. But also at $L_{acc} < L_{Edd}$ the radiation pressure of the UV photons emitted by the accretion disk can effectively launch and accelerate powerful winds. This is because, at the right ionization state, the opacity in the UV resonance spectral lines is much greater than the opacity in

the continuum, i.e. $\sigma_{line} \gg \sigma_T$. The quantity that expresses the increase in the radiation force due to the opacity contribution of the spectral lines with respect to the pure electron scattering case, is called force multiplier, after Castor et al. (1975). A wind launched and accelerated by this mechanism is usually called line-driven (LD). Models for LD winds were first developed for the O-stars, with success (e.g., Lucy & Solomon 1970; Castor et al. 1975; Abbott 1982). As first pointed out by Murray et al. (1995), UV line-driving is able to launch equatorial accretion disk winds also in highly accreting AGN. The covering fractions and terminal velocities are similar to those observed in BAL QSOs, given that the UV absorbing gas is *shielded* from the strong X-ray continuum source by a great amount of X-ray absorbing gas. Dubbed “hitchhiking gas” by Murray et al. (1995), this high column density ($N_H \sim 10^{23-24} \text{ cm}^{-2}$) of gas was postulated to exist by the authors, with the scope of preventing the wind from becoming overionized and thus losing the acceleration due to spectral absorption line pressure (Fig. 2.5, left panel). Subsequently, detailed hydrodynamic simulations performed by Proga et al. (2000) and Proga & Kallman (2004) demonstrated how a high column density of very dense gas (a “failed wind”, see left panel of Fig. 2.6) naturally forms in the inner part of the flow, effectively shielding the farther out portion of the flow from the strong ionizing continuum, and allowing for its launch and acceleration up to velocities as high as several $0.1c$. The geometry and the dynamics of such winds depend critically on the UV/X-ray flux ratio and on the AGN accretion rate. On the other hand, for the launch and acceleration of magnetically driven

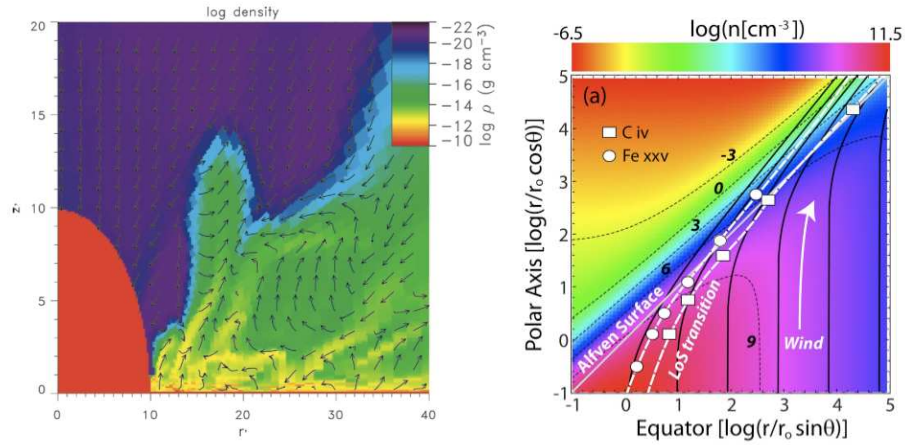


Figure 2.6. Left panel: a failed wind is formed in the inner regions of the LD wind model of Proga (2005). Right panel: the magnetically driven wind model of Fukumura et al. (2010b).

accretion disk winds, there is no need for X-ray shielding, and the accretion rate is not a critical parameter (e.g., Königl & Kartje 1994). The ionization state of the gas, that is a critical observational parameter, will however still depend on the accretion rate and on the presence of some sort of shielding gas; the latter is usually needed to explain the presence of ionization species such as Mg II, C IV, and so on (e.g., Everett 2005, see the right panel of Fig. 2.5). In this case the shielding gas could correspond to the inner portion of the flow, that would be outflowing as well, with possibly even higher terminal velocities than the outer, shielded portion of the wind (e.g., Fukumura et al. 2010b, see the right panel of Fig. 2.6). Detailed predictions for the X-ray spectra of AGN with powerful radiation driven accretion disk winds have appeared in the literature (e.g. Sim 2005; Sim et al. 2008, 2010a,b), contrary than for magnetically driven accretion disk winds that still provide only qualitative predictions and are thus invoked only when radiation-driving is found to be ineffective in matching the observations.

Coupling observations with theoretical model predictions can unveil the geometrical and the dynamical behavior of the wind, so allowing to quantify the mass outflow rate

$$\dot{M}_{out} \propto A(r)\rho(r)v(r)$$

where $\rho(r)$ and $v(r)$ are the density and velocity profiles, $A(r)$ is a geometrical factor that accounts on how the flow diverges, and the kinetic efficiency of the outflow,

$$\epsilon = \frac{1}{2}\dot{M}_{out}v_{out}^2$$

In the simplest possible approximation, assuming isotropy, spherical simmetry, and a constant terminal velocity v_{out} ,

$$\dot{M}_{out} = 4\pi r^2 \rho v_{out} \left(\frac{\delta r}{r}\right) \left(\frac{\delta\Omega}{4\pi}\right) \quad (2.1)$$

where $\delta\Omega/4\pi = C_f$ is the wind covering factor, and $(\delta r/r) \times C_f = C_v$ is the wind volume filling factor, that also accounts for the wind duty cicle.

For recent reviews on the theory of AGN accretion disk winds, see Königl (2006); Proga (2007); Everett (2007).

2.4 X-ray observations of AGN accretion disk winds at the end of 2007

Historically, BAL QSOs are known to be soft X-ray weak: a comparison of the X-ray fluxes of BAL and non-BAL QSOs with the same UV flux indicates that BAL QSOs typically have X-ray fluxes that are 10 – 30 times lower than those of non-BAL QSOs (Green et al. 1995; Laor et al. 1997). This is quantified by means of the optical-to-X-ray spectral index, $\alpha_{\text{ox}} = -0.384 \log(L_{2500}/L_{2\text{keV}})$, as defined by Tananbaum et al. (1979). For soft X-ray weak objects, $\alpha_{\text{ox}} < -2$.

Early *ROSAT* observations pointed out the extreme X-ray weakness of BAL QSOs: Green et al. (1995) detected only one out of 36 BAL QSOs drawn from the Large Bright Quasar Survey (LBQS, Hewett et al. 1995). The discovery of a correlation between the C IV absorption troughs equivalent width and the soft X-ray weakness (Brandt et al. 2000) strongly suggested absorption to be the reason for the low X-ray flux of BAL QSO, so supporting the accretion disk wind models and the underlying typical QSO spectral energy distribution (SED), rather than the evolutionary scenario.

The first direct X-ray spectroscopic measurements happened only after the launch of the *ASCA*, *Chandra*, and *XMM-Newton* satellites. Green et al. (2001) analyzed the stacked spectrum of ten BAL QSOs observed by *Chandra*, finding evidence for a high column density ($N_H \sim 7 \times 10^{22} \text{ cm}^{-2}$) of gas absorbing an underlying X-ray continuum typical of type 1 unabsorbed QSOs (i.e., $\Gamma \sim 1.8$). Furthermore, a partial covering scenario, where the X-ray absorber covers only $\sim 80\%$ of the intrinsic continuum source, seemed to be statistically preferred. Gallagher et al. (2002a) first presented individual X-ray spectra of a small sample of BAL and mini-BAL QSOs observed by *ASCA* and *Chandra*. Again, significant X-ray absorption coupled to a typical intrinsic continuum was found, and for a number of sources a partial covering absorber better reproduced the data than a totally covering absorber. A small number of other individual BAL QSOs were successfully detected by *Chandra* and *XMM-Newton* in the following years, allowing to get further insights on the physics of the inner regions of these AGN. Notably, strong absorption was detected in the Iron K band of the $z = 3.9$ gravitationally lensed BAL QSO APM 08279+5255, by both *Chandra* and *XMM-Newton*. While (Hasinger et al. 2002) interpreted the feature as an absorption edge of ionized iron, deducing super solar metal abundances, Chartas et al. (2002) were able to detect two separate absorption features identified as Fe XXV

BALs, blueshifted by up to $0.4c$ with respect to the redshift of the source. Subsequently, X-ray BALs blueshifted up to $0.3c$ were observed also in the mini-BAL QSO PG 1115+080 (Chartas et al. 2003, 2007).

Sensitive X-ray constraints on the continuum and on the amount of absorption were set on a few other BAL and mini-BAL QSOs, notably SBS 1545+541 and Q1246-057 (Grupe et al. 2003), UM 425 (Aldcroft & Green 2003), Mrk 231 (Gallagher et al. 2002b; Turner & Kraemer 2003; Braito et al. 2004; Gallagher et al. 2005), PG 1535+547 (Gallagher et al. 2001, 2002a; Schartel et al. 2005), CSO 755 (Shemmer et al. 2005), PG 2112+059 (Gallagher et al. 2001, 2002a, 2004; Schartel et al. 2005, 2007), PG 1004+130 (Miller et al. 2006). Gallagher et al. (2006) presented the *Chandra* view of the same LBQS BAL QSO sample of Green et al. (1995): 27 out of 35 sources were detected, even if with a very small number of counts. A statistical and hardness ratio analysis allowed the authors to ascribe the observed X-ray weakness to the presence of high column densities ($N_H \sim 10^{23} \text{ cm}^{-2}$) of X-ray absorbing gas. Globally, all these studies suggested strong and complex (e.g. partial covering, ionized, variable) X-ray absorption and an underlying typical continuum as the explanation of the observed X-ray weakness of BAL QSOs.

In the next Chapters, the latest developments about the study of the X-ray properties of BAL, mini-BAL, and NAL QSOs will be presented.

Chapter 3

The Large SDSS/2XMM BAL QSO Sample

The characterization of the high-energy emission of BAL QSOs is of paramount importance both for constraining the driving mechanism of AGN disk winds and for quantifying the total kinetic energy released into the environment during the AGN phase.

However, X-ray observations of BAL QSOs are very challenging, for at least two reasons. First, there is an observational bias in the classical detection of BAL QSOs: to observe from ground-based telescopes the most frequent transitions where UV BALs are found, sources at redshifts $z \gtrsim 1.7$ must be selected in the case of HiBALs (typically identified through the C IV $\lambda 1549$ transition), and at $z \gtrsim 0.5$ for the more rare LoBALs (typically identified through the Mg II $\lambda 2800$ transition). The brighter nearby sources can be classified as BAL QSOs only through satellites observations (e.g., IUE, FUSE, HST), that are of course much less frequent. Hence there is a very low number of known BAL QSOs at low redshift, where one can more easily collect a large number of X-ray counts. Second, BAL QSOs are known to be X-ray weaker than the non-BAL QSOs, and this property only makes things worse for the X-ray observer.

A two-fold strategy has been pursued in the last years in order to overcome the X-ray weakness of BAL QSOs and determine their high-energy properties. A hardness ratio and/or stacking analysis technique was applied to snapshot observations of a large number of sources in order to characterize their mean properties (e.g. Green et al. 2001; Gallagher et al. 2006), while detailed spectral analysis of deep observations was only possible for a few bright sources (e.g. Gallagher et al. 2002a; Grupe et al. 2003; Gallagher et al. 2004; Shemmer et al. 2005; Schartel et al. 2005). Both kind of studies revealed large column

densities ($N_H \sim 10^{22-24} \text{ cm}^{-2}$) of gas absorbing a 'normal' intrinsic SED with power law spectral indices typical of radio-quiet, non-absorbed QSOs ($\Gamma \sim 1.7 - 2$, Piconcelli et al. 2005). In almost none of the sources a simple neutral absorption scenario was able to well reproduce the data, but rather complex absorbers (e.g., ionized, partially covering the source, variable) were generally observed or deduced from the available data.

Thanks to the current availability of both optical and X-ray large catalogs as the Sloan Digital Sky Survey (SDSS, York et al. 2000) and the Second *XMM-Newton* Serendipitous Source Catalog (2XMM-DR1, Watson et al. 2009), it has been possible to make a step forward in joining the two above-mentioned strategies used in BAL QSOs X-ray studies. In this Chapter the X-ray analysis of a sample of 54 BAL QSOs drawn from the cross-correlation of the above mentioned two catalogs will be presented.

3.1 The Sample

The Sloan Digital Sky Survey Data Release 5 Quasar Catalog (Schneider et al. 2007) and the Second *XMM-Newton* Serendipitous Source Catalogue (Watson et al. 2009) were cross-correlated using a radius of 5 arcseconds¹. A total of 1067 quasars of the SDSS DR5 are included in the 2XMM catalog, i.e., they have a 0.2–12 keV detection likelihood > 6 . Given the good astrometric accuracy of the 2XMM catalog and the sky density of the SDSS QSOs, the identifications are robust and random coincidence of positions between the two catalogs are not expected (see Section 9.5 of Watson et al. 2009). About 635 SDSS DR5 QSOs have *XMM-Newton* coverage but are not detected in X-rays.

The SDSS spectroscopic window covers the wavelength range of 3800 – 9200 Å and so allows to search for HiBALs in the redshift range $1.7 \leq z \leq 4.38$, and for LoBALs in the range $0.5 \leq z \leq 2.15$. Among the 1067 SDSS QSO detected in the 2XMM-DR1 catalog, 945 lie at $0.5 \leq z \leq 4.38$ and are therefore searchable for BALs. Among these, 203 QSOs are in the redshift range allowing for the search of both Lo- and HiBALs, while 151 (591) lie in the redshift range where only HiBALs (LoBALs) can be found. I choose to use both BI and AI criteria (see Section 2.1) to select the BAL QSOs candidates. 33 out of 945 sources are classified as BAL QSOs according to Trump et al. (2006) using both $BI > 0$ and $AI > 0$ criteria. To these were added 21 sources classified as BAL QSOs according to Shen et al. (2008), who use only the classical $BI > 0$ criterion, so obtaining a sample

¹This corresponds to the 3σ mean positional uncertainty for 2XMM sources.

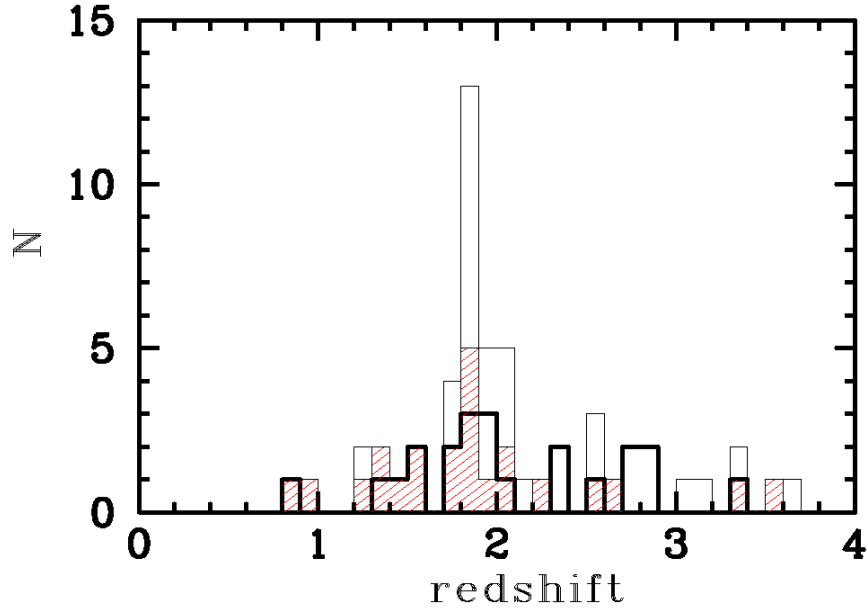


Figure 3.1. Redshift distribution of the 54 SDSS/2XMM BAL QSOs analyzed in this work. The shaded histogram refers to the 21 BAL QSOs taken from Shen et al. (2008), while the empty histogram refers to the 33 BAL QSOs taken from Trump et al. (2006). The thick histogram indicates the 22 sources on which spectral analysis has been performed.

of 54 BAL QSOs. It is worth noting that the selection criteria used by Shen et al. (2008) are somewhat different, and less restrictive, from the ones used by Trump et al. (2006). When analyzing the UV spectrum in order to measure the absorption strength (i.e. the AI and/or the BI), the former use a smoothing of 15 pixels, while the latter use a smoothing of 3 pixels.

It is also interesting to note that the number of SDSS/2XMM BAL detected sources corresponds to about one third of the BAL QSOs belonging to both the Trump et al. (2006) and the Shen et al. (2008) catalogs and with *XMM-Newton* coverage, the remaining two thirds being non-detected. Of the 54 BAL QSOs of this sample, only four sources were target of pointed observations, namely 0911+0550 (PI: J. Hjorth, see Page et al. 2005), 1141-0143 (PI: P. Hall), 1525+5136 (PI: N. Brandt, see Shemmer et al. 2005), and 1543+5359 (PI: S. Mathur, see Grupe et al. 2003). Among the selected 54 BAL QSOs there are only 22 sources for which the X-ray statistics is good enough to obtain moderate-quality spectral measures via direct spectral fitting, i.e., $\gtrsim 100$ net counts detected by the EPIC-pn instrument in the 0.2–10 keV energy band. For the remaining 32 sources, an

X-ray hardness ratio analysis will be performed.

In Table 3.1 the sample analyzed in this work is presented. The horizontal line separates the BAL QSOs taken from Trump et al. (2006), upper table, from the BAL QSOs taken from Shen et al. (2008), lower table. The first column lists the nomenclature for the sources used throughout the Thesis. In the next columns the redshift, the SDSS and 2XMM names, and the offset in arcseconds between the positions given in the two catalogs are reported for each source. Notes on individual sources (i.e. a “L” for lensed BAL QSOs, a “R” for radio-loud BAL QSOs) and a letter which specifies the kind of X-ray analysis performed (i.e. a “H” for hardness ratio analysis, a “S” for spectral analysis) are finally reported. About a half of the sources have an offset less than $1''$; only 8 sources have an offset larger than $2''$ (the largest offset being $\sim 4.1''$). The sample analyzed in this work spans a redshift $0.8 \lesssim z \lesssim 3.7$ (see Fig. 3.1), with a median $z_{\text{med}} \sim 1.9$ and a mean $\langle z \rangle \sim 2.1$.

3.2 Observations and data reduction

The observation data files (ODF) for each observation were retrieved from the public *XMM-Newton* Science Archive (XSA). Data were reduced with the Science Analysis Software (SAS) v.7.0.0 and calibration files generated from June to July 2008.

Light curves at $E > 10$ keV were inspected, and high background flaring events were filtered out using the `xmmlight_clean` script² to recursively remove all time bins which deviate more than 3σ from the mean count-rate. Bad pixels and hot columns were removed, and only good quality events (FLAG=0 for EPIC-pn, #XMMEA_EM for EPIC-MOS) were retained. Given the low fluxes involved, pile-up does not affect the data, therefore single and double events were retained for EPIC-pn (PATTERN ≤ 4), up to quadruple events were retained for EPIC-MOS (PATTERN ≤ 12).

Table 3.2 lists the observation log for the 22 sources with spectral analysis available: the first column reports the name of the source, next comes the observation ID, the nominal duration of the observation, the net exposure time after the flare filtering was applied, the local background-subtracted count-rate, and the corresponding errors reported in parenthesis for each instrument used in the spectral analysis.

Individual source spectra were generated for each instrument using circular extraction

²Available at <http://www.sr.bham.ac.uk/xmm2/scripts.html>

regions, with radii determined with the `eregionanalyse` package in order to maximize the signal-to-noise ratios (S/N). Typical extraction radii are 15–30'' for the source spectra, 30–60'' for the background spectra. Background was extracted from source-free regions as near as possible to the source, and its area was normalized to the source's one via the `backscale` task. If the source was found to lie near the edge of a CCD or near a hot column, the exposure was discarded. Ancillary response files (ARF) and redistribution matrix files (RMF) at the position of each source were generated with the `arfgen` and `rmfgen` tasks. Given the current calibration uncertainties, events with energies in the range 0.2–10 keV band in the case of EPIC-pn, 0.3–8 keV band for the two EPIC-MOS were extracted for the spectral analysis purpose.

All the spectra were grouped with a minimum of 15 counts per energy bin, and the errors were propagated using the Churazov weight (Churazov et al. 1996) to properly account for the low number of counts per bin that approximate a Gaussian distribution, and the χ^2 statistics was applied during the minimization process. Results have been checked with respect to other groupings (e.g. 20 counts/bin) and other statistics (e.g. the C-statistics, Cash 1979), the main difference being in the errors estimation. A grouping of 15 counts/bin has been chosen for the following reasons:

- the photoelectric cutoff moves at lower energies in the observer frame with increasing redshift. In order to measure the amount of neutral intrinsic absorption, the maximum accuracy in determining the spectral shape is needed at the lowest energies observed by the EPIC. This is not achieved with 20 counts/bin because of the low number of lowest energy bins. For the faintest sources, this grouping results in badly constrained parameters.
- when using the C-stat to model the ungrouped spectra, the same results were obtained, with errors even smaller than the 15 counts/bin case, but strongly background-modeling dependent. Being the EPIC background a relevant component of the signal collected, it can not be neglected, so I chose to subtract it rather than modeling it, and I used the χ^2 statistics.

3.3 X-ray spectral Analysis

The Heasoft package v.6.4, Xspec v.12.4.0 (Arnaud 1996) were used for the spectral analysis. All the models include appropriate Galactic neutral absorption (Dickey & Lockman 1990). Photoionization cross-sections are given by Balucinska-Church & McCammon (1992), while abundances are solar, given by Anders & Grevesse (1989). All quoted errors are at 90% confidence level for one parameter of interest (i.e. $\Delta\chi^2 = 2.706$, Avni 1976), unless otherwise stated.

First, the spectra were modeled with a redshifted power law continuum emission absorbed by Galactic neutral hydrogen. For each source the spectra of all the available instruments were simultaneously fitted, keeping only the power law normalizations to be free in order to account for the cross-calibration uncertainties between the EPIC-pn and EPIC-MOS, that are around 5-7% (M. Kirsch 2007³). All the model parameters were kept linked in the case of the two MOS.

An absorption component at the redshift of the source was then added, and the χ^2 improvement was registered. The addition of a neutral redshifted absorption component was found to be statistically significant at $> 90\%$ confidence level in only 13/22 sources; among these, only for 6 sources (0043+0052, 0243+0000, 0911+0550, 1425+3757, 1525+5136 and 1543+5359) the fit improvement was significant at $> 99\%$ confidence level. For the other 9/22 sources, only upper limits on the amount of intrinsic neutral absorption were found. Overall, 7/22 sources show $N_H < 4 \times 10^{21} \text{ cm}^{-2}$ at the 90% confidence level. In order to further investigate this issue, Γ and N_H were varied around their best-fit values for each source, and contours of iso- $\Delta\chi^2 = 2.30, 4.61$ and 9.21 (corresponding to 68, 90 and 99% confidence level for two parameters of interest) were generated.

Spectral analysis results are reported in Table 3.3. For each source the Galactic neutral hydrogen column density $N_{H,\text{Gal}}$, the photon index Γ , the neutral hydrogen column density at the redshift of the source N_H , the power law normalization $N_{1\text{keV}}$, and the best-fit value in terms of $\chi^2/\text{degrees of freedom (d.o.f.)}$ are listed. Next, the soft band (0.5 – 2 keV) and hard band (2 – 10 keV) observed fluxes corrected only for Galactic absorption were computed; the 2 – 10 keV rest-frame luminosities corrected for both Galactic and intrinsic absorption were also estimated from the best-fit models.

Spectra for each source are reported in Section 3.9 together with confidence contours

³XMM-SOC-CAL-TN-0018,<http://xmm2.esac.esa.int/docs/documents/CAL-TN-0018.pdf>

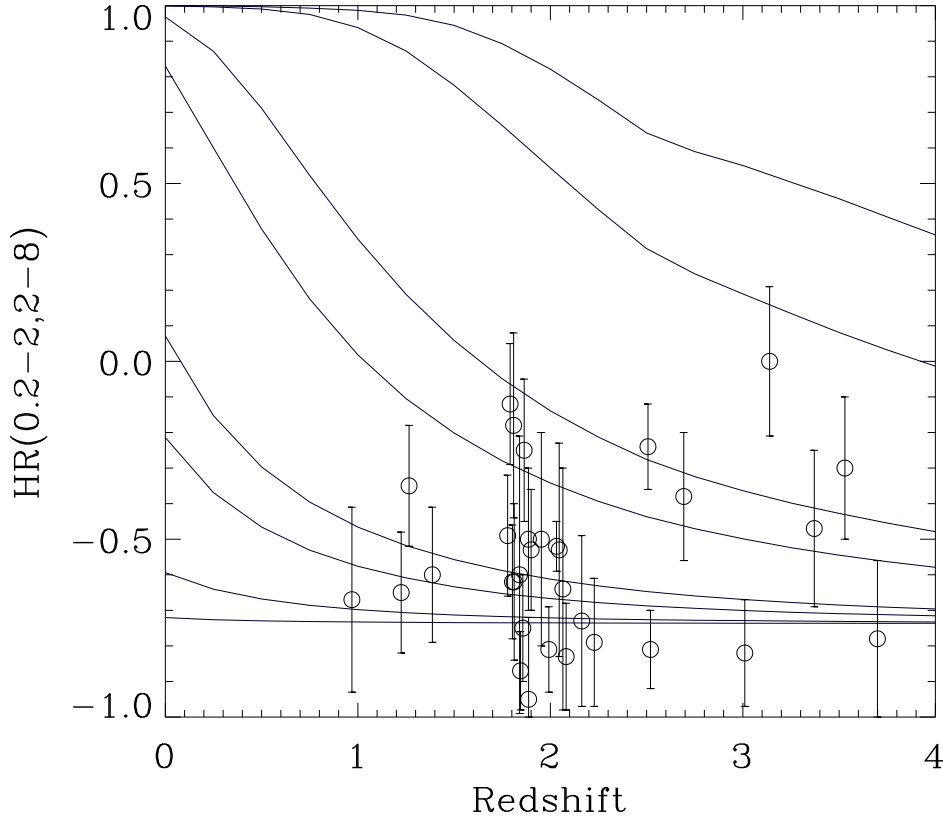


Figure 3.2. Observed hardness ratio and 1σ associate errors for the 32 SDSS/2XMM BAL QSOs with a low X-ray S/N. The continuous tracks represent the simulated hardness ratios for different redshift and column density values which are, from bottom to top: $N_H = (0.01, 0.1, 0.5, 1.0, 5.0, 10, 50, 100) \times 10^{22} \text{ cm}^{-2}$.

for Γ and N_H , where the vertical line marks the Galactic neutral hydrogen column density value.

3.4 X-ray hardness ratio analysis

A hardness ratio analysis on the 32 BAL QSOs with the worst S/N was performed, using the EPIC-pn data only. Source counts were extracted from circular regions centered at the source optical positions, and background counts from source-free circular regions as near as possible to the source. For each source and background spectra, the corresponding ARFs and RMFs were generated to account for the spatial dependence of the effective area, and hence of the counts number.

The off-axis corrected hardness ratio between 0.2–2 and 2–8 keV was then computed using the count-rates derived from Xspec. Errors on the hardness ratios are propagated

from the count-rate errors using the numerical formula of Lyons (1991). The number of counts in the 0.2 – 10 keV band is approximately 30 ÷ 60. I then simulated the observed hardness ratio for a set of fake sources modeled with a redshifted power law with $\Gamma = 2$, absorbed by a varying amount of neutral gas at the source redshift, and spanning a redshift range of $0 \leq z \leq 4$. The observed hardness ratios were then compared with the expected ones, and the appropriate amount of absorbing column density required to reproduce the data were deduced (see Fig. 3.2). Hardness ratio measurements, their 1σ errors, and the corresponding absorbing column densities are reported in Table 3.4.

3.5 Optical/X-ray photometry

The Galactic absorption corrected, source rest-frame flux densities $f_{2\text{keV}}$ and f_{2500} were measured from the *XMM-Newton* and SDSS spectra, respectively.

In order to measure $f_{2\text{keV}}$, the 0.5 – 2 keV fluxes were de-redshifted using the best-fit photon indices listed in Table 3.3. In the case of the 32 sources without spectral analysis, the 0.5 – 2 keV rest-frame fluxes were estimated from the observed count-rate using `webpimms`⁴ with the appropriate effective area, redshift, and a fixed photon index $\Gamma = 2$. For the f_{2500} measurements, the five SDSS magnitudes were used following the method outlined in Section 2.2 of Vignali et al. (2003).

Next, the $\alpha_{\text{ox}} = 0.384 \log f_{2\text{keV}} / \log f_{2500}$, was computed. This represents the spectral slope of a hypothetical power law connecting the 2500 Å and 2 keV rest-frame flux densities (Tananbaum et al. 1979). Several studies handled the α_{ox} distribution in QSOs and found a strong correlation with the rest-frame 2500 Å luminosity density ℓ_{2500} . The observed α_{ox} was then compared with the most updated best-fit correlation $\ell_{2500} - \alpha_{\text{ox}}$ for SDSS radio-quiet QSOs (Equation 3 of Just et al. 2007).

Results and measurements are reported in Table 3.5 together with other optical properties. Specifically, the AI and v_{out} (i.e. the Absorption Index and the maximum velocity outflow) measured for each source are also reported: when available, the AI/ v_{out} values given in Trump et al. (2006) are listed, otherwise they were estimated from the SDSS spectra and these values are flagged with an asterisk. The BAL subclassification is also given in the table: Hi/Lo is used to mark the HiBALs/LoBALs, while a H is used to mark those BAL QSOs for which the Mg II spectral region is redshifted outside the SDSS

⁴heasarc.gsfc.nasa.gov/Tools/w3pimms.html

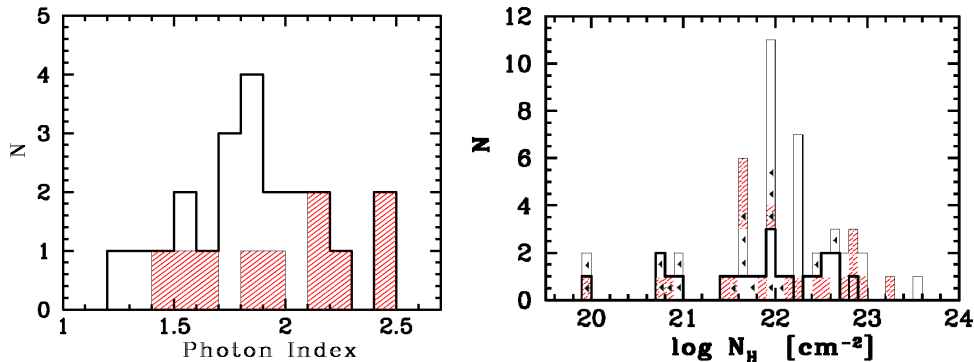


Figure 3.3. Left panel: photon index distribution for the 22 SDSS/2XMM BAL QSOs with spectral analysis available. Right panel: neutral column density distribution for the 22 SDSS/2XMM BAL QSOs with spectral analysis (thick histograms) and for the 32 SDSS/2XMM BAL QSOs with hardness ratio analysis (thin histograms) available. The shaded histogram refers to the BAL QSOs taken from Shen et al. (2008), left-pointing arrows represent upper limits.

spectroscopic window, so preventing any investigation of the presence of low-ionization absorption troughs.

3.6 Results

The best-fit photon index distribution is shown in Fig. 3.3, left panel, for the 22 BAL QSOs on which spectral analysis was performed. The sample mean photon index is $\langle \Gamma \rangle = 1.87$ with a dispersion $\sigma = 0.21$, thus compatible with typical radio-quiet type 1 AGN (e.g. Picconcelli et al. 2005); there are no differences among the distributions of the two subsamples taken from Shen et al. (2008) and from Trump et al. (2006) and introduced in Section 3.1. A couple of sources (namely 1007+5343 and 1011+5541) present rather flat photon indices $\Gamma \sim 1.3$ that could indicate the presence of more complex (e.g. ionized/partially covering) absorbers. The intrinsic neutral absorber column density distribution is shown in Fig. 3.3, right panel, for the BAL QSOs analyzed through both spectral and hardness ratio analysis, where for the latter class the photon index was fixed at $\Gamma = 2$ (see Section 3.4). While a $\langle N_H \rangle \sim 10^{23} \text{ cm}^{-2}$ was expected (see Section 2.4), a $N_H \leq 10^{22} \text{ cm}^{-2}$ was found for 28/54 sources. Again, there are no differences among the distributions of the two BAL QSO subsamples introduced in Section 3.1.

The possible Γ and N_H dependence on redshift was checked (Fig. 3.4, left and right panel respectively), and no significant correlations were found, except a shallow tendency to measure higher N_H values with increasing redshift consistent with being due to the

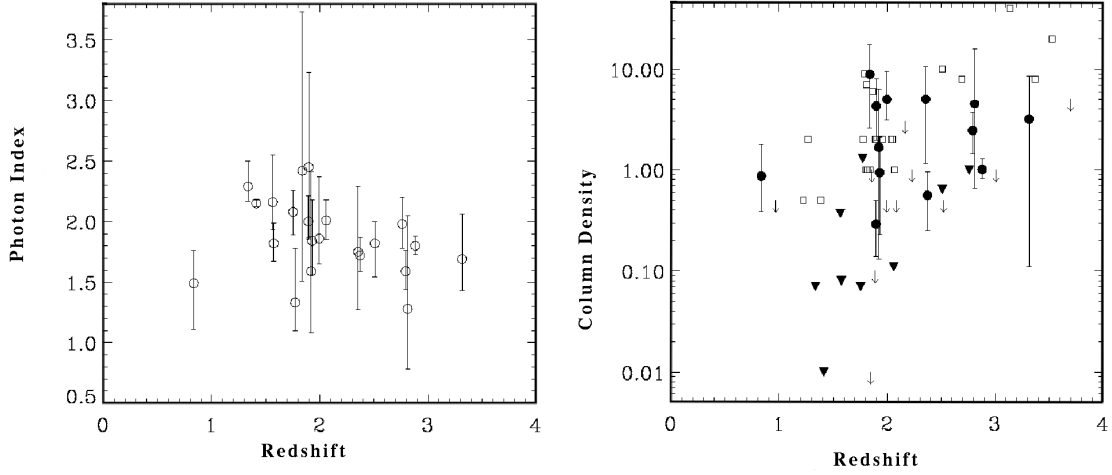


Figure 3.4. Left panel: measured photon indices versus redshift. Right panel: column densities in units of 10^{22} cm^{-2} versus redshift: filled symbols refer to the 22 SDSS/2XMM BAL QSOs with spectral analysis available, where downward-pointing triangles are upper limits at the 90% confidence level. Empty symbols refer to the 32 SDSS/2XMM BAL QSOs with hardness ratio available, where arrows are upper limits at the 68% confidence level.

shift of the photoelectric cutoff outside of the observed energy band (see e.g. discussions in Tozzi et al. 2006; Akylas et al. 2006). I then wondered whether the low measured column densities are related to the low number of spectral bins often used in spectral analysis, but sinceno correlation among the number of counts and the measured column densities was found, I concluded that this is not the case. It is worth noting that the intrinsic column densities might be much higher if either the underlying continuum is more complex than a simple power law (e.g. if there is a significant contribution from soft-excess and/or a scattered component) or if the absorber is more complex than simple neutral one (e.g. if it is ionized and/or partially covering the continuum emission source).

The observed α_{ox} distribution is shown in Fig. 3.5, left panel. Once more, there are no evident differences among the distribution of the two BAL QSOs subsamples. The observed distribution is typical of radio-quiet, unabsorbed broad-line (i.e. type 1) AGN and atypical of BAL QSOs which usually present an observed $\alpha_{\text{ox}} \sim -(2 \div 2.5)$ (e.g. Green & Mathur 1996; Gallagher et al. 2006), see Fig. 3.5, right panel.

The measured α_{ox} are plotted in Fig. 3.6, where the dashed line represents the $\alpha_{\text{ox}}(\ell_{2500})$ value expected on the basis of the rest-frame 2500 \AA luminosity density according to Eq. 3 of Just et al. (2007). As it can be seen, the subsample with X-ray spectra

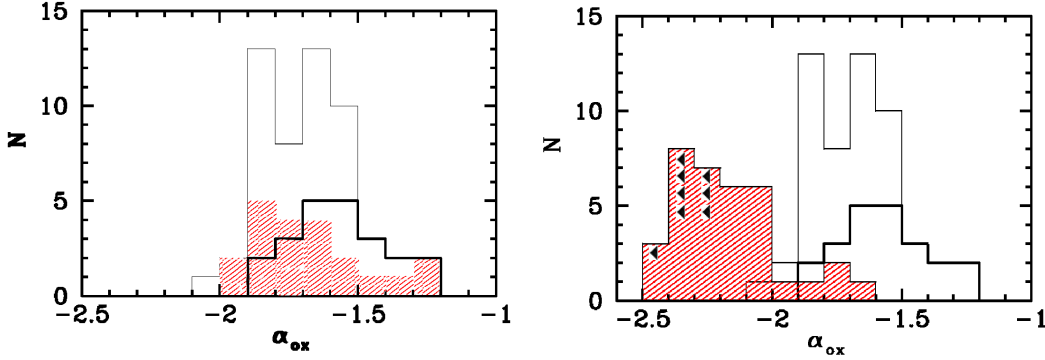


Figure 3.5. Left panel: α_{ox} distribution for the 54 SDSS/2XMM BAL QSOs, where the shaded histogram refers to the 21 sources taken from Shen et al. (2008) and the thick histogram refers to the 22 sources on which spectral analysis was performed. Right panel: comparison between the α_{ox} measured for the 54 SDSS/2XMM BAL QSOs studied in this work and for the 35 LBQS BAL QSOs (shaded histograms) studied by Gallagher et al. (2006).

seems to show a slightly flatter α_{ox} (open circles, $\langle\alpha_{\text{ox}}\rangle \sim -1.57$) than the hardness ratio analyzed one (filled circles, $\langle\alpha_{\text{ox}}\rangle \sim -1.75$), but according to a Kolmogorov-Smirnov statistic test (KS) this difference is not statistically significant (less than 2σ).

None but one of the SDSS BAL QSOs is found to lie in the typical region of “soft X-ray weak” QSOs, that is $\alpha_{\text{ox}} < -2$, but nearly all of them have an observed α_{ox} consistent, within the errors, with the $\alpha_{\text{ox}}(\ell_{2500})$.

3.7 Discussion

Two remarkable results of this analysis are the observed α_{ox} distribution, that is atypical of BAL QSOs, and the low intrinsic N_H value measured for more than a quarter of the sample (15/54 sources), $N_H < 5 \times 10^{21} \text{ cm}^{-2}$. I will discuss below in turn each of these issues, which both point independently to an unabsorbed scenario for a large fraction of the SDSS/2XMM BAL QSO sample. The most meaningful comparisons can be made with respect to the largest X-ray studied BAL QSO sample known to date, that is the Gallagher et al. (2006) *Chandra* study of 35 Large Bright Quasar Survey (LBQS, Hewett et al. 1995) BAL QSOs.

While Gallagher et al. (2006) found a mean $\Delta\alpha_{\text{ox}} \equiv \alpha_{\text{ox}} - \alpha_{\text{ox}}(\ell_{2500}) \sim -0.53$, a $\langle\Delta\alpha_{\text{ox}}\rangle \sim -0.04$ was obtained for the SDSS/2XMM sample, i.e. a difference of a factor of 3 in UV/X-ray luminosity ratio. Assuming the same amount of mean absorption for the two samples, the smaller $|\Delta\alpha_{\text{ox}}|$ measured in the SDSS/2XMM BAL sample with respect

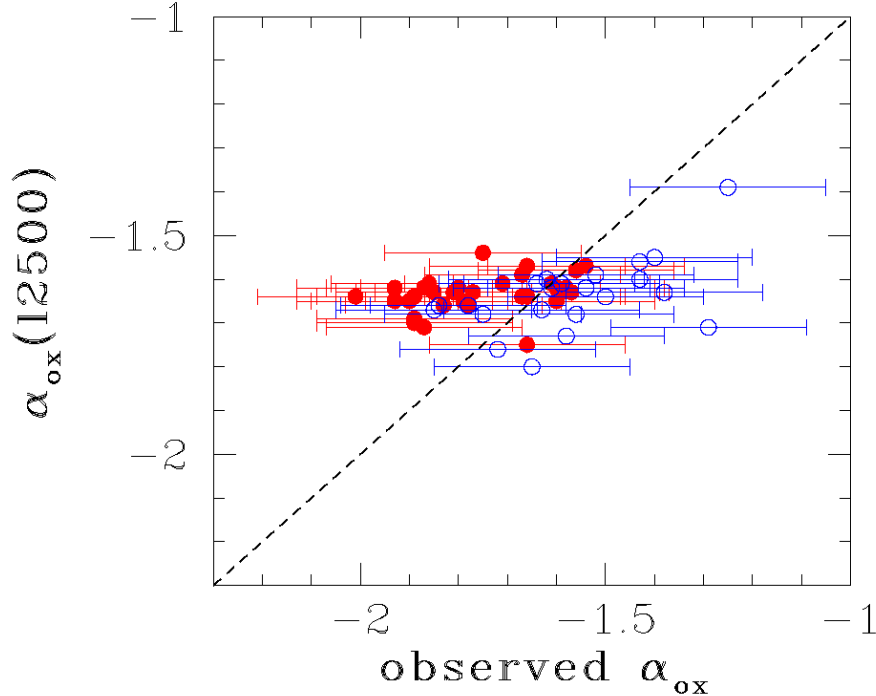


Figure 3.6. Measured α_{ox} versus $\alpha_{\text{ox}}(\ell_{2500})$, where open (blue) circles are the 22 SDSS/2XMM BAL QSOs on which X-ray spectral analysis was performed, filled (red) circles are the 32 SDSS/2XMM BAL QSOs on which X-ray hardness ratio analysis was performed.

to the LBQS BAL sample could be due to a lower optical luminosity and/or to a higher X-ray luminosity of the SDSS/2XMM BAL sample with respect to LBQS BAL QSO. A KS statistic test on the rest-frame 2500 Å luminosity densities yields a probability $< 3 \times 10^{-3}$ that the two samples are drawn for chance from the same UV parent population, with the LBQS BAL QSOs being, on average, more UV luminous than the SDSS/2XMM BAL QSOs.

While the BAL QSOs studied in this work are selected from the same parent sample used by Just et al. (2007) in their study, that is mainly based on spectroscopically confirmed, optically selected SDSS QSOs, the LBQS sample used by Gallagher et al. (2006) comprises extremely bright, luminous, color selected QSOs. It may be that the LBQS BAL QSO have a higher UV/X-ray luminosity ratio than the typical QSOs and so the $\alpha_{\text{ox}} - \ell_{2500}$ correlation may not hold. In any case, it should be stressed that this correlation has a high intrinsic dispersion ($\Delta(\alpha_{\text{ox}}) \sim 0.2$) and has been constructed excluding BAL QSOs, therefore these considerations must remain somewhat speculative.

On the other hand, in this work the sources are X-ray selected (i.e., on the basis of the 2XMM catalog, that only includes X-ray detections) BAL QSOs, and so there is a bias toward the X-ray brightest ones. The SDSS/2XMM BAL QSOs could be a particular, unexpected X-ray loud class of BAL QSOs intrinsically more X-ray luminous than those studied so far. Among the 54 BAL QSOs studied in this work, a significant number of sources with α_{ox} less negative than *absorption-corrected* Gallagher et al. (2006) values was found, and this result makes the above possibility a plausible one.

Alternatively, the main driver for the differences observed in the α_{ox} distribution could be the amount of X-ray absorption. Indeed, the most striking difference in results between the LBQS BAL QSOs and the SDSS/2XMM BAL QSOs analysis is the amount of intrinsic absorption. Gallagher et al. (2006) estimate, from hardness ratio analysis, an X-ray absorbing column density of $\langle N_H \rangle \sim 10^{23} \text{ cm}^{-2}$ for all their LBQS BAL QSOs, while in this work a much lower absorption for a large fraction of the SDSS/2XMM BAL QSOs was measured through spectral fitting and hardness ratio analysis, and no absorption at all (in excess of the Galactic one) was found for more than one third of the spectroscopically analyzed sample (see Table 3.3 and Fig. 3.10).

A possible explanation may lie in the small bandpass of *Chandra* (0.5-8 keV) that makes difficult for previous works to accurately measure the low-energy photoelectric cutoff with increasing redshift (the mean redshift of the two samples is comparable, $z \sim 2$) and so may bring to an overestimate of the intrinsic column density (see e.g. the discussions and simulations in Tozzi et al. 2006). On the other hand, the high effective area of *XMM-Newton* EPIC-pn at the lowest energies (down to 0.2 keV) makes the column densities measures robust even at the highest redshift probed by the SDSS/2XMM sample analyzed in this work.

The SDSS/2XMM BAL sample could be missing the “classical” absorbed, soft-X-ray weak BAL QSOs and may be probing the bright tail of the known distribution. A comparison of the fraction of X-ray non-detected BAL QSOs (i.e. all the BAL QSOs covered by *XMM-Newton* observations but not included in the 2XMM catalog) with the fraction of X-ray non-detected non-BAL QSOs (see Section 3.1), together with the smooth α_{ox} distribution – albeit with different $\langle \alpha_{\text{ox}} \rangle$ – among BAL QSOs analyzed through spectral fitting and hardness ratio, makes this possibility a plausible one. The study of the X-ray

properties of the X-ray non-detected BAL QSOs is beyond the scope of this Thesis and is deserved to a future work. In any case, the significant fraction of very low intrinsic column densities and very flat α_{ox} observed in the SDSS/2XMM sample strongly assess the existence of some unabsorbed, X-ray bright BAL QSOs.

The intriguing possibility that the observed X-ray properties are related to some physical properties of AGN outflows was then explored. It is interesting to note that a high UV/X-ray luminosity ratio is theoretically requested to launch a UV radiation driven wind up to very high velocities, in order to prevent overionization (and so the uneffective acceleration) of the outflowing gas. The “BAL-nicity” (quantified by either the BI or the AI) of the Gallagher et al. (2006) sample is much stronger than that of the sample of the present work, indicating somewhat faster and more powerful outflows observed in their LBQS BAL QSO sample (BI is a coarse measure of the convolution of the minimum and the mean velocity of the outflowing UV absorbing gas, and of its amount along the line of sight). The SDSS/2XMM sample could be probing the low-velocity tail of BALs, that tends to become overionized by the strong X-ray continuum and so may cause a weaker UV-absorbing outflow to be observed.

The SDSS/2XMM BAL QSO sample was then divided in low- and high-AI subsamples according to Knigge et al. (2008). 30/54 sources were found to belong to the low-AI group ($\langle \text{AI} \rangle \sim 500 \text{ km s}^{-1}$), and 24/54 sources to the high-AI group ($\langle \text{AI} \rangle \sim 2000 \text{ km s}^{-1}$). In Fig. 3.7 the N_H and α_{ox} distributions are plotted again, this time with the shaded histogram referring to the low-AI BAL QSOs. It seems that the low-AI subsample tends to occupy the low- N_H tail of the column density distribution, for which only one high-AI BAL QSO presents $N_H < 5 \times 10^{21} \text{ cm}^{-2}$, the other 14 unabsorbed BAL QSOs being low-AI. No differences are evident among the α_{ox} distributions of low- and high-AI BAL QSOs.

The Spearman’s ρ bivariate non-parametric statistic test, implemented into ASURV v.1.2 (Lavalley et al. 1992), was used to search for correlations among AI and N_H accounting for upper limits in the column density measurements. A probability of 0.0026 that AI and N_H are not correlated was found. Although this value can not be considered as a strong proof of the existence of a correlation between the two quantities, it strengthens the conclusion that the high-AI BAL QSO subsample appears to be more X-ray absorbed

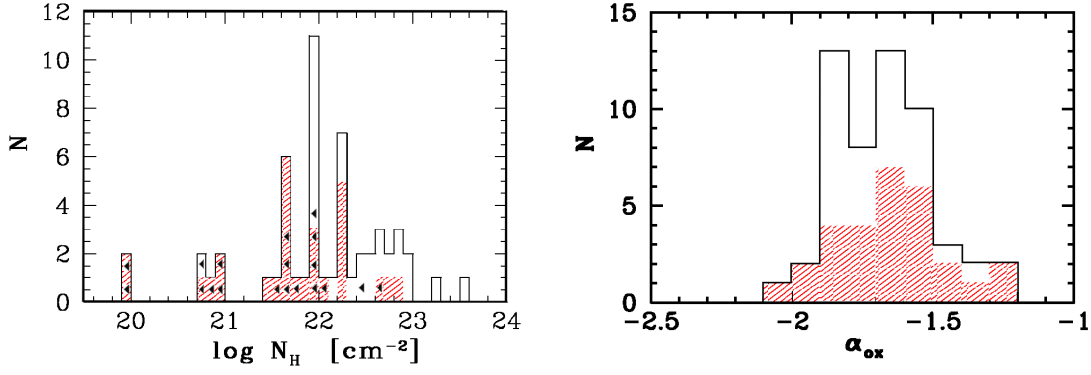


Figure 3.7. Distribution of neutral absorbing column densities (left panel) and α_{ox} (right panel), where the shaded histograms refer to the 30 SDSS/2XMM BAL QSOs with $\langle \text{AI} \rangle \sim 500 \text{ km s}^{-1}$ and the empty histograms refer to the 24 SDSS/2XMM BAL QSOs with $\langle \text{AI} \rangle \sim 2000 \text{ km s}^{-1}$. Arrows indicate upper limits.

than the low-AI one. The measured AI versus the measured N_H for all the 54 sources of the present sample are plotted in Fig. 3.8. Previous works (i.e. Knigge et al. 2008) showed that there seems to exist a subsample of low-AI BAL QSOs that are usually included in BAL QSOs samples even if their UV properties are statistically different from those of classical BAL QSOs. The present work confirms the different behaviour of these sources also from an X-ray perspective.

It is worth noting that, even considering only the high-AI BAL QSO subsample, a rather low X-ray absorbing column densities are found, together with high α_{ox} , with respect to the expectations based on known literature results and theoretical disk wind models.

The existence of a correlation between $\Delta\alpha_{\text{ox}}$ and the maximum velocity outflow for the SDSS/2SMM BAL QSOs, as found by Gallagher et al. (2006) for their LBQS BAL QSOs, was searched for. This correlation is usually interpreted as a signature of radiatively driven accretion disk wind, because of the association of the highest velocity UV outflows with the more negative $\Delta\alpha_{\text{ox}}$ (i.e. with the greatest amount of X-ray absorption). This is easily interpreted as the presence of an effectively shielding column density of X-ray absorbing gas that prevents the UV-absorbing wind from continuum overionization and makes possible to radiatively accelerate it to the highest velocities observed (see e.g. Gallagher & Everett 2007). Fig. 3.9 shows that such correlation does not hold for the SDSS/2XMM BAL QSOs sample studied in this work. The possibility that the lack of a correlation between $\Delta\alpha_{\text{ox}}$

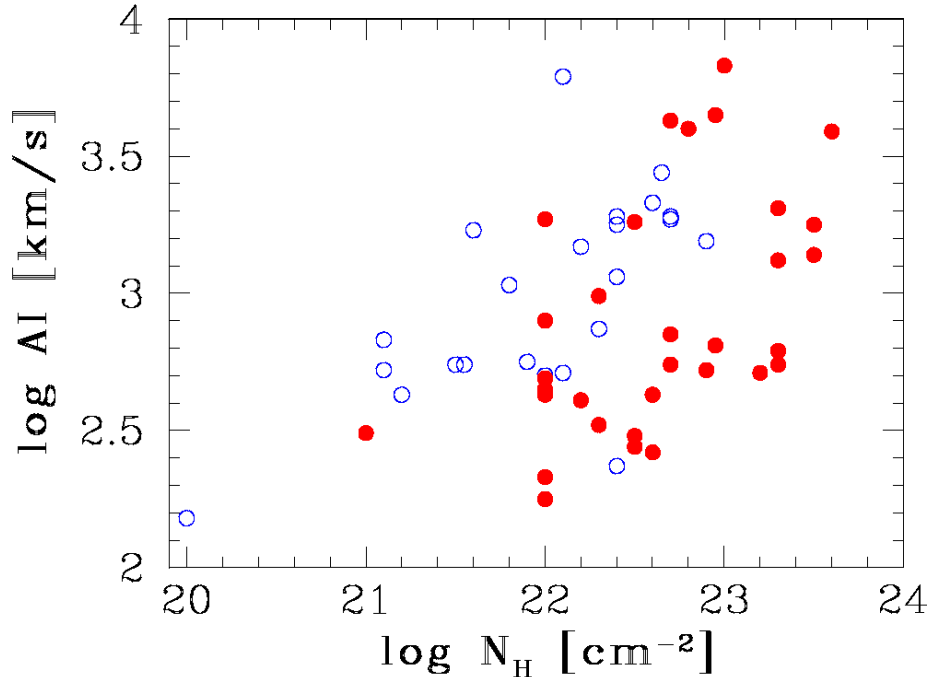


Figure 3.8. Absorption Index versus measured X-ray absorbing column density for the SDSS/2XMM BAL QSOs with spectral analysis available (open circles) and with hardness ratio analysis available (filled circles).

and the maximum velocity outflow is driven by the inclusion of the low-AI BAL QSOs in the sample was investigated, and it was found that this is not the case.

The same lack of correlation between $\Delta\alpha_{\text{ox}}$ and maximum velocity outflow also holds for the NAL QSOs sample of Misawa et al. (2008), and is interpreted by the authors as a different location above the accretion disk of the gas responsible for the UV NALs (higher latitudes above the accretion disk) and BALs (lower latitudes), with UV and X-ray absorbers being different in both cases (see Chapter 6 of this Thesis). Some of the SDSS/2XMM BAL QSOs are indeed quite precisely classified as mini-BAL QSOs, that manifest intermediate UV properties between NAL QSOs and BAL QSOs. Mini-BAL QSOs are usually thought to be related to the same physical phenomena of BAL QSOs – the difference being in the line of sight along the UV outflow – and indeed similar characteristics for their X-ray absorbers and for the other BAL QSOs of the sample were found.

Some of the BAL QSOs selected from Shen et al. (2008), namely 1001+5553, 1021+1315

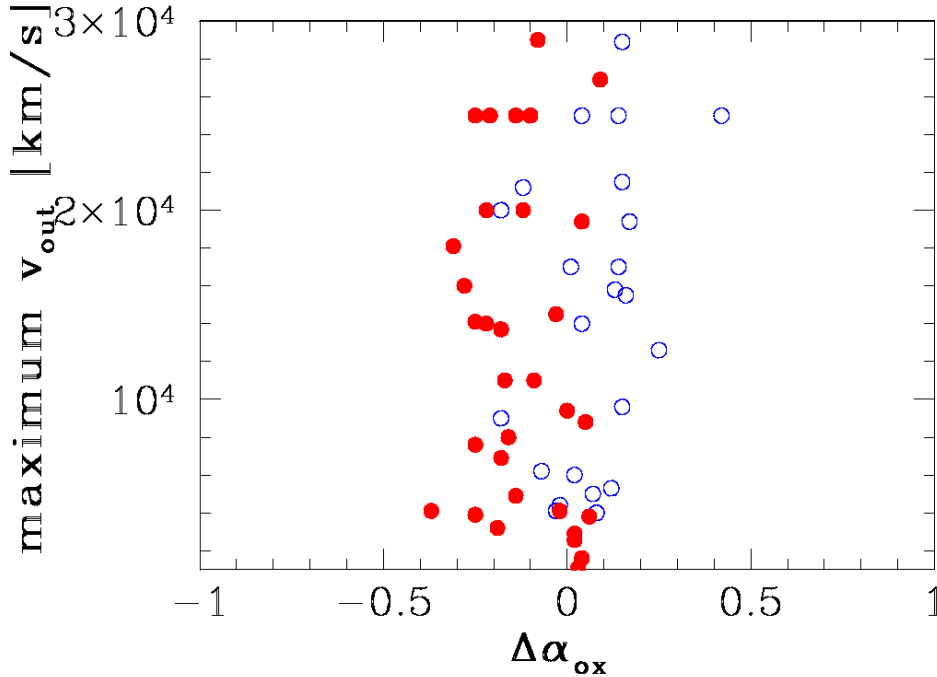


Figure 3.9. $\Delta\alpha_{\text{ox}}$ versus maximum velocity UV outflow for the SDSS/2XMM BAL QSOs with spectral analysis available (open circles) and with hardness ratio analysis available (filled circles).

and 1447+4032, may be not genuine BAL QSOs nor mini-BAL QSOs, and they could have been included in the BAL QSO sample because of the large smoothing applied by Shen et al. (2008) to the UV spectra in their analysis. Even if some of these sources could be NAL QSOs – or even if their UV spectrum could “only” bring the signature of intervening absorbers – the conclusions of the present work remain unchanged, that is, X-ray selected BAL QSOs are not soft X-ray weak and they appear less X-ray absorbed than purely optically selected BAL QSOs.

The low absorption found in the SDSS/2XMM BAL QSO sample recalls the results found by Wang et al. (2008) for a little sample of radio-loud BAL QSOs. While in this case the authors argue for either a wind launching mechanism different than for “classical” BAL QSOs (e.g. magnetically driven winds linked to the presence of radio jets) or for the presence of absorbers more complex than totally covering, neutral ones, any conclusion about these hypotheses can be reached for the present BAL QSO sample because of the low number of formally radio-loud⁵ sources (that is, 4/54, namely 0923+5127, 1141-0143,

⁵According to the Kellermann et al. (1989) definition, that is $f_{5\text{GHz}}/f_{4400\text{\AA}} > 10$, where 5 GHz and

1146+4723 and 1324+0320), and for the low statistics that prevents from constraining some physical parameters such as the ionization state and/or the covering fraction of the absorbing gas. Furthermore, if the presence of a significant soft-excess holds for the SDSS/2XMM sample as found by previous studies in a high fraction of radio-quiet QSOs (e.g. Piconcelli et al. 2005), the actual intrinsic column density could be severely underestimated. Unfortunately, the low statistics again is preventing from checking this hypothesis. The above issues suggest that the measured column densities can be safely considered as lower limits, but it is worth noting that given the redshift distribution of the sources, for most of the BAL QSOs the soft-excess would be redshifted outside the observed band. However, I stress that previous BAL QSOs studies found significantly higher column densities than mine, without accounting for the soft-excess issue. Another possibility is the presence of highly ionized absorbers, that are not detectable with the present S/N, and that could lead to a severe underestimation of the total absorbing column density.

It is also worth noting that some AGN – both BAL QSOs (see e.g. Schartel et al. 2007; Ballo et al. 2008) and non-BAL QSOs (see e.g. Grupe et al. 2007a,b) – with multiple and deep X-ray observations have revealed a transient behaviour in terms of soft X-ray weakness, related to an X-ray variability stronger than the UV one. While this could be the reason for the observed X-ray properties of some sources of the present sample (if they have been caught in a “high” X-ray state), the large number of BAL QSOs studied in this work rules out this possibility as the only explanation for the observed UV/X-ray properties of the full sample.

Overall, these results can be reconciled with theoretical accretion disk wind models if we are looking at the SDSS/2XMM BAL QSOs along lines of sight which are not nearly equatorial as they are thought to be in the case of “classical” BAL QSOs, but rather at smaller angles with respect to the accretion disk rotational axis, so missing both the bulk of X-ray shielding gas and the highest velocities, highest column densities UV outflows. If this scenario holds, one could conclude that the outflow properties of QSOs smoothly connect each other in every kind of QSO, the observed differences being driven by purely geometrical effects. This scenario could be tested by studying the X-ray properties of the remaining ~ 100 X-ray non-detected BAL QSOs taken from the SDSS DR5 QSOs catalog, as well as the X-ray properties of the much less studied mini-BAL and NAL QSOs.

4400Å are in the source rest-frame.

3.8 Conclusions

I analyzed the X-ray properties of a substantial sample of 54 BAL QSOs drawn from the cross-correlation of the SDSS DR5 and 2XMM catalogs by performing spectral analysis on 22 sources, hardness ratio analysis on the remaining ones.

The results in terms of α_{ox} and the amount of intrinsic X-ray absorption are very different with respect to the literature results, that are mainly based on purely optically selected BAL QSOs. None of the SDSS/2XMM BAL QSOs, with only one exception, are soft X-ray weak. The most striking result of the spectral analysis is the low intrinsic X-ray absorbing column density value measured for more than a half of the sample, $N_H \leq 10^{22} \text{ cm}^{-2}$.

Present observations confirm the statistical result presented by Knigge et al. (2008), who found a bimodal distribution in AI for BAL QSOs; I found that the low intrinsic neutral X-ray absorption measured for a large fraction of the SDSS/2XMM sample is linked to the low AI measured from their UV spectra. We should treat with caution such kind of sources when included in BAL QSO samples until we do not clarify their role in the quasar outflow scenarios. Overall, a lower than expected $\langle N_H \rangle$ was found also for the high-AI BAL QSO subsample.

The low measured intrinsic absorption may be reconciled with theoretical calculations by allowing either the intrinsic continuum to comprise a significant soft-excess or a scattered component, or the X-ray absorber to be ionized, or only partially covering the continuum source. Unfortunately, the rather low statistics does not allow to assess the significance of the presence of an intrinsic soft-excess or of a partially covering absorber. Furthermore, the redshift of the sources does not allow to check for the presence of the most usual X-ray spectral features due to warm absorbers, i.e. the O VII and O VIII absorption edges. Investigating the presence of more highly-ionized gas (e.g. absorption features due to Fe XXV, Fe XXVI), absorbing the X-ray continuum at the highest energies probed by the present observations, would need much deeper observations of such distant sources with the current X-ray telescopes. With these caveats in mind, it can be concluded that the measured intrinsic column densities might be lower limits to the presence of intrinsic absorption for this BAL QSO sample.

With the present work we may be probing either a tail of the known BAL QSO population, probably related to a line of sight with larger angle with respect to the accretion

disk plane, or a different outflow launching mechanism that does not need a large amount of X-ray absorbing, shielding gas to accelerate the wind, i.e. a different than radiatively driven quasar wind or a scenario which includes magnetic forces as shielding and/or accelerating factors. The relative number of X-ray non-detected BAL QSOs compared to the number of X-ray non-detected SDSS DR5 QSOs, together with the smooth connection of X-ray properties between bright (i.e. spectrally analyzed) and faint (i.e. hardness ratio analyzed) X-ray detected BAL QSOs, strongly suggests the former hypothesis. If this were true, one can expect more X-ray absorption in the ~ 100 BAL QSOs with only X-ray upper limits. These intriguing results deserve to be investigated more accurately with the increase of the number of BAL QSOs well-studied in both the UV and X-ray band in order to test the accretion disk wind models and the quasar outflow scenarios.

3.9 Tables and Spectra

Table 3.1. The SDSS/2XMM BAL QSO sample

Name	z	SDSS name	2XMM name	Offset [""]	Notes	Analysis
(1)	(2)	(3)	(4)	(5)	(6)	(7)
0042-0912	1.778	SDSS J004206.18-091255.7	2XMM J004206.1-091255	0.78		H
0231-0739	2.508	SDSS J023148.80-073906.3	2XMM J023148.8-073905	0.36		S
0243+0000	1.995	SDSS J024304.68+000005.4	2XMM J024304.6+000005	0.54		S
0734+3203	2.082	SDSS J073405.24+320315.2	2XMM J073405.2+320315	0.78		H
0855+3757	1.929	SDSS J085551.24+375752.2	2XMM J085551.1+375752	0.60		S
0911+0550	2.793	SDSS J091127.61+055054.0	2XMM J091127.5+055054	0.36	L	S
0921+5131	1.845	SDSS J092142.57+513149.4	2XMM J092142.5+513148	1.32		H
0922+5121	1.753	SDSS J092238.43+512121.2	2XMM J092238.3+512120	0.72		S
0923+5127	2.163	SDSS J092345.19+512710.0	2XMM J092345.1+512711	1.14	R	H
1001+0140	2.059	SDSS J100116.78+014053.5	2XMM J100116.7+014053	1.68		S
1001+0224	2.032	SDSS J100145.15+022456.9	2XMM J100145.2+022456	1.08		H
1007+5343	1.772	SDSS J100728.69+534326.7	2XMM J100728.8+534327	1.86	L	S
1011+5541	2.813	SDSS J101144.33+554103.1	2XMM J101144.4+554103	1.02		S
1019+0825	3.010	SDSS J101954.54+082515.0	2XMM J101954.6+082515	2.16		H
1106+5222	1.840	SDSS J110637.16+522233.4	2XMM J110637.0+522233	1.08		H
1123+0524	3.699	SDSS J112300.25+052451.0	2XMM J112300.3+052448	2.46		H
1135+4913	1.992	SDSS J113537.67+491323.2	2XMM J113537.6+491322	0.24		H
1141-0143	1.266	SDSS J114111.61-014306.6	2XMM J114111.5-014305	1.26	R	H
1223+1034	2.761	SDSS J122307.52+103448.2	2XMM J122307.4+103448	0.12		S
1227+0126	1.953	SDSS J122708.29+012638.4	2XMM J122708.2+012638	0.30		H
1236+6158	2.520	SDSS J123637.45+615814.4	2XMM J123637.7+615813	1.26		H
1245-0021	2.354	SDSS J124520.72-002128.2	2XMM J124520.6-002127	0.48		S
1324+0320	3.371	SDSS J132401.53+032020.6	2XMM J132401.4+032019	1.08	R	H
1328+5818	3.139	SDSS J132827.07+581836.9	2XMM J132827.3+581839	3.78		H
1340-0019	1.857	SDSS J134059.24-001944.9	2XMM J134059.1-001945	1.32		H
1435+4841	1.886	SDSS J143513.89+484149.3	2XMM J143513.9+484149	0.78		H
1446+0255	1.864	SDSS J144625.48+025548.6	2XMM J144625.6+025549	1.80		H
1508+5652	1.803	SDSS J150858.15+565226.5	2XMM J150858.2+565227	1.14		H
1517+0016	1.887	SDSS J151729.70+001652.6	2XMM J151729.6+001651	1.08		H
1525+5136	2.882	SDSS J152553.89+513649.1	2XMM J152553.8+513649	0.60		S
1533+3243	1.900	SDSS J153322.80+324351.4	2XMM J153322.8+324351	0.60		H
1543+5359	2.370	SDSS J154359.44+535903.2	2XMM J154359.4+535902	0.36		S
2039-0102	2.065	SDSS J203941.04-010201.6	2XMM J203941.2-010202	3.72		H
<hr/>						
0043+0046	1.574	SDSS J004338.10+004615.9	2XMM J004338.0+004616	0.48		S
0043+0052	0.834	SDSS J004341.24+005253.3	2XMM J004341.3+005253	1.02		S
0109+1328	1.225	SDSS J010941.97+132843.8	2XMM J010941.8+132844	1.62		H
0242-0000	2.507	SDSS J024230.65-000029.6	2XMM J024230.6-000030	1.32		H
0302+0006	3.315	SDSS J030222.08+000631.0	2XMM J030222.0+000630	0.90		S
0729+3700	0.969	SDSS J072945.33+370031.9	2XMM J072945.3+370032	0.54		H
0919+3030	1.387	SDSS J091914.23+303019.0	2XMM J091914.2+303018	0.42		H
0939+3556	2.046	SDSS J093918.07+355615.0	2XMM J093918.1+355612	2.64		H
0943+4811	1.809	SDSS J094309.56+481140.5	2XMM J094309.8+481142	3.42		H
1001+5553	1.413	SDSS J100120.84+555349.5	2XMM J100120.7+555351	1.32	L	S
1021+1315	1.565	SDSS J102117.74+131545.9	2XMM J102117.7+131546	0.78		S
1052+4414	1.791	SDSS J105201.35+441419.8	2XMM J105201.3+441417	1.62		H
1124+3851	3.530	SDSS J112432.14+385104.3	2XMM J112432.0+385104	1.02		H
1146+4723	1.895	SDSS J114636.88+472313.3	2XMM J114636.9+472313	0.42	R	S
1205+4431	1.921	SDSS J120522.18+443140.4	2XMM J120522.1+443141	0.90		S
1335+5147	1.838	SDSS J133553.61+514744.1	2XMM J133553.7+514744	1.20		S
1336+5146	2.228	SDSS J133639.40+514605.2	2XMM J133639.1+514608	4.14		H
1425+3739	2.693	SDSS J142555.22+373900.7	2XMM J142555.2+373900	0.54		H
1425+3757	1.897	SDSS J142539.38+375736.7	2XMM J142539.3+375736	0.54		S
1426+3753	1.812	SDSS J142652.94+375359.9	2XMM J142652.8+375401	2.10		H
1447+4032	1.335	SDSS J144727.49+403206.3	2XMM J144727.4+403206	0.60		S

Notes: Col.(1): Source name used throughout the paper; Col.(2): Redshift, taken from SDSS; Col.(3): SDSS source name; Col.(4): 2XMM source name; Col.(5): Offset between the positions given in the two catalogs; Col.(6): Notes on individual objects: L = lensed QSO, R = Radio-loud QSO; Col.(7): Kind of X-ray analysis used in this work: S = spectral analysis, H = hardness ratio analysis. The horizontal line separates BAL QSOs taken from Trump et al. (2006) (upper table) from BALQSOs taken from Shen et al. (2008) (lower table).

Table 3.2. X-ray observations log for the 22 SDSS/2XMM BAL QSOs with Spectral Analysis available

Name	OBSID	Duration	Exposure	Count-rate
		[ks]	M1/M2/pn [ks]	M1/M2/pn [ct ks ⁻¹]
(1)	(2)	(3)	(4)	(5)
0231-0739	0200730401	44.9	41.7/42.4/33.7	1.41(0.24)/1.58(0.22)/7.33(0.68)
0243+0000	0111200101	42.2	36.7/34.3/-	3.02(0.30)/2.84(0.31)/-
	0111200201	46.4	33.5/32.3/-	2.73(0.33)/2.55(0.35)/-
0855+3757	0302581801	29.1	27.2/27.1/17.8	2.09(0.29)/1.55(0.27)/7.19(0.85)
0911+0550	0083240201	20.7	19.3/19.2/13.4	10.59(0.86)/12.48(0.90)/34.75(2.18)
0922+5121	0300910301	40.9	37.6/37.8/33.2	3.41(0.39)/3.05(0.38)/11.80(1.08)
1001+0140	0302351001	43.5	42.5/42.0/33.9	2.23(0.26)/2.61(0.28)/11.43(0.81)
1007+5343	0070340201	34.2	21.7/21.6/16.5	1.87(0.42)/3.50(0.53)/9.01(0.95)
1011+5541	0085170101	33.2	-/-/24.1	-/-/3.65(0.51)
1223+1034	0108860101	22.1	20.3/20.4/15.3	5.31(0.64)/5.72(0.62)/22.75(1.46)
1245-0021	0110980201	58.2	56.4/56.2/47.8	0.58(0.14)/0.82(0.16)/3.68(0.38)
1525+5136	0011830201	38.7	29.9/30.1/23.7	22.21(0.91)/20.71(0.89)/79.60(1.97)
1543+5359	0060370901	34.1	24.8/23.3/21.5	12.41(0.81)/12.66(0.84)/45.20(2.33)
0043+0046	0090070201	21.1	20.3/20.3/16.3	3.15(0.45)/5.02(0.56)/17.56(1.30)
0043+0052	0090070201	21.1	-/-/16.3	-/-/13.55(1.02)
0302+0006	0041170101	51.7	46.4/45.9/37.1	1.76(0.21)/1.31(0.21)/4.10(0.42)
1001+5553	0147760101	44.4	30.9/32.3/25.8	56.45(1.41)/54.19(1.34)/311.40(4.02)
1021+1315	0146990101	21.9	19.5/19.8/15.3	4.29(0.52)/5.15(0.61)/19.02(1.22)
1146+4723	0047540601	28.6	26.2/27.0/20.0	9.11(0.72)/9.57(0.71)/35.60(1.65)
1205+4431	0156360101	52.2	-/-/18.7	-/-/4.75(0.78)
1335+5147	0084190201	48.8	-/-/35.3	-/-/2.88(0.37)
1425+3757	0112230201	25.8	24.0/24.5/18.4	2.20(0.34)/1.14(0.33)/6.32(0.85)
1447+4032	0109080601	22.0	19.0/19.2/16.2	5.35(0.63)/4.95(0.63)/20.01(1.24)

Notes: Col.(1): Source name; Col.(2): Observation ID; Col.(3): Nominal duration of the observation; Col.(4): Net exposure time for each instrument after the background flaring filtering was applied; Col.(5): Net count-rate for each instrument after the local background subtraction was applied, with corresponding errors reported in parentheses.

Table 3.3. SDSS/2XMM BAL QSOs: spectral analysis results

Name	$N_{\text{H,Gal}}$ [10^{20} cm^{-2}]	Γ	N_{H} [10^{22} cm^{-2}]	$N_{1\text{keV}}$ [$10^{-4} \text{ ph keV}^{-1} \text{ cm}^{-2} \text{ s}^{-1}$]	χ^2/dof	$\log f_{\text{X}}(0.5-2)$ [$\text{erg s}^{-1} \text{ cm}^{-2}$]	$\log f_{\text{X}}(2-10)$ [$\text{erg s}^{-1} \text{ cm}^{-2}$]	$\log L(2-10)$ [erg s^{-1}]
(1)	(2)	(3)	(4)	(5)	(6)	(7)	(8)	(9)
0231-0739	3.14	$1.82_{-0.28}^{+0.18}$	< 0.64	$0.62_{-0.15}^{+0.39}$	50/31	-13.8	-13.7	45.0
0243+0000	3.56	$1.86_{-0.21}^{+0.51}$	$5.02_{-1.92}^{+4.48}$	$1.14_{-0.46}^{+2.28}$ (*)	30/26	-13.8 (*)	-13.2 (*)	45.0 (*)
0855+3757	2.92	$1.84_{-0.28}^{+0.34}$	$0.94_{-0.71}^{+1.17}$	$0.50_{-0.19}^{+0.45}$	10/15	-14.0	-13.7	44.6
0911+0550	3.64	$1.59_{-0.15}^{+0.17}$	$2.45_{-0.99}^{+1.23}$	$2.71_{-0.88}^{+1.67}$	55/71	-13.3	-12.8	45.7
0922+5121	1.43	$2.08_{-0.19}^{+0.18}$	< 0.07	$0.51_{-0.09}^{+0.10}$	75/72	-13.8	-13.8	44.6
1001+0140	2.60	$2.01_{-0.16}^{+0.17}$	< 0.11	$0.51_{-0.07}^{+0.15}$	41/48	-13.9	-13.8	44.7
1007+5343	0.71	$1.33_{-0.23}^{+0.45}$	< 1.29	$0.29_{-0.09}^{+0.41}$	22/20	-13.78	-13.3	44.9
1011+5541	0.79	$1.28_{-0.50}^{+0.77}$	$4.52_{-3.86}^{+11.46}$	$0.18_{-0.09}^{+0.81}$	5/5	-14.2	-13.7	44.7
1223+1034	2.22	$1.98_{-0.20}^{+0.22}$	< 0.99	$1.96_{-0.63}^{+1.01}$	45/41	-13.7	-13.5	45.3
1245-0021	1.70	$1.75_{-0.48}^{+0.54}$	$5.03_{-3.87}^{+5.52}$	$0.43_{-0.10}^{+0.95}$	25/20	-14.2	-13.7	44.8
1525+5136	1.57	$1.80_{-0.07}^{+0.08}$	$1.01_{-0.19}^{+0.28}$	$4.87_{-0.71}^{+0.78}$	179/197	-13.1	-12.8	45.9
1543+5359	1.25	$1.72_{-0.13}^{+0.15}$	$0.56_{-0.31}^{+0.40}$	$0.50_{-0.19}^{+0.45}$	184/147	-13.3	-13.0	45.5
0043+0046	2.31	$1.82_{-0.15}^{+0.17}$	< 0.08	$0.64_{-0.10}^{+0.16}$	37/40	-13.6	-13.4	44.7
0043+0052	2.32	$1.49_{-0.38}^{+0.27}$	$0.87_{-0.48}^{+0.92}$	$0.39_{-0.17}^{+0.44}$	16/13	-13.7	-13.1	44.3
0302+0006	7.16	$1.69_{-0.26}^{+0.37}$	$3.17_{-3.06}^{+5.33}$	$0.54_{-0.21}^{+0.73}$	19/21	-14.2	-13.6	45.0
1001+5553	0.82	$2.15_{-0.03}^{+0.03}$	< 0.01	$21.80_{-0.60}^{+0.60}$	513/522	-12.1	-12.1	46.0
1021+1315	3.92	$2.16_{-0.23}^{+0.39}$	< 0.37	$1.66_{-0.39}^{+0.83}$	35/31	-13.3	-13.3	45.0
1146+4723	2.22	$2.00_{-0.14}^{+0.21}$	$0.29_{-0.15}^{+0.21}$	$2.53_{-0.50}^{+0.80}$	98/94	-13.2	-13.1	45.3
1205+4431	1.15	$1.59_{-0.51}^{+0.82}$	$1.67_{-1.54}^{+4.73}$	$0.25_{-0.11}^{+0.91}$	2/7	-14.1	-13.5	44.5
1335+5147	0.94	$2.42_{-0.91}^{+1.31}$	$8.91_{-6.31}^{+8.42}$	$1.49_{-0.51}^{+8.51}$	9/6	-14.2	-14.0	44.6
1425+3757	0.95	$2.45_{-0.58}^{+0.78}$	$4.28_{-2.34}^{+3.80}$	$2.38_{-1.45}^{+7.79}$	19/15	-13.7	-13.7	45.1
1447+4032	1.23	$2.29_{-0.12}^{+0.21}$	< 0.07	$1.08_{-0.12}^{+0.25}$	34/36	-13.5	-13.6	44.6

Notes: Col.(1): Source name; Col.(2): Galactic neutral hydrogen column density, taken from Dickey & Lockman (1990); Col.(3): Photon Index; Col.(4): Neutral hydrogen column density at the source redshift; Col. (5): EPIC-pn power law normalization at 1 keV; Col.(6): Best-fit χ^2 value over degrees of freedom; Col.(7): Logarithm of EPIC-pn 0.5 – 2 keV observed flux, corrected for Galactic neutral absorption; Col.(8): Logarithm of EPIC-pn 2 – 10 keV observed flux, corrected for Galactic neutral absorption; Col.(9): Logarithm of EPIC-pn 2 – 10 keV rest-frame luminosity, corrected for both Galactic and intrinsic absorption. Values marked with (*) refer to EPIC-MOS instrument.

Table 3.4. SDSS/2XMM BAL QSOs: hardness ratio analysis results

Name	HR	$N_{\text{H,Gal}}$ [10^{20} cm^{-2}]	N_{H} [10^{22} cm^{-2}]
(1)	(2)	(3)	(4)
0042-0912	-0.49 ± 0.17	2.77	2.0 (0.5-4.0)
0109+1328	-0.65 ± 0.17	3.26	0.5 (0.01-1.0)
0242-0000	-0.24 ± 0.12	2.91	10.0 (7.0-15.0)
0729+3700	-0.67 ± 0.26	5.77	< 0.5
0734+3203	-0.83 ± 0.15	4.46	< 0.5
0919+3030	-0.60 ± 0.19	1.64	0.5 (0.01-2.0)
0921+5131	-0.87 ± 0.11	1.29	< 0.01
0923+5127	-0.73 ± 0.24	1.34	< 3.0
0939+3556	-0.53 ± 0.30	1.07	2.0 (0.01-6.0)
0943+4811	-0.18 ± 0.26	1.22	7.0 (3.0-15.0)
1001+0224	-0.52 ± 0.07	1.78	2.0 (1.0-3.0)
1019+0825	-0.82 ± 0.15	2.52	< 1.0
1052+4414	-0.12 ± 0.17	1.08	9.0 (5.0-15.0)
1106+5222	-0.60 ± 0.39	0.89	1.0 (0.01-2.0)
1123+0524	-0.78 ± 0.22	3.71	< 5.0
1124+3851	-0.30 ± 0.20	2.01	20.0 (7.0-30.0)
1135+4913	-0.81 ± 0.12	1.68	< 0.5
1141-0143	-0.35 ± 0.17	2.16	2.0 (1.0-4.0)
1227+0126	-0.50 ± 0.30	1.72	2.0 (0.5-5.0)
1236+6158	-0.81 ± 0.11	1.07	< 0.5
1324+0320	-0.47 ± 0.22	1.82	8.0 (1.0-20.0)
1328+5818	0.00 ± 0.21	1.58	40.0 (20.0-50.0)
1336+5146	-0.79 ± 0.18	0.92	< 1.0
1340-0019	-0.75 ± 0.15	1.79	< 1.0
1425+3739	-0.38 ± 0.18	1.04	8.0 (3.0-15.0)
1426+3753	-0.62 ± 0.22	1.10	1.0 (0.05-2.0)
1435+4841	-0.50 ± 0.20	2.91	2.0 (0.01-8.0)
1446+0255	-0.25 ± 0.20	3.16	6.0 (3.0-10.0)
1508+5652	-0.62 ± 0.16	1.64	1.0 (0.01-3.0)
1517+0016	< -0.72	4.36	< 0.1
1533+3243	-0.53 ± 0.12	2.24	2.0 (0.05-3.0)
2039-0102	-0.64 ± 0.34	6.30	1.0 (0.01-6.0)

Notes: Col.(1): Source name; Col.(2): Hardness ratio computed between (0.2-2) and (2-8) keV. Errors are at 1σ , propagated from the count-rate errors using the numerical method of Lyons (1991); Col.(3): Galactic neutral hydrogen column density, taken from Dickey & Lockman (1990); Col.(4): Neutral hydrogen column density at the source redshift estimated from hardness ratio, where the number in parentheses are the 1σ confidence intervals.

Table 3.5. SDSS/2XMM BAL QSOs: optical/X-ray properties

Name (1)	$\log f_{2 \text{ keV}}$ (2)	$\log f_{2500}$ (3)	α_{ox} (4)	$\log \ell_{2500}$ (5)	$\alpha_{\text{ox}}(\ell_{2500})$ (6)	$\Delta\alpha_{\text{ox}}$ (7)	Type (8)	AI (9)	v_{out} (10)
0042-0912	-31.26	-27.06	-1.61	30.84	-1.61	0.00	Hi	276	9400
0231-0739	-31.11	-27.38	-1.43	30.77	-1.60	0.17	H	510	19400
0243+0000	-31.24	-26.68	-1.75	31.31	-1.68	-0.07	Hi	1792	6200
0734+3203	-31.67	-27.31	-1.67	30.71	-1.59	-0.08	Hi	333	29000
0855+3757	-31.40	-26.77	-1.78	31.18	-1.66	-0.12	Hi	1482	21200
0911+0550	-30.67	-26.55	-1.58	31.69	-1.73	0.15	H	1149	21500
0921+5131	-31.12	-27.00	-1.58	30.92	-1.62	0.04	Hi	404	1600
0922+5121	-31.16	-27.50	-1.40	30.38	-1.55	0.15	Lo	1075	9600
0923+5127	-31.19	-27.04	-1.59	31.00	-1.63	0.04	Hi	3956	19400
1001+0140	-31.23	-27.28	-1.52	30.72	-1.59	0.07	Hi	427	5000
1001+0224	-31.47	-27.47	-1.54	30.53	-1.57	0.03	Hi	547	1100
1007+5343	-31.23	-27.09	-1.59	30.80	-1.61	0.02	Lo	748	6000
1011+5541	-31.66	-27.38	-1.64	30.85	-1.61	-0.03	H	2139	4100
1019+0825	-30.78	-26.47	-1.66	31.82	-1.75	0.09	H	425	26900
1106+5222	-31.93	-27.05	-1.87	30.87	-1.62	-0.25	Hi	2048	3900
1123+0524	-31.48	-27.30	-1.60	31.13	-1.65	0.05	H	508	8800
1135+4913	-31.72	-27.01	-1.81	30.97	-1.63	-0.18	Hi	306	13700
1141-0143	-31.78	-26.55	-2.01	31.06	-1.64	-0.37	Lo	261	4100
1223+1034	-30.99	-26.93	-1.56	31.29	-1.68	0.12	H	1707	5300
1227+0126	-32.09	-27.05	-1.93	30.92	-1.62	-0.31	Hi	1820	18100
1236+6158	-31.77	-26.79	-1.91	31.37	-1.69	-0.22	H	621	14100
1245-0021	-31.57	-27.34	-1.62	30.76	-1.60	-0.02	H	2735	4400
1324+0320	-31.80	-26.89	-1.89	31.48	-1.70	-0.19	H	1369	3200
1328+5818	-31.63	-26.75	-1.87	31.57	-1.71	-0.16	H	3890	8000
1340-0019	-31.40	-27.32	-1.56	30.60	-1.58	0.02	Hi	488	2560
1435+4841	-31.09	-26.99	-1.57	30.94	-1.63	0.06	Hi	1879	3800
1446+0255	-31.72	-27.03	-1.80	30.90	-1.62	-0.18	Hi	1784	6900
1508+5652	-31.16	-26.99	-1.60	30.91	-1.62	0.02	Hi	979	2900
1517+0016	-31.86	-26.93	-1.89	31.01	-1.64	-0.25	Hi	451	14100
1525+5136	-30.39	-26.09	-1.65	32.17	-1.80	0.15	H	6216	28900
1533+3243	-31.26	-26.94	-1.66	31.01	-1.64	-0.02	Hi	714	4100
1543+5359	-30.67	-26.19	-1.72	31.92	-1.76	0.04	H	503	14000
2039-0102	-31.56	-26.90	-1.79	31.11	-1.65	-0.14	Hi	311	4900
0043+0046	-31.04	-27.31	-1.43	30.48	-1.56	0.13	Lo	530(*)	15800(*)
0043+0052	-31.25	-27.99	-1.25	29.27	-1.39	0.14	Lo	570(*)	17000(*)
10109+1328	-31.40	-27.07	-1.66	30.52	-1.57	-0.09	Lo	180(*)	1000(*)
0242-0000	-31.75	-26.98	-1.83	31.17	-1.66	-0.17	H	6700(*)	12000(*)
0302+0006	-31.49	-27.48	-1.54	30.88	-1.62	0.08	H	1570(*)	4000(*)
0729+3700	-31.60	-27.04	-1.75	30.35	-1.54	-0.21	Lo	430(*)	25000(*)
0919+3030	-31.68	-26.85	-1.86	30.84	-1.61	-0.25	Lo	215(*)	25000(*)
0939+3556	-31.89	-26.86	-1.93	31.14	-1.65	-0.28	Hi	520(*)	16000(*)
0943+4811	-31.78	-26.96	-1.85	30.95	-1.63	-0.22	Hi	640(*)	20000(*)
1001+5553	-29.54	-26.18	-1.29	31.52	-1.71	0.42	Lo	150(*)	25000(*)
1021+1315	-30.70	-26.78	-1.50	31.01	-1.64	0.14	Lo	550(*)	25000(*)
1052+4414	-31.53	-26.91	-1.77	30.98	-1.63	-0.14	Hi	4500(*)	25000(*)
1124+3851	-31.69	-27.33	-1.67	31.07	-1.64	-0.03	H	1320(*)	14500(*)
1146+4723	-30.57	-26.97	-1.38	30.97	-1.63	0.25	Lo	550(*)	12600(*)
1205+4431	-31.60	-26.80	-1.84	31.15	-1.66	-0.18	Hi	1900(*)	20000(*)
1335+5147	-31.52	-26.70	-1.85	31.22	-1.67	-0.18	Lo	1890(*)	9000(*)
1336+5146	-31.93	-26.99	-1.90	31.08	-1.65	-0.25	H	4300(*)	7600(*)
1425+3739	-31.65	-27.00	-1.78	31.21	-1.66	-0.12	H	550(*)	20000(*)
1425+3757	-30.95	-26.69	-1.63	31.26	-1.67	0.04	Hi	1880(*)	25000(*)
1426+3753	-31.56	-27.10	-1.71	30.80	-1.61	-0.10	Hi	790(*)	25000(*)
1447+4032	-30.94	-26.75	-1.61	30.91	-1.62	0.01	Lo	670(*)	17000(*)

Notes: Col.(1): Source name; Col.(2): Logarithm of 2 keV observed flux density in units of $\text{erg s}^{-1} \text{cm}^{-2} \text{Hz}^{-1}$; Col.(3): Logarithm of 2500 Å observed flux density in units of $\text{erg s}^{-1} \text{cm}^{-2} \text{Hz}^{-1}$; Col.(4): Observed optical-X spectral index; Col.(5): Logarithm of 2500 Å intrinsic luminosity density in units of $\text{erg s}^{-1} \text{Hz}^{-1}$; Col.(6): Optical-X spectral index expected from Eq.(3) of Just et al. (2007); Col.(7): Difference between observed and expected α_{ox} ; Col.(8): BAL QSO subclassification, Lo=LoBAL, Hi=HiBAL, H=BAL QSO for which the Mg II spectral region is redshifted outside the SDSS window, so preventing from checking the presence of low-ionization absorption troughs; Col.(9): Absorption Index (AI) taken from Trump et al. (2006) when available, in units of km s^{-1} ; Col.(10): Maximum velocity outflow taken from Trump et al. (2006) when available, in units of km s^{-1} . The values of AI and v_{out} marked with (*) are estimated by us from SDSS spectra.

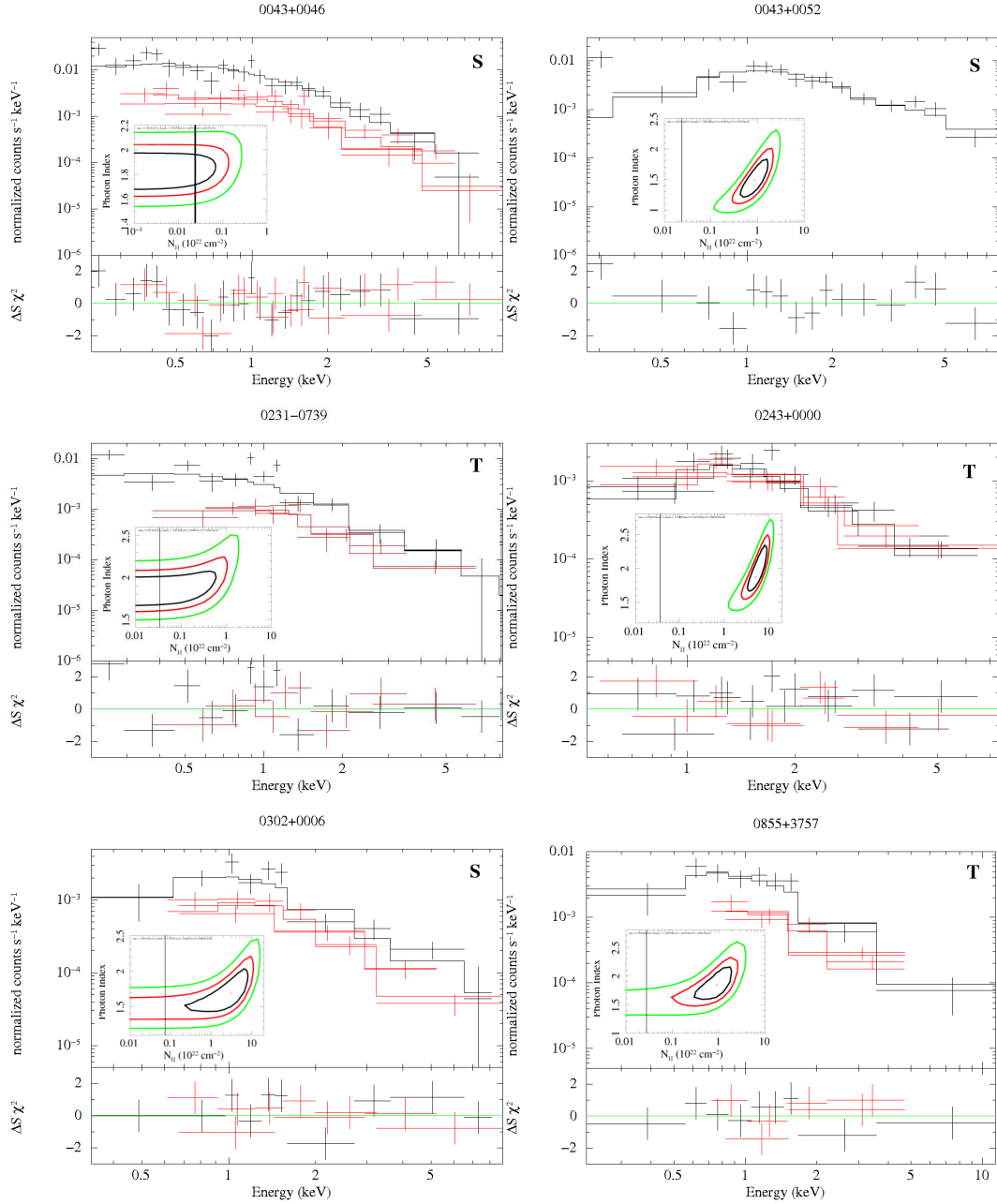


Figure 3.10. Source spectra of the 22 SDSS/2XMM BAL QSOs with spectral analysis available. EPIC-pn data points are plotted thick and black, while EPIC-MOS data are plotted thin and red. The inset contains confidence contours at 68, 90 and 99% confidence level for the column density N_H and photon index Γ , where the vertical line marks the amount of Galactic neutral absorption. In the top-right corner is reported a “T” for BALQSOs selected from Trump et al. (2006), a “S” for BALQSOs selected from Shen et al. (2008).

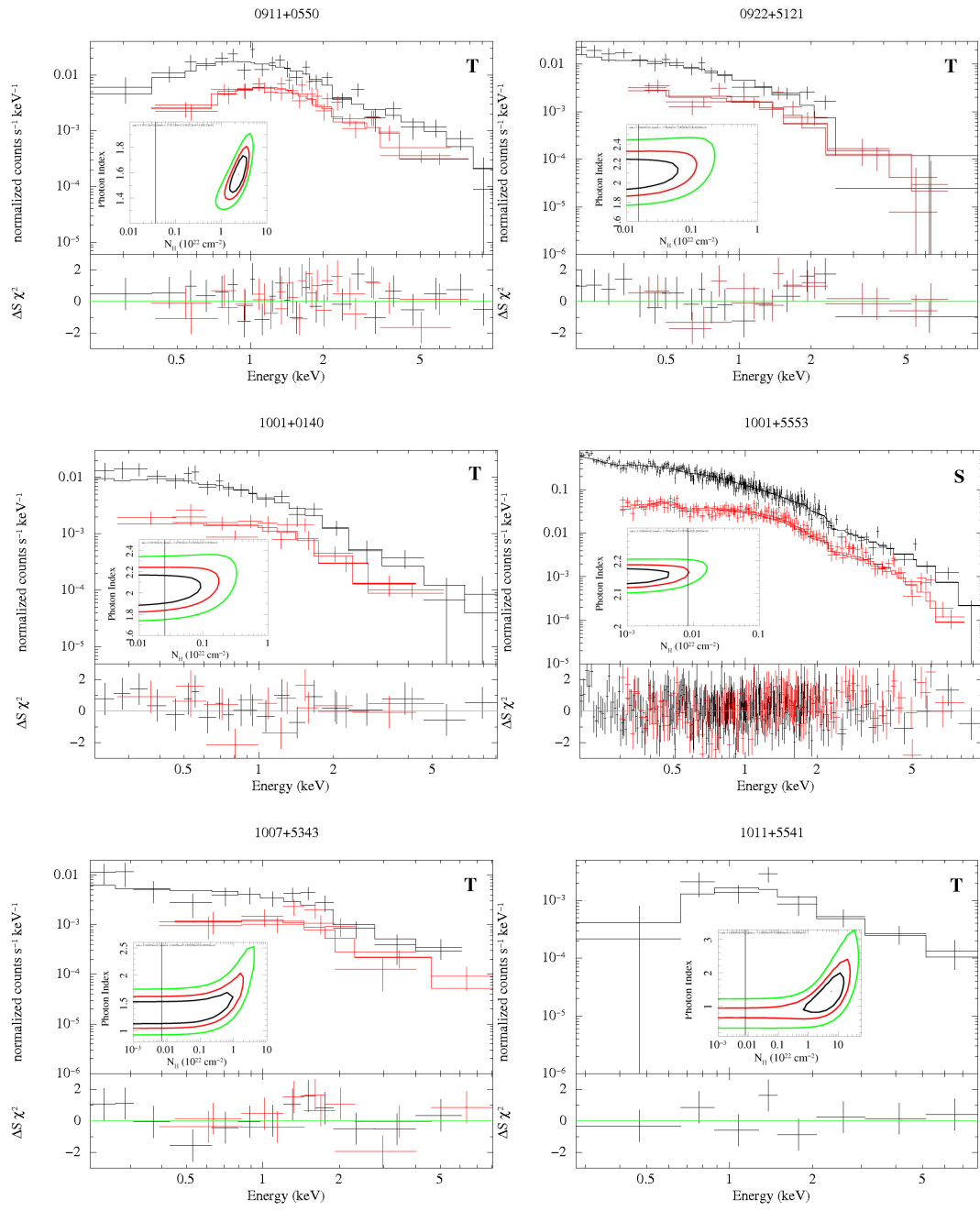


Figure 3.10. – Continued

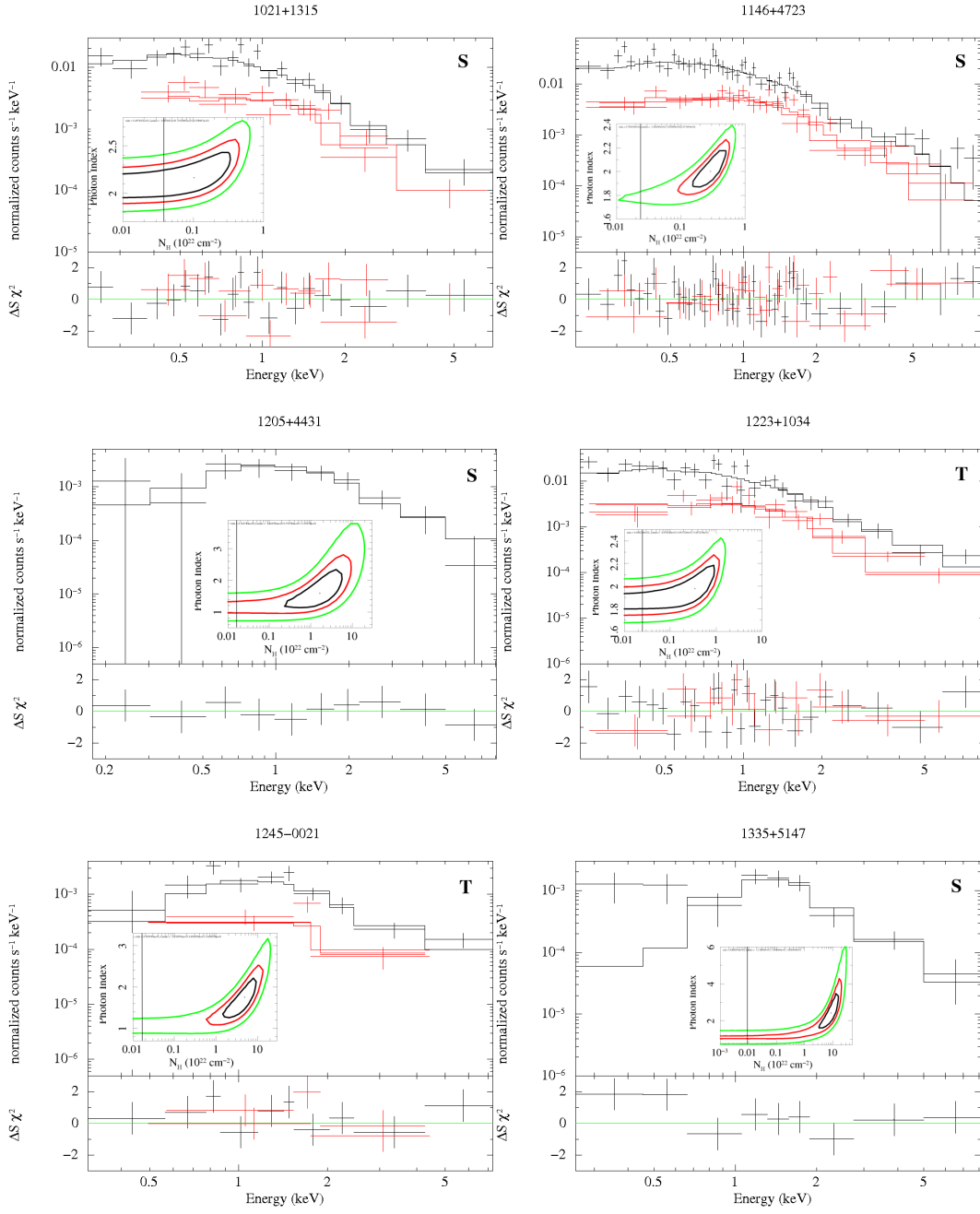


Figure 3.10. – Continued

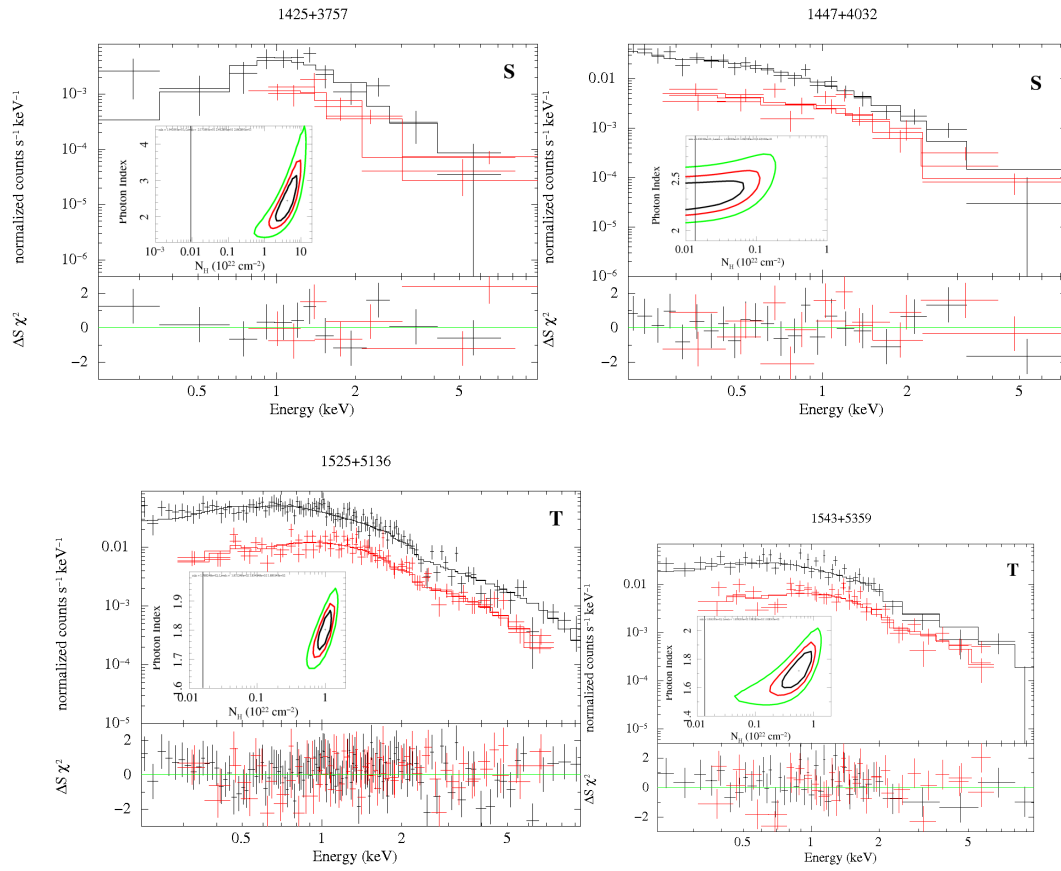


Figure 3.10. – Continued

Chapter 4

Archival study of BAL, mini-BAL, and NAL PG QSOs

The broad band X-ray properties of BAL QSOs have been studied in large samples of sources through techniques such as hardness ratio, stacking analysis, and low-S/N CCD spectroscopy (from a few up to a few hundred counts in the 0.2-10 keV band). Altogether, these studies were able to roughly characterize the continuum slope to be typical of type 1 AGN, $\Gamma \sim 1.8$. Neutral absorption intrinsic to the AGN was generally found to be significant, $N_H \sim 10^{23} \text{ cm}^{-2}$, but not in every BAL QSO, with some sources having absorbing column density of just a few of 10^{21} cm^{-2} . More detailed studies of moderate S/N spectra (from a few hundred up to several thousand counts) have been limited to a few bright BAL and mini-BAL QSOs with pointed observation of either *ROSAT*, *ASCA*, *Chandra*, or *XMM – Newton*, and have often revealed interesting complexities in the absorbers: ionized, blueshifted, partial covering, and variable X-ray absorption have all been detected at least once, at least in one BAL or mini-BAL QSO. However, such studies have been sporadic and related to basically randomly selected sources. On the other hand, the properties of NAL QSOs as a population are basically unknown in the X-ray band such as at other wavelengths, because these objects are very difficult to identify and still have to be collected in large samples that would allow for systematic studies.

In this Chapter I will present the analysis of 32 XMM-Newton pointed observations of a small sample of 15 BAL, mini-BAL, and NAL QSOs, bright enough to be studied with moderate resolution, possibly temporally resolved X-ray spectroscopy, with the aim to present the flavor of their X-ray spectral characteristics.

4.1 The Sample

The sources have been selected from the Palomar-Green bright quasar survey (PG QSOs, Schmidt & Green 1983; Green et al. 1986). The PG catalog is the archetypal sample of UV-excess selected, bright ($m_B < 16$) and blue ($U - B < -0.44$) QSOs, and the best studied AGN sample with an impressive multiwavelength coverage performed over the past three decades (see e.g. Tananbaum et al. 1986; Neugebauer et al. 1987; Sanders et al. 1989; Kellermann et al. 1989; Boroson & Green 1992; Miller et al. 1992; Laor et al. 1997; Brandt et al. 2000; Piconcelli et al. 2005; Dasyra et al. 2007). Because of the magnitude and color selection, the PG QSOs are mostly at low redshift, with a $\langle z \rangle \sim 0.2$, thus often bright enough to make it possible to perform a more detailed X-ray spectral analysis than for the dimmer $z \sim 2$ SDSS (e.g, Chapter 3 of this Thesis) or LBQS (Gallagher et al. 2006) BAL QSOs, using reasonable exposure times with the current X-ray observatories. About the possible peculiar properties of the PG QSOs with respect to the mean QSO population, Jester et al. (2005) demonstrated how the PG sample properties are well representative of those of the much larger (both in covered area and in redshift) sample given by the SDSS QSOs.

The instrument chosen to study the X-ray properties of the BAL, mini-BAL, and NAL PG QSOs is the EPIC-pn camera aboard the *XMM-Newton* observatory. The EPIC-pn has the largest effective area among the current flying X-ray detectors (A_{Eff} up to $\sim 1000 \text{ cm}^2$) over a broad energy range ($A_{Eff} > 100 \text{ cm}^2$ from ~ 0.2 up to $\sim 10 \text{ keV}$), and a moderate spectral resolution ($E/\Delta E \sim 20 - 30$). These characteristics make the EPIC-pn the ideal instrument to perform spectral analysis on X-ray weak sources such as BAL QSOs, the large effective area assuring a high number of counts collected, the broad band assuring a proper characterization of the circumnuclear gas absorbing the intrinsic continuum. Furthermore, the EPIC-pn can effectively probe a very broad range of ionization states of the absorbing matter, from the neutral photoelectric cutoff affecting the lowest energies up to the highly ionized iron affecting the highest energies probed by the EPIC-pn. Another feature that makes *XMM-Newton* an excellent instrument to study BAL QSOs is the presence onboard of the optical monitor (OM) that operates simultaneously with the other detectors. Given the bandwidth of the most used optical filters (U, UVW1, and UVM2, covering $\sim 2000 - 4000 \text{ \AA}$), this allows to measure the $f_{2500 \text{ \AA}}$ for sources at redshift $z \gtrsim 0.5$, giving an optical to X-ray spectral index α_{ox} *simultaneously* measured in the X-ray and in

the UV band, as opposite to what can be usually measured. AGN are known to be highly variable in flux, especially at X-ray wavelengths. In order to gain meaningful insights onto their physical characteristics using UV/X-ray relative properties (that probe the accretion disk and the hot corona, respectively), the simultaneous measure of α_{ox} is highly preferred to a non-simultaneous one.

The classical PG sample as introduced by Schmidt & Green (1983) includes 114 QSOs, while the whole sample as refined by Green et al. (1986) includes 123 QSOs. 20 PG QSOs are classified either as NAL, mini-BAL, or BAL QSOs. Of these, all but five (the BAL QSOs PG 0946+301, PG 1254+047, and PG 1552+085; the NAL QSOs PG 1222+228 and PG 1329+412) have XMM-Newton archival data available as January 2011. It is worth noting that not every PG QSO has a high S/N optical/UV spectrum available in the wavelength interval where BALs can be identified, so that drawing a percentage of BAL QSO among the PG sample is not yet possible, and the selection made in this work is not complete. The same is true also for mini-BAL and NAL QSOs, that are both more difficult to identify, and not yet studied in a systematic way (see the selection effects discussed in Chapter 2).

Table 4.1 lists the name, the coordinates (J2000), the redshift, the Galactic column density, the Galactic extinction, the optical magnitude in the B band, the BAL sub-type for the 15 sources analyzed, and the literature reference for this classification. Of the 15 selected sources, one is a NAL+BAL QSO (PG 0043+039), one is a NAL+mini-BAL QSO (PG 1411+442), 6 are mini-BAL QSOs, 1 is a NAL QSO, and 6 are BAL QSOs. The “discussed” BAL QSO PG 1416-129 was also included (see Green et al. 1997), given the possible variability that might have occurred between the different UV observations performed by IUE and HST (it is worth noting that at the time of the Green et al. analysis, no QSO was known to be variable in its BAL character: the first QSOs possessing variable BALs have been discovered around 2007). Table 4.2 reports the observation log for the 32 EPIC-pn exposures analyzed: the X-ray observation ID, the observing mode, the adopted filter, the date of observation, the nominal duration of the pointing, the net exposure, the background-subtracted count-rate in the 0.2-10 keV band, and the references for detailed X-ray analyses that have already been published in the literature.

Table 4.1. General properties of the 15 QSOs analyzed in this work. These are all the PG QSOs classified as BAL, mini-BAL, or NAL QSOs with public archival *XMM-Newton* observations as of January 2011.

Name (1)	RA (2)	dec (3)	z (4)	N_H^{gal} (5)	$E(B - V)$ (6)	m_B (7)	Type (8)
PG 0043+039	00h45m47.3s	+04d10m24s	0.385	3.25	0.021	15.40	BAL + NAL
PG 0935+417	09h38m57.0s	+41d28m21s	1.935	1.42	0.014	16.30	mini-BAL
PG 1001+054	10h04m20.1s	+05d13m00s	0.160	1.83	0.016	16.13	BAL
PG 1004+130	10h07m26.1s	+12d48m56s	0.241	3.56	0.038	15.21	BAL
PG 1114+445	11h17m06.4s	+44d13m33s	0.144	1.77	0.016	16.05	mini-BAL
PG 1115+080	11h18m16.9s	+07d45m58s	1.735	3.57	0.041	15.84	mini-BAL
PG 1126-041	11h29m16.6s	-04d24m08s	0.062	4.35	0.055	14.92	mini-BAL
PG 1351+640	13h53m15.8s	+63d45m46s	0.088	1.98	0.020	15.42	mini-BAL
PG 1411+442	14h13m48.3s	+44d00m14s	0.090	0.87	0.008	14.99	mini-BAL + NAL
PG 1416-129	14h19m03.8s	-13d10m44s	0.129	7.08	0.094	16.42	possibly BAL
PG 1535+547	15h36m38.3s	+54d33m33s	0.039	1.40	0.015	15.31	mini-BAL
PG 1700+518	17h01m24.8s	+51d49m20s	0.292	2.26	0.035	15.43	BAL
PG 2112+059	21h14m52.6s	+06d07m42s	0.466	6.09	0.091	15.52	BAL
PG 2233+134	22h36m07.7s	+13d43m55s	0.326	4.51	0.064	16.04	BAL
PG 2302+029	23h04m45.0s	+03d11m46s	1.044	4.88	0.057	16.03	NAL

Col. (1): source name; Col. (2): right ascension (J2000); Col. (3): declination (J2000); Col. (4): redshift; Col. (5): Galactic hydrogen equivalent column density in [10^{22} cm^{-2}], from Kalberla et al. (2005); Col. (6): Galactic extinction in [mag], from Schlegel et al. (1998); Col. (7): optical apparent magnitude in the B band, from Schmidt & Green (1983); Col. (8): blueshifted UV absorption classification.

4.2 Data reduction

I used SAS v.10.0.0, and calibration files generated in February, 2011. Every dataset has been reduced in a uniform way, with the following prescriptions: light curves of single events with energies $10 \text{ keV} < E < 12 \text{ keV}$ extracted in the whole FOV were inspected, and time intervals where the EPIC-pn count rate was exceeding 0.4 count s^{-1} were removed from the event files, as flaring background-dominated. FOV light curves are reported in the left panels of Fig. ?? for each exposure. From the filtered event files, source counts were collected in circular regions of radii 30-45'' centered on the optical position of the QSO. For on-axis observations, these correspond to $\sim 90\%$ of the encircled energy fraction of the PSF. Background counts were extracted from circular regions of the same size of the source's ones, in regions free of sources, as close as possible to the source position. All the sources are detected by EPIC-pn, except than PG 0043+039¹. Light curves at the

¹The presence of a bright X-ray source at a few arcsec from the position of PG 0043+039 prevents from placing upper limits on the X-ray flux of this BAL QSO; a high angular resolution (i.e., Chandra observations) would be required to disentangle the X-ray emission of these two sources.

Table 4.2. X-ray observation log of the BAL, mini-BAL, and NAL PG QSOs.

Name (1)	instrument (2)	OBSID (3)	Mode (4)	Filter (5)	date (6)	duration (7)	exposure (8)	count-rate (9)
PG 0043+039	EPIC-pn	0300890101	FF	th	2005-06-15	31.8	22.2	not detected
PG 0935+417	EPIC-pn	0504621001	FF	th	2007-05-06	20.5	4.4	0.0123 ± 0.003
PG 1001+054	EPIC-pn	0150610101	FF	th	2003-05-04	23.6	8.3	0.055 ± 0.003
PG 1004+130	EPIC-pn	0140550601	FF	M	2003-05-04	22.2	17.5	0.111 ± 0.003
PG 1114+445	EPIC-pn	0109080801	LW	th	2002-05-14	43.5	35.3	0.726 ± 0.005
PG 1115+080	EPIC-pn	0082340101	FF	th	2001-11-25	63.2	40.5	0.211 ± 0.003
		0203560201	FF	th	2004-06-10	81.9	55.6	0.220 ± 0.002
		0203560401	FF	th	2004-06-26	86.5	54.6	0.186 ± 0.002
PG 1126-041	See Chapter 4 of this Thesis							
PG 1351+640	EPIC-pn	0205390301	FF	M	2004-06-23	50.9	41.0	0.695 ± 0.004
		0556230101	FF	th	2008-06-08	28.7	7.8	0.113 ± 0.004
		0556230201	FF	th	2008-06-10	29.4	11.2	0.129 ± 0.004
PG 1411+442	EPIC-pn	0103660101	FF	th	2002-07-10	41.8	21.0	0.154 ± 0.003
PG 1416-129	EPIC-pn	0203770201	LW	th	2004-07-14	50.0	19.7	1.446 ± 0.009
PG 1535+547	EPIC-pn	0150610301			2002-11-03	29.7	9.9	0.158 ± 0.005
		0300310501			2006-01-24	25.9	5.5	0.622 ± 0.011
		0300310301			2006-01-16	27.8	11.0	0.395 ± 0.006
		0300310401			2006-01-22	29.5	11.4	0.449 ± 0.007
PG 1700+518	EPIC-pn	0601870101			2009-12-19	19.5	3.9	0.006 ± 0.002
		0601870201			2009-12-31	19.9	6.7	0.006 ± 0.002
		0601870301			2010-01-02	19.9	12.0	0.007 ± 0.001
PG 2112+059	EPIC-pn	0150610201			2003-05-14	16.9	7.2	0.137 ± 0.005
		0300310201			2005-11-20	76.1	59.1	0.014 ± 0.001
		0500500601			2007-05-03	24.3	16.0	0.020 ± 0.002
		0500500701			2007-05-19	100.3	37.2	0.021 ± 0.001
		0500500801			2007-05-21	99.2	58.5	0.021 ± 0.001
		0500500901			2007-11-05	51.9	35.4	0.018 ± 0.001
PG 2233+134	EPIC-pn	0153220601			2003-05-28	12.9	5.8	0.719 ± 0.012
PG 2302+029	EPIC-pn	0033541001			2001-11-29	13.1	8.3	0.265 ± 0.006

Col. (1): source name; Col. (2): instrument; Col. (3): observation ID; Col. (4): observing mode: FF = full frame, LW = large window; Col. (5): optical filter: th = thin, M = medium, TH = thick; Col. (6): date of observation; Col. (7): nominal duration of the pointing, in [ks]; Col. (8): net exposure time after the flaring background time intervals were removed, in [ks]; Col. (9): 0.2-10 keV net count rate, in [s^{-1}].

source position were generated with the task `epic1ccorr`, that corrects both for the local background, and for instrumental effects such as the time loss due to CCD read-out and the MIPS events. Source light curves are reported in the right panels of Fig. ??, for each exposure. Source and background spectra were generated including up to double events, flagged with the highest quality (FLAG=0). Given the current calibration uncertainties, events in the 0.2-10 keV range were retained. For each exposure, the appropriate response files, generated with the `rmfgen` and `arfgen` tasks, were used. The background spectra were subtracted from the source's ones, and the spectra were grouped with a minimum of 20 counts per energy bin, in order to apply the χ^2 statistics in the search for the best

fit model. In the case of the very low S/N exposure relative to PG 0935+417 and PG 1700+518, the spectra were grouped with a minimum of 15 counts per energy bin, and the low number of counts was accounted for by using the Churazov weight (Churazov et al. 1996) for the error determination.

4.3 X-ray spectral analysis

For the spectral analysis, I used the Heasoft v.6.4, Xspec v.12.6.0 software. All the models include appropriate absorption by the Galactic interstellar medium as derived from the maps by Kalberla et al. (2005) and listed in Table 4.1. All the errors quoted are at 1σ confidence level ($\Delta\chi^2 = 1$ for one parameter of interest, Avni 1976), unless otherwise stated. In the Tables reporting the spectral analysis results, errors are quoted only when the reduced chi square $\chi^2/\nu < 2$; values of $\chi^2/\nu \lesssim 1.2$ are marked in boldface.

A power law analysis

First, I analyzed the time averaged pn spectrum of each exposure of each source. As a first step, a power law model (**Model 1**) was fitted to the pn spectra in the 0.2-10 keV band. Results are reported in the first column of Table 4.3. The corresponding spectra along with the data/model ratio are reported in the left panels of Fig. 4.7, for each exposure. Visually, most of the sources show complex spectral shapes. This is confirmed by the observed photon indices, that for 23/31 spectra are significantly different from the mean of type 1 AGN, which show $\langle\Gamma\rangle \sim 1.8$ with a dispersion of ~ 0.2 (e.g., Piconcelli et al. 2005). In particular, 18/31 spectra show very flat photon indices $\Gamma < 1.6$, with 15/18 with $\Gamma < 1.2$; only 4/31 spectra show steep $\Gamma > 2$. The power law fit was then repeated in several different rest frame energy intervals, in order to characterize the broad band spectral shape of all the sources detected with a high enough S/N ($\gtrsim 500$ counts in the 0.2-10 keV band, namely all but PG 0935+547 and PG 1700+518). I used the 0.2-2, 2-5, 5-10, and 2-10 keV band in the rest frame of the sources. These bands have been chosen as following:

0.2-2 keV: approximately corresponds to the *ROSAT* bandpass. Several low redshift BAL and mini-BAL QSOs were first observed by *ROSAT* (e.g., PG 1351+640, PG 1126-041), and characterized to have a steep power law intrinsic emission ($\Gamma_{0.2-2} \gtrsim 2.5$). For this reason, BAL and mini-BAL QSOs have been compared to the NLS1,

suggesting a common physical scenario (e.g., a high accretion rate, Brandt & Gallagher 2000). Comparing the slope measured in the 0.2-2 keV band with the slope of a power law measured in the broad band can assess whether BAL and mini-BAL QSOs really do have a steep intrinsic continuum, or if this is a selection effect due to the narrow energetic band of *ROSAT* coupled to a complex spectral shape.

2-5 keV: this is the spectral range where AGN are often considered to show their intrinsic continuum, and hence it is often used as the reference spectral range to determine the slope and the amplitude of the power law emission. This is because the strongest reprocessing features in AGN X-ray spectra, absorption and reflection, mostly manifest themselves at energies lower than 2 keV, and higher than 5 keV, respectively.

5-10 keV: this is the energy range where both highly ionized absorption and reflection mostly affect the spectral shape, with a steepening of the observed Γ_{5-10} the former, with a flattening the latter. A measure of the slope of a power law in this band, compared with the slope of a power law in the 2-5 keV band, can approximately provide hints on the likely relative contribution of iron K absorption and of reflection to the observed spectral shape. In particular, one can expect $\Gamma_{5-10} > \Gamma_{2-5}$ in the case of strong ionized absorption, vice versa in the case of strong reflection.

2-10 keV: several AGN spectra can be very well fitted by a power law in this band, but when extrapolated to the whole energy range they show a prominent excess of counts at lower energies, the so-called soft excess. Fitting the spectra with a power law in this energy range can thus allow to quantify the number of spectra that present a soft excess.

The results obtained by using this simple power law analysis are reported in Table 4.3. The middle and right panels of Fig. 4.7 show the pn spectra modeled with a power law in the 2-5 keV and 2-10 keV range, and then extrapolated to the whole energy band. As it can be seen, the continuum placement is of paramount importance in the analysis of these sources, and in most cases it is not a trivial task. The photon indices obtained considering the 2-10 keV band still remain very flat: only 7/27 spectra show $\Gamma_{2-10} \sim \langle \Gamma \rangle$, while 20/27 spectra show $\Gamma_{2-10} < 1.6$. This flatness is not seen in the fit performed in the rest frame 5-10 keV band alone: it is found $\Gamma_{5-10} > 1.6$ for 23/27 spectra. Visually, negative residuals at $E \gtrsim 6$ keV are visible in the data/model ratio of the fit performed both in

the 2-5 and in the 5-10 keV band of several spectra (Fig. 4.7). Comparing Γ_{5-10} with Γ_{2-5} , 23/27 spectra show $\Gamma_{2-5} < \Gamma_{2-10}$; of these, 17/23 show $\Gamma_{2-5} < 1$, indicating strong complexity in an energy band that in the mean AGN is usually free of strong reprocessing features. Only two sources, PG 2233+134 and PG 2302+029, show $\Gamma_{2-5} > \Gamma_{2-10}$. As for the fit in the 0.2-2 keV soft band, 21/27 spectra show $\Gamma_{0.2-2} > 2$; of these, 15/21 show $\Gamma < 1$ when fitted over the whole 0.2-10 keV band. Of the 6/27 spectra with $\Gamma_{0.2-2} < 2$, four have typical photon indices (PG 1004+130, PG 1114+445, PG 1115+080A, and PG 1416-129), while two are flat (PG 1115+180 B and C), suggesting the possible presence of low ionization or neutral absorption. An excess of counts in the soft band with respect to the power law fit to the 2-10 keV band is visible in 18 out of 27 spectra: PG 1001+054, PG 1126-041 D, PG 1351+640 A and C, PG 1411+442, PG 1416-129, PG 1535+547 A, B, C, and D, PG 2112-059 A, B, C, D, E, and F, PG 2233+134, and PG 2302+029.

Absorption models

I applied to every time-averaged spectrum a number of models $M(E)$ with increasing complexity:

Model 2: a power law emission absorbed by neutral gas, $M(E) = N_{1\text{keV}} E^{-\Gamma} e^{-\tau}$, where Γ is the photon index, $N_{1\text{keV}}$ is the power law normalization, in photons $\text{keV}^{-1} \text{s}^{-1} \text{cm}^{-2}$ at 1 keV, $\tau = N_H \sigma(E)$ is the optical depth, with N_H being the absorbing gas column density and $\sigma(E)$ being the absorption cross section;

Model 3 a partially covered power law emission, $M(E) = N_{1\text{keV}} E^{-\Gamma} (C_f e^{-\tau} + (1 - C_f))$, where $0 < C_f < 1$ is the fraction of the solid angle as seen by the source covered by the absorber, and $1 - C_f$ is the fraction of the intrinsic continuum that escapes unabsorbed;

Model 4 a power law absorbed by ionized gas, where the ionization state of the gas is defined by $\xi \equiv L_{ion}/nR^2$, where L_{ion} is the ionizing continuum luminosity integrated over the 13.6 eV-13.6 keV eberg range, R is the absorber's distance from the continuum source, and n is the gas number density. A constant density n and photoionization equilibrium are assumed, and the standard absorption model `grid 25` generated with `XSTAR` is applied.

Results are reported in Table 4.4. In some cases, the models adopted are not able to provide statistically good fit to the data. On the other hand, the S/N ratio is, in most cases, too low to test more complex models. However, the models adopted are simple enough to give a good parametrization of the spectra in order to characterize them in a broad sense (e.g., the primary power law slope, the amount and the character of intrinsic absorption, the presence of the soft excess).

A simple neutral absorber (Model 2) is detected in only one source, PG 1115+080, with a low column density, $N_H \sim (1 - 3) \times 10^{21} \text{ cm}^{-2}$. The neutral absorber of PG 1115+080 is found to vary in column density over year time scales; there are hints ($\sim 1\sigma$) of possible variability in the column density also over shorter time scales, namely the ~ 6 (rest-frame) days elapsed between the two 2004 observations. Of the 31 spectra, 24 do not require intrinsic neutral absorption, and tight upper limits on the column density can be placed in most cases. The exception, apart from PG 1115+080, is PG 1535+547 for which the addition of this component significantly improves the fit allowing for the presence of $\sim (2 - 10) \times 10^{22} \text{ cm}^{-2}$ of neutral gas during the different epochs of observation. However, the resulting fit statistics is too poor to constrain the absorber parameters, so I do not discuss the simple neutral absorption scenario for this source anymore.

The situation completely changes if one allows for the absorber to be only partially covering the continuum source (Model 3) or to be ionized (Model 4). These models were not applied to the low S/N spectra of PG 0935+547 and PG 1700+518, leaving 27 spectra to be fitted. For 25 out of 27 spectra, the fit statistics significantly improves ($> 99.9\%$, $\Delta\chi^2 > 10$ for one parameter of interest, C_f) with Model 3 with respect to Model 1 or 2. The exceptions are PG 1115+080 C and PG 1004+130, for which the statistical improvement is not significant with respect to a totally covering neutral absorber; however, the neutral partial covering model fits well also these two spectra. The absorbing column densities derived using this model are high, from $N_H \sim 10^{22} \text{ cm}^{-2}$ up to several 10^{23} cm^{-2} . The covering fraction distribution is shown in Fig. 4.1. The vast majority (20/27) of the spectra show $C_f > 0.8$, with a peak at $C_f \sim 0.95$; the other seven spectra show covering fractions scattered around 0.5. Globally, there is no correlation between the derived N_H and C_f values: only 2/7 sources with $C_f < 0.8$ have $N_H > 10^{23} \text{ cm}^{-2}$. The two different distributions of C_f correspond to very different spectral shapes, and could reflect different physical scenarios for the sources: for example, in the high $C_f > 0.95$ scenarios the low

fraction of emerging continuum could correspond to a secondary component emerging only at soft energies, such as a scattered component, or an underlying thermal emission due to collisionally ionized gas. With the moderate CCD spectral resolution and the low S/N ratio of these sources, disentangling between these different scenarios with a single-epoch spectrum is not possible. In the spectra where $0.3 < C_f < 0.6$ (PG 1001+054, PG 1115+080 A, B, and C, PG 1351+640 A, PG 1416-129, and PG 2302+029) the effect of the partial covering absorber is greatest around 2-3 keV and this can not be mimicked by a steep secondary soft component - anyway it could be equivalent, for example, to the effect of a totally covering, ionized absorber and the two would be again difficult to disentangle, given the low S/N ratio of most of the observations, and the moderate spectral resolution of the EPIC-pn. These different effects related to the different values of C_f on the spectra of AGN are illustrated in the right panel of Fig. 4.1. Here I plot the theoretical model for a neutral partial covering absorber with $N_H = 10^{23} \text{ cm}^{-2}$ affecting an AGN at $z = 0.1$ with an intrinsic power law emission with $\Gamma = 2.6$ and $N_{1 \text{ keV}} = 1 \text{ ph keV}^{-1} \text{ cm}^{-2} \text{ s}^{-1}$; what changes between the two plots is only the covering fraction, $C_f = 0.5$ and $C_f = 0.996$. Even if the neutral partial covering absorber provides a good fit ($\chi^2/\nu \lesssim 1.2$) for 13/27 spectra, the derived photon indices are quite large, $\Gamma > 2$ for 6/13 spectra well modeled by model 4 (red points in left panel of Fig. 4.2).

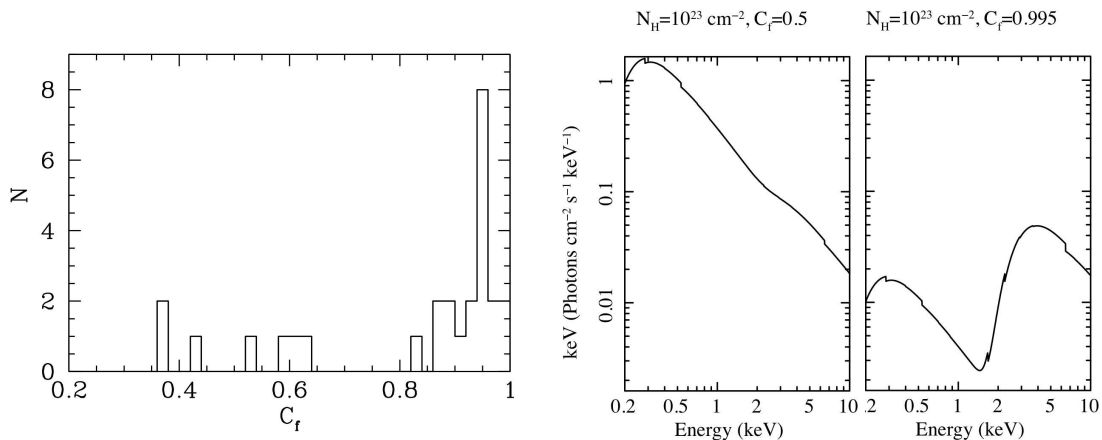


Figure 4.1. Left panel: histogram of covering fraction values obtained from fitting a neutral partial covering absorber model to the PG sources. Right panel: theoretical model for a neutral absorber covering 5% (left) and 99.6% (right) of the same continuum source.

Finally, Model 4 was tested, that is a ionized absorber at the source; the velocity shift of the absorber has been fixed to be null, so the number of model parameters is the same as

for Model 3. Results are reported in Table 4.4, third column. For 18/27 spectra, Model 4 provides a better fit than Model 3; for 5/27 spectra, the two are equivalent, with a $\Delta\chi^2 \leq 2$ for the same number of degrees of freedom. Only for PG 1535+547 A, PG 1416-129, PG 2112+029 B, and PG 2302+029 a neutral partial covering absorber provides a better fit than a totally covering, ionized absorber. The resulting photon indices are flatter than in the partial covering scenario, and closer to the typical values found in type 1 AGN. For most of the sources the absorber is observed to have high column densities N_W , from a few up to several tens of 10^{22} cm^{-2} , and a ionization state corresponding to $\log \xi \sim (1.5 - 3)$ erg cm s^{-1} . However, only a half of the spectra are statistically well reproduced either by the neutral partial covering (13/27) or by the ionized absorber (14/27) models, the QSOs being the same except than for PG 1126-041 B and C, well reproduced only by Model 4, and PG 2302+029, well reproduced only by model 3. Finding a best-fit model for all the sources is beyond the scope of this Thesis, and will be deserved to a future work. In Fig. 4.2 I plot the measured values of the neutral column density versus covering fraction, and ionized column density versus ionization parameter, for the QSOs with acceptable fits to these models. The column densities measured in Model 4 are a factor 3-5 higher than those measured in Model 3. Spectra and residuals to Models 3 and 4 (also Model 2 for PG 1115+080) are reported in Fig. 4.8 for each exposure.

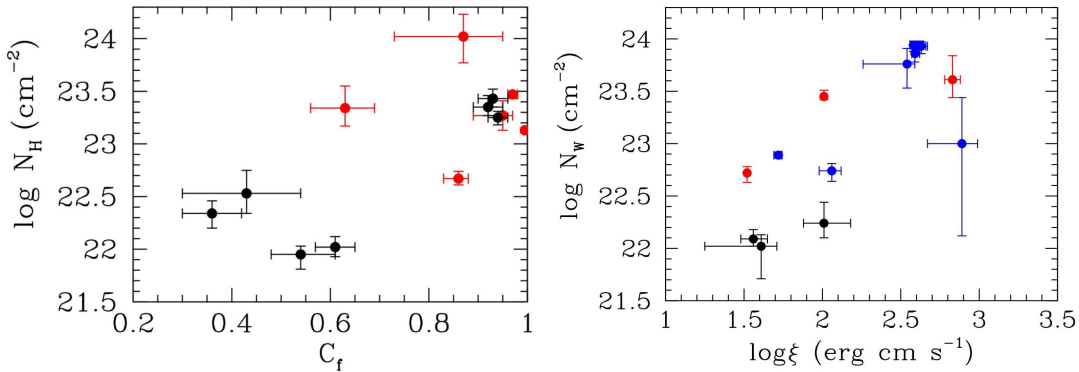


Figure 4.2. Left panel: covering fraction versus neutral column density for the 13 spectra of the PG sources well reproduced by the neutral partial covering absorber model. Right panel: ionization parameter versus warm column density for the 14 spectra well reproduced by the ionized absorber model. Red points mark spectra with a $\Gamma > 2$, black points mark spectra with $\Gamma \sim \langle \Gamma \rangle$, blue points mark spectra with $\Gamma < 1.6$.

High velocity, highly ionized outflows

It is interesting to see whether the X-ray data allow for the presence of X-ray UFOs or X-ray BALs in the BAL, mini-BAL, and NAL QSOs. One case is well known from the literature, and is the complex of Fe XXV/XXVI BALs of PG 1115+080 (Chartas et al. 2003); another case is the Fe XXV/XXVI UFO of PG 1126-041 described in Chapter 5 of this Thesis. Actually, several other sources with a moderate-to-high S/N ratio show strong negative spectral residuals in the iron K band when fitted to a simple power law model: PG 1114+445, PG 1351+640, PG 1411+442, PG 1416-129, PG 1535+547, and PG 2112+059. Also PG 2302+029 is suggested to host a high velocity X-ray outflow by Sabra et al. (2003). The presence of highly ionized outflowing gas is however impossible to assess with high statistical significance given the current S/N ratio, with the exception of the very best cases (again, PG 1115+080 and PG 1126-041), so that until we will have deep pointed observation of other sources, considerations about the dynamical link between the X-ray and the UV high velocity outflows must remain confined to a few sources.

Spectral variability over long and short time scales

All the sources with multiple X-ray exposures show strong spectral variability. Furthermore, a number of them also shows variability over very short time scales (a few ks). Given the low S/N ratio and the strong complexity of most of the spectra, a thorough analysis of the timing properties of all the sources of the sample is quite delicate, and is deserved to future works. However, a few examples of both long and short term variability are shown below, to give a first idea of the complex behavior of the sources.

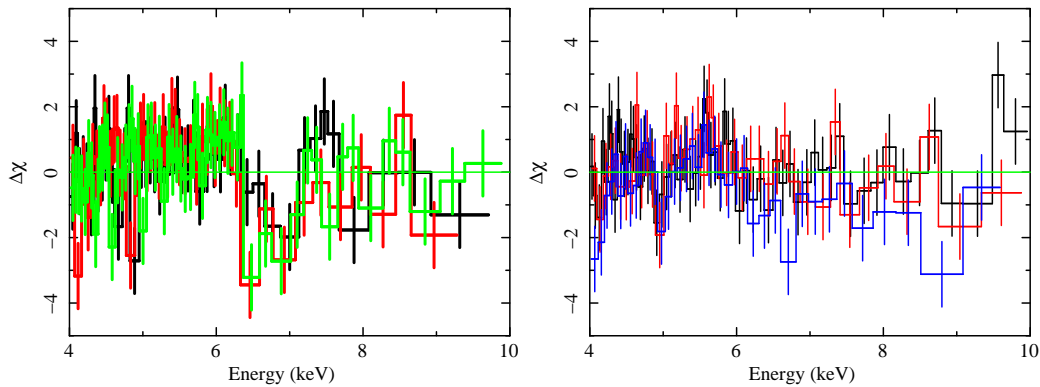


Figure 4.3. Example of variability over ks time scales of X-ray absorption lines in the iron K band of the mini-BAL QSOs PG 1126-041 (on the left) and PG 1114+445 (on the right).

Fig. 4.3 shows an example of variability of absorption structures in the iron K band, occurring on time scales of a few ks. The left panel refers to PG 1126-041 D, the right panel to PG 1114+445. In both cases, the different colors correspond to different time slices taken within the same observation, following the observed flux variability. The highly ionized absorber is clearly much better detected in the high S/N ratio PG 1126-041 D exposure, that is discussed in detail in the next Chapter. Fig. 4.4 shows the three EPIC-pn spectra of the mini-BAL QSO PG 1115+080. As already discussed by Chartas et al. (2003) and Chartas et al. (2007) in their comprehensive analysis, the source shows flux and spectral variability over year time scales. In the left panel of Fig. 4.4 the broad band spectra are shown, with the variable low-energy cutoff due to variable low-ionization absorption. In the right panel of the same figure, a zoom in the rest-frame iron K band is shown, where the X-ray BALs are observed to vary both in energy and in intensity between the different epochs. In Fig. 4.5 broad band spectral variability over different

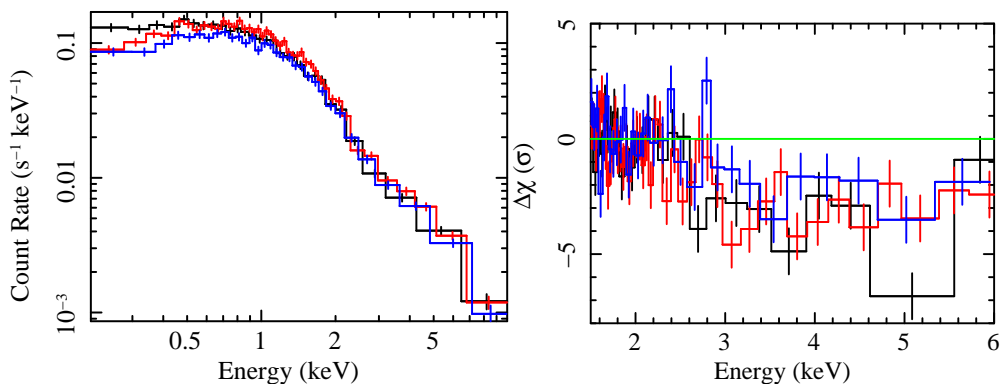


Figure 4.4. Example of variability over long time scales of both the low ionization absorber (on the left) and the X-ray BALs (on the right) of the mini-BAL QSO PG 1115+080

time scales is shown: years for PG 1351+640 (left panel), days for PG 1535+547 (right panel, see also Ballo et al. 2008). Finally, in Fig. 4.6 the complex variability of the BAL QSO PG 2112+059 is illustrated. In the left panel, strong variability in both flux and spectral shape is observed over year time scales; in the right panel, spectral variability is observed within the same exposure (PG 2112+059 E) over time scales of a few ks.

4.4 Results and Conclusions

This was the first attempt to study moderate quality X-ray spectra of a sizeable sample of low redshift BAL, mini-BAL, and NAL QSOs. 15 sources with public pointed XMM-

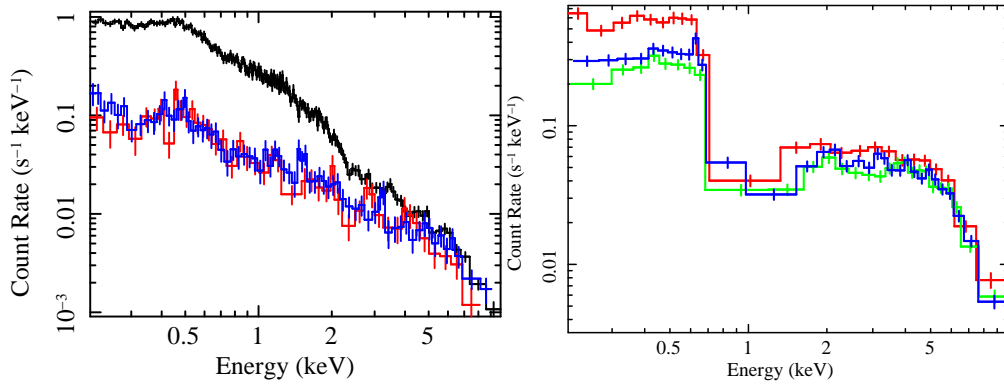


Figure 4.5. Example of broad band spectral variability over year time scales in the mini-BAL QSO PG 1351+640 (left), over day time scales in the mini-BAL QSO PG 1535+547 (right).

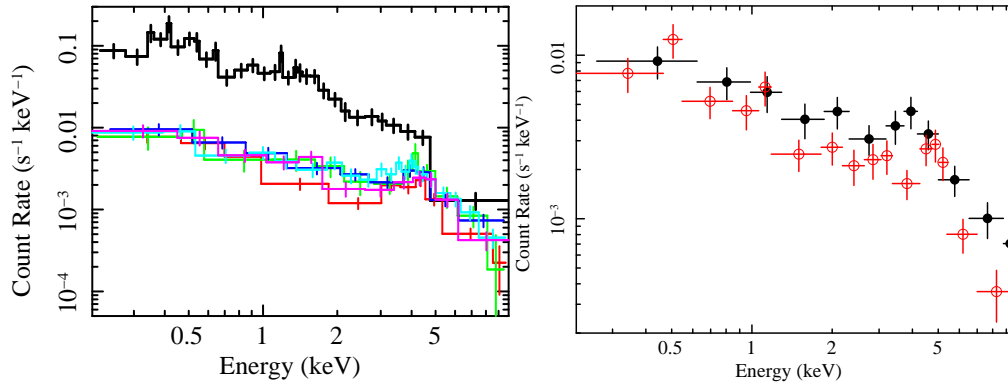


Figure 4.6. Example of spectral variability of the BAL QSO PG 2112+059 over year time scales (left panel) and on ks time scales (right panel).

Newton observations available as of January 2011 were selected from the PG catalog. Several sources were observed multiple times, and the total number of exposures analyzed is 32. Of the 15 sources, all are detected by EPIC-pn except than one, PG 0043+039.

The most notable result of the analysis is the extremely complex spectral shape of the vast majority of the sources, coupled to a strong spectral variability on different time scales: years, days, ks, depending on the sources and on the available data. The 0.2-2 keV photon indices are generally very steep, as already revealed by *ROSAT*. However, this is the result of a complex spectral shape coupled with the limited *ROSAT* bandpass: when the larger bandpass of EPIC-pn is considered, the photon indices flattens considerably for all the sources. Almost none of the spectra require the presence of intrinsic neutral absorption when modeled with a simple absorbed power law. On the other hand, high column densities ($N_W \sim 10^{22-24} \text{ cm}^{-2}$) of X-ray absorbing gas are required by the data

of basically all the spectra, when allowing the absorber to be either partial covering or ionized. However, only about a half of the spectra are statistically well reproduced by either a neutral partial covering or a ionized absorber model alone. The other half of the spectra resulted to be more complex, and the limited S/N ratio makes testing more complex models very difficult. Also for the simple partial covering and ionized absorber models there is a substantial degeneracy and they provide similar fit statistics, making it hard to discriminate among the two (Fig. 4.2). A lot of the sources show however the clear sign of high column densities of ionized gas affecting their X-ray spectra, as deep absorption troughs around 0.5-1.5 keV in their rest-frame, an energy range where the opacity of warm absorber-like gas is maximum (for the most evident examples, see the spectra of PG 1114+445, PG 1126-041, and PG 1535+547). Much more highly ionized gas such as Fe XXV and Fe XXVI could also be affecting the spectra of several sources at high energies, given the residuals often visible at $E \gtrsim 6$ keV. This possibility is also suggested by the steep photon index Γ_{5-10} found for the vast majority of the sources, with $\Gamma_{5-10} > \Gamma_{2-5}$. Indeed, highly ionized iron is surely present in the inner regions of PG 1115+080 (Chartas et al. 2003, 2007) and PG 1126-041 (Chapter 5 of this Thesis), and most probably also of PG 1114+445 (Fig. 4.3). The spectral variability between different exposures is dramatic in several cases, especially at $E \lesssim 6$ keV. As a consequence, also the α_{ox} is observed to be variable for several objects. This makes stronger the case for a transient nature of the Soft X-ray Weakness of some QSOs, as found by Ballo et al. (2008) in their detailed analysis of PG 1535+547. The spectral variability is an important piece of information about the accretion/ejection flow in AGN; the shortest time scale variability, in particular, can unveil the flow in the very inner regions around the SMBH. In the sources where spectral variability was observed on ks time scales (notably PG 1114+445, PG 1126-041, PG 1535+547, and PG 2112+029), future deep X-ray observations could start to map the dynamics of the inner accretion flow.

4.5 Tables and Spectra

Table 4.3. Fit to the PG QSOs with simple power law models

Name	Model 1 ^a : 0.2-10		Model 1 ^b : 0.2-2		Model 1 ^c : 2-5		Model 1 ^d : 5-10		Model 1 ^e : 2-10	
	Γ $N_{1 \text{ keV}}$	χ^2/ν	Γ $N_{1 \text{ keV}}$	χ^2/ν	Γ $N_{1 \text{ keV}}$	χ^2/ν	Γ $N_{1 \text{ keV}}$	χ^2/ν	Γ $N_{1 \text{ keV}}$	χ^2/ν
PG 0935+417	$0.93^{+0.26}_{-0.30}$ $0.10^{+0.61}_{-0.61}$	12/14								
PG 1001+054	3.85 0.14	114/47	3.91 0.11	52/25	0.14 0.03	9/3	3.11 4.30	2/1	0.96 0.10	16/7
PG 1004+130	$1.44^{+0.04}_{-0.02}$ $0.68^{+0.02}_{-0.02}$	85/68	$1.64^{+0.09}_{-0.02}$ $0.68^{+0.02}_{-0.02}$	33/28	$1.40^{+0.14}_{-0.11}$ $0.67^{+0.11}_{-0.16}$	34/22	$2.17^{+0.46}_{-0.29}$ $2.90^{+1.80}_{-1.98}$	8/10	$1.44^{+0.08}_{-0.10}$ $0.70^{+0.09}_{-0.09}$	45/35
PG 1114+445	1.19 2.91	3243/157	1.94 2.67	2441/38	$1.36^{+0.06}_{-0.04}$ $4.14^{+0.17}_{-0.28}$	55/48	$1.72^{+0.22}_{-0.22}$ $7.84^{+2.25}_{-2.74}$	46/54	$1.41^{+0.02}_{-0.02}$ $4.35^{+0.14}_{-0.14}$	110/105
PG 1115+080 A	$1.76^{+0.02}_{-0.02}$ $5.85^{+0.13}_{-0.13}$	289/260	$1.69^{+0.11}_{-0.11}$ $5.46^{+0.26}_{-0.26}$	58/49	$1.70^{+0.05}_{-0.10}$ $5.74^{+0.34}_{-0.62}$	97/101	$2.08^{+0.13}_{-0.19}$ $10.52^{+0.29}_{-0.32}$	52/56	$1.82^{+0.04}_{-0.05}$ $6.55^{+0.33}_{-0.33}$	157/160
PG 1115+080 B	$1.65^{+0.01}_{-0.01}$ $5.32^{+0.09}_{-0.09}$	419/310	$1.13^{+0.10}_{-0.10}$ $3.97^{+0.19}_{-0.19}$	47/49	$1.66^{+0.04}_{-0.04}$ $6.10^{+0.28}_{-0.28}$	96/105	$1.96^{+0.11}_{-0.11}$ $9.24^{+0.21}_{-0.21}$	60/82	$1.79^{+0.03}_{-0.03}$ $7.01^{+0.28}_{-0.28}$	169/190
PG 1115+080 C	$1.62^{+0.01}_{-0.01}$ $4.38^{+0.09}_{-0.09}$	415/309	$1.17^{+0.11}_{-0.16}$ $3.42^{+0.20}_{-0.21}$	61/49	$1.61^{+0.05}_{-0.08}$ $4.68^{+0.29}_{-0.42}$	114/104	$1.87^{+0.19}_{-0.12}$ $6.77^{+0.21}_{-1.37}$	117/81	$1.73^{+0.03}_{-0.03}$ $5.30^{+0.26}_{-0.26}$	249/188
PG 1126-041 A	0.58 0.43	1366/252	2.73 0.38	344/86	$0.29^{+0.11}_{-0.07}$ $0.45^{+0.07}_{-0.07}$	116/101	$2.63^{+0.16}_{-0.27}$ $20.68^{+6.94}_{-7.98}$	56/57	$0.95^{+0.06}_{-0.08}$ $0.90^{+0.08}_{-0.08}$	327/161
PG 1126-041 B	0.74 0.80	287/63	2.83 0.74	69/27	$0.87^{+0.25}_{-0.47}$ $1.33^{+0.53}_{-0.57}$	22/20	$2.84^{+0.57}_{-0.54}$ $37.27^{+21.14}_{-31.43}$	11/10	$1.25^{+0.17}_{-0.18}$ $2.02^{+0.53}_{-0.43}$	48/33
PG 1126-041 C	0.79 1.46	364/72	3.29 1.00	163/34	$1.02^{+0.13}_{-0.25}$ $3.05^{+0.05}_{-0.08}$	26/26	3.86 350.55	3/6	$1.51^{+0.08}_{-0.12}$ $4.92^{+0.58}_{-0.76}$	47/35
PG 1126-041 D	0.72 0.51	2933/466	2.83 0.49	696/144	$0.20^{+0.08}_{-0.13}$ $0.37^{+0.04}_{-0.14}$	175/186	$2.60^{+0.11}_{-0.19}$ $18.90^{+4.18}_{-5.42}$	209/127	0.89 0.77	670/316
PG 1351+640 A	2.42 3.69	829/322	2.57 3.47	389/158	$1.96^{+0.11}_{-0.06}$ $2.61^{+0.25}_{-0.16}$	79/114	$1.85^{+0.25}_{-0.21}$ $2.33^{+1.38}_{-0.78}$	42/42	$1.90^{+0.04}_{-0.06}$ $2.48^{+0.12}_{-0.18}$	123/159
PG 1351+640 B	1.44 0.48	143/45	$2.18^{+0.11}_{-0.11}$ $0.42^{+0.02}_{-0.02}$	54/27	$0.42^{+0.34}_{-0.44}$ $0.21^{+0.14}_{-0.18}$	15/9	2.18 2.65	1/3	$1.28^{+0.13}_{-0.21}$ $0.55^{+0.11}_{-0.14}$	23/15
PG 1351+640 C	1.34 0.55	171/71	$2.13^{+0.11}_{-0.10}$ $0.51^{+0.03}_{-0.03}$	64/43	$1.07^{+0.07}_{-0.21}$ $0.45^{+0.16}_{-0.10}$	10/14	1.58 1.28	5/8	$1.07^{+0.14}_{-0.09}$ $0.46^{+0.06}_{-0.09}$	16/25
PG 1411+442	2.70 0.46	604/74	2.94 0.40	62/30	$-0.09^{+0.19}_{-0.35}$ $0.06^{+0.02}_{-0.02}$	19/16	$2.01^{+0.37}_{-0.25}$ $3.35^{+3.34}_{-1.24}$	35/21	0.20 0.09	99/40
PG 1416-129	1.77 0.96	308/150	$1.91^{+0.02}_{-0.02}$ $9.55^{+0.07}_{-0.06}$	44/39	$1.60^{+0.07}_{-0.04}$ $7.79^{+0.66}_{-0.34}$	54/46	$1.46^{+0.10}_{-0.10}$ $6.28^{+1.97}_{-1.97}$	82/52	$1.56^{+0.03}_{-0.03}$ $7.52^{+0.29}_{-0.28}$	138/101
PG 1535+547 A	0.00 0.17	406/91	$2.64^{+0.01}_{-0.01}$ $0.18^{+0.02}_{-0.02}$	37/27	$-1.27^{+0.10}_{-0.18}$ $0.06^{+0.01}_{-0.01}$	33/32	$2.35^{+0.33}_{-0.32}$ $15.10^{+7.06}_{-7.06}$	32/24	0.37 0.35	188/61
PG 1535+547 B	0.32 0.64	1674/139	3.58 0.58	572/62	$0.18^{+0.09}_{-0.10}$ $0.90^{+0.10}_{-0.10}$	74/47	$2.87^{+0.30}_{-0.33}$ $80.50^{+59.37}_{-36.80}$	19/23	0.94 2.06	184/76
PG 1535+547 C	0.29 0.51	1511/195	2.92 0.46	500/69	$-0.05^{+0.07}_{-0.16}$ $0.53^{+0.05}_{-0.10}$	84/75	$2.47^{+0.18}_{-0.32}$ $31.73^{+12.70}_{-14.34}$	66/43	0.77 1.29	271/124
PG 1535+547 D	0.35 0.58	1955/212	3.09 0.53	659/76	$0.22^{+0.07}_{-0.13}$ $0.79^{+0.07}_{-0.12}$	92/82	$2.60^{+0.22}_{-0.24}$ $41.07^{+21.28}_{-15.07}$	40/46	$0.96^{+0.04}_{-0.04}$ $1.84^{+0.13}_{-0.12}$	251/133
PG 1700+518 A	$2.48^{+0.45}_{-0.40}$ $0.07^{+0.02}_{-0.02}$	4/10								
PG 1700+518 B	$1.93^{+0.05}_{-0.40}$ $0.07^{+0.01}_{-0.01}$	23/19								
PG 1700+518 C	$1.71^{+0.23}_{-0.25}$ $0.05^{+0.01}_{-0.01}$	12/14								
PG 2112+059 A	1.66 1.23	111/53	2.53 1.30	55/27	$1.43^{+0.21}_{-0.45}$ $1.06^{+0.28}_{-0.42}$	9/14	$4.27^{+1.05}_{-0.91}$ $198.33^{+156.66}_{-82.53}$	6/4	$1.66^{+0.14}_{-0.13}$ $1.35^{+0.27}_{-0.22}$	28/21
PG 2112+059 B	0.69 0.05	151/59	$2.65^{+0.31}_{-0.30}$ $0.11^{+0.01}_{-0.01}$	21/23	$-1.10^{+0.87}_{-0.52}$ 0.02 ± 0.01	12/10	$2.56^{+0.35}_{-0.60}$ $2.26^{+2.07}_{-2.31}$	22/14	0.22 0.02	66/27
PG 2112+059 C	$0.53^{+0.12}_{-0.13}$ $0.06^{+0.01}_{-0.01}$	37/23	3.02 ± 0.53 0.10 ± 0.02	5/6	$0.33^{+0.62}_{-0.50}$ 0.05 ± 0.03	3/4	$2.04^{+0.61}_{-1.05}$ $1.65^{+2.55}_{-1.05}$	4/4	$0.34^{+0.17}_{-0.31}$ 0.05 ± 0.02	12/11
PG 2112+059 D	$0.67^{+0.09}_{-0.09}$ $0.07^{+0.01}_{-0.01}$	92/55	2.10 ± 0.33 0.14 ± 0.01	23/18	$0.16^{+0.33}_{-0.62}$ $0.03^{+0.02}_{-0.02}$	11/11	$1.56^{+0.50}_{-0.47}$ $0.54^{+0.88}_{-0.38}$	9/13	$0.25^{+0.11}_{-0.19}$ 0.04 ± 0.01	34/28
PG 2112+059 E	$0.55^{+0.06}_{-0.06}$ $0.07^{+0.01}_{-0.01}$	149/92	2.42 ± 0.29 0.12 ± 0.01	26/30	$-0.55^{+0.42}_{-0.25}$ 0.02 ± 0.01	24/22	$1.90^{+0.40}_{-0.27}$ $1.13^{+1.26}_{-0.46}$	24/25	$0.34^{+0.08}_{-0.12}$ 0.05 ± 0.01	80/50
PG 2112+059 F	$0.75^{+0.01}_{-0.08}$ $0.07^{+0.01}_{-0.01}$	79/43	2.66 ± 0.29 0.12 ± 0.01	9/14	$0.88^{+0.37}_{-0.71}$ 0.02 ± 0.01	11/8	$1.71^{+0.61}_{-0.42}$ $0.63^{+0.48}_{-0.58}$	11/10	$0.42^{+0.11}_{-0.19}$ 0.04 ± 0.01	31/21
PG 2233+134	$2.64^{+0.03}_{-0.03}$ $7.12^{+0.12}_{-0.12}$	79/57	2.71 ± 0.05 7.07 ± 0.13	32/29	$2.28^{+0.31}_{-0.15}$ $4.83^{+1.82}_{-0.74}$	18/17	0.98 0.47	3/4	$2.18^{+0.10}_{-0.15}$ $4.38^{+0.59}_{-0.77}$	26/24
PG 2302+029	$2.42^{+0.05}_{-0.05}$ $6.92^{+0.24}_{-0.24}$	79/46	2.80 ± 0.11 7.47 ± 0.24	15/15	$2.06^{+0.23}_{-0.23}$ $4.39^{+1.27}_{-0.82}$	26/18	1.69 2.21	5/4	$2.06^{+0.09}_{-0.14}$ $4.41^{+0.54}_{-0.72}$	26/24

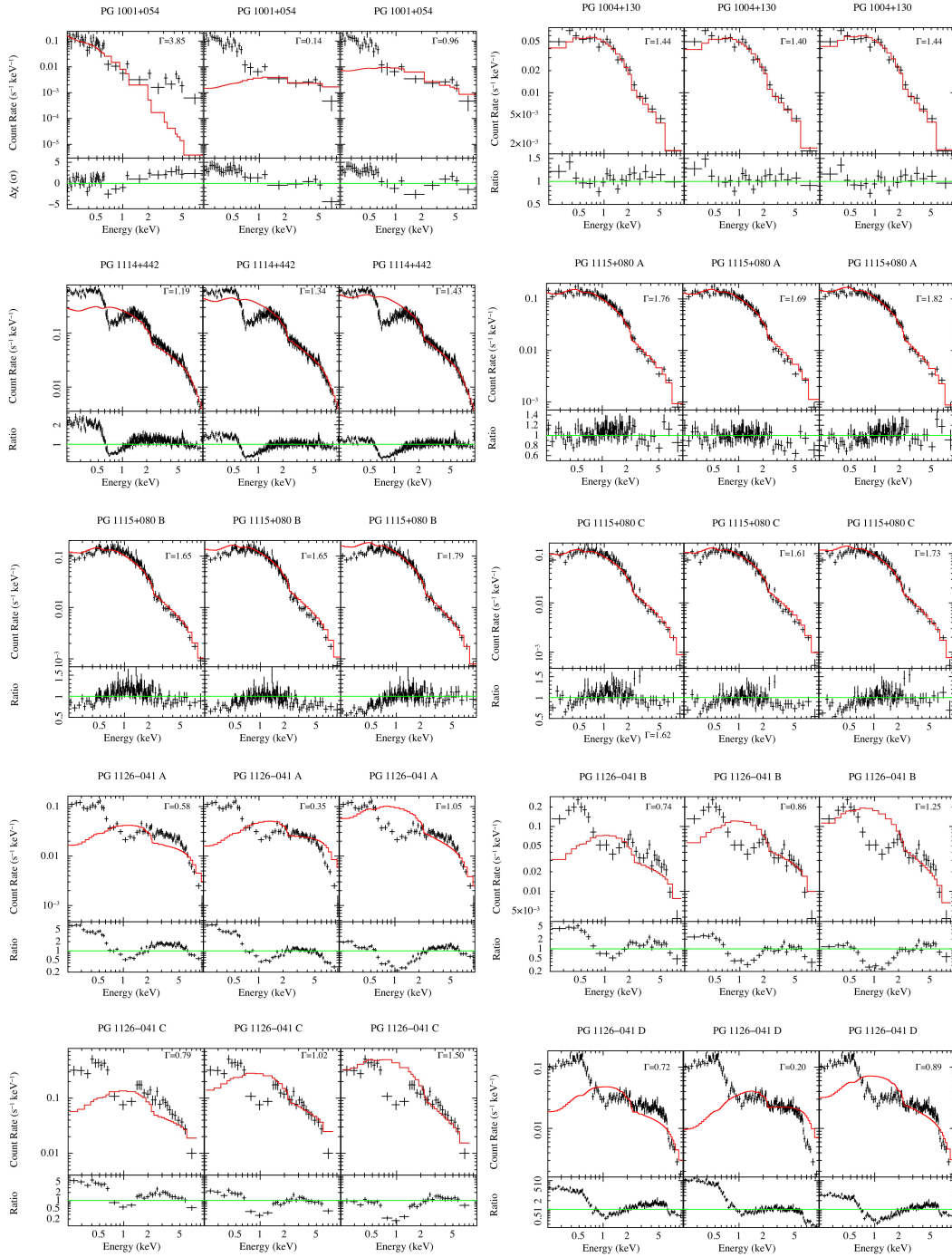


Figure 4.7. 0.2-10 keV pn spectra for each exposure, for each PG QSO with $\gtrsim 500$ net counts collected. Data points have been visually rebinned to 8σ significance. For each source, the left, middle, and right panel report the result of a fit to a power law model in the 0.2-10, 2-5, and 2-10 keV range, respectively. The bottom small panels report the data/model ratio, or the data/model residuals in unit of σ for the sources with the lowest S/N, $\lesssim 800$ net counts.

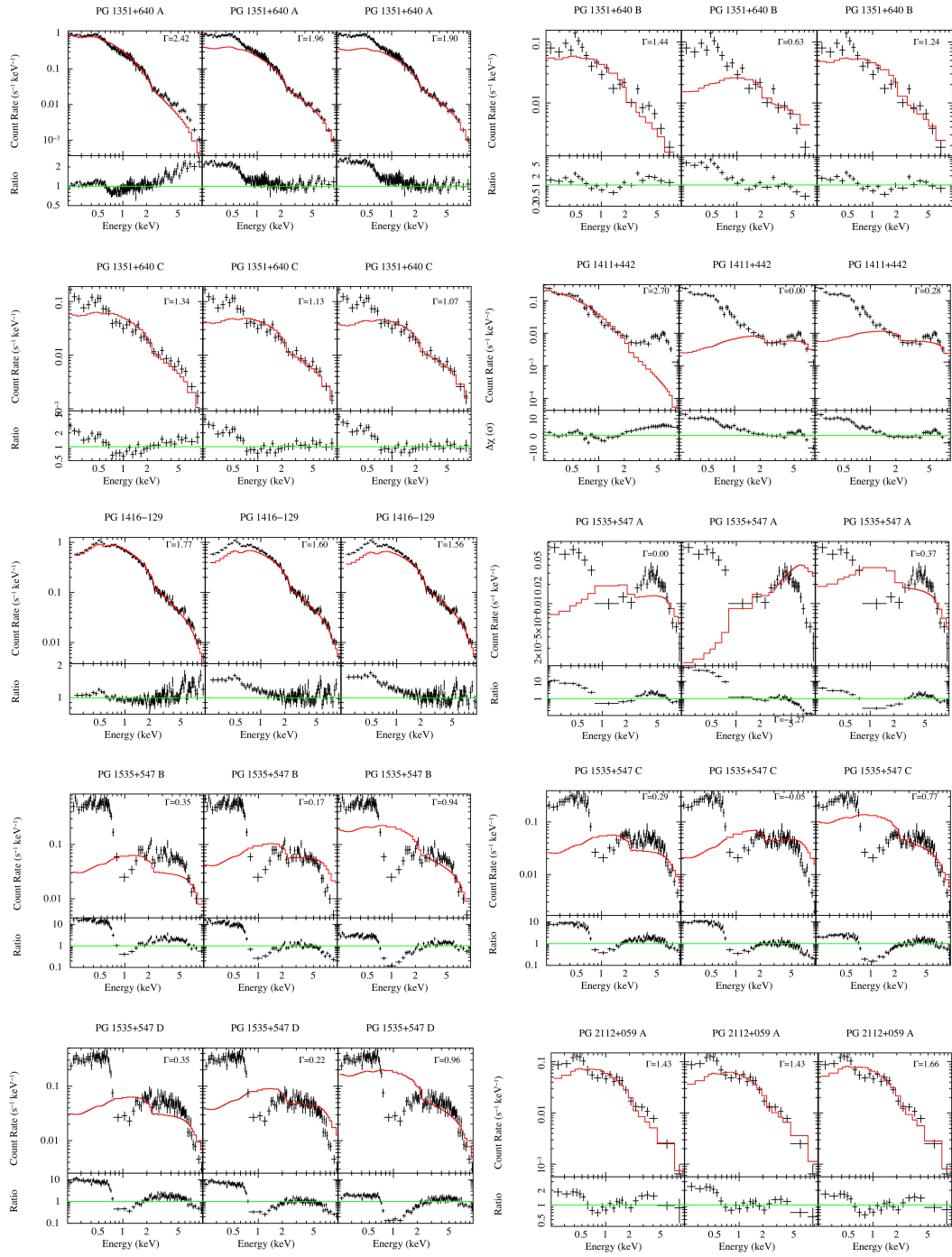


Figure 4.7. – Continued

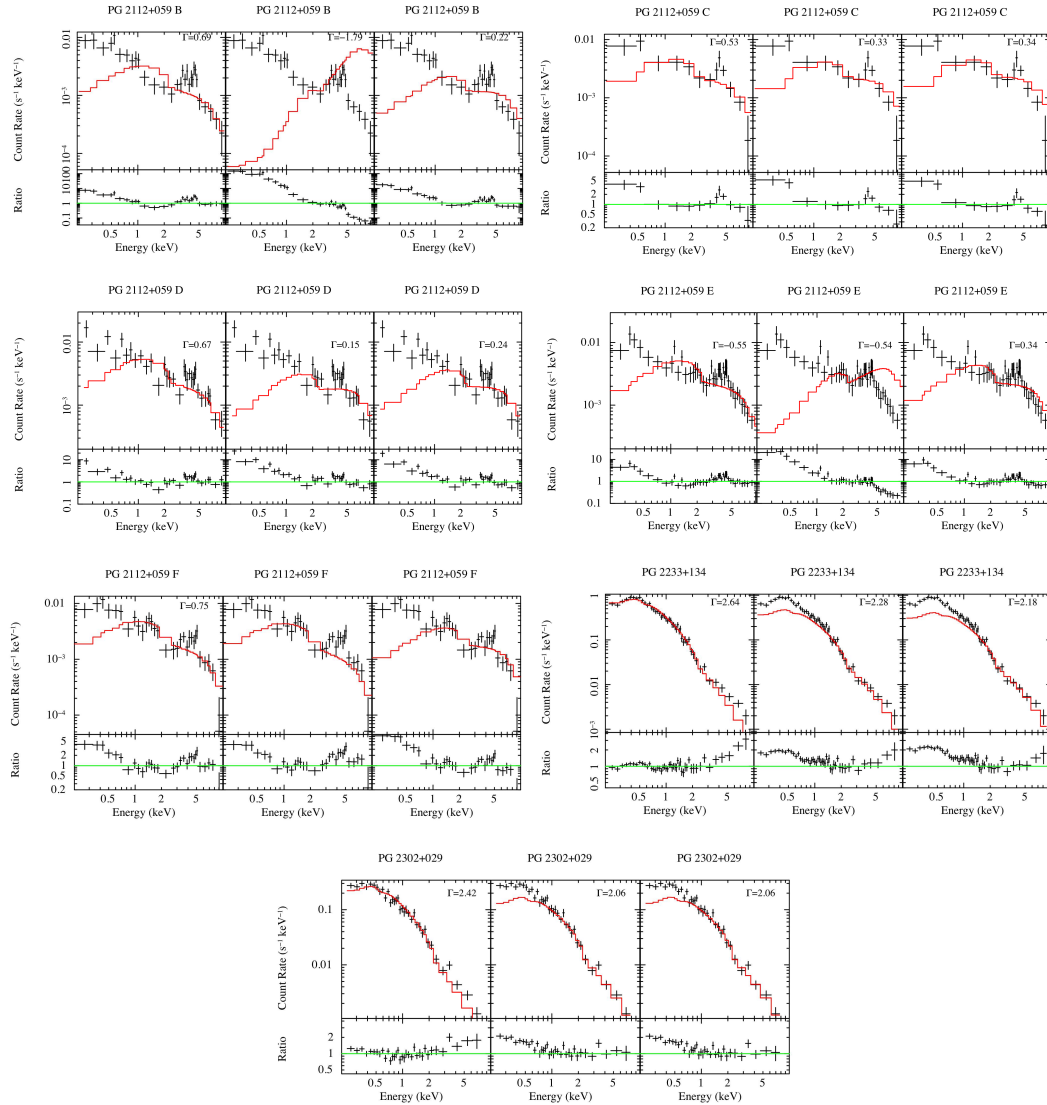


Figure 4.7. – Continued

Table 4.4. Fit to the PG QSOs with absorption models

Name (1)	Model 2				Model 3					Model 4				
	Γ (2)	N_{H} keV (3)	N_{H} (4)	χ^2/ν (5)	Γ (6)	N_{H} keV (7)	N_{H} (8)	C_f (9)	χ^2/ν (10)	Γ (11)	N_{H} keV (12)	N_{W} (13)	$\log \xi$ (14)	χ^2/ν (15)
PG 0935+417	$\equiv 2$	$1.87^{+0.80}_{-0.34}$	$22.28^{+14.20}_{-10.18}$	11/14										
PG 1001+054(15)	4.20	0.14	0.02	114/46	$3.90^{+0.09}_{-0.11}$	$35.27^{+2.31}_{-2.89}$	$19.59^{+3.80}_{-2.51}$	$0.996^{+0.002}_{-0.004}$	70/45	$1.71^{+0.08}_{-0.07}$	$1.21^{+0.11}_{-0.11}$	$86.08^{+8.79}_{-8.71}$	$1.71^{+0.08}_{-0.07}$	61/45
PG 1004+130	$1.44^{+0.04}_{-0.03}$	0.68 ± 0.02	< 0.003	85/67	$1.69^{+0.11}_{-0.11}$	1.15 ± 0.23	$3.42^{+0.16}_{-0.22}$	$0.43^{+0.11}_{-0.13}$	79/66	$1.44^{+0.02}_{-0.04}$	0.78 ± 0.04	$9.93^{+17.61}_{-8.61}$	$2.89^{+0.10}_{-0.22}$	77/66
PG 1114+445	1.19	2.91	0	3243/156	2.39	21.06	2.24	0.90	1513/155	1.94	11.16	2.11	1.40	348/155
PG 1115+080 A	1.83 ± 0.03	6.61 ± 0.30	0.10 ± 0.03	280/259	$1.96^{+0.05}_{-0.05}$	$8.74^{+0.96}_{-0.83}$	$2.20^{+0.67}_{-0.62}$	$0.36^{+0.06}_{-0.06}$	265/258	$1.94^{+0.06}_{-0.04}$	$8.52^{+1.02}_{-0.82}$	$1.74^{+1.04}_{-0.49}$	$2.01^{+0.17}_{-0.13}$	266/258
PG 1115+080 B	1.85 ± 0.02	7.81 ± 0.29	0.34 ± 0.03	283/309	$1.92^{+0.04}_{-0.03}$	$9.04^{+0.68}_{-0.48}$	$1.05^{+0.57}_{-0.20}$	$0.61^{+0.04}_{-0.04}$	269/308	$1.93^{+0.04}_{-0.03}$	$9.27^{+0.81}_{-0.55}$	$1.22^{+0.50}_{-0.17}$	$1.56^{+0.09}_{-0.08}$	269/308
PG 1115+080 C	1.78 ± 0.03	5.89 ± 0.27	0.26 ± 0.04	355/308	$1.83^{+0.04}_{-0.03}$	$6.55^{+0.56}_{-0.40}$	$0.90^{+0.36}_{-0.26}$	$0.54^{+0.07}_{-0.06}$	349/307	$1.84^{+0.04}_{-0.04}$	$6.69^{+0.29}_{-0.54}$	$1.05^{+0.29}_{-0.36}$	$1.61^{+0.10}_{-0.10}$	348/307
PG 1126-041 A	0.58	0.45	0	1366/251	$2.66^{+0.02}_{-0.02}$	$21.03^{+0.48}_{-0.47}$	$6.36^{+0.18}_{-0.17}$	$0.98^{+0.01}_{-0.01}$	428/250	$1.93^{+0.05}_{-0.05}$	$6.64^{+0.62}_{-0.60}$	$8.17^{+0.18}_{-0.20}$	$1.63^{+0.03}_{-0.02}$	357/250
PG 1126-041 B	0.72	0.77	0	287/62	$2.77^{+0.04}_{-0.04}$	$29.65^{+1.35}_{-1.33}$	$5.46^{+0.38}_{-0.35}$	$0.98^{+0.01}_{-0.01}$	93/61	$1.93^{+0.12}_{-0.19}$	$8.55^{+2.02}_{-2.48}$	$7.80^{+0.57}_{-0.56}$	$1.72^{+0.23}_{-0.09}$	61/61
PG 1126-041 C	0.79	1.46	0	364/71	2.45	26.46	3.25	0.95	159/70	$2.19^{+0.10}_{-0.09}$	$20.18^{+4.77}_{-3.83}$	$5.20^{+0.88}_{-0.92}$	$1.52^{+0.01}_{-0.01}$	65/70
PG 1126-041 D	0.72	0.51	0	2933/465	2.35	11.35	6.14	0.95	1169/464	$1.84^{+0.04}_{-0.03}$	$5.02^{+0.37}_{-0.55}$	$8.20^{+0.11}_{-0.18}$	$1.81^{+0.04}_{-0.03}$	688/464
PG 1351+640 A	2.42	3.69	0	829/321	$2.61^{+0.02}_{-0.02}$	$8.32^{+0.40}_{-0.36}$	$4.43^{+0.75}_{-0.58}$	$0.59^{+0.02}_{-0.02}$	517/320	$2.34^{+0.01}_{-0.01}$	$4.71^{+0.06}_{-0.06}$	$1.69^{+0.18}_{-0.21}$	$2.08^{+0.08}_{-0.08}$	397/320
PG 1351+640 B	1.44	0.48	0	143/44	$2.28^{+0.10}_{-0.11}$	$3.70^{+0.84}_{-0.69}$	$5.23^{+0.83}_{-0.70}$	$0.89^{+0.02}_{-0.03}$	67/43	$1.63^{+0.06}_{-0.06}$	$1.26^{+0.14}_{-0.14}$	$7.75^{+1.73}_{-1.55}$	$2.15^{+0.07}_{-0.07}$	64/43
PG 1351+640 C	1.34	0.55	0	171/70	$2.19^{+0.10}_{-0.10}$	$3.35^{+0.60}_{-0.52}$	$4.68^{+0.77}_{-0.61}$	$0.86^{+0.02}_{-0.03}$	78/69	$1.62^{+0.05}_{-0.05}$	$1.30^{+0.14}_{-0.14}$	$5.48^{+1.03}_{-1.13}$	$2.06^{+0.06}_{-0.08}$	52/69
PG 1411+442	2.70	0.46	0	604/73	2.61	9.84	17.48	0.95	206/72	2.06	4.01	25.82	2.09	190/72
PG 1416-129	1.77	0.96	0	308/149	$1.89^{+0.02}_{-0.02}$	$14.89^{+0.66}_{-0.34}$	$10.22^{+3.19}_{-2.07}$	$0.36^{+0.03}_{-0.03}$	202/148	$1.73^{+0.01}_{-0.01}$	$10.96^{+0.15}_{-0.15}$	$14.01^{+3.31}_{-2.81}$	$2.92^{+0.02}_{-0.02}$	208/148
PG 1535+547 A	2.14	12.91	10.14	310/90	$2.61^{+0.03}_{-0.03}$	$33.71^{+1.79}_{-1.81}$	$13.54^{+0.75}_{-0.70}$	$0.995^{+0.001}_{-0.003}$	97/89	$1.79^{+0.39}_{-0.14}$	$9.30^{+19.50}_{-2.14}$	$28.12^{+4.00}_{-1.89}$	$2.01^{+0.01}_{-0.01}$	103/89
PG 1535+547 B	1.39	5.11	2.26	1551/138	2.12	17.19	5.00	0.95	1050/136	$1.84^{+0.03}_{-0.03}$	$14.75^{+1.51}_{-1.51}$	$13.35^{+1.45}_{-1.45}$	$2.01^{+0.03}_{-0.03}$	250/136
PG 1535+547 C	1.49	5.07	2.97	1455/194	2.00	12.58	9.60	0.95	814/193	$1.53^{+0.03}_{-0.02}$	$6.70^{+1.27}_{-0.50}$	$11.32^{+1.23}_{-0.94}$	$2.02^{+0.01}_{-0.01}$	334/193
PG 1535+547 D	1.58	6.38	3.04	1865/211	2.08	14.66	9.17	0.95	1027/210	$1.61^{+0.03}_{-0.02}$	$7.61^{+0.45}_{-0.27}$	$10.21^{+1.19}_{-0.28}$	$2.02^{+0.01}_{-0.01}$	363/210
PG 1700+518 A	$\equiv 2$	0.07 ± 0.02	< 0.05	4/10										
PG 1700+518 B	$\equiv 2$	0.09 ± 0.02	< 0.07	22/19										
PG 1700+518 C	$\equiv 2$	0.08 ± 0.01	$0.09^{+0.07}_{-0.05}$	11/14										
PG 2112+059 A	1.66	1.23	0	111/52	2.58 ± 0.06	$7.50^{+0.72}_{-0.68}$	4.45 ± 0.32	0.84 ± 0.01	77/51	$2.14^{+0.08}_{-0.08}$	$3.82^{+0.58}_{-0.56}$	$6.39^{+0.67}_{-1.25}$	$2.07^{+0.07}_{-0.07}$	63/51
PG 2112+059 B	0.69	0.05	0	151/58	2.56 ± 0.04	4.44 ± 0.25	$29.34^{+2.34}_{-2.19}$	0.97 ± 0.01	54/57	$1.32^{+0.05}_{-0.06}$	$0.47^{+0.07}_{-0.07}$	$87.60^{+7.38}_{-11.74}$	$2.58^{+0.02}_{-0.02}$	66/57
PG 2112+059 C	$0.49^{+0.17}_{-0.09}$	$0.06^{+0.02}_{-0.01}$	< 0.04	37/22	$2.08^{+0.13}_{-0.37}$	2.10 ± 0.45	$18.74^{+7.05}_{-5.36}$	$0.95^{+0.02}_{-0.06}$	21/21	$1.13^{+0.11}_{-0.13}$	$0.44^{+0.12}_{-0.15}$	$57.47^{+23.87}_{-23.54}$	$2.54^{+0.05}_{-0.28}$	17/21
PG 2112+059 D	$0.66^{+0.10}_{-0.08}$	0.07 ± 0.01	< 0.01	92/54	$1.93^{+0.08}_{-0.14}$	$1.67^{+1.08}_{-0.51}$	$22.33^{+6.36}_{-3.90}$	$0.92^{+0.03}_{-0.03}$	51/53	$1.16^{+0.07}_{-0.08}$	$0.49^{+0.11}_{-0.09}$	$85.61^{+9.81}_{-13.37}$	$2.63^{+0.04}_{-0.03}$	54/53
PG 2112+059 E	0.55 ± 0.06	0.06 ± 0.01	< 0.01	149/91	$1.99^{+0.15}_{-0.15}$	$1.87^{+0.69}_{-0.57}$	$17.62^{+2.79}_{-2.42}$	$0.94^{+0.02}_{-0.02}$	88/90	$1.11^{+0.06}_{-0.06}$	$0.47^{+0.62}_{-0.60}$	$72.31^{+10.47}_{-11.51}$	$2.59^{+0.03}_{-0.02}$	83/90
PG 2112+059 F	0.74 ± 0.09	0.07 ± 0.01	< 0.01	79/42	$1.98^{+0.21}_{-0.17}$	$1.67^{+1.04}_{-0.54}$	$27.11^{+6.28}_{-4.70}$	$0.93^{+0.03}_{-0.03}$	42/41	$1.23^{+0.07}_{-0.08}$	$0.47^{+0.09}_{-0.08}$	$85.82^{+8.58}_{-12.49}$	$2.62^{+0.04}_{-0.03}$	43/41
PG 2233+134	2.64 ± 0.03	7.12 ± 0.12	< 0.002	79/56	2.69 ± 0.03	$54.37^{+19.16}_{-28.40}$	$105.63^{+65.54}_{-47.16}$	$0.87^{+0.05}_{-0.14}$	59/55	2.48 ± 0.04	$8.49^{+0.39}_{-0.35}$	$40.43^{+28.39}_{-12.95}$	$2.98^{+0.16}_{-0.05}$	56/55
PG 2302+029	2.42 ± 0.05	6.92 ± 0.24	< 0.003	79/45	$2.67^{+0.08}_{-0.07}$	$20.24^{+4.45}_{-3.63}$	$21.92^{+13.64}_{-7.09}$	$0.63^{+0.05}_{-0.07}$	51/44	2.43 ± 0.04	$10.59^{+1.24}_{-0.77}$	$32.33^{+11.90}_{-11.30}$	2.83 ± 0.05	57/44

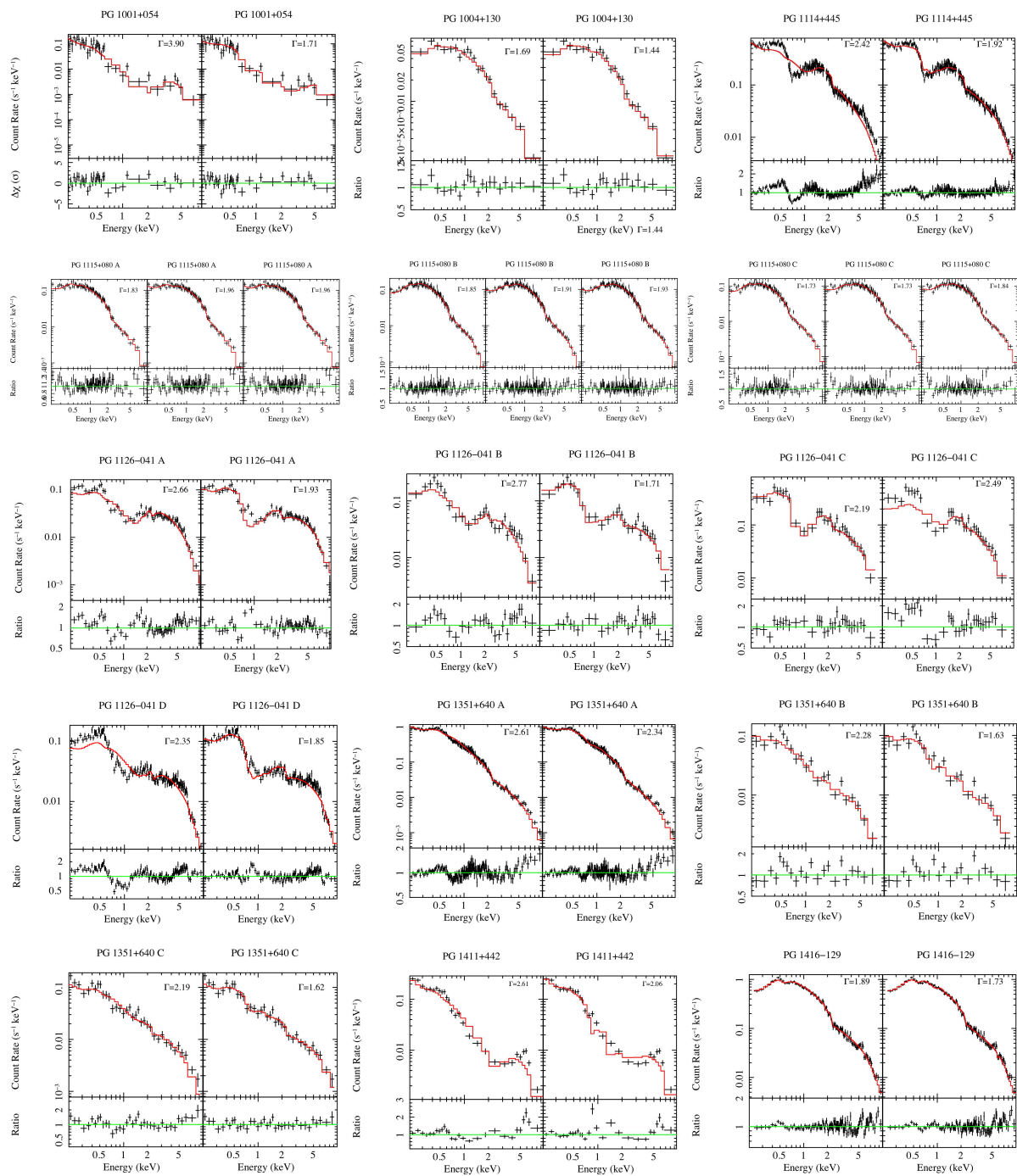


Figure 4.8. 0.2-10 keV pn spectra for each exposure, for each PG QSO with $\gtrsim 500$ net counts collected. Data points have been visually rebinned to 8σ significance. For each source, the left and right panel report the result of the fit to Model 3 and 4, respectively. For PG 1115+080 also the fit to Model 2 is reported, in the leftmost panel, for each epoch. The bottom small panels report the data/model ratio, or the data/model residuals in unit of σ for the sources with the lowest S/N, $\lesssim 800$ net counts.. The photon index value corresponding to each model is reported in the top right corner of each panel.

Chapter 5

The new observational campaign on the mini-BAL QSO PG 1126-041

In this chapter I will present the results of the new *XMM-Newton* observational campaign on the mini-BAL QSO PG 1126-041, that provides both the largest dataset (four pointings) and the deepest X-ray exposure (130 ks) on a mini-BAL QSO to date. The source is extremely interesting in showing three of the absorbers discussed above: mini-BALs in the UV, an X-ray warm absorber, and a highly ionized, high velocity X-ray outflow. Constraining the X-ray/UV properties of this source can give precious insights into the physics of AGN winds.

5.1 The source

PG 1126-041 (a.k.a. Mrk 1298) is a nearby ($z = 0.06$) radio quiet AGN with a luminosity in between those typical of Seyferts and QSOs ($M_B = -22.8$, $L_{\text{bol}} \sim 10^{12} L_{\odot}$, Schmidt & Green 1983; Sanders et al. 1989; Surace et al. 2001). Its optical strong Fe II and weak [O III] line emission (Boroson & Green 1992) are characteristics of Narrow Line Seyfert 1 galaxies (NLS1), although the FWHM of its $H\beta$ line of 2150 km s^{-1} is slightly larger than the 2000 km s^{-1} value used in defining NLS1s (Shuder & Osterbrock 1981). Its black hole mass is estimated to be $\log(M_{\text{BH}}/M_{\odot}) \sim 7.7$ using the $L_{\lambda}(5100\text{\AA})$ continuum luminosity density and the FWHM($H\beta$) measured from a single-epoch optical spectrum, and the empirical relations reported by Vestergaard & Peterson (2006). However, the stellar velocity dispersion in the host galaxy of PG 1126-041 measured from the stellar

Table 5.1. Main properties of PG 1126-041

RA	11 29 16.6	(a)
DEC	-04 24 08	(a)
z	0.062	(a)
D_L	284 Mpc	
N_H^{gal}	$4.35 \times 10^{20} \text{ cm}^{-2}$	(b)
$E(B - V)$	0.055 mag	(c)
M_{BH}	$5.0 - 82 \times 10^7 M_\odot$	(d-e)
m_B	14.92 mag	(a)
L_{bol}	$8.9 \times 10^{41} L_\odot$	(f)
L_{2-10}	$2 \times 10^{43} \text{ erg s}^{-1}$	(h)
v_{out}^{uv}	5, 000 km s^{-1}	(f)
v_{out}^X	15, 000 km s^{-1}	(h)

References: (a) Schmidt & Green (1983); (b) Kalberla et al. (2005); (c) Schlegel et al. (1998); (d) Vestergaard & Peterson (2006); (e) Dasyra et al. (2007); (f) Surace et al. (2001); (g) Wang et al. (1999); (h) This work.

CO absorption line width in the VLT H-band spectra gives a slightly higher black hole mass of $\log(M_{BH}/M_\odot) \sim 8.1$ (Dasyra et al. 2007). PG 1126-041 is also classified as “soft X-ray weak”¹ by Brandt et al. (2000), who measured an $\alpha_{ox} \sim -2.19$ based on *ROSAT* X-ray observations and on the optical flux density as given by Neugebauer et al. (1987). Tananbaum et al. (1986) measured an $\alpha_{ox} = -1.90$ referring to an earlier *Einstein* X-ray observations and the 2500 Å rest-frame flux density as given by Schmidt & Green (1983). Neither of these α_{ox} measurements were based on simultaneous X-ray and optical/UV observations. Wang et al. (1999) report on the *IUE* and *ROSAT* observations of PG 1126-041. The 1992 *IUE* observation shows a high velocity UV absorbing outflow as mini-BALs in the C IV, N V, and Si IV ions blueshifted up to $\sim 5000 \text{ km s}^{-1}$. The simultaneous *ROSAT* pointing revealed a 0.2-2 keV spectrum best fitted by a steep powerlaw emission with $\Gamma \sim 2.8$, absorbed by a column density $N_W \sim 3 \times 10^{22} \text{ cm}^{-2}$ of ionized gas, $\log \xi \sim 1.7 \text{ erg cm s}^{-1}$. A subsequent *IUE* spectrum taken in 1995 showed a continuum brighter by a factor of two and weaker absorption lines. Komossa & Meerschweinchen (2000) confirmed the detection of ionized absorption in the 1992 *ROSAT* spectrum and also suggested X-ray flux variability on timescales as short as 800 s.

The main properties of PG 1126-041 are summarized in Table 5.1.

¹Soft X-ray weak sources are those being characterized by an observed optical-to-X-ray spectral index $\alpha_{ox} < -2$, see Sec. 2.4 and 5.6.

5.2 Observations and data reduction

XMM-Newton observed PG 1126-041 four times, once in 2004 December, twice in 2008 June and December, and once more in 2009 June. Table 5.2 lists the main parameters of each dataset. All the datasets were reduced using the *XMM-Newton* SAS v.10.0.0 and calibration files generated in August 2010. Light curves of events with energies greater than 10 keV were extracted from the whole field of view of each EPIC instrument (i.e., pn, MOS1, and MOS2) and for each dataset. The time periods in which there was significant background flaring were then filtered out. Source counts from the cleaned event files were extracted from circular regions centered on the PG 1126-041 optical position, with $\sim 30\text{--}45''$ radii, depending on the signal-to-noise ratio (S/N) as determined with the `eregionanalyse` task. Background counts were extracted from circular regions of the same area as the source ones. Up to double events (flagged as `#XMMEA_EP`) for the pn dataset, and up to quadruple events (flagged as `#XMMEA_EM`) for the MOS datasets were retained. For each dataset, the ancillary response file and the redistribution matrix file at the source position were generated using the tasks `arfgen` and `rmfgen`. Source light curves were created in different energy bands and corrected with the `epiclccorr` task for both the local background and the mirrors/detector inefficiencies. Due to the low X-ray fluxes involved, pile-up effects are negligible. For the same reason the reflection grating spectrometer (RGS) aboard *XMM-Newton* can not be used, giving only a $\sim 2\sigma$ detection during the 2009 June observation. Optical Monitor (OM) data were all taken in Image mode and were processed using the standard procedure as suggested by the *XMM-Newton* SOC.

5.3 X-ray timing analysis

The left panel of Fig. 5.1 shows the background-subtracted 0.2-10 keV pn light curves of PG 1126-041, for each epoch of observation, binned to 2 ks. Compared to the light travel time $t_L = r_g/c$, the time bin corresponds to $\sim 3\text{--}8r_g$ for the two different estimates for the black hole mass of PG 1126-041. The variations on month timescales are large: the source flux increases by a factor of ~ 3 from December 2004, to June 2008, to December 2008, then comes back to a low count-rate regime in June 2009. For comparison, the average 0.2-10 keV pn spectra of each epoch of observation are shown in the right panel of Fig. 5.1.

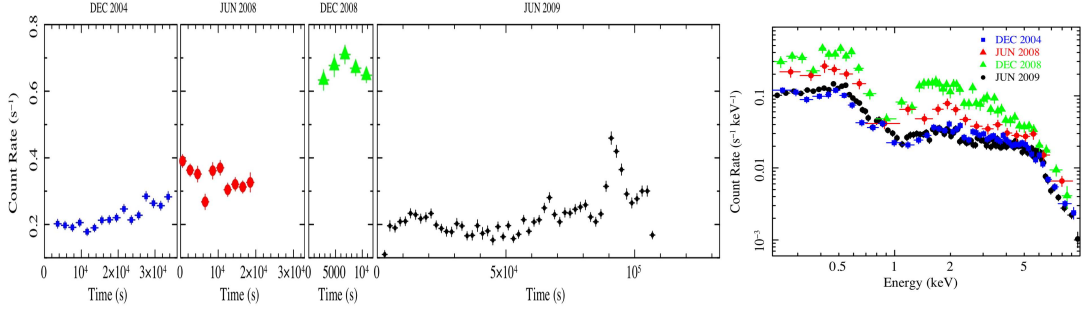


Figure 5.1. Variability over month time scales. Left panel: background subtracted 0.2-10 keV pn light curves extracted in the four different epochs of observations of PG 1126-041 and binned to 2 ks: December 2004 (blue circles), June 2008 (red squares), December 2008 (green triangles), and 2009 Long Look (black circles). Right panel: the time-averaged pn spectra corresponding to the time intervals shown on the left and using the same color codes.

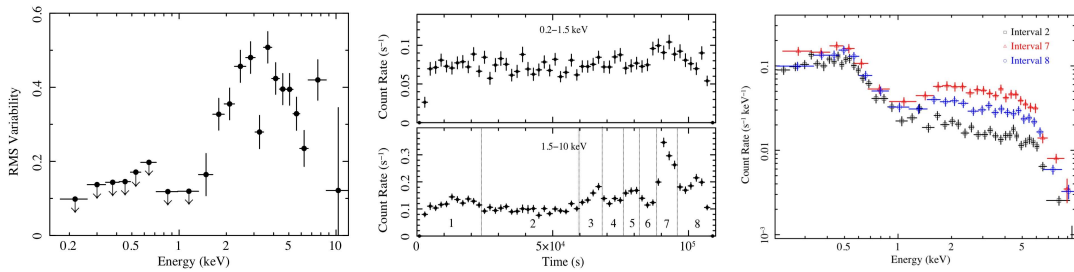


Figure 5.2. Variability over kilosecond time scales detected during the 2009 Long Look observation. Left panel: RMS variability computed for the pn observation over the 0.2-10 keV band; arrows mark upper limits, error bars are at 1σ confidence level. Middle panel: 0.2-1.5 and 1.5-10 keV background subtracted pn light curves binned to 2 ks; the numbers in the 1.5-10 keV light curve mark the eight time intervals on which time resolved spectral analysis was performed. Right Panel: three representative spectra extracted during the 2nd, the 7th, and the 8th time intervals of the 2009 Long Look observation.

Most of the spectral variability on month time scales occurs at energies $E \lesssim 6$ keV. The spectral shape is peculiar and obviously deviates from a simple power law. A prominent broad absorption feature is evident in all the spectra around $E \sim 0.6-1.5$ keV.

The high S/N ratio and the long contiguous good exposure time allowed to perform a more detailed timing analysis on the 2009 Long Look pn exposure. Figure 5.2 summarizes the results. The left panel shows the Root Mean Square variability (RMS; Vaughan et al. 2003; Ponti et al. 2004) computed in the 0.2-10 keV band: on very short time scales (ks) the source flux is varying up to 50% at energies $E \gtrsim 1.5$ keV, while it is constant at lower energies. The middle panel shows the background subtracted light curves extracted in the 0.2-1.5 and 1.5-10 keV band. The eight time intervals on which temporally resolved

spectral analysis was performed are marked. Three representative spectra extracted during the 2nd, the 7th, and the 8th time interval are shown in the right panel of Figure 5.2: most of the spectral variability on ks time scales occurs at $1.5 \text{ keV} \lesssim E \lesssim 9 \text{ keV}$.

From the timing analysis, it follows that the X-ray spectra of PG 1126-041 can be divided in two spectral components: one dominates at $E \gtrsim 1.5 \text{ keV}$ and contributes 100% to the ks time scale variability, while the other one dominates at lower energies and is significantly variable only over longer (month) time scales. With these considerations in mind, I will proceed with the analysis of both the average (Sec. 5.4) and the time resolved (Sec. 5.5) spectra.

5.4 X-ray spectral analysis: the average spectra

Since the 2009 Long Look spectrum has the highest S/N, it will be used as the starting point to find the best-fitting model. Data from the other three epochs (Dec. 2004, Jun. 2008, and Dec. 2008) will then simultaneously be fitted with the model that provides the best fit to the 2009 Long Look spectrum, to investigate the causes of the observed variability on month time scales. The `Xspec v.12.6.0` software was used for the spectral analysis. All the spectra were grouped to a minimum number of 20 counts per energy bin in order to apply the χ^2 statistics in the search for the best fit model (Avni 1976). Errors are quoted at 1σ confidence, unless otherwise stated. All the models include Galactic absorption by a column density $N_{\text{H}}^{\text{Gal}} = 4.35 \times 10^{20} \text{ cm}^{-2}$ (Kalberla et al. 2005). The spectral analysis will be focused on the 0.2-10 keV band of the pn data, and on the 0.3-8 keV band of the MOS data.

A fit with a power law continuum emission model is very poor, with a reduced chi square $\chi^2/\nu \sim 10$ and a very flat photon index $\Gamma \sim 0.6$; Fig. 5.3 shows the 2009 Long Look pn and MOS spectra along with the data/model ratio. The pn 0.2-10 keV residuals to this model, scaled by the error bar, are reported for the 2009 Long Look and for the other three epochs in the upper left and upper right panels (labelled I) of Fig. 5.4, respectively. Three main deviations from the simple power law model are consistently observed in spectra from all the three instruments and in all the four epochs of observation: (a) both negative and positive residuals in the soft band ($E \lesssim 1.5 \text{ keV}$), (b) a deficit of counts at the highest energies probed by the EPIC camera ($E \sim 7 - 10 \text{ keV}$), and (c) a low energy cutoff at $E \sim 2 \text{ keV}$.

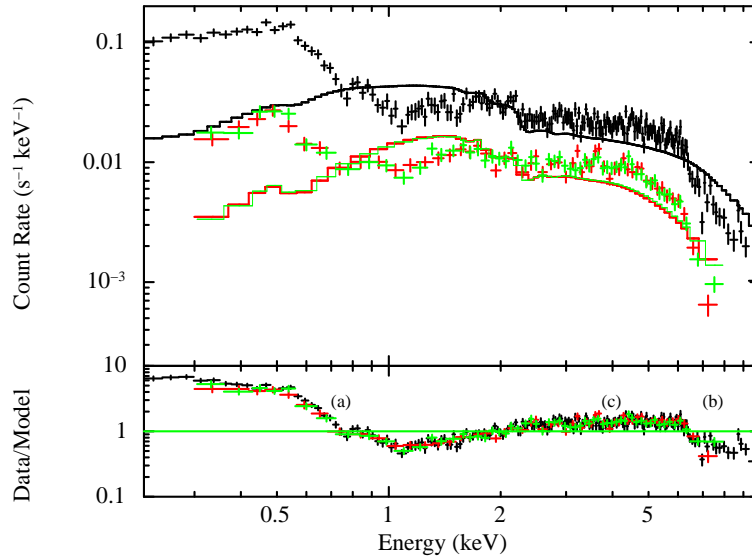


Figure 5.3. Average 2009 Long Look pn (black), MOS1 (red), and MOS2 (green) spectra of PG 1126-041 modelled with a powerlaw absorbed by the Galactic interstellar medium. Bottom panel shows data/model ratio and identifies three main deviations from the simple powerlaw: (a) strong residuals, both positive and negative, in the soft band $E \lesssim 1.5$ keV; (b) negative residuals in the hard band, $E \gtrsim 7$ keV; and (c) a low energy cutoff at $2 \lesssim E \lesssim 6$ keV.

A moderately ionized absorber

The presence of “warm” (i.e. moderately ionized) absorption was tested by adding a layer of photoionized gas modeled with `XSTAR` (Kallman & Bautista 2001), which self-consistently computes the transmitted spectrum through a spherical gas shell of constant density n , thickness ΔR , with the innermost radius at a distance $R \gg \Delta R$ from the ionizing source. The continuum luminosity is given by $L_{ion} = \int_{13.6eV}^{13.6keV} L_E dE$. The `XSTAR` output parameters that can be fitted to the spectra are the ionization parameter $\xi \equiv L_{ion}/nR^2$ at the innermost shell surface, the absorber column density $N \sim n\Delta R$, the turbulent velocity of the gas v_{turb} , and the velocity shift of the absorber v_{out} with respect to the continuum redshift. The precompiled `grid25`², which is computed for an ionizing continuum with $\Gamma = 2$, a gas shell with $n = 10^{12} \text{ cm}^{-3}$, a turbulent velocity $v_{turb} = 200 \text{ km s}^{-1}$, and solar abundances, was applied.

The addition of this component improved dramatically the fit in all the observations, with $\Delta\chi^2/\Delta\nu = 4444/2$ for the fit to the 2009 Long Look, $\Delta\chi^2/\Delta\nu = 2314/6$ for the joint fit to the other three epochs. A moderately ionized (m.i.) absorber with $\log \xi_{m.i.} \sim 1.52$

²ftp://legacy.gsfc.nasa.gov/software/plasma_codes/xstar/xspectables/grid25/

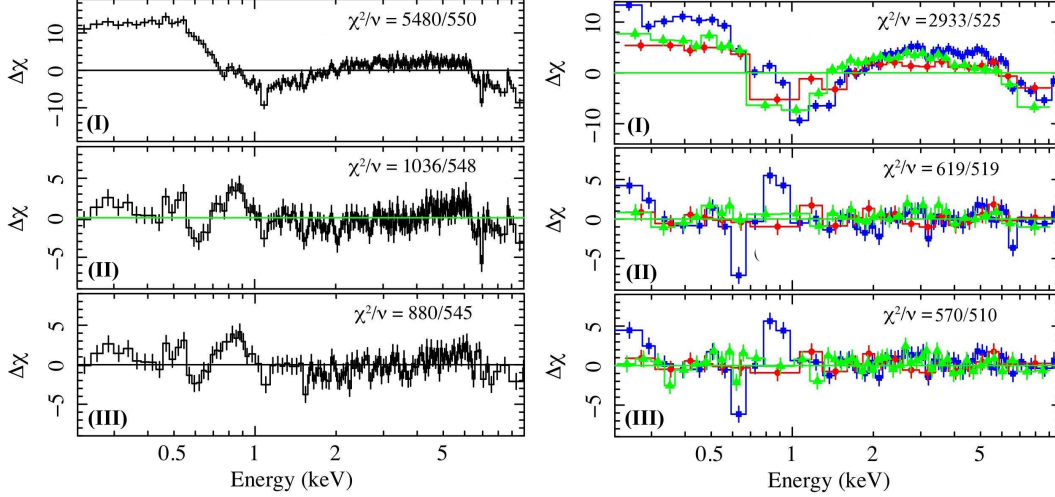


Figure 5.4. Average 0.2-10 keV pn spectral residuals in units of σ to the baseline model, after the inclusion of each component: (I) top panels: a power law continuum emission; (II) middle panels: after the inclusion of a moderately ionized absorber; (III) bottom panels: after the inclusion of a highly ionized outflowing absorber. Left column: 2009 Long Look data; right column: simultaneous fit to the Dec. 2004 (blue squares), Jun. 2008 (red circles), and Dec. 2008 (green triangles) data. The spectra have been rebinned for plotting purposes only to 8σ significance.

erg cm s⁻¹ and $N_{m.i.} \sim 4 - 8 \times 10^{22}$ cm⁻² absorbing a power law with $\Gamma \sim 1.85$ is now able to reproduce, to first order, the complex spectral shape in the soft band. Contours at the 68% and 90% confidence level for the column density and ionization parameter of the moderately ionized absorber are shown in the left panel of Fig. 5.5 for each epoch. The absorber ionization state is consistent within the errors to be constant during the different epochs, while the column density is significantly varying between the minimum $N_{m.i.} \sim 4 \times 10^{22}$ cm⁻² measured in Dec. 2008 and the maximum $N_{m.i.} \sim 7.5 \times 10^{22}$ cm⁻² measured in the Dec. 2004 and 2009 Long Look epochs. The theoretical model for the moderately ionized absorber is plotted in the right panel of Fig. 5.5 for the two extreme cases of the Dec. 2004 and Dec. 2008 epochs. It is worth noting that, at this level of ionization, most of the opacity is due to species such as C VI, N VII, O VII-VIII, Ne IX-X, Mg IX-XI, Si X-XIII, Fe XV-XX, and affects photons of $E \lesssim 2$ keV, i.e. in the spectral range where PG 1126-041 shows no variability over kilosecond time scales (Sec. 5.3). One can conclude that over short time scales the moderately ionized absorber is not varying in column density nor in ionization state. The residuals of the pn spectra relative to this model are plotted in panel II of Fig. 5.4. While the Jun. 2008 and Dec. 2008 spectra

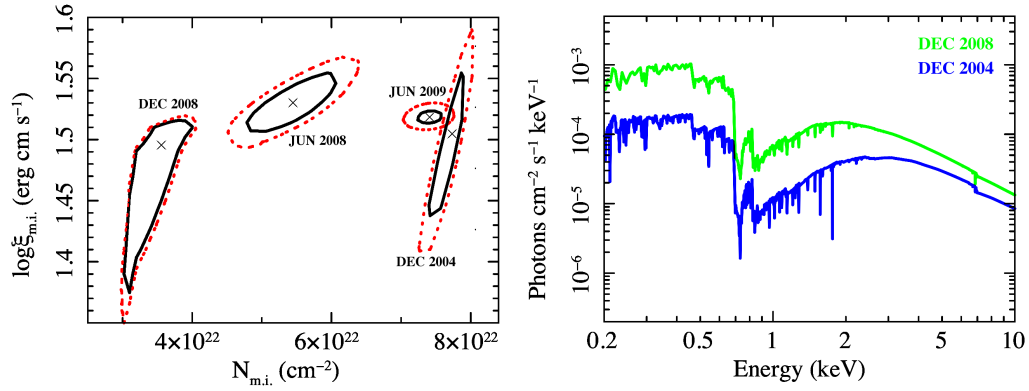


Figure 5.5. Left panel: 68% (black solid line) and 90% (red dotted line) confidence contours for the column density and ionization parameter of a moderately ionized layer of gas absorbing a power law continuum emission, for the four different epochs of observation. Right panel: theoretical model for two representative states (blue line for Dec. 2004, green line for Dec. 2008) of the moderately ionized absorber.

are overall well reproduced, the low flux states of the 2009 Long Look and Dec. 2004 still show strong residuals.

A highly ionized outflowing absorber

In particular, Panel (I) of Fig. 5.6 shows a magnified view of the 5-10 keV residuals of the 2009 Long Look pn data. The two arrows mark strong negative residuals at ~ 6.7 and 7 keV in the observer frame. An initial, phenomenological model was tried for these residuals by adding Gaussian profiles with negative normalization to the continuum model. Even though the model adopted is a rough approximation, the basic properties such as the FWHM and the EW of the absorption features are still physically meaningful. The inclusion of two narrow (unresolved, $\sigma \equiv 0$ eV) Gaussian absorption lines improves the fit statistics by $\Delta\chi^2/\Delta\nu = 74/6$. The best-fit energies and equivalent widths of the two absorption lines are $E_1 = 7.01 \pm 0.05$ and $E_2 = 7.36 \pm 0.02$ keV, $EW_1 = -80 \pm 20$ and $EW_2 = -130 \pm 30$ eV, in the source rest-frame. Allowing the widths of the absorption lines to be free parameters does not improve the fit ($\Delta\chi^2/\Delta\nu = 2/2$).

Panel (II) of Fig. 5.6 shows the 68% (black), 90% (red) and 99%(green) confidence contours for the absorption lines centroid energies and EW, in the observer frame. The two dashed vertical lines mark the *expected* FeXXV $K\alpha$ and FeXXVI $K\alpha$ transition energies (rest frame energies $E \sim 6.70$ and 6.97 keV), both blueshifted by $v_{out} = 0.055c$. The correspondence with the *detected* energies is striking, so the two absorption lines were

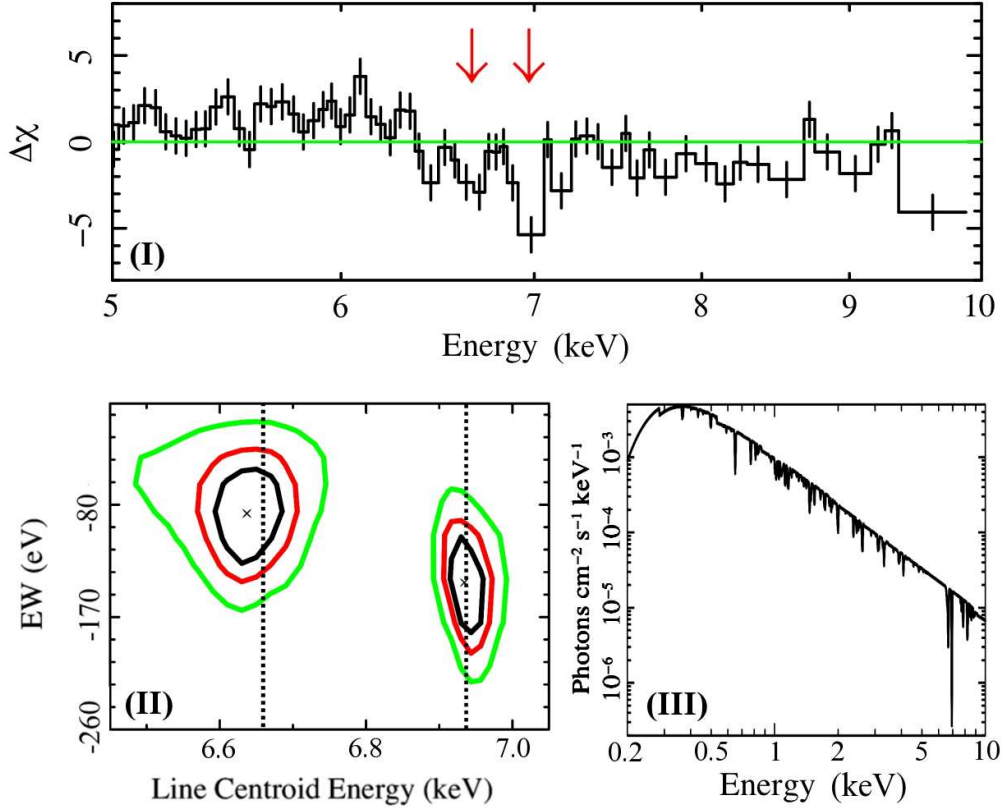


Figure 5.6. Main characteristics of the highly ionized outflowing absorber detected during the 2009 observation of PG 1126-041. Panel (I): 5-10 keV pn data residuals to a power law emission absorbed by moderately ionized gas with $N_{m.i.} \sim 8.5 \times 10^{22} \text{ cm}^{-2}$, $\log \xi_{m.i.} \sim 1.52 \text{ erg cm s}^{-1}$. The two arrows mark strong negative residuals at ~ 6.7 and 7 keV in the observer frame. Panel (II): 68% (black), 90% (red) and 99% (green) confidence contours for the observer frame centroid energies and Equivalent Widths of the two Gaussian absorption lines used to fit the residuals. The two dashed vertical lines mark the FeXXV $K\alpha$ and FeXXVI $K\alpha$ transition energies, both blueshifted by $v_{\text{out}} = 0.055c$. Panel (III): Absorption features in a model of a highly ionized absorber with $N_{h.i.} \sim 9.7 \times 10^{23} \text{ cm}^{-2}$, $\log \xi_{h.i.} \sim 3.6 \text{ erg cm s}^{-1}$, outflowing at $v_{\text{out}} \sim 0.055c$, used to fit the residuals. The opacity at the lowest energies is due to Galactic photoelectric absorption.

identified with these two transitions. The ionized absorber responsible for the opacity in the soft band has an ionization state too low to account for the absorption in the iron K band. So another layer of highly ionized gas, modeled again with XSTAR, was added. The same input parameters as for the `grid 25` were used, except than for a turbulence velocity $v_{\text{turb}} = 1500 \text{ km s}^{-1}$ found to better reproduce the residuals. A good fit is obtained, with a statistical improvement of $\Delta\chi^2/\Delta\nu = 156/3$, using a highly ionized absorber with $N_{h.i.} = 9.7^{+0.2}_{-0.7} \times 10^{23} \text{ cm}^{-2}$ and $\log \xi_{h.i.} = 3.63^{+0.02}_{-0.03} \text{ erg cm s}^{-1}$, outflowing

at $v_{out}/c = 0.054^{+0.007}_{-0.005}$.

The theoretical model for the highly ionized outflowing absorber applied to the power law continuum alone is plotted in Panel (III) of Fig.5.6. As its opacity mostly affects the $E \gtrsim 1.5$ keV band, from the previous timing analysis one can expect this component to be variable over short time scales (see Sec. 5.3).

As for the other three epochs of observation, the inclusion of the highly ionized absorber improves the joint fit statistics by $\Delta\chi^2/\Delta\nu = 49/9$. The absorber is detected at $> 3\sigma$ confidence level during the Dec. 2004 observation with $N_{h.i.} = 3.0^{+1.5}_{-1.1} \times 10^{23}$ cm⁻², $\log \xi_{h.i.} = 3.36^{+0.10}_{-0.12}$ erg cm s⁻¹, and $v_{out}/c = 0.025^{+0.011}_{-0.017}$. There is a marginal detection (2σ confidence level) of the highly ionized absorber also during the Jun. 2008 epoch ($N_{h.i.} = 2.1^{+2.0}_{-1.5} \times 10^{23}$ cm⁻², $\log \xi_{h.i.} = 3.02^{+0.06}_{-0.16}$ erg cm s⁻¹) but its velocity shift is not well constrained ($v_{out}/c < 0.09$). No significant evidence for absorption in the iron K band is detected during the Dec. 2008 observation.

Residuals relative to the power law absorbed by both the moderately and the highly ionized absorber model are shown in panel III of Fig. 5.4. I will refer to this as the baseline model ($\chi^2/\nu = 880/545$ and $570/510$ for the fit to the 2009 Long Look and the joint fit to the other three epochs, respectively), its parameters are reported in Table 5.3 . While the fit statistics for $E \gtrsim 1.5$ keV is very good for the joint fit to the Dec. 2004, Jun. 2008, and Dec. 2008 observations, a spectral curvature is still evident around the iron K band in the 2009 Long Look observation. Systematic residuals at $E < 1$ keV are also evident in both the 2009 Long Look and in the Dec. 2004 observation. These residuals will be discussed in the next sections.

A complex high energy band

The 2009 Long Look data residuals to the baseline model show an excess at $E \lesssim 6$ keV, just redward of the iron K band. In the top panel of Fig. 5.7 the thin and thick lines show the pn data/baseline model ratio rebinned to 10 and 20σ , respectively, the dashed red line marks the expected position of the Fe I K α transition, in the observer frame. This spectral curvature could be due to the improper modeling with an approximate model for the absorbers, or it could be an artifact due to the spectral variability in that energy range, or could be a real feature intrinsic to the inner accretion flow of PG 1126-041. A weak narrow Gaussian emission line is marginally detected ($\Delta\chi^2/\Delta\nu = 28/4$, $\chi^2/\nu = 852/541$)

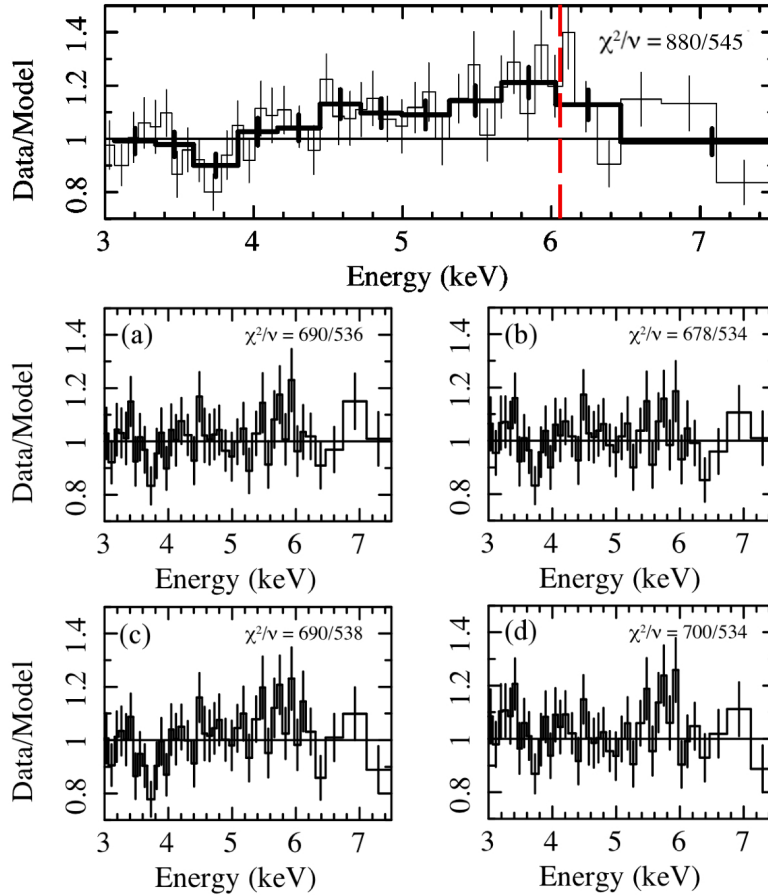


Figure 5.7. Top panel: magnified view in the 3-7.5 keV of the ratio of the average pn spectrum from the 2009 Long Look to the baseline model (bottom line in Table 5.3). The red dashed line marks the Fe I $K\alpha$ energy in the observer frame. The points have been rebinned to 10 (thin line) and 20 (thick line) σ confidence level for displaying purpose only. The remaining panels show the residuals from: (a) broad Gaussian emission line modeling; (b) Laor emission line modeling; (c) partial covering absorber modeling; (d) relativistic reflection modeling, where all the models include a weak narrow Gaussian Fe I $K\alpha$ emission line.

at $E_{\text{narow}} = 6.45_{-0.02}^{+0.01}$ keV, with an $\text{EW}_{\text{narow}} = 75_{-30}^{+20}$ eV. A broad and shallow spectral curvature is visible around 6 keV, extending down to ~ 4 keV. While narrow Gaussian emission lines associated to Compton reflection off distant, cold matter (George & Fabian 1991) are almost ubiquitous in local type 1 AGN (Yaqoob & Padmanabhan 2004; Nandra et al. 2007; Shu et al. 2010), broadened components in the iron K band are instead observed in about one to two thirds of these sources (e.g., Nandra et al. 1997, 2007; de La Calle Pérez et al. 2010). The production of Fe K fluorescence photons is also naturally associated to the presence of the absorbers, of the possible scatterer medium, of the possible reflecting

medium (we incidentally note that they may well be all the *same* physical component). The issue is very debated: (see e.g. Miller et al. 2008; Reynolds et al. 2009; Miller et al. 2009; Yaqoob et al. 2010, for a “debate” on the interpretation of the Fe K narrow emission line in the bright AGN MCG-6-30-15.).

Phenomenologically, the inclusion of a very broad Gaussian emission line with $E_{broad} = 5.33_{-0.13}^{+0.11}$ keV, $\sigma_{broad} = 980_{-100}^{+140}$ eV, $EW_{broad} = 600_{-85}^{+160}$ eV, fits very well the curvature ($\Delta\chi^2/\Delta\nu = 162/5$), as seen in the 3-7.5 keV residuals plotted in panel (a) of Fig. 5.7. Given the red-skewed profile of the spectral curvature, a relativistic profile can be also applied. The broad Gaussian was replaced with a model by Laor (1991), where the emission is assumed to come from an accretion disk surrounding a maximally spinning SMBH. A very good fit ($\Delta\chi^2/\Delta\nu = 174/7$) is obtained with $E_{Laor} = 6.9_{-0.2}^{+0.1}$ keV, $EW_{Laor} = 1750_{-110}^{+110}$ eV, emitted on a disk extending down to $r_{in} = 1.40_{-0.03}^{+0.22} r_g$ from the SMBH, with an emissivity law $\propto r^{-q}$ where $q = 5.1_{-0.2}^{+0.1}$, inclined by $i = 36_{-11}^{+2}$ deg with respect to our line of sight, see panel (b) of Fig. 5.7. The outer radius of the disk was fixed to the default value of $400r_g$; given the steep emissivity index, this choice does not affect the model.

However, two more complex physical scenarios are often invoked to explain the presence of a spectral curvature redward of 6 keV in the spectra of type 1 AGN (e.g., Miniutti & Fabian 2004; Fabian et al. 2005; Miller et al. 2008; Reynolds et al. 2009; Miller et al. 2009): the partial covering ionized absorption and the smeared ionized reflection models. In the former case, a ionized absorber is assumed to cover only a fraction $0 < C_f < 1$ of the continuum source; the sum of the absorbed (C_f) and unabsorbed ($1 - C_f$) emission fractions shapes a curvature in the spectra that depends on the absorber column density, ionization state, and covering factor (see Turner & Miller 2009, e.g.). In the latter case, it is assumed that the spectrum is dominated by a reflection component from the very inner regions of the accretion disk. This physical scenario is the same as in the Laor emission line model, but the reflected continuum is self-consistently computed according to the ionization state of the gas, as represented by $\log \xi^{ref}$, and over the whole spectral range and not only in the iron K band (Ross & Fabian 2005).

Panel (c) of Fig. 5.7 shows the pn residuals modeled within the partial covering scenario: an absorber with $N_W^{pc} = 2.7_{-0.7}^{+0.2} \times 10^{23}$ cm⁻², $\log \xi^{pc} = 2.14_{-0.03}^{+0.01}$ erg cm s⁻¹, covering a fraction $C_f = 0.54_{-0.05}^{+0.02}$ of the continuum source is able to reproduce the spectral curvature ($\Delta\chi^2/\Delta\nu = 162/3$). In this scenario, the 0.2-10 keV unabsorbed flux

of the intrinsic power law is $\sim 2.3 \times 10^{-12}$ erg s $^{-1}$ cm $^{-2}$. However, also the reflection dominated scenario (panel (d) of Fig. 5.7) is able to adequately reproduce the curvature ($\Delta\chi^2/\Delta\nu = 152/7$) if the ionized inner disk has $\log \xi^{ref} = 3.03_{-0.01}^{+0.01}$ erg cm s $^{-1}$ and extends down to $r_{in} = 4.4_{-0.4}^{+0.8} r_g$, seen face on ($i < 8.4$ deg), with an emissivity index $q = 3.77_{-0.06}^{+0.80}$. Both the reflected and the direct emission are then absorbed by the moderately and the highly ionized absorbers. According to this scenario, the 0.2-10 keV unabsorbed flux in the reflected and direct emission is $\sim 6.6 \times 10^{-13}$ and $\sim 1.5 \times 10^{-12}$ erg s $^{-1}$ cm $^{-2}$, respectively.

With the S/N of the available spectra, all of the above scenarios are able to reproduce the complex curvature. However, none of the above models can account for the weak narrow emission line associated to neutral iron, and that probably comes from reprocessing on more distant, colder material. The narrow Gaussian emission line EW is independent on the scenario adopted, $EW_{narrow} = 38_{-19}^{+20}$ eV and 48_{-18}^{+38} eV in the partial covering and in the reflection scenario, respectively. The major difference between the two scenarios is the intrinsic continuum model, that is graphically illustrated in Fig. 5.8. In the left panel, representing the partial covering scenario, the intrinsic power law continuum is plotted with a thin black line, and the same power law after the transmission through the partial covering absorber with a thick red line. The middle panel refers to the relativistic reflection scenario, the intrinsic continuum is again plotted with a thin black line; the smeared reflection continuum with a dashed blue line, and the the sum of the two components with a thick red line. The difference in the intrinsic continuum is that in the partial covering model $\Gamma = 2.15_{-0.01}^{+0.05}$ and $N_{1\text{keV}} = 1.26_{-0.02}^{+0.03} \times 10^{-3}$ ph s $^{-1}$ keV $^{-1}$ cm $^{-2}$ translates into an unabsorbed 2-10 keV luminosity $L_{2-10} \sim 2.0 \times 10^{43}$ erg s $^{-1}$, while in the smeared reflection model $\Gamma = 1.86_{-0.03}^{+0.04}$ and $N_{1\text{keV}} = 0.52_{-0.02}^{+0.01} \times 10^{-3}$ ph s $^{-1}$ keV $^{-1}$ cm $^{-2}$ translates into an unabsorbed 2-10 keV luminosity $L_{2-10} \sim 1.3 \times 10^{43}$ erg s $^{-1}$.

For comparison, adopting a Gaussian model for the spectral curvature (blue dashed line in the right panel of Fig. 5.8) gives an intermediate value for the intrinsic continuum, $\Gamma = 2.00_{-0.03}^{+0.03}$ and $N_{1\text{keV}} = 0.99_{-0.02}^{+0.02} \times 10^{-3}$ ph s $^{-1}$ keV $^{-1}$ cm $^{-2}$, and for the unabsorbed 2-10 keV luminosity $L_{2-10} \sim 1.6 \times 10^{43}$ erg s $^{-1}$. To be conservative, in the following the intermediate, phenomenological Gaussian modelization for the spectral curvature in the iron K band present in the average 2009 Long Look spectra will be adopted ($\chi^2/\nu = 690/536$).

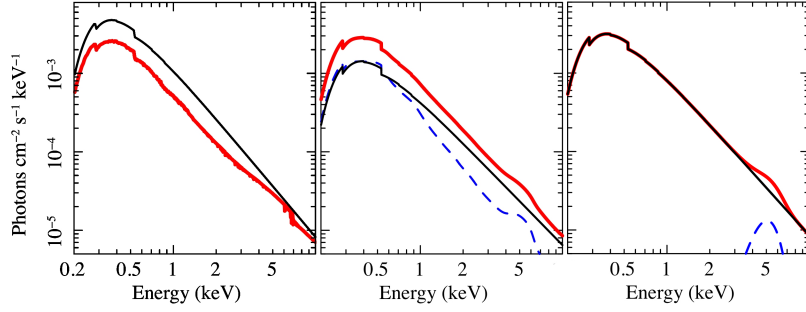


Figure 5.8. Three different models that can reproduce the spectral curvature observed in the iron K band during the 2009 Long Look observation. Left panel: a partial covering scenario; middle panel: a relativistic reflection scenario; right panel: a phenomenological Gaussian model. In all the panels, the thin black line is the intrinsic power law continuum, the blue dashed line (where present) is the reflected emission component, and the thick red line is the sum of all the components, that in all cases is then absorbed by both the moderately and the highly ionized absorber as in the baseline model.

A distant emitter/reprocessor

Significant residuals relative to the baseline model at $E < 1$ keV are present only in the 2009 Long Look and Dec. 2004 spectra (Panel III of Fig. 5.4), and do not vary over short timescales. This suggests a secondary, constant component that emerges at low energies when the source is in a low flux state. Possible contributors to the soft emission can be a scattered component accompanied by recombination lines from a photoionized gas, thermal emission from an underlying starburst component, or a mixture of the two.

As a starting point, the residuals in the higher S/N 2009 Long Look spectra were considered. The addition of a secondary power law emission improves the fit by $\Delta\chi^2/\Delta\nu = 75/4$ ($\chi^2/\nu = 615/632$); the corresponding pn data residuals in the 0.2-3 keV band are shown in the top panel of Fig. 5.9. The secondary power law is steep, $\Gamma^{\text{soft}} \sim 3$, and its normalization is about 2% of the primary power law one, typical of scattered components as observed in absorbed (type 2) AGNs. However, there are still residuals around 0.5 and 0.9 keV that can be well represented phenomenologically by two narrow ($\sigma \equiv 0$ eV) Gaussian emission lines at energies $E_1 \sim 0.5$ and $E_2 \sim 0.9$ keV (panel (a) of Fig. 5.9, $\Delta\chi^2/\Delta\nu = 76/8$). The observed energies might correspond to O VII K and Fe L emission features, but the exact identification is prohibitive with the pn spectral resolution.

Two alternative and more physical models that can account for the soft emission features are thermal emission and emission from a photoionized plasma. Panel (b) of

Fig. 5.9 shows the data residuals to a soft power law plus photoionized emission modeled with `XSTAR` ($\log \xi^{photo} = 1.05_{-0.09}^{+0.07}$ erg cm s⁻¹, $\Delta\chi^2/\Delta\nu = 44/5$), while panel (c) shows the residuals to a soft power law plus a thermal emission modeled with a `mekal` component ($kT = 0.84_{-0.07}^{+0.07}$ keV, $\Delta\chi^2/\Delta\nu = 17/4$). Removing the secondary steep power law and modelling the soft residuals with a combination of a thermal ($kT = 0.79_{-0.03}^{+0.04}$ keV) and a photoionized ($\log \xi^{photo} = 0.45_{-0.16}^{+0.28}$ erg cm s⁻¹) emission, gives an equally acceptable fit ($\Delta\chi^2/\Delta\nu = 50/5$, see Panel (d) of Fig. 5.9). In this scenario, the 0.2-3 keV unabsorbed luminosity of the photoionized emission is 2.7×10^{41} erg s⁻¹, while the luminosity of the thermal emission is 1.3×10^{41} erg s⁻¹. Basically, the photoionized component reproduces the ~ 0.5 keV residuals, while the thermal component reproduces the ~ 0.9 keV residuals. In Fig. 5.10 two theoretical models that can reproduce the soft band residuals and the broad band 2009 Long Look EPIC spectra of PG 1126-041 are plotted: the soft emission is modelled with the secondary, soft power law (dashed orange line) plus two Gaussian emission lines (thick orange lines) in the left panel, with photoionized (thin orange line) plus thermal (thin magenta line) emission in the right panel; both models also include a broad (dashed blue line) and a narrow (thick blue line) Gaussian emission line in the iron K band, and the two ionized absorbers of the baseline model. The sum of all the components is the thick red line. It is clear that the model in the soft band does not affect the other spectral components, and that all the adopted models provide acceptable fits to the data in the soft band: because there is no way to distinguish between them, the simplest model will again be chosen, that is the soft power law plus the two Gaussian emission lines ($\chi^2/\nu = 1.03$).

As for the joint fit to the other three epochs of observation, the secondary soft power law plus the two narrow Gaussian emission lines were added to the baseline model, with the model parameters tied between the epochs. The fit statistic improves by $\Delta\chi^2/\Delta\nu = 72/6$, and all the spectra are very well reproduced by the model, $\chi^2/\nu = 0.99$.

The final best fit model

The best fit model for the average spectra of PG 1126-041 is the following: the continuum is modeled as a power law emission plus a broad Gaussian emission line (detected only during the 2009 Long Look observation), and is absorbed by both a moderately ionized and a highly ionized outflowing absorber; a narrow Gaussian emission line is also detected

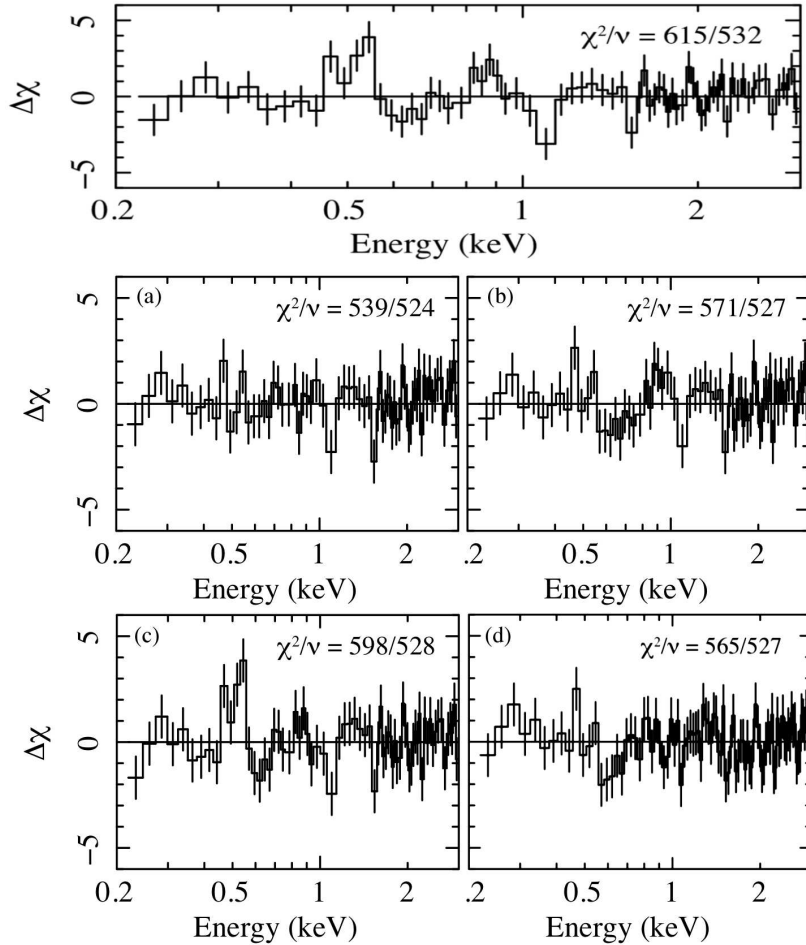


Figure 5.9. Zoom into the 0.2-3 keV 2009 Long Look pn residuals to the baseline model, after the inclusion of different further components. Top panel: a secondary, soft power law. Small panels: (a) a soft power law plus two narrow Gaussian emission lines; (b) a soft power law plus emission from a photoionized plasma; (c) a soft power law plus thermal emission; (d) photoionized plus thermal emission.

in the iron K band during the 2009 Long Look. As for the soft band, the spectra were modeled with a secondary power law plus two Gaussian emission lines. The best fit theoretical model for the 2009 Long Look is shown in the left panel of Fig. 5.10. The model parameters along with their 1σ errors for both the 2009 Long Look fit and for the joint fit to the other three epochs of observation are reported in Table 5.4.

As noted above, neither a broad nor a narrow Fe K line are required by the data of the Dec. 2004, Jun. 2008, and Dec. 2008 epochs; upper limits on the EW of these components in each epoch were set by fixing their centroid energies (and widths in the case of the broad

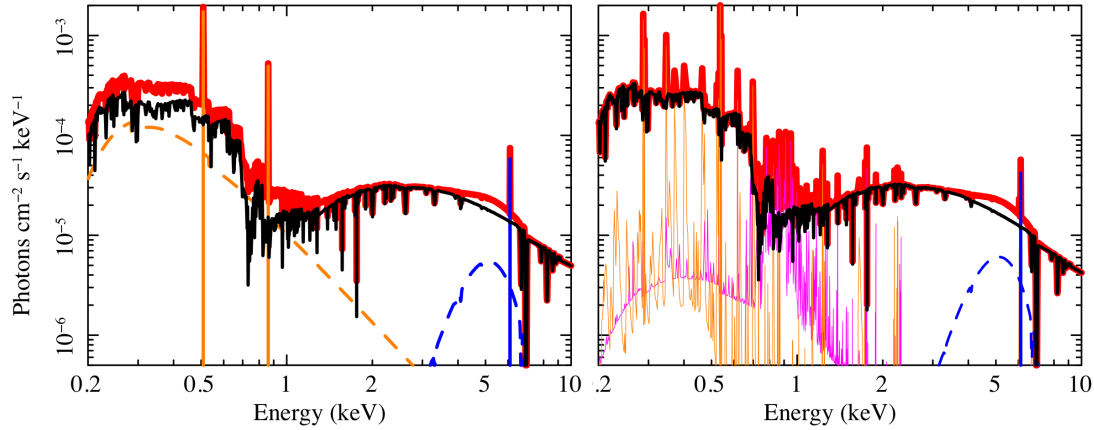


Figure 5.10. Two different models of the soft band of PG 1126-041 capable of reproducing the 2009 Long Look average EPIC spectra. Left panel: secondary soft power law (dashed orange line) plus two narrow Gaussian emission lines (thick orange lines). Right panel: photoionized emission (thin orange line) plus thermal emission (thin magenta line). Both models also include a broad (dashed blue line) and a narrow (thick blue line) Gaussian emission line in the iron K band, and the two ionized absorbers of the baseline model. The sum of all the components is the thick red line.

Gaussian) to the best fit values of the 2009 Long Look observation. The lack of detection of these components could be due to the much lower S/N of the 2004 and 2008 exposures, especially regarding the narrow Fe K emission line.

5.5 X-ray time resolved spectral analysis

Time resolved spectral analysis was performed on the EPIC pn data extracted in the eight time intervals of the 2009 Long Look observation marked in the middle panel of Fig. 5.2. Exposure time and background corrected count rates are reported in Table 5.5 for each interval. All the eight time intervals were simultaneously fitted to the best fit model described in Sec. 5.4. Given the same observed count rate, the 3rd interval was fit together with the 5th, and the 4th interval together with the 6th one.

The soft, constant spectral components (i.e., the secondary power law plus the two Gaussian emission lines) have been kept fixed to the best fit values found in the analysis of the average 2009 Long Look spectra (Sec. 5.4). All the other spectral components were left free to vary. When the model parameters were found to be constant within the errors between the different time intervals, they were forced to have the same value during the whole exposure.

Fig. 5.11 shows the ratio between the data of each interval and the best fit model of the average 2009 Long Look spectra: the fit is not acceptable, $\chi^2/\nu = 1661/892 \sim 1.86$. At energies $E \gtrsim 1.5$ keV there are deviations from the baseline model of about 50% on a few kiloseconds timescales (e.g., from the 2nd to the 3rd time interval, and from the 7th to the 8th time interval), and variations as high as 100% with respect to the average are observed during the 7th interval.

Allowing the power law normalization to be a free parameter improves the fit by $\Delta\chi^2/\Delta\nu = 699/5$. Fig. 5.12 shows the 5-8 keV data residuals for each spectral slice. The presence of the highly ionized absorber is clear in some of the intervals, namely the 1st, the 7th and the 8th. Because of the much lower S/N in individual time slices, it is not possible to resolve the two narrow absorption features in the iron K band identified with the highly ionized outflowing absorber in Sec. 5.4. A single absorption line with width σ as a free parameter was therefore used to model the negative residuals around 7 keV. The best fit values for the absorption line energy and width are $E_{abs} = 7.2 \pm 0.1$ keV and $\sigma_{abs} = 260 \pm 90$ eV; its EW is found to vary between time slices, as reported in Table 5.6 and as visible in Fig. 5.12.

All the other spectral components (i.e. the moderately ionized absorber and the broad and narrow Gaussian emission lines used to model the iron K band) are found to be constant during the observation.

5.6 Optical/X-ray photometry

Thanks to the presence of the OM aboard *XMM-Newton*, simultaneous optical/X-ray photometry was performed for each epoch of observation. The OM data were all taken in Image mode, and were reduced and calibrated using standard pipeline procedures through the `omichain` SAS task. Background corrected count rates were converted in magnitudes for each exposure (exposure times are ranging between 1 and 4 ks). We are interested in measuring f_{2500} to compute the optical-to-X-ray spectral index $\alpha_{\text{ox}} = -0.384 \log(L_{2500\text{\AA}}/L_{2\text{keV}})$, as defined by Tananbaum et al. (1979). The weighted mean of the magnitudes measured in the filters with effective wavelength straddling 2650 Å in the observed frame (2500 Å in the rest frame) were used. The relevant filters are the UVW1 and UVM2 ($\lambda_{eff} = 2910$ and 2310 Å, respectively). This magnitude was then corrected for the Galactic extinction $A_{2650} = 0.382$, estimated using the method of Cardelli et al.

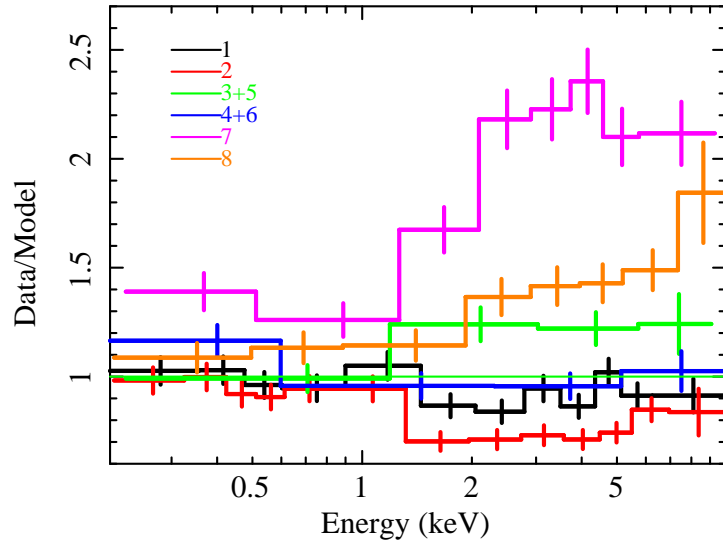


Figure 5.11. Ratio between the pn data extracted in the eight different time intervals marked in Fig. 5.2 to the best fit model for the average 2009 Long Look pn data of PG 1126-041. Points have been visually rebinned to 15σ confidence level.

(1989). Flux densities for each epoch were then computed using Vega as a calibrator. Optical photometry results are reported in Table 5.7.

As for the 2 keV flux density measurements, the best fit model was used to measure the Galactic absorption corrected rest frame $f_{2\text{keV}}$ for each observation. Flux densities were then converted to luminosity densities, and the optical-to-X-ray spectral index was computed. It is well known that the α_{ox} spectral index in AGN strongly depends on the intrinsic UV continuum luminosity (e.g., Vignali et al. 2003; Strateva et al. 2005; Steffen et al. 2006; Young et al. 2010). The observed α_{ox} was thus compared with the value $\alpha_{\text{ox}}(2500)$ expected on the basis of the 2500 Å UV luminosity of PG 1126-041, using Eq. 2 of Steffen et al. (2006), which gives the parameter $\Delta\alpha_{\text{ox}} \equiv \alpha_{\text{ox}} - \alpha_{\text{ox}}(\ell_{2500\text{Å}})$. The $L_{2\text{keV}}^{\text{corr}}$ flux densities corrected for intrinsic X-ray absorption were also computed, along with the corresponding $\alpha_{\text{ox}}^{\text{corr}}$ and $\Delta\alpha_{\text{ox}}^{\text{corr}}$. In Table 5.8 the optical/X-ray photometry results are reported. There are variations in the intrinsic luminosity density of PG 1126-041 both at UV and at X-ray wavelengths. While the observed 2500 Å flux density is steadily increasing from 2004 to 2009, and is varying by about 30%, the observed 2 keV flux density is increasing from 2004 to 2008, and then decreases again in 2009, with variations as high as 450% between the Dec. 2008 and the 2009 Long Look observation. As a result, the observed α_{ox} is variable between the different epochs, spanning from values typical of radio

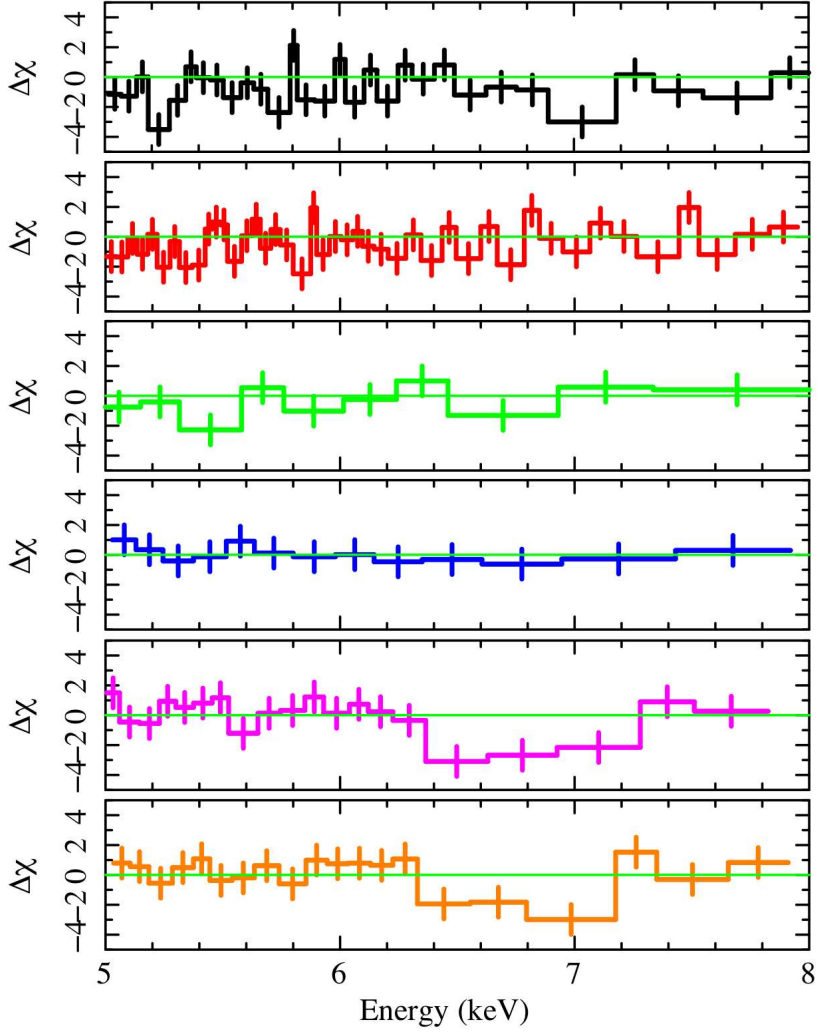


Figure 5.12. PG 1126-041: 5-8 keV residuals for each temporal slice to a model where the highly ionized outflowing absorber was removed. From top to bottom: 1st (black), 2nd (red), 3rd + 5th (green), 4th + 6th (blue), 7th (magenta), and 8th (orange) interval.

quiet type 1 AGN (i.e., $\alpha_{\text{ox}} \sim -1.7$ in the Dec. 2008 observation) to values typical of Soft X-ray Weak AGN (i.e., $\alpha_{\text{ox}} \sim -2$ in the 2009 Long Look observation). However, compared to the expected $\alpha_{\text{ox}}(2500)$, the source is found to be X-ray weak in all the epochs, with $\Delta\alpha_{\text{ox}} \sim -0.3 - 0.6$. Once the effect of intrinsic X-ray absorption is taken into account, the maximum observed variations in the 2 keV flux density between the different epochs decrease to about 200%. Consequently, also the $\Delta\alpha_{\text{ox}}$ decreases to $\Delta\alpha_{\text{ox}}^{\text{corr}} \sim 0.1 - 0.3$.

5.7 Discussion

PG 1126-041 is observed to be highly variable in X-rays on time scales of both months and kiloseconds. The RMS variability analysis performed on the 2009 Long Look pn exposure (92 ks) revealed the presence of a spectral component (up to 50% variations in flux) emerging only at $E \gtrsim 1.5$ keV (Fig. 5.2). On the other hand, the variability on time scales of months (observed to be as high as $4\times$ in flux) is dominated by a spectral component emerging at $E \lesssim 5$ keV (Fig. 5.1). A wealth of information has been obtained both on the intrinsic X-ray continuum emission of PG 1126-041 and on the reprocessing media that happen to be in the inner regions of this AGN. The SMBH mass estimate of $M_{BH} = 1.2 \times 10^8 M_\odot$ as given by Dasyra et al. (2007) will be adopted. The M_{BH} estimated by Vestergaard & Peterson (2006) through scaling relations is a factor of 2.4 lower. Adopting the bolometric luminosity $L_{bol} = 10^{12} L_\odot$ (Sanders et al. 1989) gives an accretion rate needed to power PG 1126-041 of $\dot{M} = 0.67 M_\odot/\text{yr}$ and an Eddington ratio $\lambda \equiv L_{bol}/L_{Edd} = 0.23$. The gravitational radius is $r_g = 1.8 \times 10^{13}$ cm and the corresponding light travel time is $t_L = 600$ s.

Strong variations of both the intrinsic continuum and of a highly ionized outflowing absorber are responsible of the observed kilosecond time scale variability. The power law photon index $\Gamma = 1.93$ is found not to vary on kilosecond time scales, while the intensity of the intrinsic power-law spectrum is following the pattern of the 1.5-10 keV count rate over the whole observation (see the middle bottom panel of Fig. 5.2), and doubles in a time interval Δt lasting about 8 ks (the 7th interval). The variability time scale of the intrinsic continuum can set a constrain in the geometrical size D of the X-ray emission region through the causality argument, $D < c\Delta t \sim 2.4 \times 10^{14}$ cm $\sim 13r_g$. The highly ionized absorber is observed to be outflowing at $v_{out} \sim 15,000$ km s $^{-1}$ during the average 2009 Long Look observation. In the time resolved spectral analysis of the same exposure, the outflowing absorber is found to be variable over very short time scales (Fig. 5.12). With the much lower S/N of each temporal slice it was not possible to assess whether the absorber varied in ionization state, column density, or blueshift. However, the very short time scale variability suggests that the absorber is very compact and very close to the X-ray source, and that we are possibly observing rapid mass ejections from the inner regions of the accretion disk, e.g., the base of an accretion disk wind.

At $E \lesssim 1.5$ keV the power law variability is smeared out by the presence of the soft

constant components (a moderately ionized absorber and a distant scattered emission), and at $E < 1$ keV the highly ionized absorber opacity drops (Fig.5.6), so explaining the constant soft flux measured during the whole 2009 Long Look observation.

The PG 1126-041 X-ray variability over long timescales is dramatic, and is especially strong at energies $E \lesssim 6$ keV. The $f_{2\text{keV}}$ is observed to be variable up to 4.5 higher in the six months elapsed between the Dec. 2008 and the 2009 Long Look observations (Fig. 5.1). A moderately ionized absorber is detected in every *XMM-Newton* observation of PG 1126-041 (Fig. 5.4). Its ionization state is compatible with being constant ($\log \xi_{m.i.} \sim 1.5$ erg cm s⁻¹) while its column density is significantly varying between the minimum $N_{m.i.} \sim 4 \times 10^{22}$ cm⁻² measured in the Dec. 2008 observation and the maximum $N_{m.i.} \sim 8 \times 10^{22}$ cm⁻² measured in the Dec. 2004 and 2009 Long Look observations (Fig. 5.5). In fact, the moderately ionized absorber column density variations dominate the spectral variability observed on month time scales, together with amplitude variations of the intrinsic continuum up to a factor of two (Table 5.4).

Also the highly ionized absorber is found to be variable in velocity, ionization state, and column density between the different epochs. Along with its detection in 3/4 observations, this suggests a strong short term variability coupled with a long term persistent behavior. As for the other spectral components, the spectral curvature clearly detected in the iron K band during the 2009 Long Look observation is of special interest. While we have chosen a very conservative, empirical description of the broad Fe K line in terms of a Gaussian, other, more physical scenarios are also possible. A relativistic reflection component would fit well the spectral curvature as well as a partially covering ionized absorber (Section 5.4). However, the effects on the intrinsic power law continuum parameters in the two different scenarios are limited to less than 20%.

An appealing scenario is that of a UV line driven accretion disk wind as developed by Proga & Kallman (2004) and modeled by Sim et al. (2010b). These authors computed the simulated X-ray spectra for a non-spherical, hydrodynamical accretion disk wind in an AGN with $M_{BH} = 10^8 M_{\odot}$, accreting with $\lambda = L/L_{Edd} = 0.5$, i.e., with conditions not too different to those observed in PG 1126-041. The simulated spectra change significantly for different inclination angles and different snapshots of the flow, confirming both the non-spherical character and the highly dynamical behavior of the X-ray spectrum associated with such winds. The spectral signature of such flows includes both absorption and

emission features. For example, the iron K band is shaped both by absorption by a highly ionized (Fe XXV, Fe XXVI) outflowing phase of the wind, and by emission and scattering off the highly ionized base of the flow, that produces a Compton bump that mimics a red-skewed iron K line. In the soft band ($E < 1$ keV), there are contributions by a blend of emission lines from elements such as C, O, Fe, and bremsstrahlung emission by the wind. This is exactly what we observe in the high S/N 2009 Long Look observation of PG 1126-041 once we account for the presence of the moderately ionized absorber (FIG4, PANEL II). From a dynamical point of view, the same model also predicts a flow component that qualitatively shows the same behavior of the highly ionized absorber. At intermediate inclination angles above the disk plane and above the “skin” of the fast wind, where the gas is most exposed to the X-ray ionizing source, recurrent instabilities with blobs (or “puffs”) of high density can develop. Some of these puffs quickly become overionized and fail to become part of the wind, while others can be able to be efficiently accelerated to velocities even higher than those of the fast wind, and well above the local escape velocity. This flow component would observationally be detectable in the X-ray spectra via large column density variations, and sporadic high velocity ejections, over short timescales, similar to what observed during the 2009 long look of PG 1126-041. This may suggest that radiation driven accretion disk wind models can account in a self-consistent way for most of the observed X-ray spectral features in the mini-BAL QSO PG 1126-041. Models for the X-ray spectra of accretion disk winds that can be fitted to real data are still under development, therefore we must confine ourselves to qualitative considerations. However, we note that in this scenario the radial flow assumption is invalid, and the mass outflow rate associated with the highly ionized phase is overall very different than in the spherical case.

The moderately ionized absorber, on the other hand, seems to be associated with some other physical mechanism. The possibilities include thermal evaporation of the more distant portions of the accretion disk, and/or of the inner skin of the putative dusty molecular torus (Dorodnitsyn & Kallman 2009). The observed variability is also consistent with the scenario suggested to explain the variability of the UV absorption lines of the mini-BAL QSO HS 1603+3820 over (rest-frame) time scales of weeks and months (Misawa et al. 2007b, 2010). In this scenario the variability of the UV absorption lines is the result of fluctuations of the continuum, which is caused by a screen of clumpy, highly-ionized

gas between the UV absorber and the continuum source. This clumpy screen has similar properties as the moderately ionized absorber we have found in PG 1126-041.

The soft component is found to be constant during all the epochs. It emerges only during the low-flux states (Dec. 2004 and 2009 Long Look) and contributes only $< 20\%$ to the 0.2-2 keV flux in the Dec. 2008 high-flux state. We modeled it as a soft power law plus two narrow Gaussian emission lines, but other models (i.e. photoionized or thermal emission) are statistically and physically plausible as well. Nevertheless, in every case the model parameters for the soft components in each epoch suggest a distant origin for the gas responsible for its emission. The contribution from photoionized versus collisional plasma can not be discerned, leaving the open possibility for an underlying starburst contribution. The unabsorbed 0.2-2 keV luminosity of such component would be 1.3×10^{41} erg s $^{-1}$, compared to the intrinsic X-ray continuum luminosity in the same spectral range of 3.1×10^{41} erg s $^{-1}$.

The observed optical-to-X-ray spectral index is found to be highly variable, following the moderately ionized absorber variability. Although α_{ox} never gets < -2 , when compared with the expected $\alpha_{ox}(\ell_{2500\text{\AA}})$ based on the UV continuum luminosity it is found that PG 1126-041 is observed to be Soft X-ray weak, $\Delta\alpha_{ox} = -(0.3-0.6)$. After correcting for the X-ray absorption, the source is still slightly X-ray weak, $\Delta\alpha_{ox}^{corr} = -(0.1 - 0.3)$. The 2-10 keV unabsorbed luminosity is still very low, $\langle L_{2-10} \rangle \sim 2 \times 10^{43}$ erg s $^{-1}$, and compared with L_{bol} gives a very high bolometric correction, $\kappa_{bol} \sim 200$, that still is compatible with the $\kappa_{bol} - \alpha_{ox}$ relation as in Lusso et al. (2010).

A mass loss rate rough estimate

In order to get an estimate of the mass loss rate associated to the wind of PG 1126-041, some assumptions must be made and basically all of the above considerations must be forgotten. For example, by assuming an isotropic wind and photoionization equilibrium, a limit on the mass loss rate can be placed. Alternatively, the absorbing gas can be assumed to be formed by clouds in Keplerian orbits around the SMBH, and the variability assumed to be due to the occultation of the continuum source by the absorbing clouds, to use the variability time scale to set geometrical constraints as in Risaliti et al. (2007). Most likely, both of these scenarios do not coincide with the actual scenario for BAL and mini-BAL QSOs, e.g., for the presence of the accretion disk that breaks the spherical

symmetry, not to speak about the variable character of the outflow. The geometrical and dynamical effects are most probably very important for AGN accretion disk winds, meaning that the departure from the spherically symmetric case could well be significant: actual numbers could be off by even one or two order of magnitudes with respect to the current estimates, due to uncertainties of physical parameters such as density, black hole mass, ionizing luminosity, ionization state, and above all of the covering fraction, geometry, and duty cycle of the wind. However, I will give here some reference number estimates for the PG 1126-041 system, following the photoionization equilibrium and the spherical symmetry and isotropy assumptions, that are the most used in the literature. Under these assumptions, the density of the flow scales as R^{-2} and ξ is constant throughout the shell, so that the ratio $L_{ion}/\xi \equiv nR^2$. Another widespread used assumption is $R \gg \Delta R$, i.e., the case of a geometrically thin absorber. This may well not be the case, as in proper accretion disk wind models (e.g., Proga et al. 2000; Everett 2005), where the flow is usually radially extended and absorption features can form in a wide range of distances from the wind launching point.

In any case, for a simple spherically symmetric, geometrically thin outflowing shell in photoionization equilibrium, $R < L_{ion}/\xi N_H$, where N_H is the column density of the absorbing gas, $N_H = n\Delta R$. Using the best fit parameters for the highly ionized absorber, $\log \xi_{h.i.} = 3.68$ erg cm s⁻¹ and $N_{h.i.} = 9.7 \times 10^{23}$ cm⁻², and the estimate $L_{ion} \equiv \int_{13.6 eV}^{13.6 keV} L_E dE \sim 0.1 L_{bol}$ (e.g., McKernan et al. 2007), gives $R_{h.i.} < 2.3 \times 10^{16}$ cm $\sim 1250 r_g$. For a radial flow at a constant velocity $v_{out} = 15,000$ km s⁻¹, this translates to a mass outflow rate $\dot{M}_{out}^{h.i.} \sim 11 C_{h.i.} M_{\odot} \text{ yr}^{-1}$, where $C_{h.i.}$ is the product of the highly ionized absorber covering factor and volume filling factor, as defined in Eq. 2.1. It is worth noting that for $C_{h.i.} = 0.06$, one would have $\dot{M}_{out}^{h.i.} \sim \dot{M}_{acc}$, that is, the same quantity of matter accreted would be ejected, only in the highly ionized phase of the outflow. This suggests a low value $C < 0.06$ for the highly ionized phase, naively in agreement with the clumpiness argued from the kilosecond time scale variability, and/or with a short duty cycle. In any case, the argued clumpiness breaks the continuous, homogeneous flow assumption, so that these kind of considerations will remain somewhat circular until some sensitive dynamical constraints about the wind will be placed. Using the same argument as for the highly ionized absorber, a constraint on the moderately ionized absorber flow of matter can be placed. Despite the high intrinsic continuum variability, the moderately

ionized absorber that dominates in opacity at $E < 2$ keV is found *not* to be varying in column density nor in ionization state over kilosecond timescales (Fig. 5.2). The longest time interval over which there is a continuous monitoring of the source is the $\Delta t = 91.2$ ks 2009 Long Look pn exposure. Assuming again photoionization equilibrium and spherical symmetry, one can use this time interval to set some limits on the moderately ionized absorber density $n_{m.i.}$ and its distance $R_{m.i.}$ from the SMBH. At this level of ionization, O VII and O VIII are the most abundant species of oxygen in an optically thin photoionized gas (e.g., Kallman & Bautista 2001). Therefore, it follows that the recombination time for highly ionized oxygen $t_{\text{rec}} > 91.2$ ks. Following Eq. 5 of Otani et al. (1996), one can write $n_{m.i.} < 2.2 \times 10^6 (T_5)^{0.7} \text{ cm}^{-3}$, where $T = 10^5 T_5$ K is the moderately ionized absorber temperature. Following their Eq. 6, this maximum density translates to a minimum distance of $R_{m.i.} > 2.1 \times 10^{18} (T_5)^{-0.35} \text{ cm} \sim 120,000 r_g$, where a $L_{\text{ion}} = 10^{44} \text{ erg s}^{-1}$ as the ionizing continuum luminosity, and the best fit value for the moderately ionized absorber $\log \xi_{m.i.} = 1.52 \text{ erg cm s}^{-1}$, were used. These are typical distance estimates for X-ray warm absorbers, that are usually found to be outflowing with velocities of a few hundreds km s^{-1} when observed at high energy resolution (McKernan et al. 2007). Using the same L_{ion} and $\log \xi_{m.i.}$, one can estimate the mass outflow rate to be $\dot{M}_{\text{out}}^{m.i.} \sim 10 C_{m.i.} (v_{\text{out}}/100 \text{ km s}^{-1}) M_{\odot}/\text{yr}$.

The kinetic efficiency of the two phases of the outflowing gas can be estimated as $\epsilon_k^i = \dot{M}_{\text{out}}^i (v_{\text{out}}^i)^2 / 2L_{\text{bol}}$, giving $\epsilon_k^{m.i.} = 8.2 C_{m.i.} \times 10^{-6}$ and $\epsilon_k^{h.i.} = 0.18 C_{h.i.}$. Although it is not possible to accurately measure the impact of such AGN outflows on the surrounding regions (there are several orders of magnitude of uncertainty due to the unknown C , geometrical and dynamical behavior of the wind), it is worth stressing that their detection is statistically solid and model-independent, so that in order to overcome this uncertainty the only possible way is represented by deeper studies.

5.8 Conclusions

The present *XMM-Newton* observational campaign on PG 1126-041 allowed to characterize the complex high energy spectral behavior of a mini-BAL QSO with unprecedented sensitivity. Data for four different pointed observations, that totally span 4.5 yr, have been analyzed.

The most evident and model-independent result is the detection of high column densi-

ties of ionized gas along the line of sight, that contribute to the observed spectral variability on both kilosecond and month time scales for the highly ionized and moderately ionized absorbers, respectively. Also the intrinsic X-ray continuum emission is observed to be variable, mostly in intensity, over both short and long time scales. Other spectral features suggest the possible presence of further complexities, although short time scale variability could contribute to mimic average fake spectral features. A line-driven accretion disk wind is a very promising scenario to explain the observed high velocity outflow, the complex iron K band, and the weak soft emission components. However, other scenarios such as a relativistic reflection from the inner regions of the accretion disk, or a third, partially covering ionized absorber, cannot be really ruled out nor constrained with the present data and model quality. In the soft band there is a constant secondary emission component that may be due to scattered or reflected continuum emission or emission from a photoionized or collisionally ionized plasma (or a combination of the above).

Overall, the findings of this study are qualitatively consistent with radiation-driven accretion disk wind models predictions, where one expects a high column density of X-ray absorbing gas shielding the portion of the wind that is accelerated by UV photons. The hot X-ray component of the wind is also expected to be highly variable with time in such a model. The mini-BAL appearance of the wind of PG 1126-041 is qualitatively consistent with an orientation effect, in which our line of sight and the plane of the accretion disk make a larger angle than when viewing classical BAL QSOs. We are looking at a narrower range of UV velocities through the wind (hence the small width of the UV absorption features) and at the transition zone between the fast UV wind and the hot X-ray component of the flow, where we expect strong X-ray spectral variability.

The present observational campaign on the mini-BAL QSO PG 1126-041 has demonstrated how long and short term variability studies are quite powerful tools to identify the physical mechanisms at work. While longer observations are recommended, only X-ray telescopes with large collecting areas will provide statistically significant count rates to test various models.

The regions close to the AGN black hole are very complex to model. It is realistic expecting a contribution from both reflection and absorption on ionized gas. Furthermore, some of the assumptions of the models (e.g., density profiles, geometry) may need to be revised. In the context of AGN outflows (mini-BAL QSO) we can expect absorption,

reflection and scattering on the ionized gas, but at this point it is not possible to constrain all the reflection and absorption parameters simultaneously. A coverage of the hard X-ray band where the Compton hump peaks, an X-ray polarimeter which can trace the scattered emission, a better spectral resolution either with a microcalorimeter or with bigger grating instruments, would be the keys to constrain reflection, scattering, absorption, and hence the geometry and the dynamical behavior of accretion disk winds in AGN. Given the X-ray weakness of these sources, a large collecting area would be also highly recommended, so making the future studies of these objects challenging and fascinating both from a theoretical, an interpretative, and a technological point of view. On this respect, the future Astro-H and IXO missions are very promising.

Table 5.2. X-ray observation log for PG 1126-041

OBSID	Date	Duration	Exposure	Mode	Filter	Count-rate	$\log f_{0.2-2}$	$\log f_{2-10}$	Epoch
(1)	(2)	[ks]	M1 / M2 / pn [ks]	(5)	(6)	MOS / pn [0.1 ct s ⁻¹]	pn [erg cm ⁻² s ⁻¹]	pn [erg cm ⁻² s ⁻¹]	(10)
0202060201	12/31/2004	33.8	32.9 / 32.9 / 28.3	LW	t	0.61±0.02 / 1.96±0.03	-12.89	-11.93	Dec. 2004
0556230701	06/15/2008	31.4	3.7 / 3.5 / 2.7	FF	m	0.91±0.05 / 3.31±0.02	-12.57	-11.76	Jun. 2008
0556231201	12/13/2008	11.9	4.9 / 4.7 / 3.4	FF	m	1.68±0.06 / 5.73±0.02	-12.31	-11.60	Dec. 2008
0606150101	06/21/2009	134.3	85.4 / 89.2 / 91.2	FF	m	0.57±0.01 / 1.96±0.02	-12.81	-11.99	2009 Long Look

Notes: Col.(1): Observation ID; Col.(2): Date of observation; Col.(3): Nominal duration of the observation; Col.(4): Net exposure time for each instrument after the background flaring filtering was applied; Col.(5): Observing Mode, LW= Large Window, FF=Full Frame; Col.(6): Optical Filter applied, t=thin, m=medium; Col.(7): Net count-rate in the 0.2-10 keV and 0.3-8 keV range for the EPIC-pn and EPIC-MOS instruments, respectively, after the local background subtraction; Col.(8): Observed EPIC-pn flux in the 0.2-2 keV band; Col.(9): Observed EPIC-pn flux in the 2-10 keV band; Col.(10): Epoch name as used in the text.

Table 5.3. Average pn spectra of PG 1126-041 reproduced by the baseline model.

Epoch	Γ (1)	N_1 keV [10^{-4} ph s $^{-1}$ keV $^{-1}$ cm $^{-2}$] (2)	$N_{m.i.}$ [10^{22} cm $^{-2}$] (3)	$\log \xi_{m.i.}$ [erg cm s $^{-1}$] (4)	$N_{h.i.}$ [10^{22} cm $^{-2}$] (5)	$\log \xi_{h.i.}$ [erg cm s $^{-1}$] (6)	v_{out} [c] (7)	χ^2/ν (8)
Dec. 2004	$1.82^{+0.02}_{-0.03}$	$6.1^{+20.2}_{-0.1}$	$8.5^{+0.2}_{-0.2}$	$1.52^{+0.01}_{-0.01}$	30^{+15}_{-11}	$3.36^{+0.10}_{-0.12}$	$0.025^{+0.011}_{-0.017}$	570/510
Jun. 2008	$1.88^{+0.03}_{-0.02}$	$10.1^{+0.5}_{-0.4}$	$7.6^{+0.7}_{-0.8}$	$1.59^{+0.02}_{-0.02}$	21^{+20}_{-15}	$3.02^{+0.06}_{-0.16}$	< 0.09	
Dec. 2008	$2.05^{+0.04}_{-0.03}$	$16.4^{+31.2}_{-0.5}$	$4.6^{+0.2}_{-0.2}$	$1.52^{+0.01}_{-0.01}$	(...)	(...)	(...)	
2009 Long Look	$1.76^{+0.01}_{-0.01}$	$7.7^{+0.1}_{-0.1}$	$8.7^{+0.1}_{-0.1}$	$1.541^{+0.005}_{-0.003}$	$97.4^{+2.0}_{-7.3}$	$3.63^{+0.02}_{-0.03}$	$0.054^{+0.007}_{-0.005}$	880/545

Notes: Col.(1): Photon Index; Col.(2): Power law normalization at 1 keV; Col.(3): Moderately ionized absorber column density; Col.(4): Moderately ionized absorber ionization parameter; Col.(5): Highly ionized outflowing absorber column density; Col.(6): Highly ionized outflowing absorber ionization parameter; Col.(7): Highly ionized outflowing absorber velocity blueshift; Col.(8) chi square over degrees of freedom. The first line refers to the fit of the 2009 Long Look data, while the other three lines refer to the joint fit of the Dec. 2008, Jun. 2008, and Dec. 2004 data.

Table 5.4. Spectral analysis on the average spectra of PG 1126-041: best fit model.

Epoch	Continuum	Soft Band			M.I.	H.I.	iron K band		Fit Statistics
	Γ	Γ^{soft}	E_1	E_2	$N_{m.i.}$	$N_{h.i.}$	E_{broad}	E_{narrow}	χ^2/ν
	$N_{1\text{keV}}$	$N_{1\text{keV}}^{\text{soft}}$	EW ₁	EW ₂	$\log \xi_{m.i.}$	$\log \xi_{h.i.}$	σ_{broad}	EW _{narrow}	
Dec. 2004	$1.93^{+0.11}_{-0.04}$	$3.01^{+0.09}_{-0.23}$	$0.553^{+0.003}_{-0.001}$	$0.90^{+0.03}_{-0.04}$	$7.6^{+0.2}_{-0.08}$	30^{+15}_{-11}	(...)	(...)	498/504
	$9.5^{+5.1}_{-1.5}$	$0.17^{+0.2}_{-0.1}$	43^{+11}_{-9}	60^{+18}_{-22}	$1.517^{+0.004}_{-0.015}$	$3.36^{+0.10}_{-0.12}$ $0.025^{+0.011}_{-0.017}$	(...)	< 79	
Jun. 2008	$1.91^{+0.08}_{-0.02}$	$\equiv 3.01$	$\equiv 0.553$	$\equiv 0.90$	$5.3^{+0.6}_{-0.6}$	21^{+20}_{-15}	(...)	(...)	
	$12.0^{+6.2}_{-0.9}$	0.17	20^{+5}_{-5}	36^{+11}_{-13}	$1.52^{+0.03}_{-0.04}$	$3.02^{+0.06}_{-0.16}$ < 0.09	(...)	< 180	
Dec. 2008	$2.07^{+0.03}_{-0.02}$	$\equiv 3.01$	$\equiv 0.553$	$\equiv 0.90$	$3.9^{+0.2}_{-0.2}$	(...)	(...)	(...)	
	$16.1^{+9.1}_{-0.7}$	0.17	11^{+2}_{-3}	31^{+9}_{-11}	$1.52^{+0.02}_{-0.02}$	(...)	(...)	< 66	
2009 Long Look	$2.06^{+0.01}_{-0.01}$	$2.96^{+0.05}_{-0.05}$	$0.558^{+0.002}_{-0.007}$	$0.91^{+0.01}_{-0.01}$	$7.47^{+0.07}_{-0.23}$	$97.3^{+0.5}_{-0.6}$	$5.25^{+0.12}_{-0.09}$	$6.45^{+0.03}_{-0.02}$	539/524
	$10.5^{+0.3}_{-0.5}$	$0.21^{+0.7}_{-0.6}$	33^{+5}_{-4}	43^{+10}_{-10}	$1.519^{+0.005}_{-0.004}$	$3.68^{+0.05}_{-0.07}$ $0.056^{+0.004}_{-0.006}$	1160^{+135}_{-244} 1100^{+96}_{-90}	51^{+20}_{-17}	

Notes: The first three lines refer to the joint fit to the Dec. 2004, Jun. 2008, and Dec. 2008 data, while the fourth line refers to the fit to the 2009 Long Look data. The best fit model is the following: a power law continuum emission ($\Gamma, N_{1\text{keV}}$) absorbed by both a moderately (m.i.) and a highly (h.i.) ionized absorber; a soft unabsorbed power law ($\Gamma^{\text{soft}}, N_{1\text{keV}}^{\text{soft}}$); two soft Gaussian emission lines (E_1, EW_1, E_2, EW_2); a broad ($E_{broad}, \sigma_{broad}, EW_{broad}$) and a narrow (E_{narrow}, EW_{narrow}) Gaussian emission line in the iron K band; In Xspec terminology: `wabs*(zpowerlaw + zgauss + zgauss + XSTAR(M.I)*XSTAR(H.I.)*(zpowerlaw + zgauss + zgauss))`. Units are the following: [10^{-4} ph s $^{-1}$ keV $^{-1}$ cm $^{-2}$] for the power law normalizations; [keV] for the Gaussian emission lines centroid energies; [eV] for the Gaussian emission lines widths and equivalent widths; [10^{22} cm $^{-2}$] for the column densities; [erg cm s $^{-1}$] for the ionization parameters. Errors are at 1σ confidence level. Parameters without errors have been kept fixed between the different epochs; (...) means a lack of detection.

Table 5.5. 2009 Long Look observation time slices over which time resolved analysis was performed.

Interval	Exposure	Count-rate
1	21.1	0.180 ± 0.003
2	30.0	0.156 ± 0.003
3	5.4	0.212 ± 0.007
4	7.5	0.195 ± 0.005
5	4.6	0.215 ± 0.007
6	5.4	0.194 ± 0.006
7	7.7	0.338 ± 0.007
8	9.2	0.245 ± 0.006

Notes: Col.(1): Time interval as marked in Fig. 5.2; Col.(2): Exposure time in ks; Col.(3): count rate in ct s^{-1} .

Table 5.6. PG 1126-041: time resolved spectral analysis of the 2009 Long Look pn observation

Interval (1)	Γ (2)	$N_{1,\text{keV}}$ (3)	$N_{m.i.}$ (4)	$\log \xi_{m.i.}$ (5)	E_{broad} (6)	σ_{broad} (7)	N_{broad} (8)	E_{narrow} (9)	N_{narrow} (10)	E_{abs} (11)	σ_{abs} (12)	EW_{abs} (13)
1		$4.79^{+0.27}_{-0.32}$										-150^{+96}_{-94}
2		$3.75^{+0.21}_{-0.28}$										> -105
3+5	$1.93^{+0.02}_{-0.03}$	$6.51^{+0.39}_{-0.52}$	$7.4^{+0.4}_{-0.1}$	$1.49^{+0.02}_{-0.16}$	$5.55^{+0.18}_{-0.25}$	852^{+211}_{-160}	$12.2^{+3.2}_{-2.0}$	$6.44^{+0.06}_{-0.05}$	$1.6^{+0.8}_{-0.5}$	$7.21^{+0.10}_{-0.09}$	257^{+90}_{-70}	> -250
4+6		$5.37^{+0.31}_{-0.41}$										> -170
7		$12.27^{+0.65}_{-0.80}$										-372^{+91}_{-91}
8		$7.91^{+0.46}_{-0.55}$										-349^{+105}_{-106}

Notes: Col.(1): time interval over which spectral analysis was performed; Col.(2): power law photon index; Col.(3): power law normalization at 1 keV, in units of 10^{-4} ph s $^{-1}$ keV $^{-1}$ cm $^{-2}$; Col.(4): moderately ionized absorber column density, in units of 10^{22} cm $^{-2}$; Col.(5): moderately ionized absorber ionization parameter, in erg cm s $^{-1}$; Col.(6): broad Gaussian emission line centroid energy, in keV; Col.(7): broad Gaussian emission line width, in eV; Col.(8): broad Gaussian emission line normalization, in units of 10^{-6} ph cm $^{-2}$ s $^{-1}$; Col.(9) narrow Gaussian emission line centroid energy, in keV; Col.(10): narrow Gaussian emission line normalization, in units of 10^{-6} ph cm $^{-2}$ s $^{-1}$; Col.(11) Gaussian absorption line centroid energy, in keV; Col.(12): Gaussian absorption line width, in eV; Col.(13): Gaussian absorption line equivalent width, in eV. Errors are at 1σ confidence level. The model also includes the constant soft spectral components as found in the 2009 Long Look average spectral analysis.

Table 5.7. PG 1126-041: optical photometry

Epoch (1)	V (2)	U (3)	UVW1 (4)	UVM2 (5)	UVW2 (6)	M(2500) (7)
Dec. 2004	14.71±0.01	14.09±0.01	13.87±0.01	14.13±0.02	14.01±0.04	13.60
Jun. 2008	(...)	(...)	13.71±0.01	13.92±0.01	(...)	13.42
Dec. 2008	(...)	(...)	13.82±0.01	13.86±0.02	(...)	13.46
2009 Long Look	(...)	(...)	13.564±0.004	13.656±0.008	13.72±0.02	13.22

Notes: The magnitudes measured in each filter are not corrected for the Galactic extinction, while the extrapolated M(2500) magnitude at 2500 Å is corrected for the Galactic extinction.

Table 5.8. PG 1126-041: optical/X-ray photometry

Epoch (1)	$\log f_{2500}$ (2)	$\log f_{2keV}$ (3)	$\log L_{2500}$ (4)	$\log L_{2keV}$ (5)	α_{ox} (6)	$\Delta\alpha_{ox}$ (7)	$\log L_{2keV}^{corr}$ (8)	α_{ox}^{corr} (9)	$\Delta\alpha_{ox}^{corr}$ (10)
Dec. 2004	-25.46	-30.46	29.49	24.49	-1.92	-0.52	25.28	-1.68	-0.28
Jun. 2008	-25.39	-30.17	29.56	24.77	-1.84	-0.43	25.31	-1.63	-0.22
Dec. 2008	-25.40	-29.80	29.55	25.15	-1.69	-0.28	25.57	-1.53	-0.12
2009 Long Look	-25.30	-30.46	29.64	24.49	-1.98	-0.56	25.26	-1.62	-0.20

Notes: Col.(1): Epoch of observation. Col.(2): 2500 Å rest frame flux density corrected for Galactic extinction, in $\text{erg s}^{-1} \text{cm}^{-2} \text{Hz}^{-1}$. Col.(3): 2 keV rest frame flux density corrected for Galactic absorption, in $\text{erg s}^{-1} \text{cm}^{-2} \text{Hz}^{-1}$. Col.(4): 2500 Å rest frame luminosity density corrected for Galactic extinction, in $\text{erg s}^{-1} \text{Hz}^{-1}$. Col.(5): 2 keV rest frame luminosity density corrected for Galactic absorption, in $\text{erg s}^{-1} \text{Hz}^{-1}$. Col.(6): Observed optical-to-X-ray spectral index. Col.(7): Difference between the observed α_{ox} and the one expected on the basis of the L_{2500} luminosity (from Steffen et al. 2006). Col.(8): 2 keV rest frame luminosity density corrected for Galactic and intrinsic absorption, in $\text{erg s}^{-1} \text{Hz}^{-1}$. Col.(9): Optical-to-X-ray spectral index corrected for the intrinsic X-ray absorption. Col.(10): Difference between the corrected α_{ox}^{corr} and the one expected on the basis of the L_{2500} luminosity.

Chapter 6

Serendipitous studies

In this Chapter I will introduce two recent studies that have a taste of serendipity: the X-ray observations of the first NAL QSO sample, and the review of the X-ray properties of the X-ray BALs of APM 08279+5255. More details about these works can be found in Chartas et al. (2009a) and Chartas et al. (2009c), respectively.

6.1 X-ray observations of high-velocity NAL QSOs

The first NAL QSO sample ever has been given by Misawa et al. (2007a), where the authors serendipitously detected a number of intrinsic, high velocity UV NALs in a sample of $z \sim 2 - 4$ QSOs observed with the Keck/HIRES spectrograph in the context of another scientific project, the study of the metal abundances in the Ly α forest. Thanks to the excellent S/N ratio and spectral resolution, the authors were able to use the partial covering diagnostic to distinguish intrinsic NAL systems from cosmologically intervening ones. They estimated an intrinsic fraction of $\sim 50\%$ for NAL QSOs, meaning that a half of the QSO population hosts at least one intrinsic NAL system, regardless of its v_{out} . The authors also demonstrated how about 10-17% of the systems that are usually classified as intervening systems are actually high-velocity NALs intrinsic to the QSO.

The first X-ray look at this NAL QSO sample has been given by Misawa et al. (2008) using Chandra and XMM-Newton archival observations of four NAL QSOs. In Chartas et al. (2009a), we presented the results of new XMM-Newton and Suzaku pointed observations of NAL QSOs as well as the reanalysis of the Misawa et al. (2008) NAL QSOs, for a total of 16 sources at $2.2 \lesssim z \lesssim 3$. Being discovered serendipitously, the sources are unbiased with respect to the UV NAL properties; however, there is a possible X-ray

bias in that we only selected the sources bright enough to obtain a moderate S/N ratio with reasonable XMM-Newton or Suzaku exposure times. X-ray spectral analysis was performed by fitting two simple models to the spectra: a power law, and a power law plus a neutral intrinsic absorber. Only 2/12 NAL QSOs show the presence (at $\sim 90\%$ confidence level) of cold absorption in excess to the Galactic one, with column densities of a few 10^{22} cm^{-2} ; all the other sources appear X-ray unabsorbed. This is similar to what was found for the SDSS/2XMM BAL QSOs studied in Chapter 3. The S/N ratio of the X-ray observations of the two samples is similar, and in both cases more complex models such as ionized or partial covering absorption could not be tested.

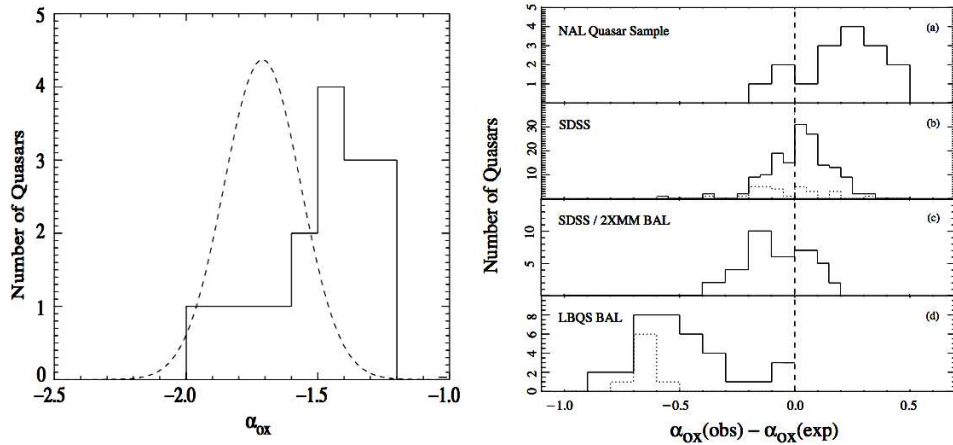


Figure 6.1. Left panel: histogram of the measured α_{ox} for the NAL QSO sample of Chartas et al. (2009a), compared with the α_{ox} distribution for type 1 RQ SDSS QSOs taken from Steffen et al. (2006). Right panel: measured $\Delta\alpha_{\text{ox}}$ distribution for different samples of QSOs, from top to bottom: the NAL QSO sample of Chartas et al. (2009a); the (UV unabsorbed) type 1 RQ SDSS QSOs taken from Steffen et al. (2006); the SDSS/2XMM BAL QSOs taken from Giustini et al. (2008); and the LBQS BAL QSO sample taken from Gallagher et al. (2006).

Optical/X-ray photometry was also performed, in order to compare the NAL QSOs properties with those of BAL and mini-BAL QSOs. Given the known $\alpha_{\text{ox}} - \ell_{UV}$ correlation (e.g. Vignali et al. 2003; Steffen et al. 2006), also the $\Delta\alpha_{\text{ox}} \equiv \alpha_{\text{ox}} - \alpha_{\text{ox}}(\ell_{UV})$ quantity was computed to rescale for the intrinsic UV luminosity. The histogram of the measured α_{ox} distribution is plotted in the left panel of Fig. 6.1, together with the α_{ox} distribution of RQ type 1 SDSS AGN with the same ℓ_{UV} as the NAL QSOs of this study (dashed line). The offset between the two distributions is evident, with the NAL QSOs being shifted toward less negative α_{ox} values. The right panel of Fig. 6.1 reports the histogram of the $\Delta\alpha_{\text{ox}}$ distribution for the NAL QSOs sample (panel a) compared with the SDSS QSOs (panel b,

taken from Steffen et al. 2006), the SDSS/2XMM BAL QSOs (panel c, taken from Giustini et al. 2008, , see Chapter 3 of this Thesis), and the LBQS BAL QSOs (panel d, taken from Gallagher et al. 2006). As it can be seen, the $\Delta\alpha_{\text{ox}}$ is different between each sample, but nonetheless it follows a smooth trend of increasing X-ray weakness going from NAL QSOs, to SDSS QSOs, to SDSS/2XMM BAL QSOs, to LBQS BAL QSOs. Furthermore, as found for the SDSS/2XMM BAL QSOs, there is no hint of correlation between the maximum outflow velocity and the X-ray weakness expressed by $\Delta\alpha_{\text{ox}}$, as opposite as found in the LBQS BAL QSOs. A more comprehensive study of the connections between NAL and BAL QSOs, and their implications for AGN physics, is ongoing and will not be complete until more intrinsic high velocity NAL systems will be identified.

6.2 The X-ray BALs of APM 08279+5255

In Chartas et al. (2009c) the comprehensive set of *Chandra* and *XMM-Newton* observations of the BAL QSO APM 08279+5255 was reviewed and thoroughly analyzed.

The source is very distant, with a redshift $z = 3.91$; however, thanks to the magnification provided by gravitational lensing, the flux is greatly increased and to date, these are the highest signal-to-noise ratio X-ray data of any BAL QSO. Significant X-ray iron BALs were detected in each observation, with varying outflow velocities and absorption trough depths (see Fig. 6.2). If associated with Fe XXV resonance absorption, the X-ray

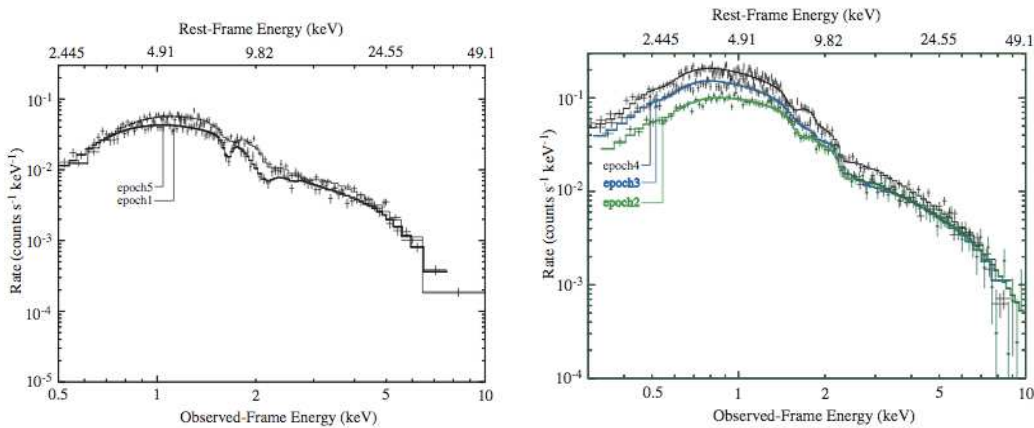


Figure 6.2. Left Panel: *Chandra* spectra of APM 08279+5255; right panel: *XMM-Newton* spectra of APM 08279+5255. The best fit model (solid thick line) is a power law absorbed by neutral gas at the source, plus two broad, blueshifted absorption lines in the iron K band with variable depth and velocity shift between the different observations.

BALs imply an outflow of matter with velocities up to $0.7c$. Such a high terminal velocity strongly points to a launching radius for the wind very close (a few tens of r_g) to the SMBH. The kinetic efficiency associated to this outflow is capable of providing effective feedback between the central SMBH and its environment. At the same time, the variable parameters of the X-ray BALs suggests a variable energy injection into the surrounding media. The shortest continuum time scale variability detected implies an X-ray source size of about $\sim 10r_g$,

While collecting the APM wind physical parameters observed during the different epochs of monitoring, and with different instruments, a serendipitous correlation was found between the measured photon index Γ and the maximum terminal velocity of the wind v_{out} , see Fig. 6.3. Such a correlation gives precious insights onto the physical mechanism responsible for the APM 08279+5255 wind: it is qualitatively expected in the case of a radiation-driven wind, where the radiation driving the flow is this time mostly in the X-rays and for flatter Γ , the high number of hard X-ray photons could overionize the gas and making it lose acceleration. This intriguing correlation would fit in the scenario sketched in the right panel of Fig. 6.3, where the X-ray and UV observations probe different line of sight toward the AGN, and different wind components. The UV-absorbing wind is launched at large radii by the accretion disk radiation pressure, while the X-ray absorbing wind is much more compact, and is accelerated by the X-ray corona itself. The same phenomenological scenario would fit into the X-ray observations of NAL and mini-BAL QSOs, that

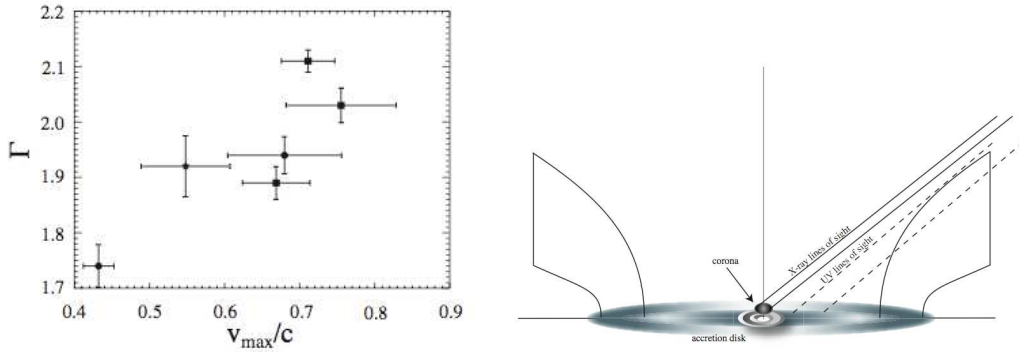


Figure 6.3. Left panel: $\Gamma - v_{out}$ correlation for the X-ray BALs of APM 08279+5255, from Chartas et al. (2009c); right panel: a sketch of a possible geometry for accretion disk winds that can explain the X-ray BALs of APM 08279+5255, from (Chartas et al. 2009a).

Chapter 7

Theoretical considerations

As introduced in Section 2.3, two main mechanisms associated to the accretion disk are able to launch winds as powerful as those observed in absorption against the UV and X-ray continua of some AGN: radiation and magnetic pressure. In fact, the thermal pressure from the heated disk atmosphere is able to launch and accelerate winds only at large distance from the central SMBH. Given the scaling between the launching radius and the terminal velocity of disk winds, this means that the thermal mechanism can account only for low to moderate velocity winds such as the X-ray warm absorber or the UV low-velocity NALs. Radiation pressure from highly accreting accretion disks has been demonstrated to be able to launch powerful winds, with the maximum force due to the opacity in the UV resonance lines (e.g., Murray et al. 1995; Proga & Kallman 2004). *Conditio sine qua non* for a steady line-driven accretion disk wind to exist in AGN is a tuning between the UV flux coming from the disk, and the X-ray flux coming from the hot corona. The former is responsible for the launch and the acceleration of the UV absorbing wind; in order to be efficiently accelerated, the wind material must not be too overionized, meaning that the opacity in the UV lines must be high in order for an efficient wind to be launched. But AGN emit a lot of X-rays as well, and these energetic photons will strip electrons from the wind gas, so decreasing the opacity in the UV resonance lines, so decreasing the acceleration force on the gas. Thus, for radiation pressure on the UV resonant absorption lines to be able to launch a powerful accretion disk wind, the X-ray/UV flux ratio should be small, or the X-rays should be absorbed by a screen of highly dense gas that can shield the UV absorbing wind. If the X-ray photons dominate, the wind will not be able to escape the system and will fall back on the accretion disk surface, forming a failed wind (e.g., Proga 2005). On the other hand, for magnetic launching and driving of powerful

accretion disk winds there is no need for an X-ray shield, nor for a low X-ray/UV flux ratios. However, these are still necessary to produce the right ionization state of the wind as is observed in both the UV and the X-ray band (e.g., Everett 2005). Radiation

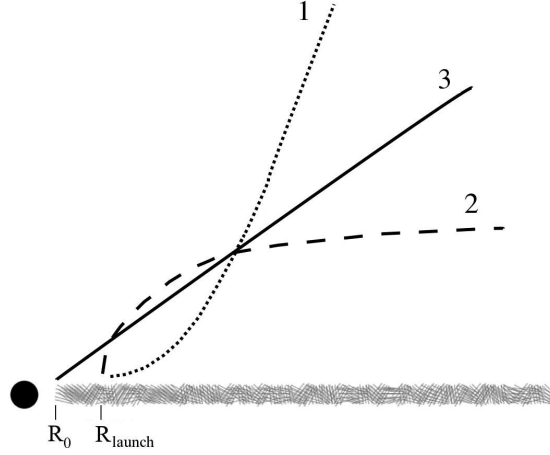


Figure 7.1. The three “typical” streamlines for accretion disk winds. Number 1: MHD-typical, polar and convex streamline. Number 2: LD-typical, equatorial and concave streamline. Number 3: a radial streamline typical of spherically symmetric winds. R_0 marks the inner radius of the accretion disk; R_{launch} the wind launching radius.

driven and magnetically driven accretion disk winds differ for the geometry of the flow, as sketched in Fig. 7.1. Radiation line-driven disk winds are typically equatorial, with concave streamlines, while magnetically driven disk winds show a polar geometry, with convex streamlines. Another difference between the two scenarios is the terminal velocity of the wind. Magnetically driven disk winds generically have no limits in how fast the wind can be accelerated (the only limit being of course the speed of light), depending on the launching radius and on the magnetic field configuration. For radiation driven winds, the terminal velocity v_{out} of the wind launched at R_{launch} is proportional to the escape velocity at that radius. In particular, for LD winds launched by Keplerian disks, it is found that $v_{out} \sim 3v_{esc}(R_{launch})$ (Castor et al. 1975; Groenewegen et al. 1989; Proga 1999).

Understanding what is the physical mechanism responsible for launching and accelerating AGN accretion disk winds is not just an academic exercise: the wind duty cycle, mass outflow rate, and kinetic efficiency all strongly depend on the wind geometry and dynamics. Theories and observations of accretion disk winds in AGN must go together if we want to arrive to have a thorough understanding of this phenomenon and of its impact

on the surrounding media. The study of radiation driven accretion disk wind is nowadays starting to be mature, and provides predictions that can be tested against the observations (e.g., UV and X-ray absorption/emission line profiles, dynamical constraints, see Proga & Kallman 2004; Sim et al. 2010b). The magnetically driven accretion disk wind predictions are instead still generic (e.g., kinematical or ionization state constraints, Fukumura et al. 2010a,b). For this reason, constraining the mechanism at work in AGN accretion disk winds is not yet directly possible, and magnetic driving is deduced by exclusion when radiation driving is not able to explain the observations. In the following, I will illustrate first a tentative of falsification of the LD mechanism for AGN accretion disk winds, and second some consequences of breaking down the assumption of spherical symmetry when interpreting observational signatures of accretion disk winds.

A tentative falsification of the LD scenario

As an example, one can try to falsify the LD wind scenarios by asking: “Can a LD wind launched from a standard Shakura-Sunyaev accretion disk account for the highest terminal velocities observed in BAL QSOs?” If the answer is no, then the LD scenario would be falsified and one would be left only with the magnetic mechanism to explain the most powerful disk winds. The highest known terminal velocities are observed in the X-ray BALs of the BAL QSO APM 08279+5255 (v_{out} up to $0.7c$, see Section 6.2). A physical constrain for a UV line-driven accretion disk wind is given by the temperature of the accretion disk surface, that depends on the M_{BH} and on $\lambda \equiv \dot{M}_{acc}/\dot{M}_{Edd}$. If the temperature exceeds some value, say $T \sim 50\,000$ K, the gas will exit from the UV regime to enter in the X-ray one, and thus will lose acceleration, will fail and fall back to the disk. Figure 7.2 answers the question above. In the left panel, the temperature of a standard Shakura-Sunyaev accretion disk as a function of radius is plotted for a $M_{BH} = 10^8 M_{\odot}$, for different Eddington ratio regimes. In the right panel, the radius at which the temperature reaches 50 000 K (and thus escapes from the UV regime) is plotted as a function of the M_{BH} , for different Eddington ratios. The radial coordinate is normalized to the inner radius of the disk. A non-rotating SMBH was considered, so that $R_0 = 6r_g$. Taking a fiducial AGN with $M_{BH} = 10^8 M_{\odot}$, $\lambda = 0.5$ (i.e. as in the model of Proga & Kallman 2004), one can see that at radii $R \gtrsim 7R_0$ the temperature of the disk atmosphere is still $T(R) \lesssim 50\,000$ K, so that in principle the gas is still in the UV regime. A wind launched at

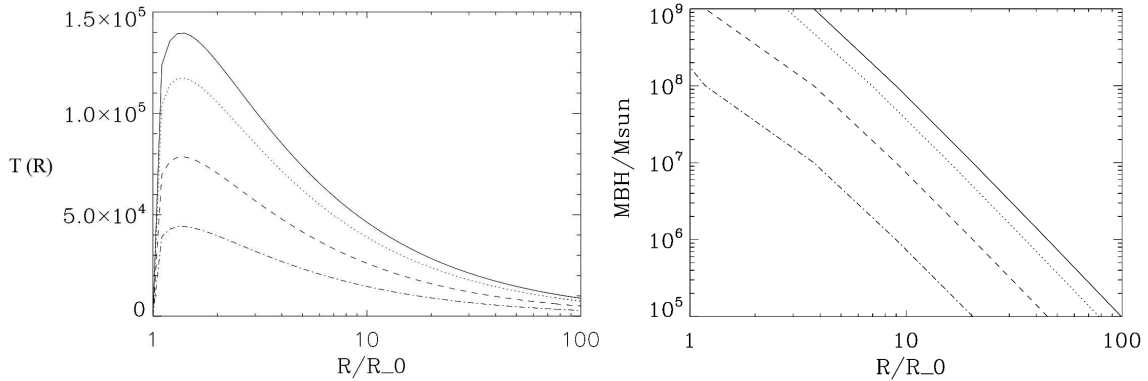


Figure 7.2. Left: accretion disk surface temperature $T(R)$ for a black hole with $M_{BH} = 10^8 M_\odot$, at different accretion rates: $\lambda = 1$ (solid), 0.5 (dotted), 0.1 (dashed), and 0.01 (dashed-dotted line). Right: radius at which $T(R) = 50\,000$ K as a function of the central M_{BH} , for different accretion rates where the lines are coded as in the left panel. In both panels, the radius is normalized to the inner disk radius R_0 , that is assumed to be $6r_g$.

$R_{launch} \sim 7R_0$ would have a terminal velocity $v_{out} \sim 3 v_{esc}(R_{launch}) \sim 0.65 c$, that is much higher than what is usually observed in BAL QSOs. The fiducial AGN case is conservative with respect to the APM 08279+5255 case study. The latter AGN has indeed a higher black hole mass $> 10^9 M_\odot$, so that the gas would be in the UV regime still at $\lesssim 4R_0$ even with a $\lambda = 1$. Rescaling for the APM 08279+5255 case, a wind launched at $R_{launch} \sim 4R_0$ would have a terminal velocity $v_{out} \sim 0.86 c$, higher than the maximum velocity observed in this BAL QSO. Thus, the LD accretion disk wind scenario can in principle work well in reproducing the whole range of terminal velocities that has been observed to date in absorption against the UV and X-ray continua of AGN. However, to see whether the LD or the magnetically driven model are truly compatible with the observations, the appropriate ionization parameter of the wind should be computed to check whether it is compatible with the highly ionized iron as detected in APM 08279+5255.

Breaking down the assumption of spherical symmetry

The main observables of spectral absorption lines are the shape of the profile, the ionization state of the species responsible for absorption, the optical depth, the velocity shift with respect to the systemic frame of the continuum source, the covering fraction. These are simple quantities by definition, but very hard to measure in AGN, requiring modern instruments with both a big sensitivity and a high spectral resolution, and a lot of observing time and efforts in the data reduction and analysis. As a matter of fact, UV and X-ray

observers are forced to make strong assumptions when interpreting the data relative to spectral absorption lines, and they usually adopt the simplest possible scenario, that is a spherically symmetric, continuous, homogeneous, and isotropic flow at constant velocity, then adopting some corrective factor to try to account for the actual departure from the simple, approximate case. How reliable are observer's estimates of wind properties, when based on the spherical symmetry assumption? What are the implications of spherical or non-spherical geometry assumptions when deriving physical quantities related to AGN outflows?

To give a first taste of the answer to this question, I will illustrate the case of absorption line profiles studies, generated using one snapshot in time, corresponding to a stationary flow state, of the velocity and density profiles as given by the LD accretion disk wind of Proga & Kallman (2004) and illustrated in Fig. 7.3. In each panel, the accretion disk rotational axis coincides with the z-axis, the plane of the accretion disk is in the (x,y) plane, and symmetry around the z-axis is assumed. The X-ray continuum source lies at the origin; the radial distance is normalized to $r_* = R_0$ that is the disk inner radius, assumed to be $6r_g$, and the computational domain spans the $10R_0 \leq R \leq 500R_0$. Only the radial component of the wind velocity field will be considered: this is equivalent to assuming a continuum point source, so that only proper lines of sight (instead than cylinders of sight) effects are treated. This kind of approach is mostly viable for analyzing e.g. the X-ray properties of AGN winds, because of the compactness of the X-ray source continuum. Having the density $\rho(r)$ and the radial velocity $v_r(r)$ for each point of the computational domain of the Proga & Kallman (2004) model, synthetic line profiles corresponding to different line of sight inclination angles can be computed with the following procedure. Resonance points along the flow are searched for, using the resonance condition

$$\frac{(\nu - \nu_o)}{\nu_o} = \frac{v_r}{c}$$

where ν_o is the continuum frequency, ν is the Doppler shifted flow frequency, and v_r is the velocity along the line of sight with respect to the continuum. The Sobolev approximation (Sobolev 1960) is then used to compute the total optical depth τ_ν at each resonance point in the flow,

$$\tau_\nu \propto \frac{\rho(r)}{|dv_r(r)/dr|}$$

where $dv_r(r)/dr$ is the radial velocity gradient. The resulting optical depth is then applied

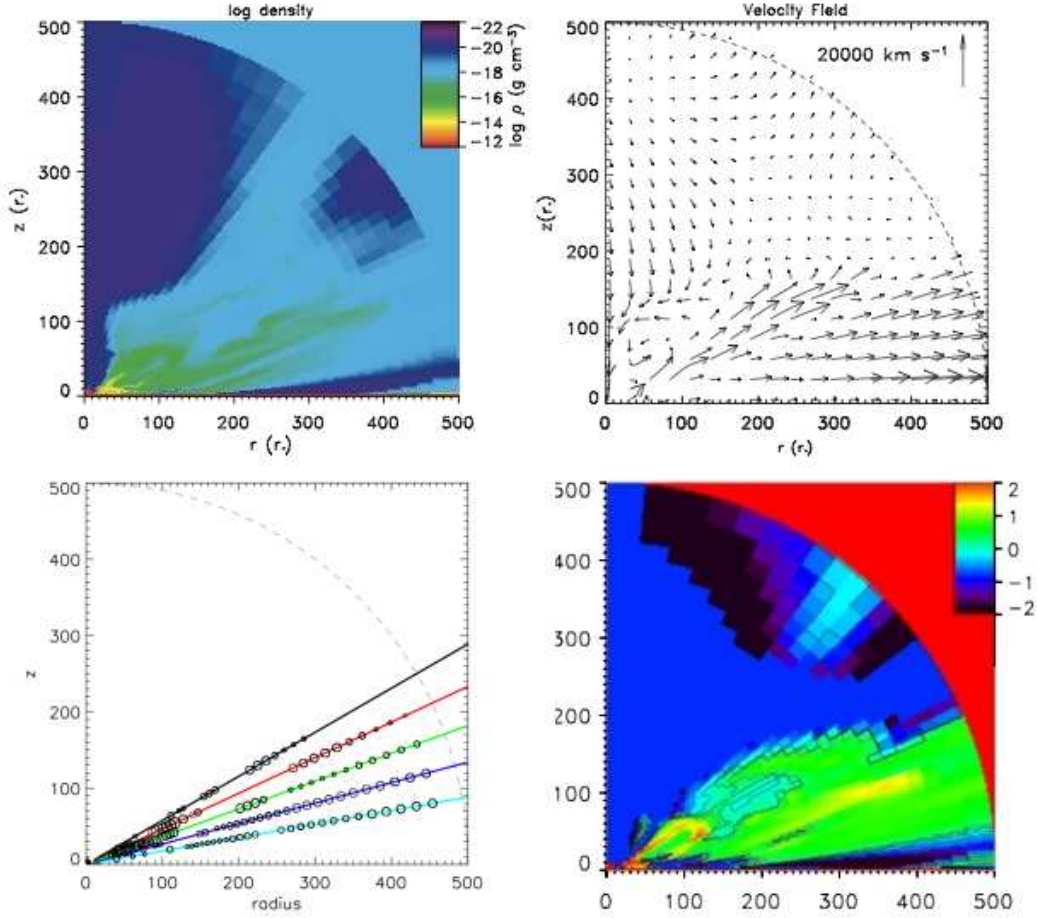


Figure 7.3. Representative profiles of interesting physical parameters of a LD accretion disk wind taken from the Proga & Kallman (2004) 2D model, see text for details. From top left, in clockwise direction: (a) map of the density distribution; (b) map of the poloidal velocity distribution; (c) the location of the resonance points along the flow for five different inclination angles, with the blueshift velocity proportional to the size of the empty circles; (d) map of $\log \dot{M}_{out}^{sph} / \dot{M}_{out}$, where \dot{M}_{out}^{sph} is the mass loss rate computed assuming spherical symmetry, \dot{M}_{out} is the actual disk wind mass loss rate.

to the intrinsic continuum,

$$I = I_o e^{-\tau_\nu}$$

assumed to be a flat power law. Resulting synthetic line profiles are shown in the top panel of Fig. 7.4 for five different line of sight inclination angles θ measured from the polar axis, $\theta = 60, 65, 70, 75, 80$ deg for the black, red, green, blue, and light blue lines respectively. The bottom panels of Fig. 7.4 show instead the velocity, optical depth, and density radial profiles for the same five line of sight inclination angles as above. The density

and optical depth have been normalized because at this point what is interesting is the relative contribution of the different parts of the flow and not their absolute magnitude, this latter being strongly dependent on the actual details of the AGN system such as the M_{BH} and λ . For the same reason, the optical depth at each inclination angle has been normalized in order to have each profile reaching the zero flux level, so that each profile shape is well visible. What is immediately clear from the bottom panels of Fig. 7.4 is the departure from the spherical symmetry in the case of a LD accretion disk wind: both the radial velocity and the density are not monotonic. Interesting physical insights can be obtained when looking at the 65 and 70 deg line of sight, that is, the red and green lines in bottom left panel of Fig. 7.3, and in Fig. 7.4. These two inclination angles roughly correspond to the beginning of the transitional zone of the flow as described by Proga & Kallman (2004), and to the beginning of the fast stream zone, respectively. Observationally, the 65 deg red spectral line profile shows much more blueshifted absorption than the 70 deg green profile (Fig. 7.4, top panel). However, when looking at the bottom left panel of Fig. 7.3 and at the radial velocity plot in Fig. 7.4, it can be seen that the absorption at high velocity for the 65 deg line of sight happens close to the origin ($R \lesssim 150R_0$), where the dynamical instabilities of the transitional zone of the wind are maximum. At larger radii along the 65 deg line of sight, the radial velocity decreases: the deep absorption signature at $v_{out} \sim 2 \times 10^9 \text{ cm s}^{-1}$ is due to a portion of the wind (a puff) that will shortly fall back toward the disk plane. On the other hand, for the 70 deg line of sight the maximum of the absorption reaches much lower velocities, and shapes a broad deep trough at $2 \times 10^8 \lesssim v_{out} \lesssim 10^9 \text{ cm s}^{-1}$. One can see that most of this absorption happens at large radii, $R \gtrsim 300R_0$, and that this portion of the wind is effectively accelerated outside the computational domain. Among the five considered line of sight for this particular model, only the largest inclination angles (70, 75, and 80 deg) track portions of the flow that will successfully escape the system, albeit they show the less blueshifted absorption profiles (Fig. 7.4). All these considerations can be also visualized in the bottom right panel of Fig. 7.3, that reports the map of the logarithmic ratio between the mass loss rate computed under the spherical symmetric assumption and the actual mass loss rate. The strong blueshifted absorption seen along the $\theta = 65$ deg line of sight corresponds to the structure close to the origin, where the mass loss rate estimated under spherical symmetry is maximally overestimated (up to a factor of 100). Along the $\theta = 70$ deg line of sight the discrepancy between the two mass loss

rates is much smaller, up to an order of magnitude. This simple example illustrates how different (and sometimes counter-intuitively) behaves a realistic non-spherical wind from a simple, homogeneous spherical case. Moreover, a number of important effects have been neglected: one for all, the ionization state of the flow, that will significantly contribute to further complicate the appearance of absorption line profiles in realistic cases. The power of this kind of studies is notable, in that they can help to join the observational and theoretical efforts in understanding AGN accretion disk winds, that is probably the only way - or the quickest - to solve both the SMBH accretion/ejection connection, and the contribution to the cosmic feedback during the AGN phase. The space of parameters to be investigated is very large from both a theoretical and an observational point of view.

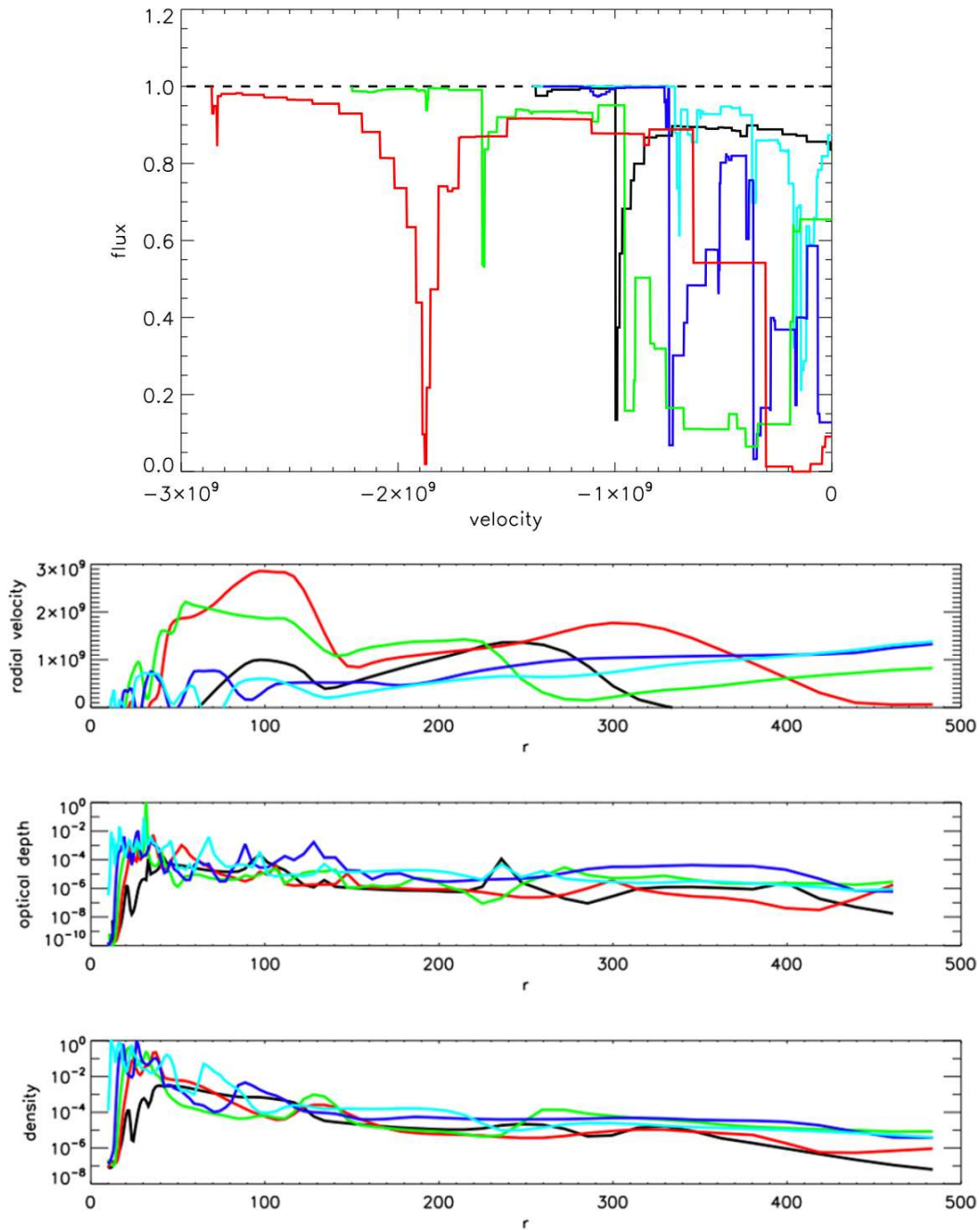


Figure 7.4. Top panel: blueshifted absorption line profiles computed for the LD accretion disk wind model of Proga & Kallman (2004) as seen by five different inclination angles, i , 60, 65, 70, 75, and 80 degrees from the disk rotational axis for the black, red, green, blue, and light blue, respectively; see text for details. Bottom panels: velocity, optical depth, and density radial profiles for the same inclination angles and the same color code as above.

Chapter 8

Summary of observational results and Conclusions

In the present Thesis the BAL, mini-BAL, and NAL phenomena have been thoroughly studied for the first time in the same context, the X-ray properties of AGN accretion disk winds. Even if data from several instruments have been analyzed and discussed, the vast majority of the present work is based on *XMM-Newton* observations.

The main observational results presented in this Thesis are the following:

- the paradigm of exclusively X-ray weak BAL QSOs has been questioned after the discovery of a significant population of X-ray bright BAL and mini-BAL QSOs (reported in Chapter 3 and in Giustini et al. 2008).
- X-ray bright BAL QSOs were generally found to be unabsorbed in X-rays, often with sensitive upper limits on the amount of intrinsic neutral absorption $N_H \lesssim 10^{21} \text{ cm}^{-2}$.
- the recognition of strong X-ray flux variability on both short and long time scales for some BAL and mini-BAL QSOs had as a consequence to make the X-ray weakness a transient characteristics for several of these sources (Chapter 4, 5, and Ballo et al. 2008, Giustini et al. 2011).
- NAL QSOs are found to be X-ray bright, regardless of the maximum outflow velocity observed (Chapter 6, and Chartas et al. 2009a).
- there is a smooth connection of UV/X-ray properties between BAL, mini-BAL, and NAL QSOs, with the X-ray weakness increasing with increasing the width of the UV

blueshifted absorption troughs. This suggests a common physical origin for these objects, and important geometrical effects.

- for the X-ray bright BAL and NAL QSOs, there is no correlation between the X-ray weakness and the terminal velocity of the UV wind (as found by Gallagher et al. 2006, for the LBQS BAL QSOs). However, for the X-ray bright BAL QSOs a correlation between the X-ray absorbing column density and the UV absorption index is found; a correlation between the X-ray power law photon index and the maximum velocity of the X-ray iron BALs of APM 08279+5255 is also found.
- when the X-ray S/N ratio was high enough, ionized absorbers were found to cover, either totally or partially, the X-ray continuum source (Chapter 4, 5, 6, and Giustini et al. 2011).
- no evidences were found for an intrinsic continuum different from that of type 1, RQ QSOs for neither BAL, mini-BAL, nor NAL QSOs.
- an X-ray UFO has been detected in the mini-BAL QSO PG 1126-041, with an observed maximum outflow velocity $\sim 3\times$ the UV mini-BAL outflow velocity.
- strong X-ray spectral variability on both short and long time scales is quite common among BAL and mini-BAL QSOs. The fact that ionized absorbers variations contribute to the observed spectral variability, suggests a spatial origin for the wind very close to the central SMBH.
- the temporally resolved X-ray spectral analysis field has been finally opened for BAL and mini-BAL QSOs. Studies of their variability on very short time scales are extremely promising tools to unveil the dynamics of the inner accretion/ejection flow in AGN.

The fact that the physical properties (e.g. the X-ray absorbing column density and the optical-to-X-ray spectral index) of NAL QSOs and mini-BAL QSOs are different, but smoothly connected, to those of BAL QSOs is consistent with a geometrical effect, where the different observed physical properties reflect different lines of sight toward an equatorial accretion disk wind, with the angle between the accretion disk rotational axis and our line of sight increasing going from NAL, to mini-BAL, to BAL QSOs. However,

the situation is likely more complex, because the disk wind geometrical and dynamical properties strongly depend on AGN parameters such as the black hole mass, the Eddington ratio, the X-ray/UV flux ratio. Furthermore, as shown in Chapter 7, the likely physical scenario is more complicated than what usually is assumed in terms of breaking of spherical symmetry, photoionization equilibrium, and so on. Despite the complex scientific case, the field of AGN disk wind studies is rapidly growing, and more and more pieces are being placed on the big puzzle, thanks to the contribution of both observational and theoretical large efforts. Understanding the physical details of the accretion/ejection process in AGN is mandatory not only to understand the physics of SMBHs, but also to quantify the impact of AGN feedback on the surrounding media and to unveil the growth of the cosmic structures.

Appendices

Appendix A

Publications

Refereed Publications

2011 A& A, submitted

Giustini M., et al.

“Variable X-ray absorption in the mini-BAL QSO PG 1126-041”

2009 ApJ 706, 644

Chartas G., Saez C., Brandt W.N., **Giustini M.**, and Garmire G.P.

“Confirmation of and Variable Energy Injection by a Near-Relativistic Outflow in APM 08279+5255”

2009 A&A 504, 401

Cappi M., Tombesi F., Bianchi S., Dadina M., **Giustini M.**, et al.

“X-ray evidence for a mildly relativistic and variable outflow in the luminous Seyfert 1 galaxy Mrk 509”

2009 NewAR 53, 128

Chartas G., Charlton J., Eracleous M., **Giustini M.**, et al.

“High velocity outflows in narrow absorption line quasars”

2008 A&A 491, 425,

Giustini M., Cappi M., and Vignali C.

“On the absorption of X-ray bright broad absorption line quasars”

2008 A&A 483, 137,

Ballo L., **Giustini M.**, Schartel N., et al.

“X-ray spectral variability in PG 1535+547: the changing look of a ‘soft X-ray weak’ AGN”

Non refereed Publications

2010, AIPC 1248, 437,

Giustini M., Cappi M., Chartas G., Eracleous M., Palumbo G.G.C., and Vignali C.

“A Deep Look at the Inner Regions of the mini-BAL QSO PG 1126-041 with XMM-Newton”

2010, IAUS 267, 397,

Giustini M., Cappi M., Chartas G., Eracleous M., Palumbo G.G.C., and Vignali C.

“Complex X-ray spectral variability in mini-BAL QSOs”

2010, AAS 21541130,

Chartas G., Brandt W.N., Saez C., **Giustini M.**, and Garmire G.P.

“Confirmation of a Near-relativistic Wind in the $z=3.91$ Quasar APM 08279+5255”

2010, ASPC 427, 108,

Giustini M., Cappi M., Chartas G., Eracleous M., Palumbo G.G.C., and Vignali C.

“Variable X-ray Absorption in mini-BAL QSOs”

2009 AIPC 1126, 245

Giustini M., Cappi M., Vignali C., Palumbo G.G.C., Fiore F., and Malaguti G.

“The Simbol-X perspective on the physics of quasar outflows”

2008 MmSAI 79, 123, Cappi M., Tombesi F., and **Giustini M.**,

“Outflows and winds in AGNs: a case for Simbol-X”

Appendix B

List of acronyms

2XMM: Second XMM-Newton (serendipitous catalog)

ACIS: Advanced CCD Imaging Spectrometer

AGN: Active Galactic Nuclei

AI: Absorption Index

APM: Automatic Plate Machine

ARF: Ancillary Response File

ASCA: Advanced Satellite for Cosmology and Astrophysics

BAL: Broad Absorption Line

BeppoSAX: Beppo - Satellite per Astronomia in raggi X

BH: Black Hole

BI: Balnicity Index

CCD: Charge-Coupled Device

CR: Cosmic Ray

CSO: Case Stellar Object

CXB: Cosmic X-ray Background

EPIC: European Photon Imaging Camera

EXOSAT: European X-Ray Observatory Satellite

FITS: Flexible Image Transport System

FOV: Field of View

FUSE: Far Ultraviolet Spectroscopic Explorer

FWHM: Full Width at Half Maximum

HiBAL: High ionization Broad Absorption Line

HST: Hubble Space Telescope

IAU: International Astronomical Union

IRAS: Infrared Astronomical Satellite

IUE: International Ultraviolet Explorer

LBQS: Large Bright Quasar Survey

Λ CDM: Λ Cold Dark Matter

LD: Line Driven

LoBAL: Low ionization Broad Absorption Line

mini-BAL: mini-Broad Absorption Line

MOS: Metal Oxide Semi-conductor

NAL: Narrow Absorption Line

NIR: Near Infrared

NLR: Narrow Line Region

ODF: Observation Data File

OM: Optical Monitor

PG: Palomar-Green

PSF: Point Spread Function

QSO: Quasi Stellar Object, used in this Thesis as a synonym for Quasar

RGS: Reflection Grating Spectrometer

RL: Radio Loud

RMF: Redistribution Matrix File

RMS: Root Mean Square

ROSAT: Roentgen Satellite

RQ: Radio Quiet

SAS: Science Analysis Software

SDSS: Sloan Digital Sky Survey

SED: Spectral Energy Distribution

SMBH: Super Massive Black Hole

UFO: Ultra Fast Outflow

UV: Ultraviolet

VLT: Very Large Telescope

XIS: X-ray Imaging Spectrometer

XMM: X-ray Multi-mirror Mission

XSA: XMM-Newton Science Archive

List of Figures

2.1	Top left panel: STIS spectrum of the BAL QSO PG 0946+301, from Arav et al. (2001). Middle left panel: Lick spectrum of the mini-BAL QSO PG 0935+417, from Rodríguez Hidalgo et al. (2011). Bottom left panel: VLT (red) and Keck (black) spectra of the NAL QSO J2123-0050, from Hamann et al. (2011). Top right panel: <i>XMM-Newton</i> RGS spectrum of IRAS 13349+2438, showing the X-ray warm absorber, from Sako et al. (2001). Middle right panel: Suzaku XIS spectrum of PDS 456, showing a X-ray UFO in the iron K band, from Reeves et al. (2009). Bottom right panel: X-ray BALs detected by <i>Chandra</i> ACIS in APM 08279+5255, from Chartas et al. (2009c) To appreciate the different width of the absorption features, notice the different wavelength/energy scale in the different panels.	10
2.2	Composite SDSS spectra of different BAL subclasses, compared with the mean QSO (in black), taken from Reichard et al. (2003a).	13
2.3	Two phenomenological scenarios for accretion disk winds. Top panel: Figure 1 from Elvis (2000). Bottom panel: Figure 13 from Ganguly et al. (2001).	17

2.4	The veracity of X-ray UFOs has been lately confirmed. Panel a): measured outflow velocity versus cosmological recession velocity for a sample of high-velocity X-ray outflows, from McKernan et al. (2004). Panel b): location in the sky of the AGN with high-velocity X-ray outflows detected, taken from Cappi (2006), superimposed on the <i>ROSAT</i> 0.75 keV map taken from Snowden et al. (1997) where the color scale is in 10^{-6} ct s $^{-1}$ arcmin $^{-2}$. Panel c): equivalent width and its associate error for the absorption lines associated to high-velocity X-ray outflows taken from Vaughan & Uttley (2008), plotted in logarithmic scale. Panel d): equivalent width and its associate error for the absorption lines associated to high-velocity X-ray outflows taken from Tombesi et al. (2010a), plotted in linear scale.	19
2.5	Sketches of two possible geometries for accretion disk winds. Left panel: the UV line-driven wind of Murray et al. (1995), as readapted by Gallagher & Everett (2007); right panel: the magnetically driven wind of Everett (2005).	21
2.6	Left panel: a failed wind is formed in the inner regions of the LD wind model of Proga (2005). Right panel: the magnetically driven wind model of Fukumura et al. (2010b).	22
3.1	Redshift distribution of the 54 SDSS/2XMM BAL QSOs analyzed in this work. The shaded histogram refers to the 21 BAL QSOs taken from Shen et al. (2008), while the empty histogram refers to the 33 BAL QSOs taken from Trump et al. (2006). The thick histogram indicates the 22 sources on which spectral analysis has been performed.	29
3.2	Observed hardness ratio and 1σ associate errors for the 32 SDSS/2XMM BAL QSOs with a low X-ray S/N. The continuous tracks represent the simulated hardness ratios for different redshift and column density values which are, from bottom to top: $N_H = (0.01, 0.1, 0.5, 1.0, 5.0, 10, 50, 100) \times 10^{22}$ cm $^{-2}$	33

3.3	Left panel: photon index distribution for the 22 SDSS/2XMM BAL QSOs with spectral analysis available. Right panel: neutral column density distribution for the 22 SDSS/2XMM BAL QSOs with spectral analysis (thick histograms) and for the 32 SDSS/2XMM BAL QSOs with hardness ratio analysis (thin histograms) available. The shaded histogram refers to the BAL QSOs taken from Shen et al. (2008), left-pointing arrows represent upper limits.	35
3.4	Left panel: measured photon indices versus redshift. Right panel: column densities in units of 10^{22} cm^{-2} versus redshift: filled symbols refer to the 22 SDSS/2XMM BAL QSOs with spectral analysis available, where downward-pointing triangles are upper limits at the 90% confidence level. Empty symbols refer to the 32 SDSS/2XMM BAL QSOs with hardness ratio available, where arrows are upper limits at the 68% confidence level.	36
3.5	Left panel: α_{ox} distribution for the 54 SDSS/2XMM BAL QSOs, where the shaded histogram refers to the 21 sources taken from Shen et al. (2008) and the thick histogram refers to the 22 sources on which spectral analysis was performed. Right panel: comparison between the α_{ox} measured for the 54 SDSS/2XMM BAL QSOs studied in this work and for the 35 LBQS BAL QSOs (shaded histograms) studied by Gallagher et al. (2006).	37
3.6	Measured α_{ox} versus $\alpha_{\text{ox}}(\ell_{2500})$, where open (blue) circles are the 22 SDSS/2XMM BAL QSOs on which X-ray spectral analysis was performed, filled (red) circles are the 32 SDSS/2XMM BAL QSOs on which X-ray hardness ratio analysis was performed.	38
3.7	Distribution of neutral absorbing column densities (left panel) and α_{ox} (right panel), where the shaded histograms refer to the 30 SDSS/2XMM BAL QSOs with $\langle \text{AI} \rangle \sim 500 \text{ km s}^{-1}$ and the empty histograms refer to the 24 SDSS/2XMM BAL QSOs with $\langle \text{AI} \rangle \sim 2000 \text{ km s}^{-1}$. Arrows indicate upper limits.	41
3.8	Absorption Index versus measured X-ray absorbing column density for the SDSS/2XMM BAL QSOs with spectral analysis available (open circles) and with hardness ratio analysis available (filled circles).	42

3.9	$\Delta\alpha_{\text{ox}}$ versus maximum velocity UV outflow for the SDSS/2XMM BAL QSOs with spectral analysis available (open circles) and with hardness ratio analysis available (filled circles).	43
3.10	Source spectra of the 22 SDSS/2XMM BAL QSOs with spectral analysis available. EPIC-pn data points are plotted thick and black, while EPIC-MOS data are plotted thin and red. The inset contains confidence contours at 68, 90 and 99% confidence level for the column density N_H and photon index Γ , where the vertical line marks the amount of Galactic neutral absorption. In the top-right corner is reported a “T” for BALQSOs selected from Trump et al. (2006), a “S” for BALQSOs selected from Shen et al. (2008).	52
3.10	– Continued	53
3.10	– Continued	54
3.10	– Continued	55
4.1	Left panel: histogram of covering fraction values obtained from fitting a neutral partial covering absorber model to the PG sources. Right panel: theoretical model for a neutral absorber covering 5% (left) and 99.6% (right) of the same continuum source.	66
4.2	Left panel: covering fraction versus neutral column density for the 13 spectra of the PG sources well reproduced by the neutral partial covering absorber model. Right panel: ionization parameter versus warm column density for the 14 spectra well reproduced by the ionized absorber model. Red points mark spectra with a $\Gamma > 2$, black points mark spectra with $\Gamma \sim \langle \Gamma \rangle$, blue points mark spectra with $\Gamma < 1.6$	67
4.3	Example of variability over ks time scales of X-ray absorption lines in the iron K band of the mini-BAL QSOs PG 1126-041 (on the left) and PG 1114+445 (on the right).	68
4.4	Example of variability over long time scales of both the low ionization absorber (on the left) and the X-ray BALs (on the right) of the mini-BAL QSO PG 1115+080	69

4.5	Example of broad band spectral variability over year time scales in the mini-BAL QSO PG 1351+640 (left), over day time scales in the mini-BAL QSO PG 1535+547 (right).	70
4.6	Example of spectral variability of the BAL QSO PG 2112+059 over year time scales (left panel) and on ks time scales (right panel).	70
4.7	0.2-10 keV pn spectra for each exposure, for each PG QSO with $\gtrsim 500$ net counts collected. Data points have been visually rebinned to 8σ significance. For each source, the left, middle, and right panel report the result of a fit to a power law model in the 0.2-10, 2-5, and 2-10 keV range, respectively. The bottom small panels report the data/model ratio, or the data/model residuals in unit of σ for the sources with the lowest S/N, $\lesssim 800$ net counts.	73
4.7	– Continued	74
4.7	– Continued	75
4.8	0.2-10 keV pn spectra for each exposure, for each PG QSO with $\gtrsim 500$ net counts collected. Data points have been visually rebinned to 8σ significance. For each source, the left and right panel report the result of the fit to Model 3 and 4, respectively. For PG 1115+080 also the fit to Model 2 is reported, in the leftmost panel, for each epoch. The bottom small panels report the data/model ratio, or the data/model residuals in unit of σ for the sources with the lowest S/N, $\lesssim 800$ net counts.. The photon index value corresponding to each model is reported in the top right corner of each panel.	77
5.1	Variability over month time scales. Left panel: background subtracted 0.2-10 keV pn light curves extracted in the four different epochs of observations of PG 1126-041 and binned to 2 ks: December 2004 (blue circles), June 2008 (red squares), December 2008 (green triangles), and 2009 Long Look (black circles). Right panel: the time-averaged pn spectra corresponding to the time intervals shown on the left and using the same color codes.	82

5.2	<p>Variability over kilosecond time scales detected during the 2009 Long Look observation. Left panel: RMS variability computed for the pn observation over the 0.2-10 keV band; arrows mark upper limits, error bars are at 1σ confidence level. Middle panel: 0.2-1.5 and 1.5-10 keV background subtracted pn light curves binned to 2 ks; the numbers in the 1.5-10 keV light curve mark the eight time intervals on which time resolved spectral analysis was performed. Right Panel: three representative spectra extracted during the 2nd, the 7th, and the 8th time intervals of the 2009 Long Look observation.</p>	82
5.3	<p>Average 2009 Long Look pn (black), MOS1 (red), and MOS2 (green) spectra of PG 1126-041 modelled with a powerlaw absorbed by the Galactic interstellar medium. Bottom panel shows data/model ratio and identifies three main deviations from the simple powerlaw: (a) strong residuals, both positive and negative, in the soft band $E \lesssim 1.5$ keV; (b) negative residuals in the hard band, $E \gtrsim 7$ keV; and (c) a low energy cutoff at $2 \lesssim E \lesssim 6$ keV.</p>	84
5.4	<p>Average 0.2-10 keV pn spectral residuals in units of σ to the baseline model, after the inclusion of each component: (I) top panels: a power law continuum emission; (II) middle panels: after the inclusion of a moderately ionized absorber; (III) bottom panels: after the inclusion of a highly ionized outflowing absorber. Left column: 2009 Long Look data; right column: simultaneous fit to the Dec. 2004 (blue squares), Jun. 2008 (red circles), and Dec. 2008 (green triangles) data. The spectra have been rebinned for plotting purposes only to 8σ significance.</p>	85
5.5	<p>Left panel: 68% (black solid line) and 90% (red dotted line) confidence contours for the column density and ionization parameter of a moderately ionized layer of gas absorbing a power law continuum emission, for the four different epochs of observation. Right panel: theoretical model for two representative states (blue line for Dec. 2004, green line for Dec. 2008) of the moderately ionized absorber.</p>	86

- 5.6 Main characteristics of the highly ionized outflowing absorber detected during the 2009 observation of PG 1126-041. Panel (I): 5-10 keV pn data residuals to a power law emission absorbed by moderately ionized gas with $N_{m.i.} \sim 8.5 \times 10^{22} \text{ cm}^{-2}$, $\log \xi_{m.i.} \sim 1.52 \text{ erg cm s}^{-1}$. The two arrows mark strong negative residuals at ~ 6.7 and 7 keV in the observer frame. Panel (II): 68% (black), 90% (red) and 99%(green) confidence contours for the observer frame centroid energies and Equivalent Widths of the two Gaussian absorption lines used to fit the residuals. The two dashed vertical lines mark the FeXXV $K\alpha$ and FeXXVI $K\alpha$ transition energies, both blueshifted by $v_{\text{out}} = 0.055c$. Panel (III): Absorption features in a model of a highly ionized absorber with $N_{h.i.} \sim 9.7 \times 10^{23} \text{ cm}^{-2}$, $\log \xi_{h.i.} \sim 3.6 \text{ erg cm s}^{-1}$, outflowing at $v_{\text{out}} \sim 0.055c$, used to fit the residuals. The opacity at the lowest energies is due to Galactic photoelectric absorption. 87
- 5.7 Top panel: magnified view in the 3-7.5 keV of the ratio of the average pn spectrum from the 2009 Long Look to the baseline model (bottom line in Table 5.3). The red dashed line marks the Fe I $K\alpha$ energy in the observer frame. The points have been rebinned to 10 (thin line) and 20 (thick line) σ confidence level for displaying purpose only. The remaining panels show the residuals from: (a) broad Gaussian emission line modeling; (b) Laor emission line modeling; (c) partial covering absorber modeling; (d) relativistic reflection modeling, where all the models include a weak narrow Gaussian Fe I $K\alpha$ emission line. 89
- 5.8 Three different models that can reproduce the spectral curvature observed in the iron K band during the 2009 Long Look observation. Left panel: a partial covering scenario; middle panel: a relativistic reflection scenario; right panel: a phenomenological Gaussian model. In all the panels, the thin black line is the intrinsic power law continuum, the blue dashed line (where present) is the reflected emission component, and the thick red line is the sum of all the components, that in all cases is then absorbed by both the moderately and the highly ionized absorber as in the baseline model. 92

5.9	Zoom into the 0.2-3 keV 2009 Long Look pn residuals to the baseline model, after the inclusion of different further components. Top panel: a secondary, soft power law. Small panels: (a) a soft power law plus two narrow Gaussian emission lines; (b) a soft power law plus emission from a photoionized plasma; (c) a soft power law plus thermal emission; (d) photoionized plus thermal emission.	94
5.10	Two different models of the soft band of PG 1126-041 capable of reproducing the 2009 Long Look average EPIC spectra. Left panel: secondary soft power law (dashed orange line) plus two narrow Gaussian emission lines (thick orange lines). Right panel: photoionized emission (thin orange line) plus thermal emission (thin magenta line). Both models also include a broad (dashed blue line) and a narrow (thick blue line) Gaussian emission line in the iron K band, and the two ionized absorbers of the baseline model. The sum of all the components is the thick red line.	95
5.11	Ratio between the pn data extracted in the eight different time intervals marked in Fig. 5.2 to the best fit model for the average 2009 Long Look pn data of PG 1126-041. Points have been visually rebinned to 15 σ confidence level.	97
5.12	PG 1126-041: 5-8 keV residuals for each temporal slice to a model where the highly ionized outflowing absorber was removed. From top to bottom: 1 st (black), 2 nd (red), 3 rd + 5 th (green), 4 th + 6 th (blue), 7 th (magenta), and 8 th (orange) interval.	98
6.1	Left panel: histogram of the measured α_{ox} for the NAL QSO sample of Chartas et al. (2009a), compared with the α_{ox} distribution for type 1 RQ SDSS QSOs taken from Steffen et al. (2006). Right panel: measured $\Delta\alpha_{\text{ox}}$ distribution for different samples of QSOs, from top to bottom: the NAL QSO sample of Chartas et al. (2009a); the (UV unabsorbed) type 1 RQ SDSS QSOs taken from Steffen et al. (2006); the SDSS/2XMM BAL QSOs taken from Giustini et al. (2008); and the LBQS BAL QSO sample taken from Gallagher et al. (2006).	114

- 6.2 Left Panel: *Chandra* spectra of APM 08279+5255; right panel: *XMM-Newton* spectra of APM 08279+5255. The best fit model (solid thick line) is a power law absorbed by neutral gas at the source, plus two broad, blueshifted absorption lines in the iron K band with variable depth and velocity shift between the different observations. 115
- 6.3 Left panel: $\Gamma - v_{out}$ correlation for the X-ray BALs of APM 08279+5255, from Chartas et al. (2009c); right panel: a sketch of a possible geometry for accretion disk winds that can explain the X-ray BALs of APM 08279+5255, from (Chartas et al. 2009a). 116
- 7.1 The three “typical” streamlines for accretion disk winds. Number 1: MHD-typical, polar and convex streamline. Number 2: LD-typical, equatorial and concave streamline. Number 3: a radial streamline typical of spherically symmetric winds. R_0 marks the inner radius of the accretion disk; R_{launch} the wind launching radius. 118
- 7.2 Left: accretion disk surface temperature $T(R)$ for a black hole with $M_{BH} = 10^8 M_\odot$, at different accretion rates: $\lambda = 1$ (solid), 0.5 (dotted), 0.1 (dashed), and 0.01 (dashed-dotted line). Right: radius at which $T(R) = 50000$ K as a function of the central M_{BH} , for different accretion rates where the lines are coded as in the left panel. In both panels, the radius is normalized to the inner disk radius R_0 , that is assumed to be $6r_g$ 120
- 7.3 Representative profiles of interesting physical parameters of a LD accretion disk wind taken from the Proga & Kallman (2004) 2D model, see text for details. From top left, in clockwise direction: (a) map of the density distribution; (b) map of the poloidal velocity distribution; (c) the location of the resonance points along the flow for five different inclination angles, with the blueshift velocity proportional to the size of the empty circles; (d) map of $\log \dot{M}_{out}^{sph} / \dot{M}_{out}$, where \dot{M}_{out}^{sph} is the mass loss rate computed assuming spherical symmetry, \dot{M}_{out} is the actual disk wind mass loss rate. 122

7.4 Top panel: blueshifted absorption line profiles computed for the LD accretion disk wind model of Proga & Kallman (2004) as seen by five different inclination angles, , 60, 65, 70, 75, and 80 degrees from the disk rotational axis for the black, red, green, blue, and light blue, respectively; see text for details. Bottom panels: velocity, optical depth, and density radial profiles for the same inclination angles and the same color code as above. 125

List of Tables

3.1	The SDSS/2XMM BAL QSO sample	47
3.2	X-ray observations log for the 22 SDSS/2XMM BAL QSOs with Spectral Analysis available	48
3.3	SDSS/2XMM BAL QSOs: spectral analysis results	49
3.4	SDSS/2XMM BAL QSOs: hardness ratio analysis results	50
3.5	SDSS/2XMM BAL QSOs: optical/X-ray properties	51
4.1	General properties of the 15 QSOs analyzed in this work. These are all the PG QSOs classified as BAL, mini-BAL, or NAL QSOs with public archival <i>XMM-Newton</i> observations as of January 2011.	60
4.2	X-ray observation log of the BAL, mini-BAL, and NAL PG QSOs.	61
4.3	Fit to the PG QSOs with simple power law models	72
4.4	Fit to the PG QSOs with absorption models	76
5.1	Main properties of PG 1126-041	80
5.2	X-ray observation log for PG 1126-041	107
5.3	Average pn spectra of PG 1126-041 reproduced by the baseline model.	108
5.4	Spectral analysis on the average spectra of PG 1126-041: best fit model.	109
5.5	2009 Long Look observation time slices over which time resolved analysis was performed.	110
5.6	PG 1126-041: time resolved spectral analysis of the 2009 Long Look pn observation	111
5.7	PG 1126-041: optical photometry	112
5.8	PG 1126-041: optical/X-ray photometry	112

Bibliography

- Abbott, D. C. 1982, *ApJ*, 263, 723
- Akylas, A., Georgantopoulos, I., Georgakakis, A., Kitsionas, S., & Hatziminaoglou, E. 2006, *A&A*, 459, 693
- Aldcroft, T. L. & Green, P. J. 2003, *ApJ*, 592, 710
- Allen, J. T., Hewett, P. C., Maddox, N., Richards, G. T., & Belokurov, V. 2011, *MNRAS*, 410, 860
- Anders, E. & Grevesse, N. 1989, *Geochim. Cosmochim. Acta*, 53, 197
- Arav, N., de Kool, M., Korista, K. T., et al. 2001, *ApJ*, 561, 118
- Arnaud, K. A. 1996, in *Astronomical Society of the Pacific Conference Series*, Vol. 101, *Astronomical Data Analysis Software and Systems V*, ed. G. H. Jacoby & J. Barnes, 17
- Avni, Y. 1976, *ApJ*, 210, 642
- Ballo, L., Giustini, M., Schartel, N., et al. 2008, *A&A*, 483, 137
- Balsara, D. S. & Krolik, J. H. 1993, *ApJ*, 402, 109
- Balucinska-Church, M. & McCammon, D. 1992, *ApJ*, 400, 699
- Barlow, T. A., Hamann, F., & Sargent, W. L. W. 1997, in *Astronomical Society of the Pacific Conference Series*, Vol. 128, *Mass Ejection from Active Galactic Nuclei*, ed. N. Arav, I. Shlosman, & R. J. Weymann, 13–+
- Barlow, T. A. & Sargent, W. L. W. 1997, *AJ*, 113, 136
- Becker, R. H., Gregg, M. D., Hook, I. M., et al. 1997, *ApJL*, 479, L93+

Becker, R. H., White, R. L., Gregg, M. D., et al. 2000, *ApJ*, 538, 72

Boroson, T. A. & Green, R. F. 1992, *ApJS*, 80, 109

Boroson, T. A. & Meyers, K. A. 1992, *ApJ*, 397, 442

Braitto, V., Della Ceca, R., Piconcelli, E., et al. 2004, *A&A*, 420, 79

Braitto, V., Reeves, J. N., Dewangan, G. C., et al. 2007, *ApJ*, 670, 978

Brandt, W. N. & Gallagher, S. C. 2000, *NewAR*, 44, 461

Brandt, W. N., Laor, A., & Wills, B. J. 2000, *ApJ*, 528, 637

Canalizo, G. & Stockton, A. 2001, *ApJ*, 555, 719

Cappi, M. 2006, *Astronomische Nachrichten*, 327, 1012

Cappi, M., Tombesi, F., Bianchi, S., et al. 2009, *A&A*, 504, 401

Cappi, M., Tombesi, F., & Giustini, M. 2008, *MemSAIt*, 79, 123

Cardelli, J. A., Clayton, G. C., & Mathis, J. S. 1989, *ApJ*, 345, 245

Cash, W. 1979, *ApJ*, 228, 939

Castor, J. I., Abbott, D. C., & Klein, R. I. 1975, *ApJ*, 195, 157

Chartas, G., Brandt, W. N., & Gallagher, S. C. 2003, *ApJ*, 595, 85

Chartas, G., Brandt, W. N., Gallagher, S. C., & Garmire, G. P. 2002, *ApJ*, 579, 169

Chartas, G., Brandt, W. N., Gallagher, S. C., & Proga, D. 2007, *AJ*, 133, 1849

Chartas, G., Charlton, J., Eracleous, M., et al. 2009a, *New Astronomy Review*, 53, 128

Chartas, G., Kochanek, C. S., Dai, X., Poindexter, S., & Garmire, G. 2009b, *ApJ*, 693, 174

Chartas, G., Saez, C., Brandt, W. N., Giustini, M., & Garmire, G. P. 2009c, *ApJ*, 706, 644

Chelouche, D. & Netzer, H. 2005, *ApJ*, 625, 95

Churazov, E., Gilfanov, M., Forman, W., & Jones, C. 1996, *ApJ*, 471, 673

Ciotti, L. & Ostriker, J. P. 2001, *ApJ*, 551, 131

Ciotti, L., Ostriker, J. P., & Proga, D. 2009, *ApJ*, 699, 89

Collinge, M. J., Brandt, W. N., Kaspi, S., et al. 2001, *ApJ*, 557, 2

Crenshaw, D. M., Kraemer, S. B., Boggess, A., et al. 1999, *ApJ*, 516, 750

Crenshaw, D. M., Kraemer, S. B., & George, I. M. 2003, *ARA&A*, 41, 117

Croton, D. J., Springel, V., White, S. D. M., et al. 2006, *MNRAS*, 365, 11

Dadina, M., Cappi, M., Malaguti, G., Ponti, G., & de Rosa, A. 2005, *A&A*, 442, 461

Dai, X., Kochanek, C. S., Chartas, G., et al. 2010, *ApJ*, 709, 278

Dai, X., Shankar, F., & Sivakoff, G. R. 2008, *ApJ*, 672, 108

Dasyra, K. M., Tacconi, L. J., Davies, R. I., et al. 2007, *ApJ*, 657, 102

de La Calle Pérez, I., Longinotti, A. L., Guainazzi, M., et al. 2010, *A&A*, 524, A50+

Di Matteo, T., Springel, V., & Hernquist, L. 2005, *Nature*, 433, 604

Dickey, J. M. & Lockman, F. J. 1990, *ARA&A*, 28, 215

Dorodnitsyn, A. & Kallman, T. 2009, *ApJ*, 703, 1797

Elvis, M. 2000, *ApJ*, 545, 63

Elvis, M. 2006, *Memorie della Societa Astronomica Italiana*, 77, 573

Elvis, M., Maccacaro, T., Wilson, A. S., et al. 1978, *MNRAS*, 183, 129

Elvis, M., Marengo, M., & Karovska, M. 2002, *ApJL*, 567, L107

Elvis, M., Wilkes, B. J., McDowell, J. C., et al. 1994, *ApJS*, 95, 1

Everett, J. E. 2005, *ApJ*, 631, 689

Everett, J. E. 2007, *Ap&SS*, 311, 269

- Fabian, A. C., Iwasawa, K., Reynolds, C. S., & Young, A. J. 2000a, *PASP*, 112, 1145
- Fabian, A. C., Miniutti, G., Iwasawa, K., & Ross, R. R. 2005, *MNRAS*, 361, 795
- Fabian, A. C., Sanders, J. S., Etori, S., et al. 2000b, *MNRAS*, 318, L65
- Fabian, A. C., Sanders, J. S., Taylor, G. B., et al. 2006, *MNRAS*, 366, 417
- Farrah, D., Lacy, M., Priddey, R., Borys, C., & Afonso, J. 2007, *ApJL*, 662, L59
- Ferrarese, L. & Merritt, D. 2000, *ApJL*, 539, L9
- Foltz, C., Wilkes, B., Weymann, R., & Turnshek, D. 1983, *PASP*, 95, 341
- Frank, J., King, A., & Raine, D. J. 2002, *Accretion Power in Astrophysics: Third Edition*, ed. Frank, J., King, A., & Raine, D. J.
- Fukumura, K., Kazanas, D., Contopoulos, I., & Behar, E. 2010a, *ApJ*, 715, 636
- Fukumura, K., Kazanas, D., Contopoulos, I., & Behar, E. 2010b, *ApJL*, 723, L228
- Gallagher, S. C., Brandt, W. N., Chartas, G., & Garmire, G. P. 2002a, *ApJ*, 567, 37
- Gallagher, S. C., Brandt, W. N., Chartas, G., Garmire, G. P., & Sambruna, R. M. 2002b, *ApJ*, 569, 655
- Gallagher, S. C., Brandt, W. N., Chartas, G., et al. 2006, *ApJ*, 644, 709
- Gallagher, S. C., Brandt, W. N., Laor, A., et al. 2001, *ApJ*, 546, 795
- Gallagher, S. C., Brandt, W. N., Wills, B. J., et al. 2004, *ApJ*, 603, 425
- Gallagher, S. C. & Everett, J. E. 2007, in *Astronomical Society of the Pacific Conference Series*, Vol. 373, *The Central Engine of Active Galactic Nuclei*, ed. L. C. Ho & J.-W. Wang, 305
- Gallagher, S. C., Hines, D. C., Blaylock, M., et al. 2007, *ApJ*, 665, 157
- Gallagher, S. C., Schmidt, G. D., Smith, P. S., et al. 2005, *ApJ*, 633, 71
- Ganguly, R., Bond, N. A., Charlton, J. C., et al. 2001, *ApJ*, 549, 133
- Ganguly, R. & Brotherton, M. S. 2008, *ApJ*, 672, 102

Ganguly, R., Eracleous, M., Charlton, J. C., & Churchill, C. W. 1999, *AJ*, 117, 2594

Ganguly, R., Masiero, J., Charlton, J. C., & Sembach, K. R. 2003, *ApJ*, 598, 922

Gebhardt, K., Bender, R., Bower, G., et al. 2000, *ApJL*, 539, L13

George, I. M. & Fabian, A. C. 1991, *MNRAS*, 249, 352

George, I. M., Turner, T. J., Netzer, H., et al. 1998, *ApJS*, 114, 73

Ghez, A. M., Klein, B. L., Morris, M., & Becklin, E. E. 1998, *ApJ*, 509, 678

Gibson, R. R., Jiang, L., Brandt, W. N., et al. 2009, *ApJ*, 692, 758

Giustini, M., Cappi, M., & Vignali, C. 2008, *A&A*, 491, 425

Green, P. J., Aldcroft, T. L., Mathur, S., & Schartel, N. 1997, *ApJ*, 484, 135

Green, P. J., Aldcroft, T. L., Mathur, S., Wilkes, B. J., & Elvis, M. 2001, *ApJ*, 558, 109

Green, P. J. & Mathur, S. 1996, *ApJ*, 462, 637

Green, P. J., Schartel, N., Anderson, S. F., et al. 1995, *ApJ*, 450, 51

Green, R. F., Schmidt, M., & Liebert, J. 1986, *ApJS*, 61, 305

Groenewegen, M. A. T., Lamers, H. J. G. L. M., & Pauldrach, A. W. A. 1989, *A&A*, 221, 78

Grupe, D., Komossa, S., & Gallo, L. C. 2007a, *ApJL*, 668, L111

Grupe, D., Mathur, S., & Elvis, M. 2003, *AJ*, 126, 1159

Grupe, D., Schady, P., Leighly, K. M., et al. 2007b, *AJ*, 133, 1988

Haardt, F. & Maraschi, L. 1991, *ApJL*, 380, L51

Haardt, F., Maraschi, L., & Ghisellini, G. 1994, *ApJL*, 432, L95

Hall, P. B., Anderson, S. F., Strauss, M. A., et al. 2002, *ApJS*, 141, 267

Halpern, J. P. 1984, *ApJ*, 281, 90

- Hamann, F., Barlow, T., Cohen, R. D., Junkkarinen, V., & Burbidge, E. M. 1997a, in *Astronomical Society of the Pacific Conference Series*, Vol. 128, *Mass Ejection from Active Galactic Nuclei*, ed. N. Arav, I. Shlosman, & R. J. Weymann, 19–+
- Hamann, F., Barlow, T. A., Beaver, E. A., et al. 1995, *ApJ*, 443, 606
- Hamann, F., Barlow, T. A., & Junkkarinen, V. 1997b, *ApJ*, 478, 87
- Hamann, F., Barlow, T. A., Junkkarinen, V., & Burbidge, E. M. 1997c, *ApJ*, 478, 80
- Hamann, F., Kanekar, N., Prochaska, J. X., et al. 2011, *MNRAS*, 410, 1957
- Hamann, F. & Sabra, B. 2004, in *Astronomical Society of the Pacific Conference Series*, Vol. 311, *AGN Physics with the Sloan Digital Sky Survey*, ed. G. T. Richards & P. B. Hall, 203
- Hasinger, G., Schartel, N., & Komossa, S. 2002, *ApJL*, 573, L77
- Hazard, C., McMahon, R. G., Webb, J. K., & Morton, D. C. 1987, *ApJ*, 323, 263
- Hewett, P. C. & Foltz, C. B. 2003, *AJ*, 125, 1784
- Hewett, P. C., Foltz, C. B., & Chaffee, F. H. 1995, *AJ*, 109, 1498
- Hopkins, P. F., Hernquist, L., Cox, T. J., et al. 2006, *ApJS*, 163, 1
- Jester, S., Schneider, D. P., Richards, G. T., et al. 2005, *AJ*, 130, 873
- Junkkarinen, V. T. 1983, *ApJ*, 265, 73
- Just, D. W., Brandt, W. N., Shemmer, O., et al. 2007, *ApJ*, 665, 1004
- Kaastra, J. S., Mewe, R., Liedahl, D. A., Komossa, S., & Brinkman, A. C. 2000, *A&A*, 354, L83
- Kalberla, P. M. W., Burton, W. B., Hartmann, D., et al. 2005, *A&A*, 440, 775
- Kallman, T. & Bautista, M. 2001, *ApJS*, 133, 221
- Kaspi, S., Brandt, W. N., George, I. M., et al. 2002, *ApJ*, 574, 643
- Kaspi, S., Brandt, W. N., Netzer, H., et al. 2000, *ApJL*, 535, L17

- Kellermann, K. I., Sramek, R., Schmidt, M., Shaffer, D. B., & Green, R. 1989, *AJ*, 98, 1195
- King, A. R. & Pounds, K. A. 2003, *MNRAS*, 345, 657
- Knigge, C., Scaringi, S., Goad, M. R., & Cottis, C. E. 2008, *MNRAS*, 386, 1426
- Komossa, S. & Meerschweinchen, J. 2000, *A&A*, 354, 411
- Königl, A. 2006, *MemSAIt*, 77, 598
- Konigl, A. & Kartje, J. F. 1994, *ApJ*, 434, 446
- Kormendy, J. & Richstone, D. 1995, *ARA&A*, 33, 581
- Krolik, J. H. & Kriss, G. A. 1995, *ApJ*, 447, 512
- Krolik, J. H. & Kriss, G. A. 2001, *ApJ*, 561, 684
- Krolik, J. H. & Voit, G. M. 1998, *ApJL*, 497, L5+
- Laor, A. 1991, *ApJ*, 376, 90
- Laor, A., Fiore, F., Elvis, M., Wilkes, B. J., & McDowell, J. C. 1997, *ApJ*, 477, 93
- Lapi, A., Cavaliere, A., & Menci, N. 2005, *ApJ*, 619, 60
- Lavalley, M., Isobe, T., & Feigelson, E. 1992, in *Astronomical Society of the Pacific Conference Series*, Vol. 25, *Astronomical Data Analysis Software and Systems I*, ed. D. M. Worrall, C. Biemesderfer, & J. Barnes, 245
- Liu, Y., Jiang, D. R., Wang, T. G., & Xie, F. G. 2008, *MNRAS*, 391, 246
- Lucy, L. B. & Solomon, P. M. 1970, *ApJ*, 159, 879
- Lusso, E., Comastri, A., Vignali, C., et al. 2010, *A&A*, 512, A34+
- Lynds, C. R. 1967, *ApJ*, 147, 396
- Lyons, L. 1991, *Data Analysis for Physical Science Students* (Cambridge: Cambridge Univ. Press)
- Magorrian, J., Tremaine, S., Richstone, D., et al. 1998, *AJ*, 115, 2285

- Malkan, M. A. & Sargent, W. L. W. 1982, *ApJ*, 254, 22
- Markowitz, A., Reeves, J. N., & Braitto, V. 2006, *ApJ*, 646, 783
- McKernan, B., Yaqoob, T., & Reynolds, C. S. 2004, *ApJ*, 617, 232
- McKernan, B., Yaqoob, T., & Reynolds, C. S. 2007, *MNRAS*, 379, 1359
- Miller, B. P., Brandt, W. N., Gallagher, S. C., et al. 2006, *ApJ*, 652, 163
- Miller, L., Turner, T. J., & Reeves, J. N. 2008, *A&A*, 483, 437
- Miller, L., Turner, T. J., & Reeves, J. N. 2009, *MNRAS*, 399, L69
- Miller, P., Rawlings, S., Saunders, R., & Eales, S. 1992, *MNRAS*, 254, 93
- Miniutti, G. & Fabian, A. C. 2004, *MNRAS*, 349, 1435
- Miniutti, G., Ponti, G., Dadina, M., Cappi, M., & Malaguti, G. 2007, *MNRAS*, 375, 227
- Misawa, T., Charlton, J. C., Eracleous, M., et al. 2007a, *ApJS*, 171, 1
- Misawa, T., Eracleous, M., Charlton, J. C., & Kashikawa, N. 2007b, *ApJ*, 660, 152
- Misawa, T., Eracleous, M., Charlton, J. C., & Tajitsu, A. 2005, *ApJ*, 629, 115
- Misawa, T., Eracleous, M., Chartas, G., & Charlton, J. C. 2008, *ApJ*, 677, 863
- Misawa, T., Kawabata, K. S., Eracleous, M., Charlton, J. C., & Kashikawa, N. 2010, *ApJ*, 719, 1890
- Misawa, T., Yamada, T., Takada-Hidai, M., et al. 2003, *AJ*, 125, 1336
- Montenegro-Montes, F. M., Mack, K., Benn, C. R., et al. 2009, *Astronomische Nachrichten*, 330, 157
- Moore, R. L. & Stockman, H. S. 1984, *ApJ*, 279, 465
- Morgan, C. W., Kochanek, C. S., Dai, X., Morgan, N. D., & Falco, E. E. 2008, *ApJ*, 689, 755
- Morris, S. L. 1988, *ApJL*, 330, L83

Murray, N., Chiang, J., Grossman, S. A., & Voit, G. M. 1995, *ApJ*, 451, 498

Mushotzky, R. F., Done, C., & Pounds, K. A. 1993, *ARA&A*, 31, 717

Nandra, K., Fabian, A. C., George, I. M., et al. 1993, *MNRAS*, 260, 504

Nandra, K., George, I. M., Mushotzky, R. F., Turner, T. J., & Yaqoob, T. 1997, *ApJ*, 477, 602

Nandra, K., O'Neill, P. M., George, I. M., & Reeves, J. N. 2007, *MNRAS*, 382, 194

Nandra, K., Pounds, K. A., & Stewart, G. C. 1990, *MNRAS*, 242, 660

Narayanan, D., Hamann, F., Barlow, T., et al. 2004, *ApJ*, 601, 715

Neugebauer, G., Green, R. F., Matthews, K., et al. 1987, *ApJS*, 63, 615

Ogle, P. M., Cohen, M. H., Miller, J. S., et al. 1999, *ApJS*, 125, 1

Otani, C., Kii, T., Reynolds, C. S., et al. 1996, *PASJ*, 48, 211

Page, K. L., Reeves, J. N., O'Brien, P. T., & Turner, M. J. L. 2005, *MNRAS*, 364, 195

Piconcelli, E., Jimenez-Bailón, E., Guainazzi, M., et al. 2005, *A&A*, 432, 15

Ponti, G., Cappi, M., Dadina, M., & Malaguti, G. 2004, *A&A*, 417, 451

Ponti, G., Cappi, M., Vignali, C., et al. 2009, *MNRAS*, 394, 1487

Pounds, K. A., Reeves, J. N., King, A. R., et al. 2003, *MNRAS*, 345, 705

Priddey, R. S., Gallagher, S. C., Isaak, K. G., et al. 2007, *MNRAS*, 374, 867

Pringle, J. E. 1981, *ARA&A*, 19, 137

Proga, D. 1999, *MNRAS*, 304, 938

Proga, D. 2005, *ApJL*, 630, L9

Proga, D. 2007, in *Astronomical Society of the Pacific Conference Series*, Vol. 373, *The Central Engine of Active Galactic Nuclei*, ed. L. C. Ho & J.-W. Wang, 267–+

Proga, D. & Kallman, T. R. 2004, *ApJ*, 616, 688

Proga, D., Stone, J. M., & Kallman, T. R. 2000, *ApJ*, 543, 686

Rees, M. J. 1984, *ARA&A*, 22, 471

Reeves, J. N., O'Brien, P. T., Braito, V., et al. 2009, *ApJ*, 701, 493

Reeves, J. N., O'Brien, P. T., & Ward, M. J. 2003, *ApJL*, 593, L65

Reichard, T. A., Richards, G. T., Hall, P. B., et al. 2003a, *AJ*, 126, 2594

Reichard, T. A., Richards, G. T., Schneider, D. P., et al. 2003b, *AJ*, 125, 1711

Reynolds, C. S. 1997, *MNRAS*, 286, 513

Reynolds, C. S., Fabian, A. C., Brenneman, L. W., et al. 2009, *MNRAS*, 397, L21

Risaliti, G., Bianchi, S., Matt, G., et al. 2005, *ApJL*, 630, L129

Risaliti, G., Elvis, M., Fabbiano, G., et al. 2007, *ApJL*, 659, L111

Rodríguez Hidalgo, P., Hamann, F., & Hall, P. 2011, *MNRAS*, 411, 247

Ross, R. R. & Fabian, A. C. 2005, *MNRAS*, 358, 211

Sabra, B. M., Hamann, F., Jannuzi, B. T., George, I. M., & Shields, J. C. 2003, *ApJ*, 590, 66

Sako, M., Kahn, S. M., Behar, E., et al. 2001, *A&A*, 365, L168

Sanders, D. B., Phinney, E. S., Neugebauer, G., Soifer, B. T., & Matthews, K. 1989, *ApJ*, 347, 29

Sanders, J. S., Fabian, A. C., & Taylor, G. B. 2009, *MNRAS*, 396, 1449

Sazonov, S. Y., Ostriker, J. P., Ciotti, L., & Sunyaev, R. A. 2005, *MNRAS*, 358, 168

Scannapieco, E. & Oh, S. P. 2004, *ApJ*, 608, 62

Scannapieco, E., Silk, J., & Bouwens, R. 2005, *ApJL*, 635, L13

Schartel, N., Rodríguez-Pascual, P. M., Santos-Lleó, M., et al. 2007, *A&A*, 474, 431

Schartel, N., Rodríguez-Pascual, P. M., Santos-Lleó, M., et al. 2005, *A&A*, 433, 455

Schlegel, D. J., Finkbeiner, D. P., & Davis, M. 1998, *ApJ*, 500, 525

Schmidt, G. D. & Hines, D. C. 1999, *ApJ*, 512, 125

Schmidt, M. 1963, *Nature*, 197, 1040

Schmidt, M. & Green, R. F. 1983, *ApJ*, 269, 352

Schneider, D. P., Hall, P. B., Richards, G. T., et al. 2007, *AJ*, 134, 102

Seyfert, C. K. 1943, *ApJ*, 97, 28

Shakura, N. I. & Sunyaev, R. A. 1973, *A&A*, 24, 337

Shankar, F., Dai, X., & Sivakoff, G. R. 2008, *ApJ*, 687, 859

Shemmer, O., Brandt, W. N., Gallagher, S. C., et al. 2005, *AJ*, 130, 2522

Shen, Y., Greene, J. E., Strauss, M. A., Richards, G. T., & Schneider, D. P. 2008, *ApJ*, 680, 169

Shu, X. W., Yaqoob, T., & Wang, J. X. 2010, *ApJS*, 187, 581

Shuder, J. M. & Osterbrock, D. E. 1981, *ApJ*, 250, 55

Silk, J. & Rees, M. J. 1998, *A&A*, 331, L1

Sim, S. A. 2005, *MNRAS*, 356, 531

Sim, S. A., Long, K. S., Miller, L., & Turner, T. J. 2008, *MNRAS*, 388, 611

Sim, S. A., Miller, L., Long, K. S., Turner, T. J., & Reeves, J. N. 2010a, *MNRAS*, 404, 1369

Sim, S. A., Proga, D., Miller, L., Long, K. S., & Turner, T. J. 2010b, *MNRAS*, 408, 1396

Snowden, S. L., Egger, R., Freyberg, M. J., et al. 1997, *ApJ*, 485, 125

Sobolev, V. V. 1960, *Moving envelopes of stars*, ed. Sobolev, V. V.

Sprayberry, D. & Foltz, C. B. 1992, *ApJ*, 390, 39

Steffen, A. T., Strateva, I., Brandt, W. N., et al. 2006, *AJ*, 131, 2826

- Stocke, J. T., Morris, S. L., Weymann, R. J., & Foltz, C. B. 1992, *ApJ*, 396, 487
- Strateva, I. V., Brandt, W. N., Schneider, D. P., Vanden Berk, D. G., & Vignali, C. 2005, *AJ*, 130, 387
- Surace, J. A., Sanders, D. B., & Evans, A. S. 2001, *AJ*, 122, 2791
- Surdej, J. & Hutsemekers, D. 1987, *A&A*, 177, 42
- Tananbaum, H., Avni, Y., Branduardi, G., et al. 1979, *ApJL*, 234, L9
- Tananbaum, H., Avni, Y., Green, R. F., Schmidt, M., & Zamorani, G. 1986, *ApJ*, 305, 57
- Tombesi, F., Cappi, M., Reeves, J. N., et al. 2010a, *A&A*, 521, A57+
- Tombesi, F., Sambruna, R. M., Reeves, J. N., et al. 2010b, *ApJ*, 719, 700
- Tozzi, P., Gilli, R., Mainieri, V., et al. 2006, *A&A*, 451, 457
- Trump, J. R., Hall, P. B., Reichard, T. A., et al. 2006, *ApJS*, 165, 1
- Turner, T. J. & Kraemer, S. B. 2003, *ApJ*, 598, 916
- Turner, T. J. & Miller, L. 2009, *A&ARv*, 17, 47
- Turner, T. J., Nandra, K., George, I. M., Fabian, A. C., & Pounds, K. A. 1993, *ApJ*, 419, 127
- Turnshek, D. A. 1984, *ApJ*, 280, 51
- Turnshek, D. A., Weymann, R. J., Liebert, J. W., Williams, R. E., & Strittmatter, P. A. 1980, *ApJ*, 238, 488
- Urrutia, T., Becker, R. H., White, R. L., et al. 2009, *ApJ*, 698, 1095
- Vaughan, S., Edelson, R., Warwick, R. S., & Uttley, P. 2003, *MNRAS*, 345, 1271
- Vaughan, S. & Uttley, P. 2008, *MNRAS*, 390, 421
- Vestergaard, M. & Peterson, B. M. 2006, *ApJ*, 641, 689
- Vignali, C., Brandt, W. N., & Schneider, D. P. 2003, *AJ*, 125, 433

Voit, G. M., Weymann, R. J., & Korista, K. T. 1993, *ApJ*, 413, 95

Wang, J., Jiang, P., Zhou, H., et al. 2008, *ApJL*, 676, L97

Wang, T. G., Brinkmann, W., Wamsteker, W., Yuan, W., & Wang, J. X. 1999, *MNRAS*, 307, 821

Watson, M. G., Schröder, A. C., Fyfe, D., et al. 2009, *A&A*, 493, 339

Weymann, R. J., Carswell, R. F., & Smith, M. G. 1981, *ARA&A*, 19, 41

Weymann, R. J., Morris, S. L., Foltz, C. B., & Hewett, P. C. 1991, *ApJ*, 373, 23

Willis, A. G., Strom, R. G., & Wilson, A. S. 1974, *Nature*, 250, 625

Willott, C. J., Rawlings, S., & Grimes, J. A. 2003, *ApJ*, 598, 909

Wise, J. H., Eracleous, M., Charlton, J. C., & Ganguly, R. 2004, *ApJ*, 613, 129

Yaqoob, T., Murphy, K. D., Miller, L., & Turner, T. J. 2010, *MNRAS*, 401, 411

Yaqoob, T. & Padmanabhan, U. 2004, *ApJ*, 604, 63

Yaqoob, T., Warwick, R. S., & Pounds, K. A. 1989, *MNRAS*, 236, 153

York, D. G., Adelman, J., Anderson, Jr., J. E., et al. 2000, *AJ*, 120, 1579

Young, M., Elvis, M., & Risaliti, G. 2010, *ApJ*, 708, 1388